

TENSILE CREEP OF  
SIC WHISKER-REINFORCED ALUMINA COMPOSITES

By  
GUANG-CHUN QUAN

A Thesis  
Submitted to the School of Graduate Studies  
in Partial Fulfillment of the Requirements  
for the Degree  
Doctor of Philosophy

McMaster University

© Copyright by Guang-Chun Quan, April 2004

CREEP OF SIC WHISKER-REINFORCED  
ALUMINA COMPOSITES

DOCTOR OF PHILOSOPHY (2004)

McMaster University

(Materials Science and Engineering)

Hamilton, Ontario

TITLE: Creep of SiC whisker-reinforced Alumina.

AUTHOR: Guang-Chun Quan, M.E.S. (Monash University)

SUPERVISOR: D. S. Wilkinson

NUMBER OF PAGES: xvi, 169

## ABSTRACT

Alumina composites with 10, 20 and 30 volume % SiC whiskers were fabricated using colloidal processing methods followed by uniaxial hot pressing. The tensile creep properties of these materials have been studied between 1200°C and 1400°C.

The composite slurries showed the best stability at pH=2, which led to uniform distribution of whiskers in the final products. However, at pH $\geq$ 6 flocculation occurred between whiskers, resulting in whisker agglomerates in the matrix. Distribution of whiskers was characterised using neutron diffraction methods, which indicated that the whisker orientation could not be altered significantly by adjusting pH.

All the composites showed much superior tensile creep resistance compared to pure alumina and the effect of increasing whisker volume fraction was significant up to 30%. Relatively high stress exponents were found, which is most probably associated with much enhanced cavitation creep in tension. The activation energy varied with whisker volume fraction, temperature and applied stress in a complex manner. This combined with the temperature-dependent stress exponents makes the identification of creep mechanisms difficult. Nevertheless, it appears that at moderate stress level grain boundary diffusion and grain boundary sliding (GBS) become more significant as whisker volume fraction increases.

The composites containing 20 and 30% whiskers showed significant anelastic strain recovery (~0.001) following tensile creep, which is consistent with earlier reports that involved bending creep tests. The whisker bending effect was studied by measuring the peak width of (111) SiC planes (perpendicular to the whisker axis) at various conditions. The difference in the peak width at room temperature was found to be insignificant before and after creep. Moreover, during in-situ neutron diffraction measurement at 1400°C, no measurable variation in the peak width was recorded from the crept samples that were cooled under load. It may be that the neutron diffraction technique used in this study is not sufficiently sensitive to measure the small bending strains developed. However, These results along with other evidence in the literature suggest that Hertzian contact deformation of networked whiskers, rather than bending deformation of whiskers, may be the dominant mechanism to explain the observed anelastic strain

recovery. This mechanism predicts similar strain recovery in any composite that contains constrained 'hard' inclusions with sufficient contact numbers. Models based on this mechanism have been developed, which seem to predict the magnitude of the recoverable strain reasonably well.

## ACKNOWLEDGEMENTS

First of all, I thank God for His mercy on me.

I would like to thank my supervisor Professor David Wilkinson for his wisdom, guidance and help throughout the course of this research project. I am very grateful to Professors George Weatherly, Shiping Zhu, David Embury, Marek Niewczas. They kindly served as my supervisory committee members and provided valuable contributions to this thesis.

Constance Barry deserves a special thank who taught me how to use many things in the powder metallurgy laboratories. Without her help it was impossible to make the composite materials. She also proofread this thesis before examination, which is greatly appreciated.

Thanks to Dr. Kelly Conlon for guiding me to perform neutron scattering experiments. He was always available even by sacrificing weekends. Dr. John Root has been a source for many valuable insights and comments during my stay in Chalk River laboratories.

Drs. Yaoji Wang, Jingsong Wang and Hamid Azari taught me a lot especially on diffraction.

Doug Culley and Ed McCaffrey helped me with creep tests and Andy Duft, Steve Koprach and Fred Pearson with electron microscopy.

The graduate students and research fellows in A206 were always tremendous inspiration for me to persevere. I would like to thank them all especially Kevin Spencer, Andi Limarga, Kevin Boyle, Chad Sinclair, John Nichka and Christine Borsellino.

Special thanks to Hansoo Kim, Jia Liu, Drs. Jungsik Hwang and Sihai Wen who always supported me in good spirit. Jenny Jin really gave me a surprising lift to finish up my thesis. Thank you!

I cannot thank more Drs. Hui Guo and Jaeyoung Rhee who changed my life in amazing ways. My debt is beyond words.

Finally, I want to thank my mom and dad and sisters for their understanding and unfailing love. This thesis is dedicated to them.

# TABLE OF CONTENTS

|  |     |
|--|-----|
| <b>ABSTRACT</b> .....  | iii |
| <b>ACKNOWLEDGEMENTS</b> .....                                    | v   |
| <b>TABLE OF CONTENTS</b> .....                                   | vi  |
| <b>LIST OF FIGURES</b> .....                                     | x   |
| <b>LIST OF TABLES</b> .....                                      | xv  |
| <br>   |     |
| <b>CHAPTER 1 INTRODUCTION</b> .....                              | 1   |
| <br>   |     |
| <b>CHAPTER 2 LITERATURE REVIEW</b> .....                         | 4   |
| 2.1 Introduction.....  | 4   |
| 2.2 Ceramic powder processing.....                               | 4   |
| 2.2.1 Introduction.....  | 4   |
| 2.2.2 Stability of colloidal system.....                         | 5   |
| 2.2.3 Heteroflocculation.....                                    | 9   |
| 2.3 Constitutive relations in creep.....                         | 10  |
| 2.4 Creep in ceramics.....                                       | 12  |
| 2.4.1 Single phase ceramics.....                                 | 12  |
| 2.4.2 Multiphase ceramics.....                                   | 13  |
| 2.5 Creep of Al <sub>2</sub> O <sub>3</sub> -SiC composites..... | 16  |
| 2.5.1 SiC whisker-reinforced alumina.....                        | 16  |
| Stress exponent.....   | 17  |
| Reinforcement loading.....                                       | 21  |
| Low whisker loadings.....  | 24  |
| High whisker loadings.....                                       | 25  |
| Grain size effect on creep.....                                  | 27  |
| Creep strain recovery.....                                       | 29  |
| Tensile creep of SiC whisker-reinforced alumina.....             | 31  |
| Effect of whisker orientation on creep rate.....                 | 32  |
| Atmospheric effects on creep.....                                | 33  |
| Summary.....   | 34  |
| 2.5.2 SiC particulate-reinforced alumina.....                    | 34  |
| 2.5.3 SiC platelet-reinforced alumina.....                       | 35  |

|  |           |
|--|-----------|
| 2.5.4 Continuous fiber-reinforced ceramic composites.....                    | 37        |
| 2.6 Creep models for multiphase ceramics.....                                | 37        |
| 2.6.1 Creep in dilute systems.....   | 37        |
| 2.6.2 Creep due to particle rotation.....                                    | 38        |
| 2.6.3 Creep in constrained inclusion networks.....                           | 38        |
| 2.7 Residual stresses in Al <sub>2</sub> O <sub>3</sub> -SiC composites..... | 43        |
| 2.7.1 SiC whisker-reinforced alumina composites.....                         | 44        |
| 2.7.2 SiC particulate-reinforced alumina composites.....                     | 48        |
| 2.7.3 Summary.....   | 50        |
| <br>   |           |
| <b>CHAPTER 3 EXPERIMENTAL METHODS.....</b>                                   | <b>51</b> |
| 3.1 Introduction.....  | 51        |
| 3.2 Microscopy.....  | 51        |
| 3.2.1 Optical microscopy.....  | 51        |
| 3.2.2 Scanning electron microscopy.....                                      | 51        |
| 3.2.3 Transmission electron microscopy.....                                  | 52        |
| 3.3 Diffraction experiments.....   | 52        |
| 3.3.1 Powder diffraction.....  | 52        |
| 3.3.2 Neutron scattering.....  | 53        |
| Production of thermal neutrons for materials science.....                    | 53        |
| 3.3.3 Texture and strain measurements.....                                   | 56        |
| Instrumentation.....   | 56        |
| Texture measurement.....   | 56        |
| Quantification of whisker distribution.....                                  | 57        |
| Fitting of neutron diffraction peaks.....                                    | 61        |
| Lattice strain measurement.....  | 62        |
| 3.3.4 Residual strain/stress measurements at room temperature.....           | 63        |
| 3.3.5 In-situ high temperature neutron diffraction tests.....                | 67        |
| 3.4 Creep tests.....   | 68        |
| 3.4.1 Tensile creep test.....  | 68        |
| 3.4.2 Compressive creep test.....  | 72        |
| 3.4.3 Creep data analysis.....   | 72        |
| <br>   |           |
| <b>CHAPTER 4 MATERIALS PROCESSING.....</b>                                   | <b>74</b> |
| 4.1 Introduction.....  | 74        |



|   |            |
|---|------------|
| 4.2 Crystallography of SiC whiskers.....                          | 74         |
| 4.3 Powder characterization.....                                  | 78         |
| 4.4 Ceramic powder processing.....                                | 79         |
| 4.4.1 Introduction.....   | 79         |
| 4.4.2 Preparation of suspension.....                              | 80         |
| 4.4.3 Sintering.....  | 83         |
| <b>CHAPTER 5 RESULTS.....</b>                                     | <b>86</b>  |
| 5.1 Introduction.....   | 86         |
| 5.2 Microstructure.....   | 86         |
| 5.2.1 Optical microscopy.....                                     | 86         |
| 5.2.2 Scanning electron microscopy.....                           | 90         |
| 5.3 Creep.....  | 96         |
| 5.3.1 Introduction.....   | 96         |
| 5.3.2 Shape of creep curves.....                                  | 96         |
| 5.3.3 Steady-state strain rate plots.....                         | 99         |
| 5.3.4 Determination of activation energies.....                   | 103        |
| 5.3.5 Stress relaxation creep tests.....                          | 106        |
| 5.4 Whisker texture.....  | 107        |
| 5.5 Residual strains/stresses at room temperature.....            | 115        |
| 5.6 In-situ high temperature neutron diffraction experiments..... | 117        |
| <b>CHAPTER 6 DISCUSSIONS.....</b>                                 | <b>119</b> |
| 6.1 Introduction.....   | 119        |
| 6.2 Influence of processing on microstructure.....                | 119        |
| 6.2.1 Effect of pH.....   | 119        |
| 6.2.2 Effect of SiC content.....                                  | 120        |
| 6.3 Creep of pure alumina.....                                    | 122        |
| 6.4 Creep of composites.....                                      | 124        |
| 6.4.1 Effect of SiC content on creep.....                         | 124        |
| 6.4.2 Creep deformation mechanisms.....                           | 126        |
| Stress exponent.....  | 126        |
| Activation energy.....  | 129        |
| 6.4.3 Residual stresses.....                                      | 135        |
| 6.4.4 Effect of matrix grain size and whisker aspect ratio.....   | 138        |

|   |            |
|---|------------|
| 6.5 Anelastic strain recovery.....                                    | 140        |
| 6.5.1 Basic consideration and observations.....                       | 140        |
| 6.5.2 Peak broadening.....  | 141        |
| 6.5.3 Modeling of whisker bending.....                                | 148        |
| Assumptions.....  | 148        |
| Geometrical consideration.....  | 148        |
| Estimation of peak broadening.....                                    | 151        |
| Estimation of whisker bending from the recovered strain.....          | 154        |
| 6.5.4 Speculation on the origin of the anelastic strain recovery..... | 155        |
| <b>CHAPTER 7 SUMMARY AND CONCLUSIONS.....</b>                         | <b>162</b> |
| <b>REFERENCES.....</b>  | <b>164</b> |

## LIST OF FIGURES

|  |    |
|--|----|
| <b>Fig. 1.1</b> Rise in the operating temperature of jet engines with time. (Clark and Flemings 1986).....   | 2  |
| <b>Fig. 1.2</b> Performance progress of 300-kW metal and ceramic gas turbines. (Ohji 2001).....  | 2  |
| <b>Fig. 2.1</b> Surface charges on SiO <sub>2</sub> particles by adsorption of ions from acidic or basic solutions.....  | 6  |
| <b>Fig. 2.2</b> The distribution of positive and negative ions in the electrical double layer associated with a charged surface in a liquid.....   | 7  |
| <b>Fig. 2.3</b> Potential energy between two particles in a liquid. Flocculation occurs at M <sub>2</sub> and contact M <sub>1</sub> ....  | 7  |
| <b>Fig. 2.4</b> Zeta potential of alumina and SiC whisker as a function of suspension pH. (Jang 1992).....   | 9  |
| <b>Fig. 2.5</b> Heteroflocculation between alumina and SiC whisker particles. (Jang 1992).....   | 10 |
| <b>Fig. 2.6</b> A typical creep curve for a monolithic ceramic material. (Kingery 1962).....   | 11 |
| <b>Fig. 2.7</b> Schematic illustration of network development in a whisker-(or platelet-) reinforced ceramic. Volume fraction is above the threshold for point-contact percolation (see shaded particles). (Wilkinson 1998).....   | 14 |
| <b>Fig. 2.8</b> Schematic illustration of facet-contact percolation, in which most of the particle interactions involve full facet contacts. As shown in the inset, thin grain boundary layers separate the facets, and creep may be controlled by the squeezing of this material from between the facets under compression. (Wilkinson 1998)..... | 14 |
| <b>Fig. 2.9</b> Strain rate vs. stress relations for flexural creep of 33% SiC whisker reinforced alumina composites: ▲ 1200°C; ○ 1300°C. The bilinear behaviour yields n=1 and n=5, assuming a power-law-type constitutive relation. (Nutt and Lipetzky 1990).....  | 21 |
| <b>Fig. 2.10</b> Strain rate vs. stress plot for 9.3, 18 and 30% SiC whiskers reinforced aluminas. The stress exponents are close to 6. (Xia and Langdon, 1995).....   | 22 |
| <b>Fig. 2.11</b> Flexural creep behaviour for composites with different whisker loadings. The test was performed at 1300°C in circulated dry nitrogen. The stress exponent was ~1.5 for alumina and 2-2.3 for composites. (Nutt and Lipetzky 1993).....  | 22 |
| <b>Fig. 2.12</b> Creep curves for (a) 5% and (b) 15% whisker-reinforced alumina composites.....  | 24 |
| <b>Fig. 2.13</b> Strain rate vs. stress plot in (a) logarithmic scale (b) linear-linear scale for 6% whisker containing alumina composite crept in compression. Three samples were tested, which are represented here by different symbols. (De Arellano-Lopez et al. 2000).....   | 25 |
| <b>Fig. 2.14</b> Strain rate vs. stress plot for creep of polycrystalline alumina and (a) 20% SiC whisker reinforced aluminas. (Lin and Becher 1990). (b) 20, 30 and 50% SiC whiskers. (Lin and Becher 1991)...  | 26 |
| <b>Fig. 2.15</b> Strain rate vs. stress curves for alumina reinforced with 10% SiC whiskers tested   |    |

|  |    |
|--|----|
| (a) at 1200°C and (b) 1300°C. (Lin and Becher 1996).....   | 28 |
| <b>Fig. 2.16 (a)</b> Normalized strain rates of alumina matrix vs. stress and <b>(b)</b> absolute strain rates vs. stress at 1400°C. (De Arellano-Lopez et al. 2001).....  | 28 |
| <b>Fig. 2.17</b> Strain recovery after load removal in 15% SiC whisker reinforced alumina. (Porter 1989).....  | 30 |
| <b>Fig. 2.18 (a)</b> Schematic of whisker network deformation and <b>(b)</b> Kelvin element in series with dashpot..   | 30 |
| <b>Fig. 2.19</b> Strain rate vs. stress plot for <b>(a)</b> pure alumina <b>(b)</b> 15% whisker reinforced alumina composite showing the effect of load removal. (Gu et al. 1995).....   | 30 |
| <b>Fig. 2.20</b> Recovered strain vs. time after load removal for an alumina with 15% SiC whiskers having as an aspect ratio of <b>(a)</b> 30 and <b>(b)</b> 10. (Gu et al. 1995).....   | 31 |
| <b>Fig. 2.21</b> Strain vs. time plot for <b>(a)</b> 5% <b>(b)</b> 15% SiC particle reinforced alumina composites showing the effect of load removal. (Gu et al. 1995).....  | 31 |
| <b>Fig. 2.22</b> Strain rate vs. stress relations for creep of 33% SiC whisker reinforced alumina composite. <b>(a)</b> Bilinear behaviour yielding stress exponents of 1 and 5 for Orientation A in which HPA and the load train are coincident. <b>(b)</b> Orientation B, in which the HPA and the load train are perpendicular. (Lipetzky et al. 1988)..... | 33 |
| <b>Fig. 2.23</b> Optical micrograph of hot-pressed 30% SiC platelet reinforced alumina sample prepared from slip casts with <b>(a)</b> pH=8 and <b>(b)</b> pH=2. Different particle alignment is noted. (Ham Su 1997).....   | 36 |
| <b>Fig. 2.24</b> Schematic illustration of a dilute distribution of particles which rotate under a far stress field. (Wilkinson 1998).....   | 40 |
| <b>Fig. 2.25 (a)</b> Geometry of an idealized whisker network and <b>(b)</b> geometrical parameters associated with a single cell surrounding each particle. (Wilkinson 1998).....   | 40 |
| <b>Fig. 2.26</b> The simplified whisker bending configuration before and after creep. (Wilkinson 1998).....  | 41 |
| <b>Fig. 2.27</b> Normalized viscosity $\eta/\eta_0$ as a function of volume fraction $\phi$ and packing anisotropy factor $f$ for three mechanisms. (Wilkinson 1998).....  | 42 |
| <b>Fig. 2.28</b> Normalized total viscosity $\eta/\eta_0$ as a function of volume fraction $\phi$ and packing anisotropy factor. (Wilkinson 1998).....   | 42 |
| <b>Fig. 2.29</b> The boundary separating regions dominated by viscoelastic creep and viscoplastic creep of a constrained, oriented whisker network ( $\theta = 10^\circ$ ) loaded in the whisker plane. (Wilkinson 1998).....  | 43 |
| <b>Fig. 2.30</b> Comparison of computed strains (solid lines) and measured strains (symbols) in SiC whisker phase for <b>(a)</b> {111} and <b>(b)</b> {220} planes. (Majumdar et al. 1988).....  | 45 |
| <b>Fig. 2.31</b> Comparison of computed (solid lines) and experimentally determined average hydrostatic strains (symbols) at various temperatures in the SiC whiskers and Al <sub>2</sub> O <sub>3</sub> matrix of a composite with 18 vol.% of whiskers ( $\square$ alumina (024), $\circ$ alumina (006) and $\Delta$ SiC. (Majumdar and Kupperman 1989)..... | 46 |
| <b>Fig. 2.32</b> Comparison of computed (solid lines) and experimentally determined average hydrostatic  |    |

|   |    |
|---|----|
| strains (symbols) at room temperature and at two volume fractions of whiskers (● SiC, ○ alumina (024), □ alumina (006) and Δ alumina (104). (Majumdar and Kupperman 1989).....  | 46 |
| <b>Fig. 2.33</b> The sample geometry for X-ray measurement. (Predecki 1991).....  | 47 |
| <b>Fig. 2.34</b> Average hydrostatic stresses measured in matrix, SiC particles and composite as a function of SiC content (Todd et al. 1997).....  | 49 |
| <b>Fig. 3.1</b> Relative thermal neutron flux as a function of wavelength in NRU reactor. (Courtesy of K. T. Conlon).....   | 55 |
| <b>Fig. 3.2</b> Relative thermal neutron flux as a function of energy. (Courtesy of K. T. Conlon).....  | 55 |
| <b>Fig. 3.3</b> A photograph of the experimental setup of the E3 spectrometer for texture measurement.....  | 57 |
| <b>Fig. 3.4 (a)</b> A schematic of sample geometry and <b>(b)</b> diffraction peaks from 5% SiC whisker reinforced aluminum. The (111), $(\bar{1}11)$ and $(10\bar{1}0)$ peaks were measured 0, 70 and 90°, respectively from the extrusion direction. (Root and Rack 1995).....                                    | 59 |
| <b>Fig. 3.5</b> A schematic diagram showing the occurrence of scattering on <b>(a)</b> on-axis (111) planes whose scattering vector <b>Q</b> is parallel to whisker axis and <b>(b)</b> off-axis $(\bar{1}11)$ planes of SiC whisker where the whisker axis is ~70.53° from the scattering vector.....              | 60 |
| <b>Fig. 3.6</b> {111} SiC peaks measured from a S302 sample with the scattering vector <b>(a)</b> perpendicular and <b>(b)</b> parallel to HPA. The small peak is (104) alumina.....  | 60 |
| <b>Fig. 3.7</b> The geometry for measuring angular whisker volume fraction.....   | 61 |
| <b>Fig. 3.8</b> A schematic of the sample coordinate system for neutron diffraction measurement. Direction N is parallel to HPA.....  | 63 |
| <b>Fig. 3.9</b> The measured (220) peaks of SiC whiskers at different $\lambda$ angle.....  | 66 |
| <b>Fig. 3.10</b> An illustration of average axial and hoop strains in the local crystal coordinate system of a whisker. The strains shown are measured from a billet of S302 sample, i.e. before creep.....   | 66 |
| <b>Fig. 3.11</b> An inner view of the furnace for high temperature neutron diffraction tests. The vanadium can was used to encapsulate the samples.....   | 67 |
| <b>Fig. 3.12</b> A photograph showing the set up for the tensile creep test.....  | 70 |
| <b>Fig. 3.13</b> A schematic of creep strain measurement by laser extensometry. (Carrol et al. 1989).....   | 71 |
| <b>Fig. 3.14</b> A photograph of tensile creep specimen of pure alumina (top) and composite (bottom). Different sample geometry is noted.....   | 71 |
| <b>Fig. 3.15</b> A creep curve for 30% SiC whisker reinforced alumina at 1400°C under 59MPa.....  | 73 |
| <b>Fig. 4.1</b> The tetragonal bonding of a carbon atom with the four nearest silicon neighbours.....   | 75 |
| <b>Fig. 4.2</b> Illustration of atomic structures of some of the most common SiC polytypes described in the cubic $(11\bar{2})$ plane and hexagonal $(10\bar{1}0)$ plane. A, B and C denote the type of atomic layer, The bonds aligned along the cubic [111] axis are denoted as on-bonds otherwise off-bonds..... | 76 |

|   |     |
|---|-----|
| Fig. 4.3 Neutron powder diffraction patterns from pure SiC whiskers before and after annealing.....   | 76  |
| Fig. 4.4 A high resolution electron micrograph showing the planar defects within SiC phase.....   | 77  |
| Fig. 4.5 Particle size distribution of raw alumina powder.....  | 79  |
| Fig. 4.6 Zeta potential as a function of pH for SiC and alumina suspensions.....  | 81  |
| Fig. 4.7 Sedimentation of composite slurry at different pH values after about 6 months.....   | 81  |
| Fig. 4.8 Slip casting processing flow chart.....  | 83  |
| Fig. 4.9 Recipes for hot pressing.....  | 84  |
| Fig. 4.10 Schematic illustration of graphite die for hot pressing.....  | 85  |
| Fig. 5.1 An optical micrograph of 30% SiC whisker reinforced alumina with the surface<br>(a) parallel and (b) perpendicular to HPA.....   | 87  |
| Fig. 5.2 An optical micrograph of 20% SiC whisker reinforced alumina with the surface<br>(a) parallel and (b) perpendicular to HPA.....   | 88  |
| Fig. 5.3 An optical micrograph of 10% SiC whisker reinforced alumina with the surface (a) parallel and<br>(b) perpendicular to HPA.....   | 89  |
| Fig. 5.4 SEM micrographs of S102 before creep with the surface (a) parallel and (b) perpendicular to<br>HPA. Sample surface was gold coated.....  | 91  |
| Fig. 5.5 An SEM micrograph taken from a S202 composite with the sample surface perpendicular to<br>HPA. Unlike S102, the sample surface was not coated with gold, since the surface charges are grounded<br>through the interconnected whisker network..... | 93  |
| Fig. 5.6 A SEM micrograph of S302 with sample surface perpendicular to HPA. The surface was<br>thermally etched at 1400°C for 2 hours.....  | 94  |
| Fig. 5.7 An SEM micrograph of S302 with the surface parallel to HPA. Thermal etching caused the<br>surface porosities, esp. within whisker clusters.....  | 95  |
| Fig. 5.8 A creep curve for a pure polycrystalline alumina at 1200°C.....  | 97  |
| Fig. 5.9 A creep curve for a S102 composite at 1400°C.....  | 97  |
| Fig. 5.10 Creep curves for 20% SiC whisker reinforced alumina composites at 1400°C.....   | 98  |
| Fig. 5.11 Creep curves for the composites with different SiC content at 1400°C.....   | 99  |
| Fig. 5.12 Steady state strain rate as a function of applied stress for S302.....  | 100 |
| Fig. 5.13 Steady state strain rate as a function of applied stress for S202.....  | 101 |
| Fig. 5.14 Steady state strain rate as a function of applied stress for S102.....  | 101 |
| Fig. 5.15 Normalized steady state strain rate vs. stress plots at 1400°C for different SiC content.....   | 102 |
| Fig. 5.16 Normalized steady state strain rate vs. stress plots at 1300°C for different SiC content.....   | 102 |
| Fig. 5.17 Normalized steady state strain rate vs. stress plots at 1200°C for different SiC content.....   | 103 |
| Fig. 5.18 Arrhenius plots used to obtain the apparent creep activation energy for S302.   |     |

|  |     |
|--|-----|
| Q is $421 \pm 38$ kJ/mol at 100 MPa.....   | 105 |
| <b>Fig. 5.19</b> Arrhenius plots used to obtain the true creep activation energy for S302.....   | 105 |
| <b>Fig. 5.20</b> The stress relaxation curve for a S302.....   | 106 |
| <b>Fig. 5.21</b> The stress relaxation curve for a S202.....   | 107 |
| <b>Fig. 5.22</b> A schematic of the sample coordinate system for neutron diffraction measurement.....  | 108 |
| <b>Fig. 5.23</b> Pole figures of (111) <sub>SiC</sub> from (a) C102 and (b) S102.....  | 109 |
| <b>Fig. 5.24</b> Pole figures of (111) <sub>SiC</sub> from (a) C202 and (b) S202.....  | 109 |
| <b>Fig. 5.25</b> Pole figures of (111) <sub>SiC</sub> from (a) C302 and (b) S302.....  | 110 |
| <b>Fig. 5.26</b> Pole figures of (111) <sub>SiC</sub> from (a) C306 and (b) S306.....  | 110 |
| <b>Fig. 5.27</b> Angular distribution of whiskers with respect to HPA.....   | 111 |
| <b>Fig. 5.28</b> Cumulative angular distribution of whiskers with respect to HPA for C302 and S302. The last two digits in the sample designation represent the solid loading for slip casting.....        | 112 |
| <b>Fig. 5.29</b> Cumulative angular distribution of whiskers with respect to HPA for C202 and S202.....  | 113 |
| <b>Fig. 5.30</b> Cumulative angular distribution of whiskers with respect to HPA for C102 and S102.....  | 113 |
| <b>Fig. 5.31</b> Cumulative angular distribution of whiskers with respect to HPA for C306 and S306.....  | 114 |
| <b>Fig. 5.32</b> Distribution density of whiskers with respect to HPA.....   | 114 |
| <b>Fig. 5.33</b> The residual strains measured from SiC phase as a function of SiC content.....  | 116 |
| <b>Fig. 5.34</b> The calculated residual stresses for SiC phase as a function of SiC content from neutron diffraction measurements.....  | 116 |
| <b>Fig. 5.35</b> The residual strain and FWHM of (111) SiC in sample #11-2 as a function of annealing time at 1400°C.....  | 118 |
| <b>Fig. 5.36</b> The residual strain and FWHM of (111) SiC in sample #18 as a function of annealing time at 1400°C.....  | 118 |
| <b>Fig. 5.37</b> The residual strain and FWHM of (111) SiC in sample #2b as a function of annealing time at 1400°C.....  | 118 |
| <b>Fig. 6.1</b> A SEM micrograph of S302 with the sample surface parallel to the HPA.....  | 121 |
| <b>Fig. 6.2</b> A SEM micrograph of S306 with the sample surface parallel to the HPA.....  | 121 |
| <b>Fig. 6.3</b> Strain rate vs. stress plot for aluminas.....  | 123 |
| <b>Fig. 6.4</b> Normalized strain rate vs. stress for composites with different whisker volume fraction at (a) 1400°C (b) 1300°C and (c) 1200°C.....   | 125 |
| <b>Fig. 6.5</b> A TEM micrograph taken from a S302 sample that has been deformed to ~0.4% at 1400°C. Arrows indicate cavities.....   | 128 |
| <b>Fig. 6.6</b> Plot of logarithmic strain rates vs. $10^4/T$ for (a) S202 and (b) S102. (c) Schematic representation of the mechanical state by a surface $\ln \dot{\epsilon} = f(1/T, \ln \sigma)$ ..... | 132 |
| <b>Fig. 6.7</b> Plot of apparent activation energy vs. whisker loading from (a) tensile (current studies) and (b)  |     |

|  |     |
|--|-----|
| Bending and compressive creep tests in the literature.....   | 134 |
| <b>Fig. 6.8</b> Plot of lattice spacing of (111) SiC planes vs. temperature. The applied tensile stress reduced the lattice strain of (111) SiC.....   | 136 |
| <b>Fig. 6.9</b> Schematic illustration of evolution of (a) residual stress within matrix (m) and fibers (f) with varying (b) temperature and (c) applied stress.....   | 137 |
| <b>Fig. 6.10</b> Plot of strain rate vs. stress for S302 ( $d \sim 2 \mu\text{m}$ ) and S102 ( $d \sim 8 \mu\text{m}$ ).....   | 139 |
| <b>Fig. 6.11</b> The creep stress relaxation curve for a S202 sample.....  | 141 |
| <b>Fig. 6.12</b> Schematic illustrations of change in peak position and shape due to lattice deformation. (a) without deformation (b) uniaxial compression and (c) pure bending. The shaded peaks are after deformation.....   | 142 |
| <b>Fig. 6.13</b> Schematic of peak width change according to the whisker bending model.....  | 143 |
| <b>Fig. 6.14</b> Comparison of (111) SiC peaks measured from a single specimen before and after creep with the scattering vector nearly (a) parallel to the tensile direction and (b) perpendicular to tensile axis. Schematic illustrations for (c) $Q//L$ and (d) $Q \perp L$ .....  | 144 |
| <b>Fig. 6.15</b> Schematic illustration of whisker bending upon the applied tensile stress for the whiskers oriented nearly (a) parallel and (b) perpendicular to the tensile axis.....  | 145 |
| <b>Fig. 6.16</b> Comparison of (111) SiC peaks measured before and after creep. The instrumental broadening remained constant.....   | 146 |
| <b>Fig. 6.17</b> A schematic of whisker bending geometry.....  | 149 |
| <b>Fig. 6.18</b> (a) The calculated radius of whisker curvature versus maximum change in scattering angle (b) The calculated radius of whisker curvature versus mid-point deflection.....  | 150 |
| <b>Fig. 6.19</b> Simplified geometry of whisker bending.....   | 151 |
| <b>Fig. 6.20</b> The calculated FWHM as a function of whisker bending. If the probability of finding lattice strain between $\epsilon$ and $\epsilon+d\epsilon$ is $P(\epsilon)d\epsilon$ , model 1 assumes a linear function of $P(\epsilon)$ , model 2, a uniform $P(\epsilon)$ and model 3, a Gaussian profile of $P(\epsilon)$ ..... | 153 |
| <b>Fig. 6.21</b> Schematic illustration of Hertzian contact phenomena between (a) spheres and (b) rods in contact.....   | 156 |
| <b>Fig. 6.22</b> Illustration of load transfer due to the far field stress acting on constrained (a) fibers and (b) spherical particles through contact deformation.....   | 159 |
| <b>Fig. 6.23</b> Geometry for calculating the moment due to the shear stress on the whisker surface.....   | 158 |
| <b>Fig. 6.24</b> Computed strains due to local contact deformation as a function of applied stress. (a) for a whisker network. The shaded area covers the recovered strains that have been measured experimentally. (b) for percolative spherical particles.....   | 161 |



## LIST OF TABLES

|   |     |
|---|-----|
| <b>Table 2.1</b> Uniform mixtures. (Brady and Holum, 1984).....   | 5   |
| <b>Table 2.2</b> Creep data on SiC whisker-reinforced alumina composites.....   | 18  |
| <b>Table 2.3</b> The measured average residual strains obtained from the composite ( $\times 10^{-6}$ ). Standard deviations are $50 \times 10^{-6}$ for matrix and $50 \times 10^{-6}$ for whiskers.....                                   | 48  |
| <b>Table 2.4</b> Residual microstresses in the composite (MPa). Standard deviations are 12 MPa for matrix and 30 MPa for whiskers.....  | 48  |
| <b>Table 2.5</b> Average principal microstresses in alumina-SiC nanocomposites with different SiC content (wt%). Values in parentheses are standard deviations.....   | 50  |
| <b>Table 4.1</b> Summary of characterisation of raw powders.....  | 78  |
| <b>Table 4.2</b> Nominal content of impurities.....   | 78  |
| <b>Table 4.3</b> Experimental schemes for green body formation.....   | 82  |
| <b>Table 5.1</b> Average grain size (in micrometer) for the composites and pure alumina.....  | 95  |
| <b>Table 5.2</b> The activation energies obtained for the composites. The numbers in parentheses are the associated uncertainties.....  | 105 |
| <b>Table 5.3</b> Lattice strains ( $\times 10^{-3}$ ) measured at room temperature for SiC whiskers. The computed stresses are given in MPa. Numbers in parenthesis are uncertainties. BC: before creep; AN: Annealed; AC: after creep..... | 115 |
| <b>Table 6.1</b> Computed difference between Q and $Q_a$ , i.e. $f(T, n)$ in eq. 6.2. The unit is kJ/mol.....   | 129 |
| <b>Table 6.2</b> Activation energies (in kJ/mol) for diffusion in $Al_2O_3$ . (Frost and Ashby 1982).....   | 130 |
| <b>Table 6.3</b> Average microstrains and microstresses estimated from the measured (111) SiC lattice spacing vs. temperature. The composite contains 30% whiskers. Numbers in parentheses are uncertainties.....                           | 137 |
| <b>Table 6.4</b> The estimated Gaussian physical broadening.....  | 147 |

# 1. INTRODUCTION

Advanced ceramics have gained substantial importance in engineering applications during the last quarter of the 20th century. Monolithic high performance ceramics combine many very desirable characteristics, e.g. high strength and hardness, excellent high temperature capability, chemical inertness, wear resistance and low density. Examples of these ceramic materials include oxides, nitrides and carbides of silicon, aluminum, titanium and zirconium. However, they show little or no plasticity and are prone to catastrophic failure under mechanical and thermal loading, resulting in an extremely poor damage-tolerance. Much effort has been directed toward introducing a variety of energy -dissipating phenomena in the fracture process of ceramics. Development of ceramic matrix composite (CMC) represents a quantum leap in that direction (Chawla 1993). CMCs are made by incorporating a reinforcement phase into a continuous monolithic ceramic matrix phase. The reinforcement phase can be in the form of spheres, platelets, whiskers or short fibers, continuous fibers or sheet. CMCs provide some unique combination of mechanical, thermal, electrical and other properties. Therefore, they can be used in many situations where the monolithic or conventional materials do not meet the requirements, for example, in advanced aerospace propulsion and power systems. Figure 1.1 shows materials developed since the 1960s for jet engines with their operating temperatures. Other non-aerospace applications of CMCs include dies and tool bits, medical implants and land based power and transport engines. In particular, structural ceramics can improve fuel efficiency in heat engines because of higher operating temperatures (see Fig. 1.2), more compact design and reduction or elimination of cooling systems (Moulson 1979).

In recent years a considerable body of studies has been done on oxide matrices reinforced with SiC whiskers. The  $\text{Al}_2\text{O}_3$ -SiC whisker system is probably one of the most important systems because both the matrix and reinforcement phases have been well studied. It has been known that alumina has excellent high temperature stability and low oxygen permeability and that SiC has good resistance to high temperature oxidation because of the formation of a protective film of silica (Luthra and Park 1990). The addition of SiC whiskers into alumina has resulted in substantial improvement of fracture toughness (3 to 4 fold increases) and flexure strength, resistance to thermal shock, room temperature slow crack growth, and

the long-term elevated-temperature fatigue in flexure (Lin and Becher 1990). This system has already gained commercial success, the composites based on this system presently being used for cutting tool inserts, valves, pump components, and extrusion dies.

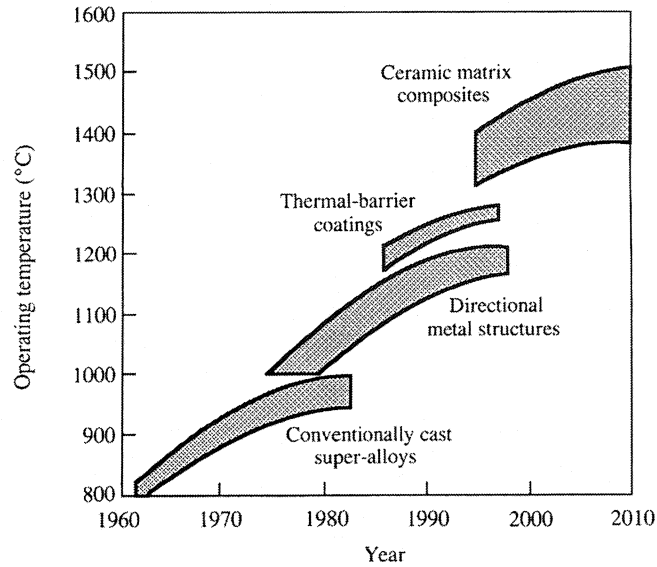


Fig. 1.1 Rise in the operating temperature of jet engines with time (Clark and Flemings 1986).

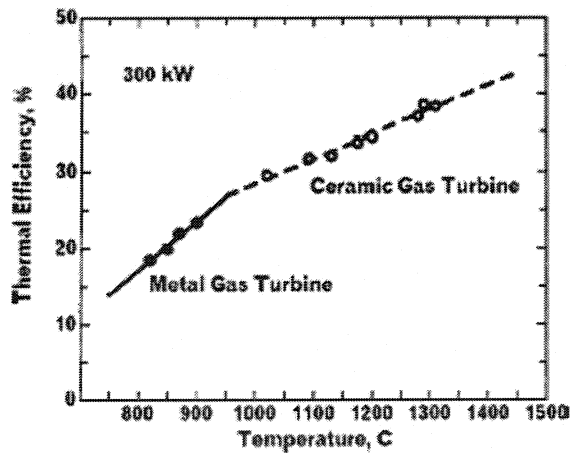


Fig. 1.2 Performance progress of 300-kW metal and ceramic gas turbines (Ohji 2001).

Creep resistance is perhaps the most critical high temperature property of ceramic composites, and it often the major limitation for high temperature applications. Creep damage of the composite can result in microscopic cavities and cracks that reduce the load-bearing capacity of the component and eventually cause failure. To be reliably employed in structural applications at high temperatures, the mechanisms of damage and deformation during creep must be understood (Lipetzky et al. 1991).

There have been numerous reports on the creep of SiC whisker reinforced alumina composites since the first report by Chokshi and Porter (1987). It has been well established that the creep rates of the composites are one to three orders of magnitude lower than unreinforced alumina and whiskers have been suggested to impede grain boundary sliding (GBS), thereby, reducing the deformation rate. Many works seem to indicate that during creep strain is generated mainly through cavity formation. In addition, the composites with more than ~15%\* whiskers showed interesting time-dependent strain recovery behaviour when the load was removed during creep. Whisker bending is commonly believed to be responsible for this effect (e.g. Porter 1989, Wilkinson 1998). However, there have been no direct experimental evidence and theoretical treatments to support this assertion. Oftentimes the creep data was collected in four-point bending and/or compression configuration and little is known about the creep response of the composites in tension.

The primary aim of this thesis project is to study and identify mechanisms of anelastic strain relaxation. In addition, the effect of slurry pH on the composite microstructure, the development of whisker texture and microscopic residual stresses/strains at various conditions, and the effect of SiC whisker content on the tensile creep behaviour of composites were also investigated. Neutron diffraction methods can help achieve these purposes, which reveal the bulk properties of the composite materials rather than surface properties. Modeling of inclusion network deformation is also necessary to verify the existing and new mechanisms for creep strain recovery.

---

\* Any percentage refers to volume, unless otherwise specified.

## **2. LITERATURE REVIEW**

### **2.1 Introduction**

This chapter is divided into five sections. The first section is devoted to the fundamentals and methods for ceramic processing with a focus on colloidal processing. The second section provides a brief discussion of general constitutive relations for creep and a survey on the understanding of creep in single-phase and multi-phase ceramics, focusing primarily the latter. The third section reviews the structural and mechanical properties of  $\text{Al}_2\text{O}_3$ -SiC systems with emphasis on the creep behaviour of SiC whisker-reinforced  $\text{Al}_2\text{O}_3$  composite systems. Due to the importance of residual stresses upon mechanical properties of the ceramic composite materials, the final section presents a survey on the studies of residual strains and stresses in the pertinent ceramic composites where diffraction techniques were employed.

### **2.2 Ceramic powder processing**

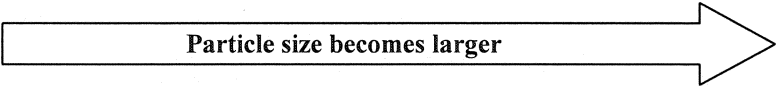
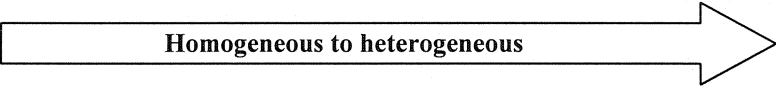
#### **2.2.1 Introduction**

The mechanical properties of ceramics are subject to the microstructure that is affected by the processing routes employed to fabricate them. Creep behaviour of ceramic matrix composites (CMC), among other characteristics, is determined by the chemical and physical nature of the reinforcement phase, its volume fraction and distribution, and diffusivity and diffusion path length of atomic species in the microstructure (Ham Su 1997). The spatial distribution of the reinforcement phase in the matrix can be controlled to a certain extent during processing. The presence of glassy phases and impurities in the microstructure (very often at interfaces) usually facilitates diffusion in ceramics, lowering the creep resistance. Therefore, detailed knowledge underlying the fabrication processes is needed to understand the high temperature mechanical behaviour of the CMC. Although processing is not the major concern of the present research project, it is necessary to explain first those underlying concepts in ceramic powder processing.

A colloid (or colloidal dispersion) belongs to a subdivision of mixtures in which the effects connected with the surface are pre-eminent. It consists of a continuous phase (gas or liquid) as the

dispersion media and fine dispersed particles (solid or liquid) that have dimensions ranging from 1 to 1000 nm. Table 2.1 compares colloidal dispersions with other mixtures. Colloidal processing is being increasingly used in the consolidation of ceramic powders to produce the green body. Compared to powder consolidation in the dry or semidry state, colloidal methods can lead to better packing uniformity in the green body, which in turn enables them to better microstructural control during sintering. Therefore, stability of the colloidal systems, as a core of the method, must be understood at a basic level.

**Table 2.1** Uniform mixtures (Brady and Holum, 1984).

|    |   |  |
|--|---|--|
| Solutions  | Colloidal Dispersions   | Suspensions  |
| All particles on the order of atoms, ions, or small molecules (0.1-1 nm)             | Particles of at least one component are large clusters of atoms, ions, or small molecules or are very large ions or molecules (1-1000 nm) | Particles of at least one component may be individually seen with a low-power microscope (1000 nm) |
| Most stable to gravity   | Less stable to gravity  | Unstable to gravity  |
| Most homogeneous   | Homogeneous but borderline  | Heterogeneous but may appear to be uniform   |
| Transparent (but often coloured)   | Often translucent or opaque; may be transparent   | Often opaque but may appear translucent  |
| No Tyndall effect  | Tyndall effect  | Not applicable (suspensions cannot be transparent)   |
| No Brownian movement   | Brownian movement   | Not applicable (particles settle)  |
| Cannot be separated by filtration  | Cannot be separated by filtration   | Can be separated by filtration   |
|  |   |  |

### 2.2.2 Stability of colloidal system

When particles are dispersed in a liquid, a surface charge is required mainly through preferential adsorption of ions, which is the most common process for ceramic particles, whereas isomorphic substitution is commonly found in clays. Figure 2.1 illustrates the generation of surface charges on SiO<sub>2</sub> particles. The stability of a colloidal system is essentially established by the interparticle potentials that mainly include the van der Waals attractive potential and the electrostatic repulsive potential introduced between the diffuse electrical double layers. Van der Waal's forces are ubiquitous, long-range and always attractive

between like particles. The origin of this force is the presence of atomic or molecular dipole moments on the particle surface. As a consequence, this force is intrinsically instantaneous. In the absence of any repulsive potential, the van der Waals potential produces a very strong, cohesive, touching particle network that requires great effort to break down (Lange et al. 1990).

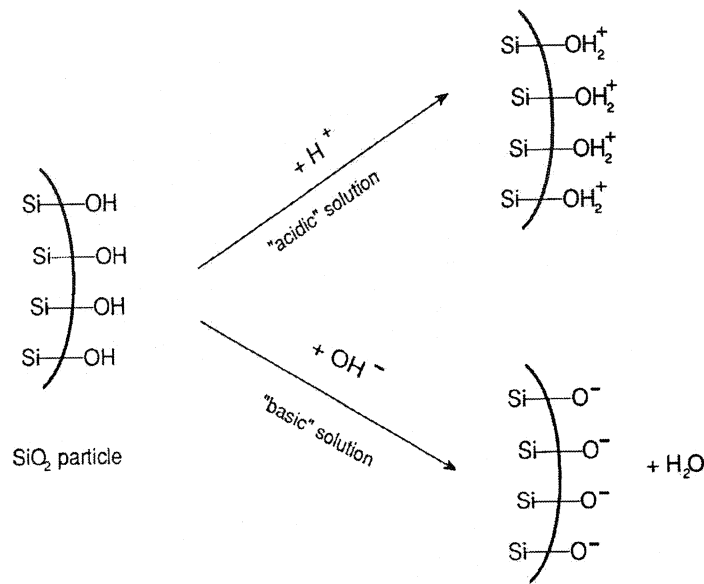


**Fig. 2.1** Surface charges on  $\text{SiO}_2$  particles by adsorption of ions from acidic or basic solutions. (Rahaman 1995)

Repulsive interparticle potentials are developed when a surface becomes charged. The charged surface and the neutralizing diffuse layer of counterions are said to form an electrical double layer. Figure 2.2 is a schematic of a double layer structure. By controlling the pH with addition of either acid or base, the net surface charge can vary from positive to negative. The surface is neutral at an intermediate pH, i.e. point of zero charge (PZC), where the surface contains equal amounts of positive and negative sites. Some of the ions in the solution with an opposite charge relative to the surface, known as counterions, are attracted towards the particle by an electric field generated by the charged surface but they are also subject to Brownian thermal motion, which tends to spread them uniformly through the surrounding medium. The result is a compromise in which a few counterions remain very close to the surface and there is a gradual

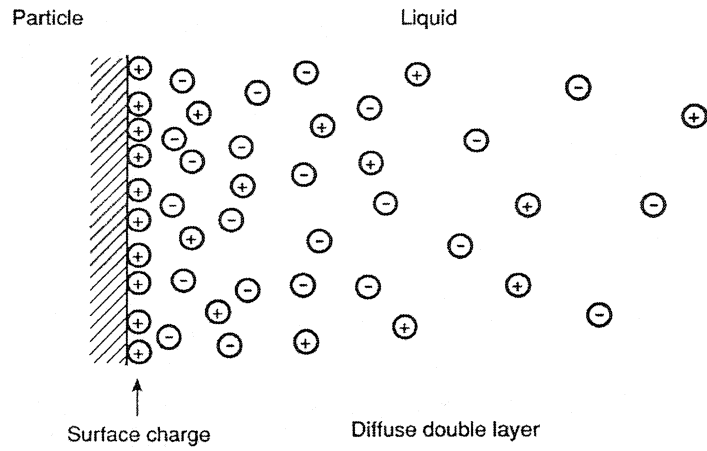


**Fig. 2.2** The distribution of positive and negative ions in the electrical double layer associated with a charged surface in a liquid. (Rahaman 1995)

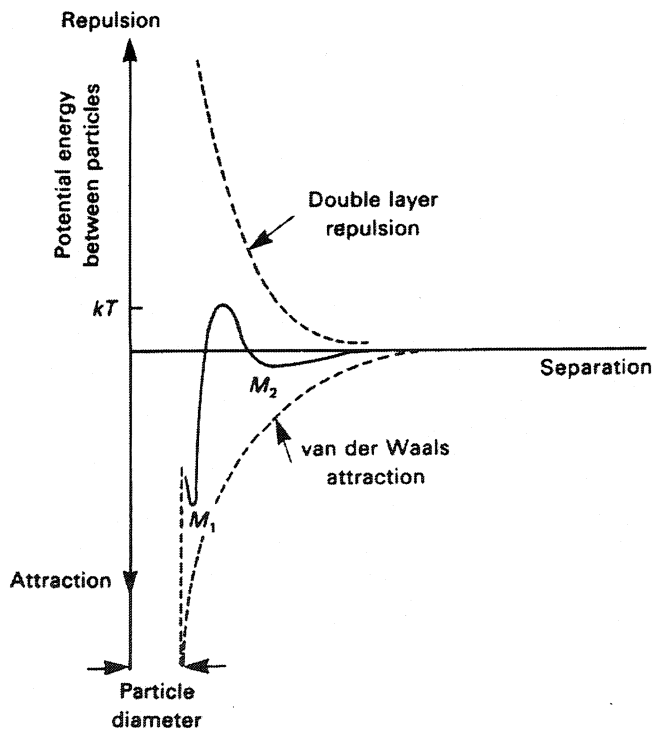


**Fig. 2.3** Potential energy between two particles in a liquid. Flocculation occurs at  $M_2$  and contact  $M_1$ . (Rahaman 1995)



decrease in the concentration of counterions away from surface, until it reaches that of the bulk solution. The extent of this diffuse layer depends upon the electrolyte concentration. The diffuse layer tends to shrink with increasing ionic concentration.

When the particle is in motion, some ions in the diffuse layer mechanically “shear off”, and the resultant potential between the surface and the shear layer plane is called the zeta potential. The pH corresponding to zero zeta potential is called the isoelectric point (IEP). The higher the zeta potential, the thicker the double layer, the more stable against coagulation are the particles. Experimentally, it is more convenient to calculate the IEP than PZC. Increasing the ionic strength (e.g. salt concentration) reduces the thickness of the diffuse double layer, resulting in a decrease in zeta potential. Zeta potential is measured by determining the electrophoretic mobility.

The origins of the repulsive interparticle potential can be many. Apart from the electrostatic potential, it may also include the osmotic (or ionic) potential and the hydration potential. The former is entropic in nature and arises due to the local increase in the concentration of counterions when double layers overlap while the latter is produced by hydrated counterions attracted to a charged surface. When the repulsion force dominates over the attractive force, a repulsive energy barrier is formed that renders the stability of the colloidal system. This repulsive force can prevent coagulation into the attractive primary minimum, provided the thermal kinetic energy ( $kT$ ) is much lower than the energy barrier (see Fig. 2.3). However, most colloids are thermodynamically unstable and will eventually coagulate. Coagulation is associated with dropping into the primary minimum and is an irreversible process. Flocculation refers to a weak collection of particles at the metastable (or transitional) secondary minimum of interaction energy, which is a reversible process, and usually weakly attractive in nature. A stable flocculation is possible if the thermal agitation is low and this can be exploited to increase the green body density that may facilitate the sintering process (Chang et al. 1994).

### 2.2.3 Heteroflocculation

In the fabrication of multicomponent ceramic composites, to obtain a homogeneous microstructure, it may be desirable to induce opposite charges on different colloidal phases by adjusting the pH, which enables an intimate mixture of different phases. This approach, termed heteroflocculation, prevents phase segregation due to flocculation and differential mass settling during processing, resulting in a uniform spatial distribution of the reinforcement phases. Lange et al. (1989) demonstrated this effect in aqueous alumina-zirconia suspensions. Figure 2.4 shows the zeta potential measured as a function of pH for  $\text{Al}_2\text{O}_3$  and SiC whisker powders by Jang et al. (1992). According to this result, heteroflocculation is anticipated to take place when the pH is between 6 and 7, which was confirmed experimentally. Figure 2.5 schematically illustrates this process.

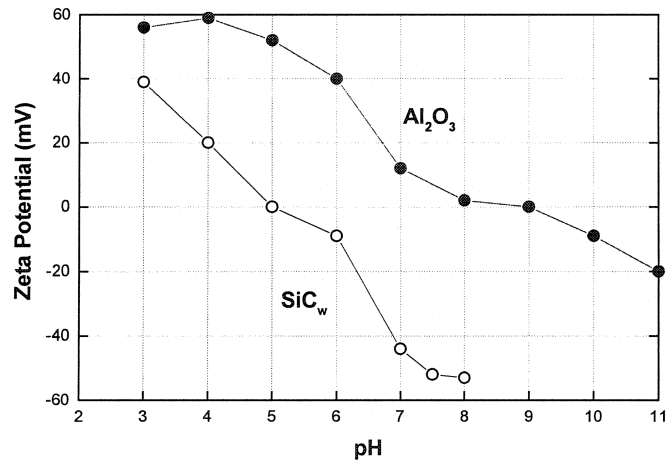


**Fig. 2.4** Zeta potential of alumina and SiC whisker as a function of suspension pH. (Jang 1992)

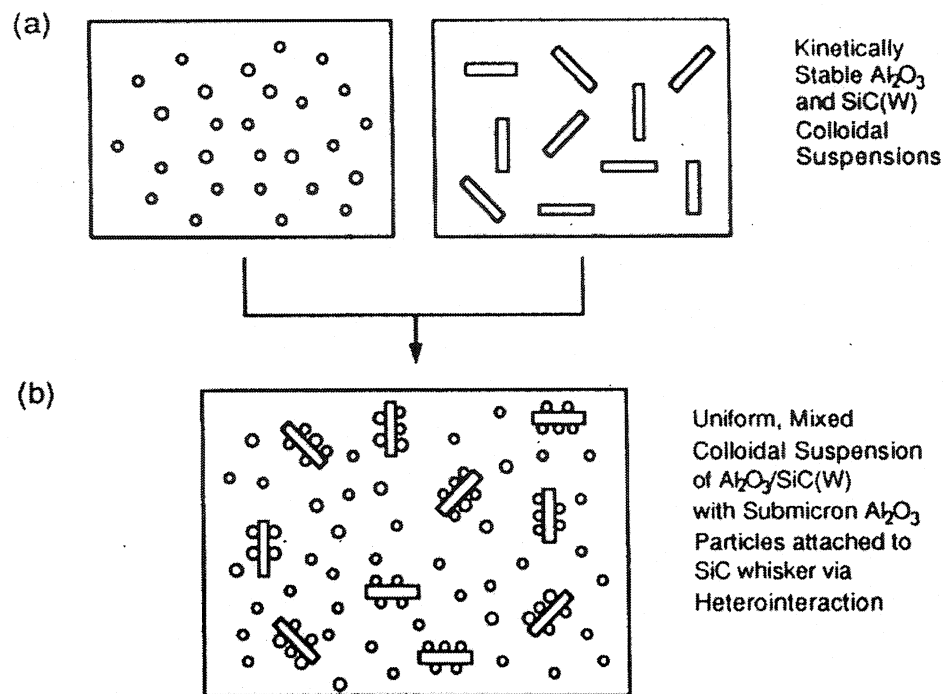


Fig. 2.5 Heteroflocculation between alumina and SiC whisker particles. (Jang 1992)

### 2.3 Constitutive relations in creep

Creep involves a slow deformation of materials at high temperature, which is often described to encompass three different stages; namely, primary (or transitional) creep, secondary (or steady-state creep) creep and tertiary creep, as shown in Fig 2.6. From an engineering point of view, the secondary creep regime is of the most importance for materials design. In a creep test a sufficient period of time giving nearly constant creep rate is studied so as to justify the fitting of models for steady-state creep or pseudo steady-state creep.

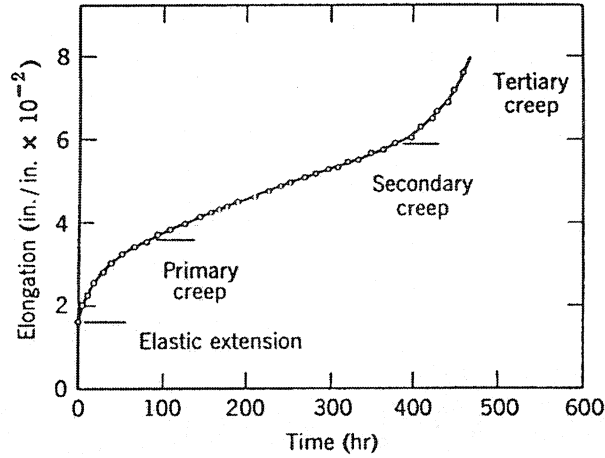


Fig. 2.6 A typical creep curve for a monolithic ceramic material. (Kingery 1976)

The most desirable general constitutive equation for creep is given (Poirier 1985) by

$$f[\sigma, \dot{\epsilon}, y(\epsilon, \dot{\epsilon} \dots), T, P] = 0 \quad (2.1)$$

where  $\sigma, \dot{\epsilon}, T, P$  are the external state variables of the system and  $y$  is an internal state variable that is dependent on the microstructure of the sample, its history etc. It is noted that time itself is not a state variable since it cannot be fixed as can temperature or stress. Also the total strain is not a good state variable because it may result from very different deformation histories.

As pointed out by many (Orowan 1940, Hart 1976), creep is not fundamentally different from plastic deformation. Creep properties can be studied using either constant stress (or load) or constant strain rate tests, the former being more time consuming but closer to the actual creep events in reality.

The steady-state creep rate is very often expressed in the form of a power law as follows (Mukherjee et al. 1969, Cannon and Langdon 1983):

$$\dot{\epsilon} = \frac{ADGb}{kT} \left(\frac{b}{d}\right)^p \left(\frac{\sigma}{G}\right)^n \quad (2.2)$$

where  $A$  is a dimensionless constant,  $D$  is the appropriate diffusion coefficient,  $G$  is the shear modulus,  $b$  is the Burger's vector,  $k$  is Boltzmann's constant,  $T$  is the absolute temperature,  $d$  is the grain size,  $\sigma$  is the applied stress,  $p$  is the exponent of the inverse grain size, and  $n$  is the stress exponent.

## 2.4 Creep in ceramics

### 2.4.1 Single-phase ceramics

According to Cannon and Langdon (1988), creep in ‘pure’ ceramics can be classified into two categories depending on the sensitivity of strain rate on stress, i.e. stress exponent,  $n$ . In the first category the stress exponent is close to 1 and the value of  $p$  is close to  $\sim 2$  to 3, which can be related to the creep mechanisms dominated by diffusion and grain boundary sliding at relatively low stress and low temperature (Evans and Langdon 1976).

If diffusion occurs through the lattice and the grains elongate along the tensile axis and maintain their adjacent neighbors (Lifshitz sliding), the process is termed Nabarro-Herring creep (Nabarro 1948, Herring 1950) and the creep rate is given by

$$\dot{\epsilon} = \frac{B_1 \Omega D_l \sigma}{d^2 kT} \quad (2.3)$$

where  $\Omega$  is the atomic volume,  $D_l$  is the coefficient for lattice self-diffusion and  $B_1$  is a constant ranging from  $\sim 12$ -40 for different test conditions. If diffusion takes place through grain boundaries, the process is termed Coble creep (Coble 1963) and the creep rate is given as

$$\dot{\epsilon} = \frac{150 \Omega \delta D_{gb} \sigma}{\pi d^3 kT} \quad (2.4)$$

where  $\delta$  is the effective width of the grain boundary for vacancy diffusion and  $D_{gb}$  is grain boundary diffusion coefficient. It can be shown (Cannon and Langdon 1988) that Coble-creep is favored over Nabarro-Herring creep when the grain size is very small and at lower testing temperatures. In practice, the two mechanisms operate independently and the total rate is the sum of the two rates. It is also noted that the presence of two ionic species in ceramics complicates the situation, which requires a modification of the rate equation. It is commonly understood that the movement of the slower diffusing species along the faster diffusion path determines the observed creep rates.

In the second category the creep rate depends on stress to a high power typically around 3 or 5 without significant grain size dependence. Creep with stress exponent 5 represents a fully ductile behavior as in FCC metals and it is associated with an intragranular dislocation motion with five active independent

slip systems and diffusion is primarily associated with the freeing of dislocations rather than with a mass transport process. However, when there is not five independent slip systems that can interpenetrate each other or there are fewer than five independent slip systems operating, dislocation climb becomes necessary and consequently rate controlling. This creep mechanism leads to a stress exponent of 3.

#### **2.4.2 Multiphase ceramics**

Wilkinson (1998) has given a critical review on the creep mechanisms in multiphase ceramics, in which the author reviewed the recent experimental data on a range of materials and the models developed to rationalize them. This section summarises the main points provided in this paper, starting with the classification of microstructure exhibited by multiphase ceramic composites followed by a summary of some important conclusions emerging from comparison of experimental data to the rheological models established according to the configuration of reinforcing particles in the matrix.

The creep resistance of the ceramic matrix can be enhanced considerably by reinforcing with harder, more creep resisting second phases often with high melting points. These additions may take many different forms, such as a dilute dispersion of fine particulates, a well-interconnected short fiber network and a complex interwoven architecture involving long fibers in a ceramic matrix.

A microstructural classification system based on the nature of the network developed by the second phases can be established, which is very useful as a guideline in developing mechanistic models. Depending on the volume fraction, morphology and distribution of reinforcement, several interactions can be envisioned. If the volume fraction of second phase is small, there is no interaction between particles, so the effect is due only to the disturbance of the flow field around particles. As the volume fraction of particles increase, interparticle interactions begin to take effect. For example, local clusters of particles may develop that increase their effective volume fraction.

When the particle volume fraction reaches a certain level, a percolative network of point-to-point contacts is developed. This is schematically shown in Fig. 2.7. Creep then requires the compatible deformation of this network in the absence of cavitation and microcracking. The percolation threshold is

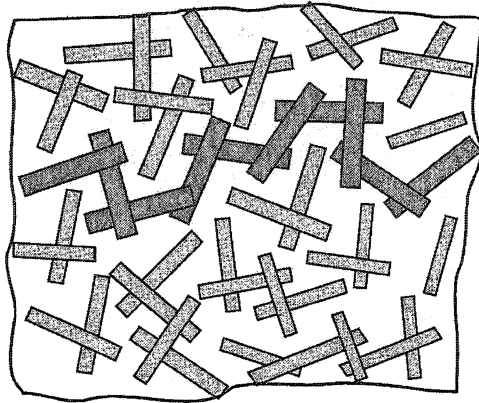


**Fig. 2.7** Schematic illustration of network development in a whisker-(or platelet-) reinforced ceramic. Volume fraction is above the threshold for point-contact percolation (see shaded particles). (Wilkinson 1998)

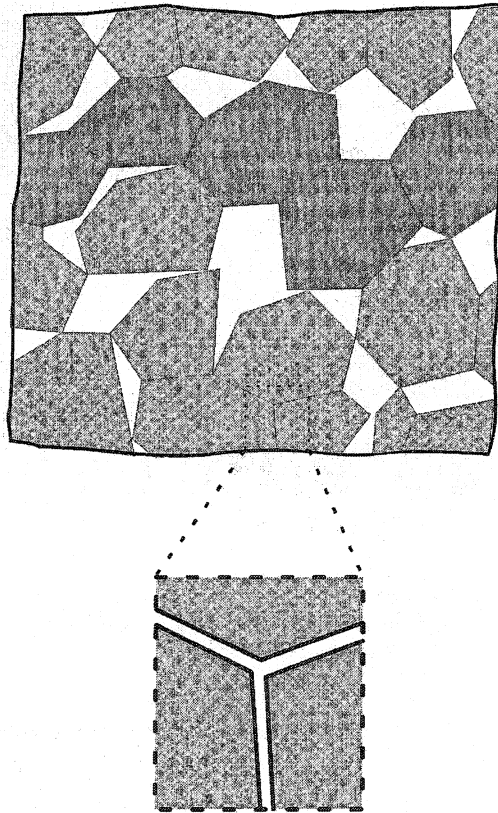


**Fig. 2.8** Schematic illustration of facet-contact percolation, in which most of the particle interactions involve full facet contacts. As shown in the inset, thin grain boundary layers separate the facets, and creep may be controlled by the squeezing of this material from between the facets under compression. (Wilkinson 1998)

dependent on particle morphology and its distribution, particularly the aspect ratio of the particle. The critical volume fraction is about 16% for randomly distributed spherical particles of uniform size (Grannan et al. 1981, Zallen 1983). For fibers with high aspect ratio, the percolation threshold for a random particle distribution is given by

$$\phi_{pcp} = \frac{0.7}{\lambda} \quad (2.5)$$

where  $\lambda$  is aspect ratio (Nan 1993).

In terms of creep response, it is unlikely that the effect of a network is experienced immediately once the percolation threshold is crossed. Instead, the density of contacts increases gradually until most particles form at least one contact with a neighbor. To form a strong network, it has been suggested that the number of contacts per particle,  $Z(\phi)$ , should be at least two (Bouvard and Lange 1991). Models for random fiber networks (Van Wyk 1946, Kallmes and Corte 1960) suggest that

$$Z = \zeta \lambda \phi \quad (2.6)$$

where  $\zeta$  is between the limits of 2 for a three-dimensional random network and  $2/\pi$  for a two-dimensional network. Setting  $\zeta = 1$  for a modest level of texturing developed during processing, the number of contacts at the percolation threshold is  $Z = 0.7$ . Thus  $\phi_{net} \approx 3\phi_{pcp}$  is required to form a strong network, of the type that is presumed to control the creep behaviour.

With a further increase in particle concentration, facet-contact percolation threshold develops. This is schematically illustrated in Fig. 2.8. With this type of microstructure, the rotation and long-range motion of individual particles becomes highly restricted, and the flow within the interface regions is likely to control the deformation. However, there has been no theoretical treatment for the onset of facet-contact percolation. The critical volume fraction for this percolation is more important in composite processing where the incorporation of large amounts of reinforcing particles into the matrix becomes a prominent problem.

Below the point-to-point contact regime, in which the particles behave independently of one another, a simplified rheological model is able to capture the main features of the creep behaviour exhibited



by many multiphase ceramics. Well above the face-to-face contact regime, when the particles are separated only by thin films of the soft phase (often amorphous), creep is often controlled by viscous flow of grain boundary phase. In this regime, the rheological model still provides very useful results to understand the creep response. However, some of the details cannot be captured because dissolution-precipitation creep and cavitation are also known to be operative in this regime. At intermediate volume fractions, however, more details of the microstructure need to be considered in order to model the creep processes. Some models based on viscoelastic bending of fibers and viscoplastic creep of the matrix phase have been developed. However, they only provide first order explanations, and this regime remains the least understood mainly due to the complexities associated with inclusion network effect.

In summary, although it is not always possible to precisely predict the creep of multiphase ceramic materials, some well-founded principles have been developed that can guide materials development.

## **2.5 Creep of Al<sub>2</sub>O<sub>3</sub>-SiC composites**

### **2.5.1 SiC whisker reinforced alumina composites**

SiC whisker reinforced alumina composites were first made by Wei and Becher (1984). Since then there have been continuous studies on the mechanical properties of these composites. It has been well established that whisker reinforcements not only increase the fracture toughness, resistance to thermal shock and erosion but also improve the creep resistance, compared to a single-phase polycrystalline alumina (e.g. Becher and Wei 1984 and 1985, Tiegs and Becher 1987, Lipetzky et al. 1991). Table 2.2 summarises all the creep data hitherto reported in the literature since Chokshi and Porter (1985) authored the first report on the creep behaviour of 18% SiC whisker reinforced alumina composite. First, it is noted that the majority of the data was obtained from four-point bending tests. This is obviously due to the low cost and relative ease of this mode of testing. However, recognition of ambiguities associated with deconvolution of creep data from bending tests (Jakus and Wiederhorn 1988) led to the use of compressive creep testing (Liu and Majidi 1990, De Arellano-Lopez 1990). It is noteworthy that tensile creep, though as necessary as compressive creep, has been rarely employed due to the high cost of specimen machining and experimental

difficulties involved (Carroll et al. 1989). Secondly, with some exceptions (e.g. Porter et al. 1987, Porter 1989) the detailed processing routes adopted by different manufacturers and researchers were often unknown due to the proprietary techniques involved. This makes a direct comparison of the reported creep data very difficult. For example, Porter et al. (1987, 1990) showed that the creep response of alumina reinforced with about 15% SiC whiskers made by different manufacturers were remarkably different. Therefore, instead of commenting on each of the studies and making direct comparisons among them, only those salient tendencies that seem to be consistent in the literature are going to be addressed.

### **Stress exponent**

The stress exponent of fine-grained pure polycrystalline alumina, in the absence of extensive microstructural damage (e.g. cavitation and macro-cracks), always seems to fall between 1 and 2, independent of the type of creep test. This conforms to the diffusion accommodated grain boundary sliding that has been widely accepted as the main creep mechanism (Cannon et al. 1980). However, for composites, the creep stress exponents seem to depend in a complex manner on many factors especially the microstructure (e.g. the amount of glassy phases), creep temperature and the type of creep test used, i.e. stress state. This appears to become more important when the volume fraction of SiC whiskers exceeds a critical level. Therefore, for multiphase materials a specific creep mechanism cannot be reliably inferred simply from the value of stress exponent (Lipetzky et al. 1988).

In general, the conventional flexural creep test based on the method of Hollenberg et al. (1971) almost always resulted in higher  $n$  value (4-8) than that from compressive creep (1-3.5). This has been found to be more significant in creep of composites with high volume fraction ( $\geq 15\%$ ) of reinforcement phase at high temperatures ( $\geq 1400$  °C) in air. Nutt and Lipetzky (1990 and 1993) conducted both bending and compressive creep tests on the same composite containing 33% whiskers. Their experiments at 1300°C in air under relatively high stress gave rise to a stress exponent of  $\sim 5$  in bending as opposed to  $\sim 3$  in compression, indicating the dependence of creep response upon stress state. Initially the stress exponent  $n \approx 5$  obtained from bending creep tests was attributed to an intragranular dislocation movement, which was

Table 2.2 Creep data on SiC whisker-reinforced alumina composites.

| Reference                       | SiC (vol%) | Test type | Atm.       | Stress (MPa) | Strain rate range      | temperature | Grain size | n          | Q (KJ/mol)                       | Manufacturer     |
|---------------------------------|------------|-----------|------------|--------------|------------------------|-------------|------------|------------|----------------------------------|------------------|
| Chokshi and Porter (1985)       | 18         | B         | air        | 40-100       | $10^{-7}$ - $10^{-4}$  | 1500        | $\leq 5$   | 5.2        | 450                              | ARCO             |
| Porter et al. (1987)            | 5-20       | B         | air        | 40-200       | $10^{-7}$ - $10^{-3}$  | 1450-1600   |            | 5          | 450                              | RISC, ORNL, ARCO |
| Lipetzky et al. (1988)          | 33         | B         | air        | 30-250       | $10^{-10}$ - $10^{-5}$ | 1200, 1300  | 1-2        | 1.5        | 450-500                          | WG-300           |
| Xia et al. (1988)               | 9.3, 18    | B         | air        | 40-200       | $10^{-7}$ - $10^{-4}$  | 1400-1550   | 1-2        | 3.8        |                                  | ARCO             |
|                                 | 30         | B         |            | 40-200       | $10^{-7}$ - $10^{-4}$  |             |            | 6.3        |                                  |                  |
| Porter (1989)                   | 5          | B         | air        | 20-200       | $10^{-10}$ - $10^{-5}$ | 1500        |            | 1.5, 2.7   |                                  | RISC             |
|                                 | 15         | B         | air        | 20-200       | $10^{-10}$ - $10^{-5}$ | 1500        |            | 7.9        |                                  |                  |
| Donaldson et al. (1989)         | 24         | B         | air        | 10-70        | $10^{-6}$ - $10^{-3}$  | 1500        | <1         | 2.88       |                                  | ARCO             |
| Wang et al. (1989)              | 29         | B         | air        | 130-320      | $10^{-9}$ - $10^{-7}$  | 1250        | 1          | 5          |                                  | ARCO             |
|                                 | 29         | B         | air        | 130-320      | $10^{-9}$ - $10^{-7}$  | 1150        | 1          | 3          |                                  |                  |
| Liu and Majidi (1990)           | 9, 18, 29  | C         | air        | 10-300       |                        | 1250-1350   | 1          | 1.8, 2.4   | 740, 590, 730                    | ARCO             |
| Lin et al. (1990)               | 20         | B         | air        | 37-300       | $10^{-9}$ - $10^{-5}$  | 1200-1400   | 2          | 2          |                                  | ORNL             |
|                                 | 20         | B         | air        | >125         | $10^{-9}$ - $10^{-5}$  | 1400        | 2          | 7-8        |                                  |                  |
| De Arellano-Lopez et al. (1990) | 6-29       | C         | argon, air | 100-300      | $10^{-8}$ - $10^{-4}$  | 1300-1500   | 1.5        | 1.2-1.8    | 620                              | ARCO             |
| Lin et al. (1991)               | 30-50      | B         | air        | 37-300       | $10^{-9}$ - $10^{-5}$  | 1300        | 1-2        | 6          |                                  | ORNL             |
|                                 | 30-50      | B         |            | 37-300       | $10^{-9}$ - $10^{-5}$  | 1200        | 1-2        | 3          |                                  |                  |
|                                 | 10         | B         |            | 37-300       | $10^{-9}$ - $10^{-6}$  | 1300        | 8          | 4          |                                  |                  |
|                                 | 10         | B         |            | 37-300       | $10^{-9}$ - $10^{-6}$  | 1200        | 8          | 2          |                                  |                  |
| Lipetzky et al. (1991)          | 33         | C         | air        | 25-250       | $10^{-9}$ - $10^{-6}$  | 1200-1400   | 1-2        | 1, 3       | 269, 655                         | WG-300           |
|                                 | 33         | C         | nitrogen   | 25-250       | $10^{-9}$ - $10^{-6}$  | 1200-1400   | 1-2        | 1, 3       | 210, 966                         |                  |
| Swan et al. (1992)              | 30         | C         | air        | 25-200       | $10^{-8}$ - $10^{-5}$  | 1200-1350   | 1-2        | 1.4-1.7    | 370                              | ARCO             |
| Nutt and Lepetzky (1990);       | 33         | B         | air        | 30-250       | $10^{-10}$ - $10^{-6}$ | 1200, 1300  | 1-2        | 1, 5       | Nitrogen                         | WG-300           |
| Nutt and Lepetzky (1993)        | 33         | C         | air        | 25-250       | $10^{-9}$ - $10^{-6}$  | 1300, 1400  | 1-2        | 3.3, 3.5   | 210, 966                         |                  |
|                                 | 33         | C         | nitrogen   | 100-350      | $10^{-9}$ - $10^{-8}$  | 1200        | 1-2        | 1          |                                  |                  |
|                                 | 33         | C         | nitrogen   | 25-250       | $10^{-9}$ - $10^{-6}$  | 1300        | 1-2        | 3.5        | Air                              |                  |
|                                 | 33         | C         | nitrogen   | 25-250       | $10^{-9}$ - $10^{-6}$  | 1400        | 1-2        | 1, 3.5     | 269, 655                         |                  |
|                                 | 10, 30     | C         | nitrogen   | 10-300       | $10^{-9}$ - $10^{-5}$  | 1300        | 1-2        | 1.8, 3.5   |                                  | ARCO             |
|                                 | 10, 20, 30 | B         | nitrogen   | 10-200       | $10^{-9}$ - $10^{-6}$  | 1300        |            | 2-2.3      | $T_c \approx 1280^\circ\text{C}$ |                  |
| De Arellano-Lopez et al. (1993) | 5, 6       | C         | argon      | 10-240       | $10^{-7}$ - $10^{-5}$  | 1400        | ?          | 1.8, 1.9   |                                  | ANL, ARCO        |
|                                 | 15-30      | C         | argon      | 80-410       | $10^{-6}$ - $10^{-4}$  | 1400        | 1.5-3.3    | 1, 2.4-5.9 |                                  | ORNL             |

|  |        |   |     |        |                        |            |       |             |                   |
|--|--------|---|-----|--------|------------------------|------------|-------|-------------|-------------------|
| Tuffe et al. (1994)                      | 10-40  | B | air | 40-200 | $10^{-10}$ - $10^{-6}$ | 1200, 1300 | 3-10  |             | FRANCE            |
|  | 30     | B | air | 40-200 | $10^{-10}$ - $10^{-6}$ | 1300       | 3-10  | 1, 5        |                   |
| Romero et al. (1995)                     | 29     | B | air | 50-350 | $10^{-11}$ - $10^{-5}$ | 1000-1300  | 1-2   | 5.5-17      | ARCO              |
| Hansson et al. (1995);<br>O'Meara (1996) | 25     | T | air | 10-70  | $10^{-10}$ - $10^{-4}$ | 1100-1300  | <1    | 3-4         | 620<br>650        |
| Xia et al. (1995)a;                      | 9.3    | B | air | 10-100 | $10^{-7}$ - $10^{-4}$  | 1400-1550  | 1-2   | 3.8         | 820-830           |
| Xia et al. (1995)b                       | 18, 30 | B | air | 20-200 | $10^{-7}$ - $10^{-4}$  | 1400-1550  | 1-2   | 3.9, 6.3(3) | 690-740, 930-1010 |
| Lin et al. (1996)                        | 10     | B | air | 50-230 | $10^{-8}$ - $10^{-7}$  | 1200       | 1.2-8 | 2           | ORNL              |
|  | 10     | B | air | 50-230 | $10^{-8}$ - $10^{-7}$  | 1300       | 1.2-8 | 3.5         |                   |

B: Four point bending

C: Compression

T: Tensile

ARCO: Advanced Materials Co. (formerly ARCO Chemical Co.), Greer, SC, US.

ORNL: Oak Ridge National Laboratory, Oak Ridge, TN, US.

ANL: Argonne National Laboratory, Argonne, IL, US.

RISC: Rockwell International Science Center, Thousand Oaks, CA, US.

WG-300: Greenleaf Co., Saegertown, PA, US.

supported by the TEM observation of a higher density of dislocation networks in the vicinity of SiC whiskers within the crept samples (Porter et al. 1987). Later, Xia et al. (1988, 1995 and 1996) arrived at the same conclusion regarding the creep mechanism. Their TEM observation revealed the occurrence of more extensive dislocation activities within the crept samples deformed to larger strains up to 14%, while very little evidence of internal cavities was observed. However, the dislocation networks were also detected in the as-processed composites and have been ascribed to internal thermoelastic stresses. The dislocation networks are stable and seem to either remain unchanged by creep deformation (Nutt 1988, Arellano-Lopez et al. 1990) or else the post-creep dislocation density is found to be negligible. Therefore, more recent studies tend to conclude that it is unlikely that dislocation glide plays a significant role in the creep deformation (Lipetzky et al. 1991, Lin and Becher 1991, Arellano-Lopez et al. 1993). Instead, microstructural damage in the form of cavitation has emerged as the primary reason for the high stress exponent found especially in bending creep, which was supported by microstructural observations by SEM and TEM (Lin and Becher 1990). This mechanism also seems to be in agreement with the observations of bilinearity in the strain rate versus stress plot by many researchers where a shift in stress exponent was seen when the applied stress reached a critical level (e.g. Lipetzky et al. 1988, Porter 1989, Lin et al. 1990, De Arellano-Lopez, 1993 and 1998, Nutt and Lipetzky, 1991 and 1993, Tuffe et al. 1994). Figure 2.9 shows one example.

Below the critical stress, the creep exponent seems to fall between 1 and 2, which was often ascribed to diffusion controlled GBS like in monolithic alumina. Above the threshold stress, the stress exponent tends to be greater than 2, which was attributed to the significant cavitation and microcracking both often coupled with oxidation related phenomena supported by very detailed TEM works by Lipetzky et al. (1988, 1991), Nutt et al. (1990, 1993) and Lin and Becher (1991).

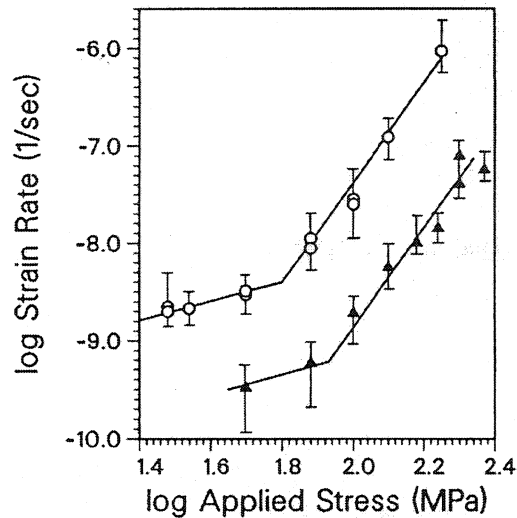


**Fig. 2.9** Strain rate vs. stress relations for flexural creep of 33% SiC whisker reinforced alumina composites: ▲ 1200°C; ○ 1300°C. The bilinear behaviour yields  $n=1$  and  $n=5$ , assuming a power-law-type constitutive relation. (Nutt and Lipetzky 1990, 1993)

### Reinforcement loading

The general consensus on the effect of whiskers during creep deformation is that they reduce the creep rate by retarding the grain boundary sliding and increasing the diffusion path for the alumina matrix. The effects of whisker loading need to be understood with much care since whisker loading strongly affects the sintering process of the composite, thus resulting in a different microstructure, particularly the grain size of the matrix and its distribution. In addition, whisker loading has counteracting effects on creep rate during creep in an oxidizing atmosphere (Lin and Becher 1991, De Arellano-Lopez 1993 and 1998).

It is evident, as pointed out by De Arellano-Lopez (1990), that a comparison of creep rate without considering the composite microstructure, especially matrix grain size is misleading. For instance, Porter et al. (1987) found similar creep rates for 5, 15 and 20% whisker reinforced aluminas at 1500°C. However, it is noted that all the samples were prepared by the same colloidal processing method and the final sintering involved the same temperature and pressure, which suggests that different matrix grain size was obtained for different whisker loading. So, it is very likely that 5% whisker-containing

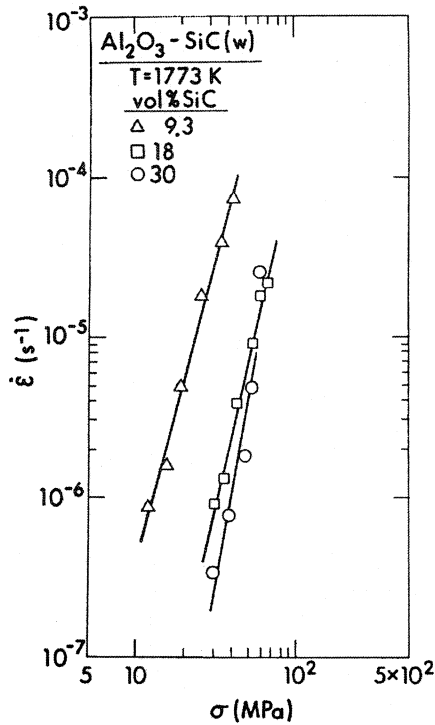


**Fig. 2.10** Strain rate vs. stress plot for 9.3, 18 and 30% SiC whiskers reinforced aluminas. The stress exponents are close to 6. (Xia and Langdon, 1995)

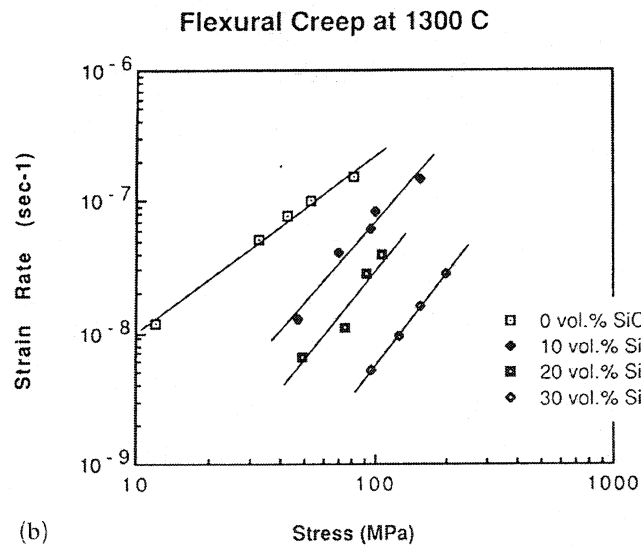


**Fig. 2.11** Flexural creep behaviour for composites with different whisker loadings. The test was performed at 1300°C in circulated dry nitrogen. The stress exponent was ~1.5 for alumina and 2-2.3 for composites. (Nutt and Lipetzky 1993)

composite had much larger grain size than the other two composites with higher whisker content, which explains the much lower creep rate due to an increase in diffusion path. Nevertheless, many studies (e.g. Xia et al. 1988 and 1995, De Arellano-Lopez et al. 1990, 1993, 1998, Nutt and Lipetzky 1991 and 1993, Tuffe et al. 1994) seem to suggest that the creep resistance generally increases with increasing whisker concentration provided that the whisker loading is not greater than about 30%, and that the microstructure (e.g. matrix grain size) and testing conditions remain comparable. However, the increase in creep resistance was not always in proportion with the increase in whisker volume fraction. There were some reports indicating that the extent of reduction in creep rate is small when the whisker loading increases from around 15% to about 30%, especially at high temperatures and stresses (Xia et al. 1988 and 1995, De Arellano-Lopez et al. 1990, 1993, 1998). Figure 2.11 provides an example from flexural creep. On the contrary, some (Nutt and Lipetzky 1993, Lin et al. 1991) reported a consistent increment in creep resistance up to about 30% of whisker loading. It is quite puzzling to note that Xia et al. (1988 and 1995) and Nutt and Lipetzky (1993) produced some contradictory results on creep rate from materials provided by the same manufacturer. This again perhaps implies the high sensitivity of creep properties of ceramic materials on the microstructure that varies from time to time and even batch to batch for the same manufacturer.

In many works (e.g. Chokshi and Porter 1985, Porter 1989), it has been shown that a more extensive primary creep stage resulted with the addition of whiskers into an alumina matrix. This is undoubtedly indicative of long-range stress relaxation processes (Wilkinson 1998). Based on the shape of strain rate versus stress curves, the reinforcement volume fraction can be roughly divided into two regimes: low (less than 10%) and high (more than 15%). With low whisker content a true steady-state stage always seems to have been reached (e.g. Porter 1989) whereas a continuously decreasing strain rate was observed during creep of the composites with higher whisker loading (e.g. Porter 1988 and 1989, Donaldson et al. 1988, Lin and Becher 1990, Swan et al. 1994). Figure 2.12 shows two creep curves reproduced from Porter (1989).



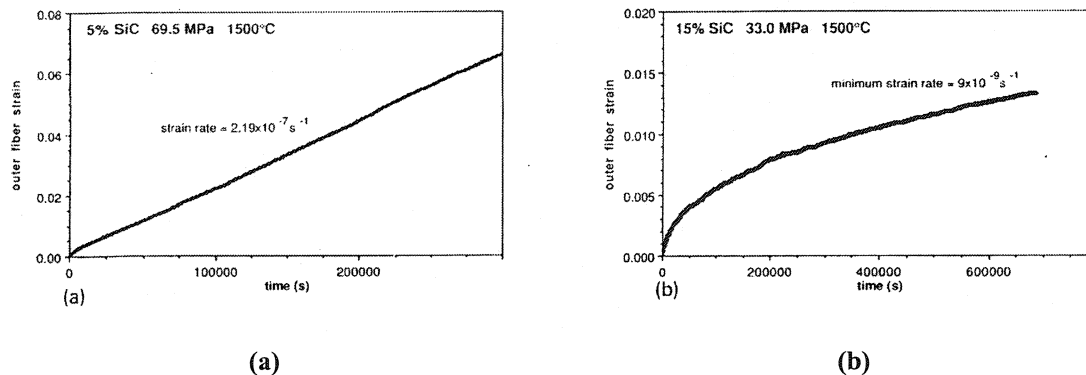
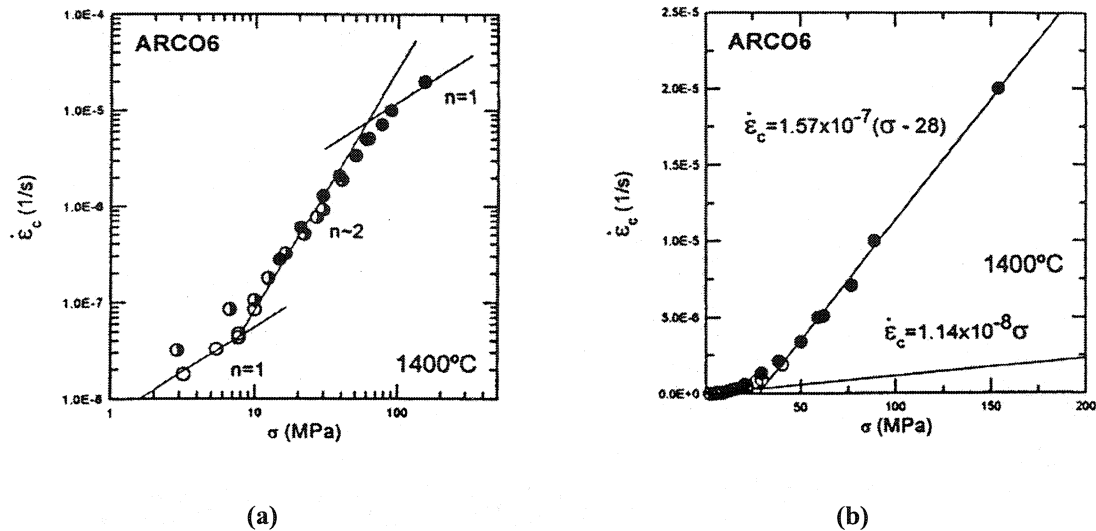


Fig. 2.12 Creep curves for (a) 5% and (b) 15% whisker-reinforced alumina composites. (Porter 1989)

### Low whisker loadings ( $\leq 10\%$ )

It is interesting to note that for composites with dilute whisker loading, say between 5-10%, all the independent compressive creep tests invariably produced a similar stress exponent i.e. 1-2 (Liu and Majidi 1990, De Arellano-Lopez 1990, 1993, 1998) while bending creep tests gave a slightly higher stress exponent (Xia et al. 1988, Lin and Becher 1991, Nutt and Lipetzky 1993). These seem to suggest that the operative creep mechanism in composites with a dilute amount of whiskers is not much different from that in monolithic alumina. However, the reduced strain to failure for the composites compared to pure alumina suggests other forms of strain generation. Indeed even at very low strain a small number of voids was observed in triple points near whisker sites where the local stress concentration is high (De Arellano-Lopez 1990, 1993). Based on this it was suggested by the same authors that the strain due to unaccommodated sliding contributes less to the total strain than the accommodated strain, and the occurrence of cavities is sufficiently slow to allow for the achievement of a quasi-steady-state creep regime. The higher stress exponents found in flexural creep tests are probably due to the enhanced damage accumulation coupled with more extensive glass formation in tension.

More recently, De Arellano-Lopez et al. (2000) characterised compressive creep behaviour of 6% whisker reinforced alumina at 1400°C in argon. In this study, they observed three intervals of behaviour: both at low and high stresses, stress exponent  $\approx 1$  while at intermediate stress range  $\approx 2$ .



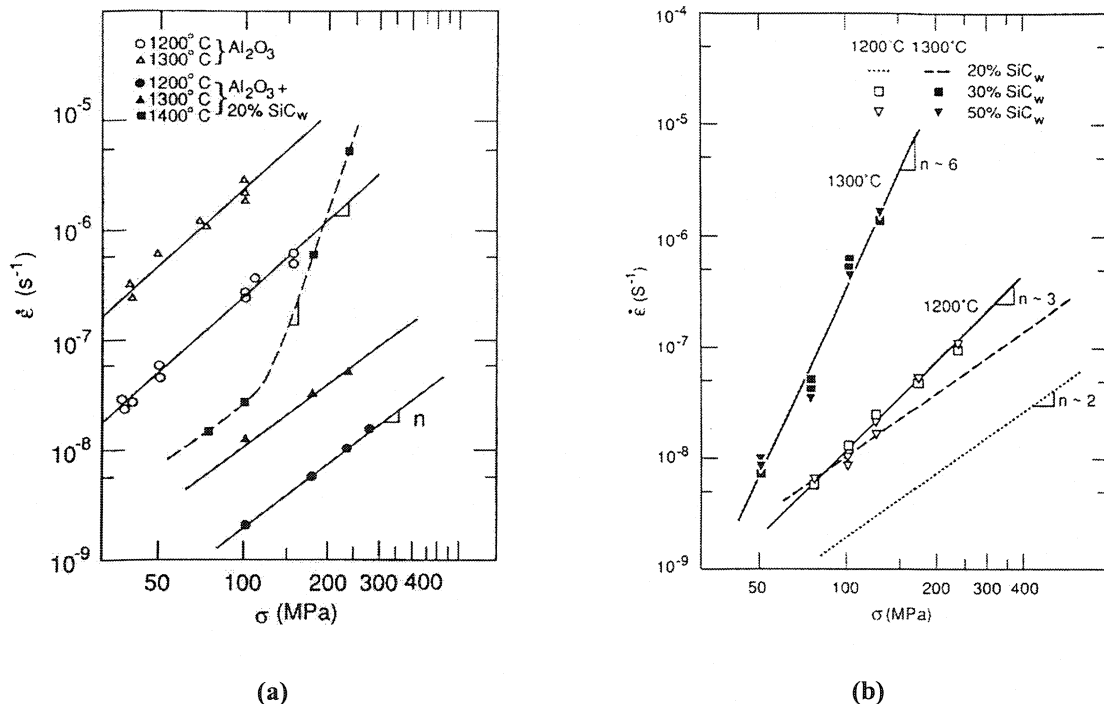
**Fig. 2.13** Strain rate vs. stress plot in (a) logarithmic scale (b) linear-linear scale for 6% whisker containing alumina composite crept in compression. Three samples were tested, which are represented here by different symbols. (De Arellano-Lopez et al. 2000)

Figure 2.13(a) shows the corresponding creep data. However, incorporation of a threshold stress above 28 MPa led to  $n=1$  for the whole stress range involved, as shown in Fig. 2.13(b). Thus it was suggested that below the point-contact percolation limit of whisker loading ( $\sim 7\%$ ) creep is controlled by diffusional flow under low stress while under high stress, flow is controlled by accommodated GBS. This was in accord with the “deformation map” they had proposed earlier (De Arellano-Lopez et al. 1998).

### Higher whisker loadings ( $\geq 15\%$ )

The continuously decreasing creep rate with time (or strain) suggests that the composites become stiffer with deformation, resulting in lower strain to failure. In general, the reduction in steady-state strain rate obtained in laboratory conditions was consistently in the range of 1 to 2 orders of magnitude when compared with unreinforced alumina (e.g. Chokshi and Porter 1985, Lin and Becher 1990, Nutt and Lipetzky 1993). It is also noticeable from some of the reported data that the improvement in creep resistance seems to be more substantial at low stress (e.g. Nutt and Lipetzky 1993, De Arellano-Lopez 1998). On the other hand, when there is a shift in stress exponent to a higher value above a critical stress as shown in Fig. 2.14(a), it is not surprising to see the improvement in creep resistance vanishing quickly

with increasing stress. In spite of some discrepancies (Nutt and Lipetzky 1993), more recent studies tend to conclude that the absolute creep rate is not strongly dependent on whisker concentration (Lin and Becher 1991, De Arellano-Lopez 1993, Wilkinson 1998). Lin and Becher (1991) demonstrated that 30 and 50% whisker reinforced aluminas exhibit essentially identical creep response as shown in Fig. 2.14(b), suggesting that the whisker loading is no longer a strong microstructural constraint on creep rate above a certain critical level. As mentioned above this is related to the counteracting effects of whiskers at high volume, so to speak. On one hand they impede GBS while on the other hand provide more stress concentration sites for nucleation and coalescence of cavities and cracks. Enhanced reduction in whisker aspect ratio during processing could well be one of the offsetting effects of high whisker volume fraction (De Arellano-Lopez 1990, Wilkinson 1998).



**Fig. 2.14** Strain rate vs. stress plot for creep of polycrystalline alumina and (a) 20% SiC whisker reinforced aluminas. (Lin and Becher 1990). (b) 20, 30 and 50% SiC whiskers. (Lin and Becher 1991)

It is commonly believed that the creep mechanism at low stress is GBS accommodated diffusional creep and at high stress GBS becomes more unaccommodated and microstructural damage starts contributing to the strain generation processes (Lipetzky et al. 1991, Swan et al. 1992, De Arellano-Lopez 1993, 1998). However, the precise creep mechanisms are not fully understood since the high temperature deformation of the composites seems to depend on many factors, especially microstructure, in a complex fashion.

### **Grain size effect on creep rate**

Lin and Becher (1996) studied the grain size effect on creep of 10% whisker reinforced composites using flexural creep tests in air. They found a grain size exponent of approximately 1 at 1200°C while at 1300°C the creep rate was independent of matrix grain size. The latter was attributed to the enhanced nucleation and coalescence of cavities and the development of macro cracks with increasing grain size. Their data is reproduced in Fig. 2.15. Later De Arellano-Lopez et al. (2000) performed compressive creep tests on the composites from the same source (ORNL) at 1400°C in argon. They normalized the grain size effect assuming grain boundary diffusion, i.e. a grain size exponent of 3 was used (see Eq.2.2). Since the free volume within the whisker network, not the nominal grain size was believed to control the creep rate, an effective grain size (EGS) (De Arellano-Lopez et al. 1995 and 1998) was invoked for normalization instead of the nominal grain size. The normalized data as shown in Fig. 2.16(a), however, cannot be fitted closely into one single line as expected. Instead there seemed to be a transitional stress region for two sets of data, which corresponds to a higher stress exponent. Assuming GBS creep (stress exponent is 1), a threshold stress was introduced to account for the higher stress exponent at the transitional stress region. However, they did not see such a transitional behaviour from one of the three composites. Careful examination of the data prior to normalization (See Fig. 2.16(b)) indicates that the composites with nominal grain size of 4.0 and 2.3  $\mu\text{m}$  seem to exhibit a monotonous increase in creep rate with increasing stress. However, the composite with 1.2  $\mu\text{m}$  grain size exhibits lower creep rate than those with larger grain size towards low stress region and there seems to be a well-established bilinearity. When the

applied stress reaches 60 MPa, all three composites show a similar creep rate. This again seems to be a case in which, without detailed knowledge of microstructure, it is difficult to understand the effect of grain size on creep rate. Nonetheless, taken overall, it may be true that the grain size effect tends to be more pronounced at low temperature and stress where diffusion through grain boundaries and/or lattice controls creep deformation.

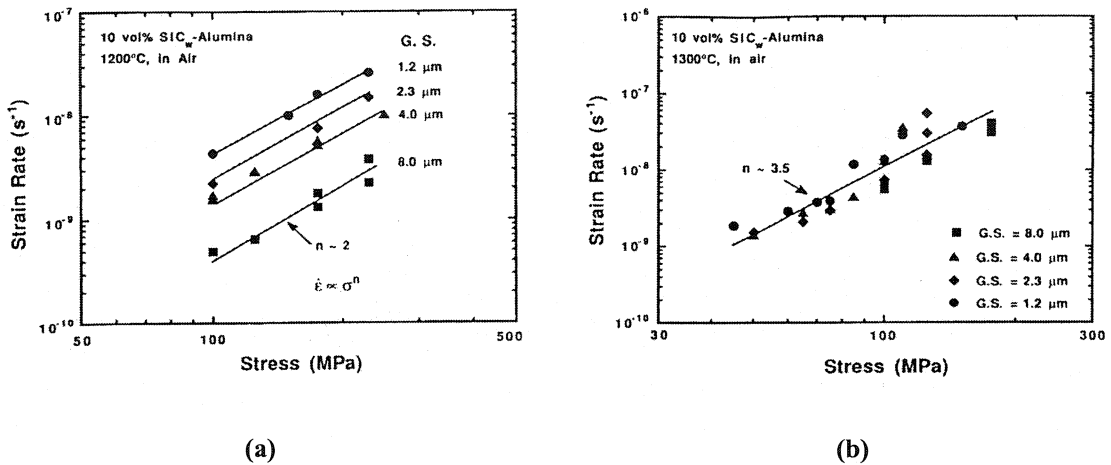


**Fig. 2.15** Strain rate vs. stress curves for alumina reinforced with 10% SiC whiskers tested (a) at 1200°C and (b) 1300°C. (Lin and Becher 1996)

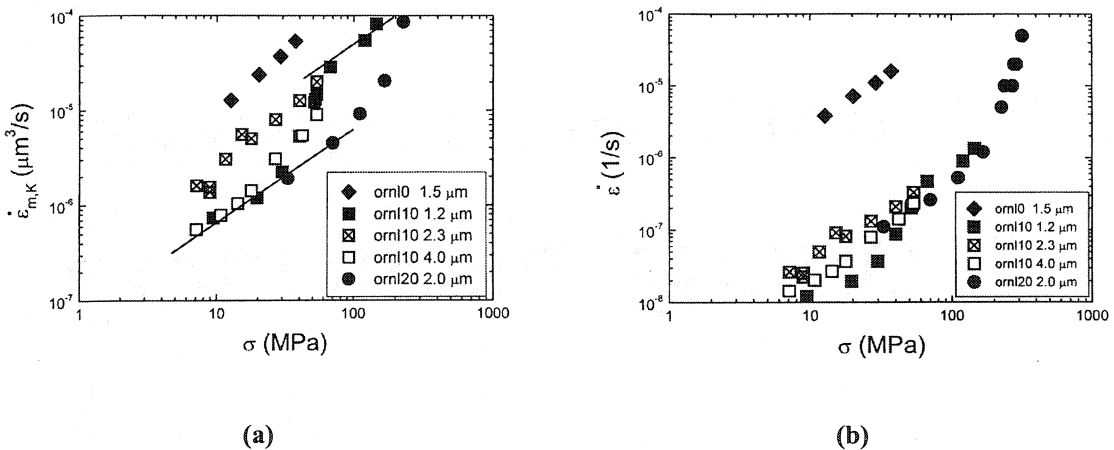


**Fig. 2.16** (a) Normalized strain rates of alumina matrix vs. stress and (b) absolute strain rates vs. stress at 1400°C. (De Arellano-Lopez et al. 2001)

### **Creep strain recovery**

Anelastic strain recovery has long been observed in some ceramic materials (e.g. Aron and Tien 1980, Morrell and Ashbee 1993, Holmes et al. 1993, Lange et al. 1980). Porter (1989) first reported the anelastic strain recovery in SiC whisker reinforced alumina using a four-point bending tests. Figure 2.17 shows the strain recovery after load removal in 15% SiC whisker reinforced alumina composite in which the magnitude of recovered strain is  $\sim 0.001$ . However, no such behaviour was observed in 5% whisker reinforced alumina. To explain the strain recovery behaviour, the author suggested a network of interconnected whiskers that are not free to rotate about their contact points. Such a network should have a lower elastic modulus as a whole than an individual whisker in tension. It was then suggested that to sustain the high degree of anelastic strain recovery on load removal, the strain energy has to be accumulated in the network by the elastic bending of whiskers. Figure 2.18(a) is a schematic given for this hypothesis and Fig. 2.18(b) a spring-dashpot model for the anelastic response. The observation of anelastic recovery in the composite was remarkable since it adds information that can be used to better understand creep mechanisms (Cannon and Haig 1995).

Later, Gu et al. (1994, 1995) did more systematic studies on the anelastic recovery behaviour of  $\text{Al}_2\text{O}_3\text{-SiC}_w$  composites. Their work indicated that the pure alumina material exhibited no anelastic recovery while the composite with 15% whiskers, in accordance with the previous result from Porter (1989), showed a significant anelastic recovery ( $\sim 0.001$ ) on load removal. This is shown in Fig. 2.19. Moreover, it is interesting that the magnitude of the recoverable strain was essentially independent of the total creep strain at which the load was removed. The effect of whisker aspect ratio was also studied (see Fig. 2.20), which indicated that whiskers with low aspect ratio resulted in more strain recovery than whiskers with high aspect ratio. It is also noted that the former clearly exhibits more extensive transitional behaviour while the latter did not. This is a quite perplexing result since high aspect ratio should be associated with more whisker bending strain according to Porter's model, thus resulting in more strain recovery. It is probably more surprising to see their result on SiC particle reinforced alumina, which is shown in Fig. 2.20. There is clearly anelastic strain recovery upon load removal with the magnitude being comparable with that in whisker reinforced alumina composites. They simply suggested that even 15%

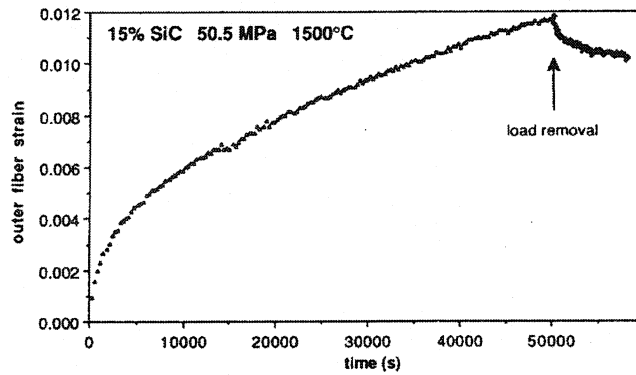


Fig. 2.17 Strain recovery after load removal in 15% SiC whisker reinforced alumina. (Porter 1989)

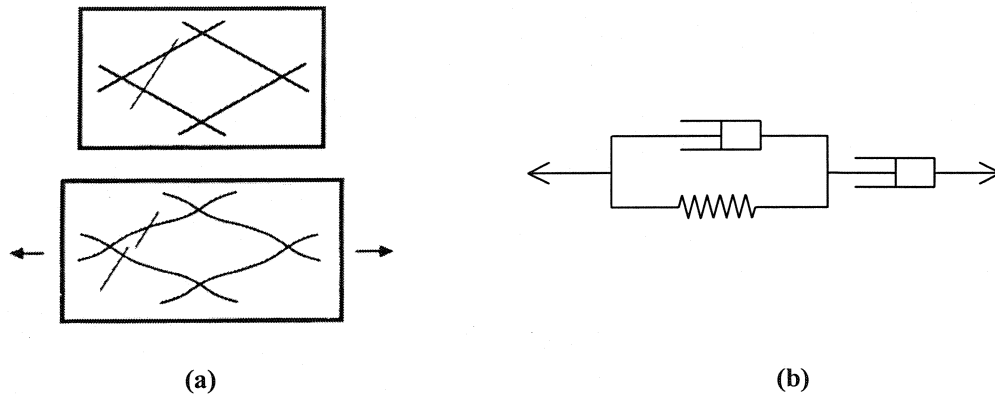


Fig. 2.18 (a) Schematic of whisker network deformation and (b) Kelvin element in series with a dashpot. (Porter 1989)

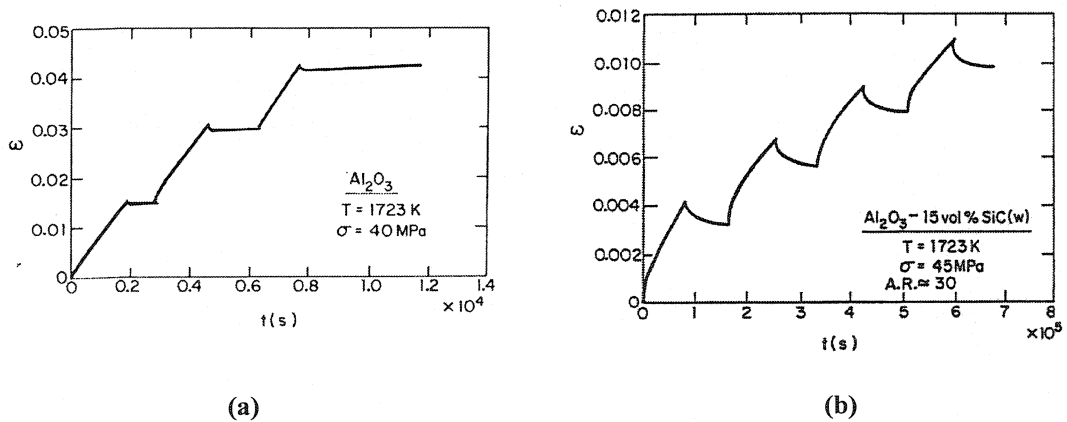
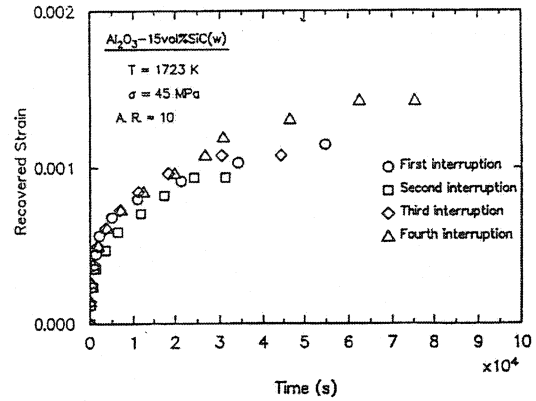
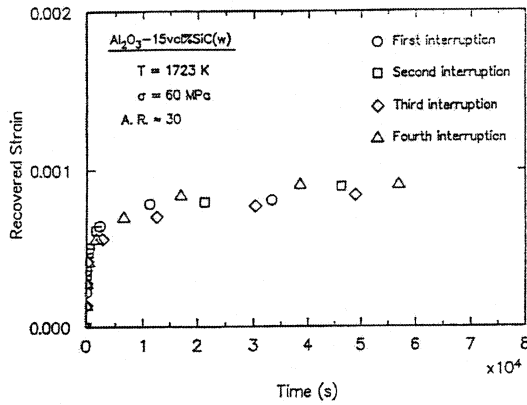
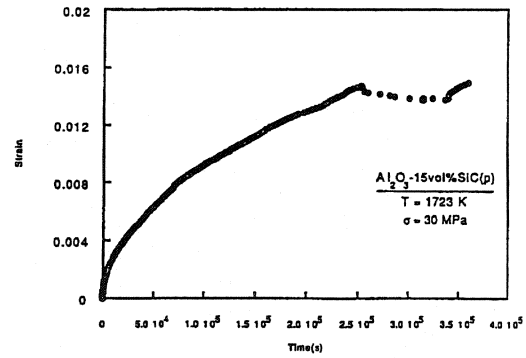
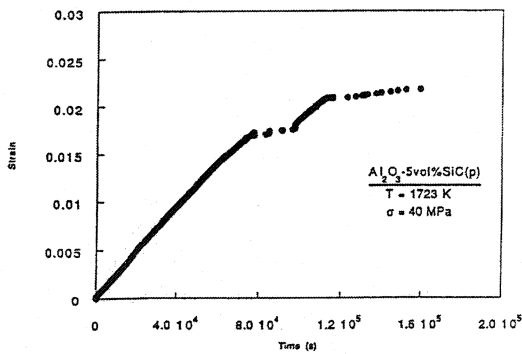


Fig. 2.19 Creep strain vs. stress plot for (a) pure alumina (b) 15% whisker reinforced alumina composite showing the effect of load removal. (Gu et al. 1995)



(a) (b)  
**Fig. 2.20** Recovered strain vs. time after load removal for an alumina with 15% SiC whiskers having as an aspect ratio of (a) 30 and (b) 10. (Gu et al. 1995)



(a) (b)  
**Fig. 2.21** Strain vs. time plot for (a) 5% (b) 15% SiC particle reinforced alumina composites showing the effect of load removal. (Gu et al. 1995)

SiC particles may have formed a network, which is responsible for the significant strain recovery. They presented a phenomenological model consisting of a Kelvin element in series with a spring, which only qualitatively describes the anelastic response.

### Tensile creep of SiC whisker reinforced alumina

It appears that there has been only one study (Hansson et al. 1995, O'Meara et al. 1996, the same work in two separate reports) in which tensile creep testing was carried out in air on a 25% SiC whisker



reinforced alumina. The composite was made by hot isostatic pressing (HIP) for 1 h at 1600°C under 160 MPa. The creep resistance of the composite was found to be even lower than the pure alumina, which was ascribed both to the inhomogeneous microstructure and to a finer grain size. Their microstructural examination revealed that the steady-state creep rate is dominated by damage accumulation processes involving cavitation and crack growth in both the SiC clusters and the whisker-free matrix channel. They found that pre-heat treatment actually lowered the density of cavities, cavity nucleation rates, and thus creep rates. This is probably due to reduced stress concentration and enhanced interface strength by heat treatment under no applied stress. A similar behaviour has been reported in nano size SiC particle reinforced alumina composites (Niihara and Nakahira 1990).

### **Effect of whisker orientation on creep rate**

Since uniaxial hot pressing is commonly employed to fabricate the composites, the whiskers tend to align with their axes perpendicular to the hot pressing axis (HPA). Therefore, the elastic creep response of the composite must be dependent on sample orientation with respect to HPA. If the elastic loading of whiskers as a whole is an important factor of the creep response, different creep response is expected for different loading direction (Ham Su 1997, Wilkinson 1998). Indeed, Lipetzky et al. (1988) demonstrated during creep of 33% whisker reinforced alumina that when the four-point flexure loading direction is coincident with the HPA, a higher creep rate was seen than with the loading direction and tensile axis are both perpendicular to the HPA. Figure 2.22 shows their results. They did not offer any explanation for this orientation dependence of the creep behaviour. However, Swan et al. (1992) did not find such behaviour during compressive creep testing of 30% SiC whisker reinforced alumina. It is noted that different materials sources were involved in the two aforementioned studies and the optical micrographs provided therein seem to show remarkable differences, the latter featuring more of a domain structure. Although both materials seem to have undergone a granulation process prior to hot pressing, it is still likely that different whisker texture was achieved in the final products due to the different processing routes and parameters adopted by different manufacturers. A more “domained” structure is probably

indicative of more random whisker distribution. This may explain a lack of sample orientation effect in the work of Swan et al. (1992). An alternative explanation would be: whisker orientation dependence is sensitive to stress state, i.e. it is more prominent in tension than in compression.

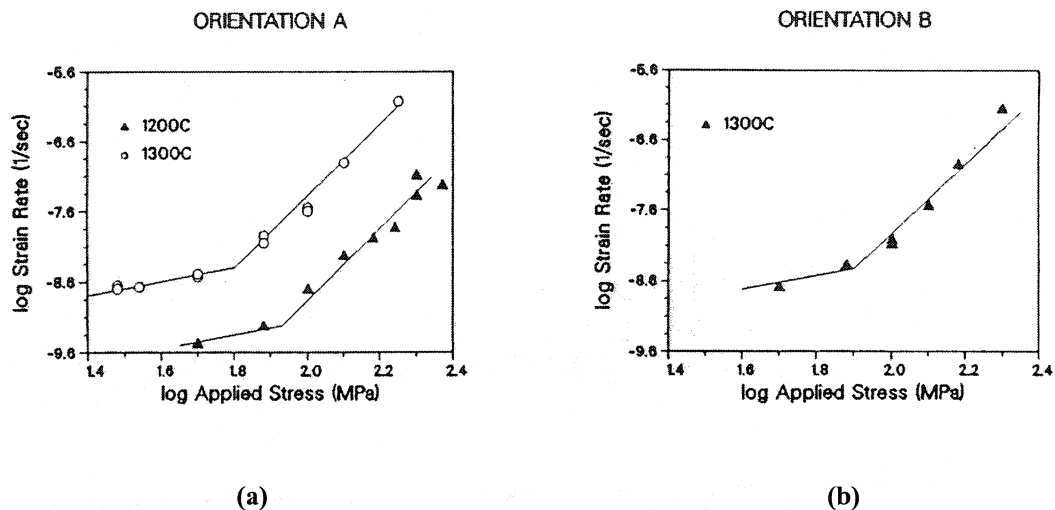


**Fig. 2.22** Strain rate vs. stress relations for creep of 33% SiC whisker reinforced alumina composite. (a) Bilinear behaviour yielding stress exponents of 1 and 5 for orientation A in which HPA and the load train are coincident. (b) Orientation B, in which the HPA and the load train are perpendicular. (Lipetzky et al. 1988)

### Atmospheric effects on creep

Atmospheric effects on creep are closely related to the properties of grain boundaries and interfaces in the composites. The general agreement in the literature is that the thermal oxidation of SiC leads to the formation of a vitreous phase along composite grain boundaries and interfaces, enhancing boundary diffusion, thus, lowering the viscosity of grain boundary phases. Consequently, under the applied stress, grain boundary sliding is facilitated and cavitation is promoted, resulting in an increase in creep rate.

There have been some reports on this issue (Nutt et al. 1991 and 1993, De Arellano-Lopez et al. 1990, 1993), in which, as anticipated, the creep rate was always found to be lower in inert atmosphere than in air. However, the difference was not large especially at low stresses and temperatures. For instance, the decrease in creep rate was within a factor of 3 at 1300°C and 5 at 1400°C, and at stresses below 50 MPa the effect of test ambient on creep response diminished (Lipetzky and Nutt 1991). This is probably due in part to the fact that all the studies aforementioned involved compressive stress state, where the effects of

oxidation would be less significant than in tension. The primary microstructural difference between specimens crept in air and in inert ambient was the abundance of glassy phase in the former, which led to a somewhat slight increase in the size and number of cavities at triple grain junctions and at sites of whisker-whisker contacts (Lipetzky and Nutt 1991). However, the stress exponent was also found to be insensitive on the testing ambient, suggesting limited effect of oxidizing atmosphere on the creep mechanisms.

### **Summary**

It has been well established that the SiC whisker reinforced alumina composites have a much better creep resistance than pure polycrystalline alumina. This is in general due to the impeded GBS by whiskers. However, the absolute creep rate is a sensitive function of the composite microstructure, which mainly depends on whisker loading, matrix grain size and the amount of glassy phase at interfaces. Stress state was also found to affect the creep response. With increase in stress, the accommodation of GBS through diffusion becomes more difficult with the presence of whiskers. Instead, microstructural damage, mainly in the form of cavities occurs at grain boundaries, grain junctions and whisker-grain interfaces. This is responsible for a shift in stress exponent above a critical stress level. The accumulation of vitreous phases by the thermal oxidation of SiC lubricates and weakens grain boundaries and whisker-grain interfaces, thus facilitates cavitation, GBS and grain boundary diffusion, leading to an accelerated creep rate.

### **2.5.2 Creep of SiC particulate-reinforced Al<sub>2</sub>O<sub>3</sub> composites**

Niihara and his co-workers (1990) first reported that the dispersion of nano-size ceramic particles into ceramic matrix grains or grain boundaries results in substantial improvements of mechanical properties. For instance, 5 vol.% SiC nano-particles in an alumina matrix gave rise to a three fold increase in fracture strength up to 1200 °C. They also reported significant augmentation in creep resistance in the nano-particle reinforced composites. For example, flexural creep tests on 17% SiC particulate reinforced alumina showed four orders of magnitude decrease in creep rate at 1000-1400°C with the applied stress

of 100 MPa. Later, Ohji et al. (1994) conducted tensile creep tests on the same composites at 1200°C and 1300°C with the stress in the range of 50-150 MPa. The results indicated that the minimum creep rate of the nanocomposite was about three orders of magnitude lower and the creep life was 10 times longer than those of the monolithic alumina. Based on TEM characterisation of the crept and fractured composite samples, they suggested that during creep, the intergranular SiC particles rotated and plunged into the neighbouring alumina grains, retarding the grain boundary sliding, thus increasing the creep resistance. A change from an intergranular to intragranular fracture mode was understood by the observation of transgranular fracture of grain boundary particles and High resolution TEM (HRTEM) study of interfaces in the composites, the conclusion being a much higher strength of the matrix/particle interface than others. As pointed out by Descamps et al. (1999) this grain boundary strengthening hypothesis may also account for the retained high fracture strength of the composites at high temperature.

There seem to be discrepancies in the reports of the anelastic recovery behaviour of SiC<sub>p</sub>-Al<sub>2</sub>O<sub>3</sub> composites. Gu et al. (1995) reported that 15% sub-micron SiC particulate-reinforced alumina composite showed anelastic strain recovery upon unloading during creep, while composite containing 5% of SiC particulates did not show such behaviour. However, Descamps et al. (1999) demonstrated that alumina matrices reinforced with 5% SiC particles (both nano and micron size) exhibit anelastic recovery behaviour, and this effect was ascribed to the pinning effect of SiC particles at the grain boundaries. The measured recoverable strains were  $\sim 10^{-3}$ , which did not show a strong dependence on particle loading and size.

### **2.5.3 Creep of SiC platelet-reinforced Al<sub>2</sub>O<sub>3</sub> composites**

Ham-Su and Wilkinson (1995 and 1997) made SiC platelet-reinforced alumina composites with varying platelet alignment using colloidal processing techniques. The optical micrographs of the composites prepared by slip and tape casting methods are reproduced in Fig. 2.23. They used neutron diffraction techniques to characterize the platelet alignment and to measure the internal strains associated with SiC platelets in various conditions, which revealed useful information on creep deformation. Compared to the

slip cast composites, tape cast composites showed higher creep rates and larger creep exponent ( $n > 2$ ), which was attributed to the enhanced cavitation due to the weakened grain boundaries. This was directly related to the presence of larger quantities of impurities in the microstructure that originated from the use of additives in tape casting. Slip cast composites, with no additives involved, however, exhibited lower strain rates and low stress exponents ( $n < 2$ ). The main conclusions from this work were:

1. Modest increase in creep resistance was achieved through the addition of SiC platelets to alumina matrix.
2. No interlocking platelet network was formed in the composites due to the geometrical nature of platelets.
3. Less aligned platelets imparted greater creep resistance due to the more enhanced interactions between platelets during creep deformation.
4. Diffusional creep was found as the main deformation mechanism.

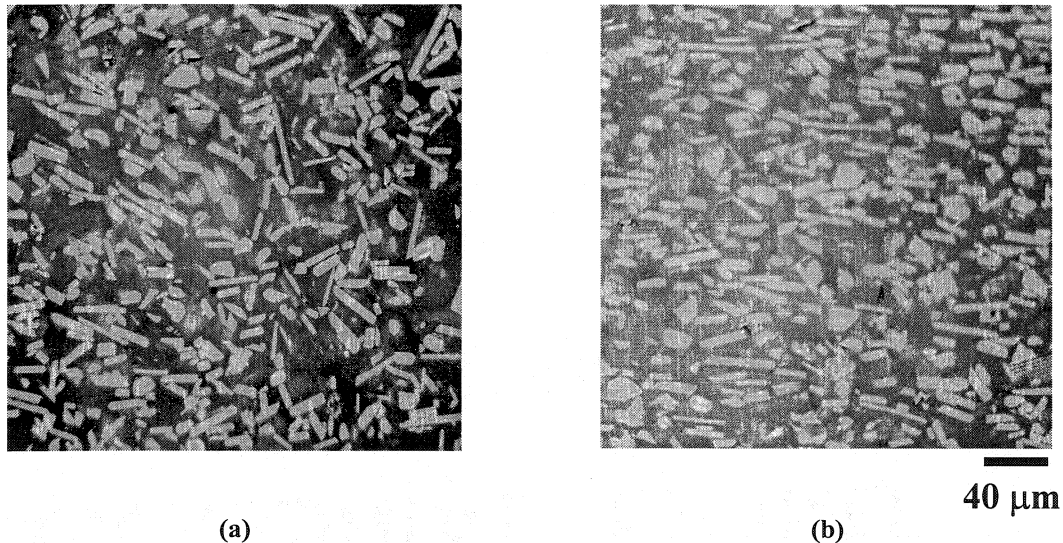


Fig. 2.23 Optical micrograph of hot-pressed 30% SiC platelet reinforced alumina sample prepared from slip casts with (a) pH=8 and (b) pH=2. Different particle alignment is noted. (Ham Su 1997)

## 2.5.4 Continuous fiber-reinforced ceramic composites

Holmes and co-workers (1991, 1993) studied tensile creep and strain recovery behaviour of continuous SiC fiber-reinforced ceramic composites. They found similar creep rates for different arrangement of fibers (namely,  $0^\circ$  and  $0^\circ/90^\circ$  ply layup). Upon unloading, both composites exhibited viscous strain recovery and the magnitude of recovered strain depended on details of fiber layout but not much on the applied stress. Since the measured anelastic strains were much higher than that reported for monolithic  $\text{Si}_3\text{N}_4$  (Lange et al. 1980, Arons and Tien, 1980), they suggested two additional mechanisms for strain recovery processes in the fiber-reinforced ceramics: (1) intrinsic recovery of the fibers upon a stress decrement and (2) change in residual stress equilibrium upon unloading. They also postulated that the differential creep rates of matrix and fiber also affect the development of residual stresses apart from their thermoelastic mismatch and that the residual stresses are relieved by in-situ creep of both phases at sufficiently high temperatures.

## 2.6 Creep models for multiphase ceramics

### 2.6.1 Creep in dilute systems

Einstein (1906, 1911) gave the classical solution for the effect of dilute spherical particle additions on viscosity as follows

$$\frac{\eta_{dl}}{\eta_o} = 1 + 2.5\phi \quad (2.6)$$

where  $\eta_{dl}$  is the viscosity of the composite,  $\eta_o$  that of the matrix and  $\phi$  is the particle volume fraction.

For whiskers aligned along the direction of principal stress again in the dilute limit the result is (Batchelor 1971)

$$\frac{\eta_{dl}}{\eta_o} = 1 + \frac{\lambda^2 \phi}{3(\ln(2\lambda) - 1.5)} \quad (2.7)$$

where  $\lambda$  is the aspect ratio and  $\lambda \gg 1$ , while for platelets, i.e.  $\lambda \ll 1$  (Barthés-Biesel and Acrivos 1973)

$$\frac{\eta_{dl}}{\eta_o} = 1 + \frac{1}{3\pi} \phi \lambda^{-3/2} \quad (2.8)$$

These relations seem to predict only a modest increase in viscosity even with high aspect ratios (Wilkinson 1998). For example, with 5% of whiskers and an aspect ratio of 10, the viscosity is doubled. Therefore, they appear to be applicable only at very low volume fraction of dispersoid.

### 2.6.2 Creep due to particle rotation

Wilkinson and Pompe (1998) considered the kinetics of particle rotation as limiting the creep rate of the overall composite. Figure 2.24 schematically illustrates this mechanism. They related the effect of misaligned whiskers with respect to the applied stress to an increase in the effective volume fraction of constrained regions in the matrix. According to this model, the material far from the particles has the viscosity of the unreinforced matrix phase,  $\eta_o$ , while the constrained regions around the particles have a much higher viscosity,  $\eta_r$ . Their expression for the normalized effective viscosity is given by

$$\frac{\eta_{reff}}{\eta_o} = 1 + 2.5 \frac{v_{con}}{1 - v_{con}} \quad (2.9)$$

where  $v_{con}$  is the volume fraction of the constrained regions, which is estimated from Fig.2.24 as follows,

$$v_{con} = \frac{1}{2} \left[ \langle \sin 2\theta \rangle \left( \lambda + \frac{1}{\lambda} \right) + 1 \right] \phi \quad (2.10)$$

This model predicts significantly higher viscosity increments and is more sensitive to the aspect ratio than the misorientation angle.

### 2.6.3 Creep in constrained networks

Wilkinson and Pompe (1998) used a highly simplified composite structure for formulating their conceptual viscous creep models. Figure 2.25 shows the geometry of an idealized composite structure where the whiskers are aligned primarily in one plane. Three parameters were used to define the

geometry: the particle aspect ratio,  $\lambda$ , the particle volume fraction  $\phi$ , and the packing efficiency,  $f$ . The latter is defined by  $L/l=fR/w$ .

Two creep mechanisms were considered. Figure 2.26 shows the simplified whisker bending configuration. First, the whiskers approach one another as matrix material is squeezed from between the regions of near contact, contributing a viscoplastic strain,  $\varepsilon_{vp} = -\Delta h / 2w$ , where  $\Delta h$  is the change in the thickness of the near-contact region. In addition, the offsetting whisker network will induce elastic bending of whiskers around points of contact, accommodated by local creep of the surrounding matrix material. This contributes a viscoelastic strain of  $\varepsilon_{ve} = \delta / 4w$ , where  $\delta$  is the elastic deflection of the neutral axis. Both of these processes are time dependent and transient, i.e. creep ceases once the load is fully borne by the fiber network. However, the initial effective viscosity of the composite due to each process was derived to characterize the kinetics of the flow.

Based on a basic result from lubrication theory for the rate at which a viscous phase is squeezed from between two plates, the normalized effective viscosity for viscoplastic creep was derived as

$$\frac{\eta_{vp}}{\eta_o} = \frac{2(1+f)}{k_p \lambda^2 f} \left[ \left( \frac{f^2}{\phi} \right)^{1/3} - 1 \right]^{-3} \quad (2.11)$$

where  $k_p$  is a stress concentration factor given as

$$k_p = \frac{1}{2} \sin 2\theta \quad (2.12)$$

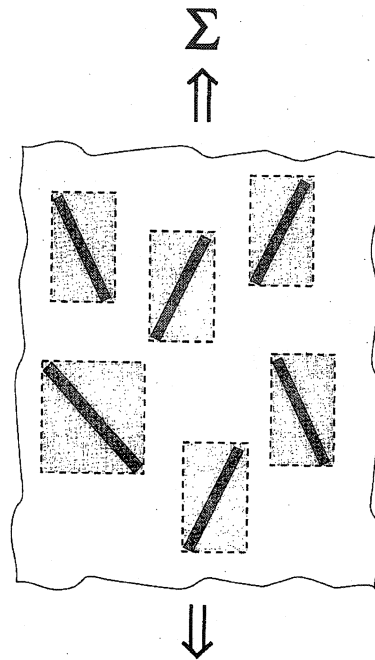
The treatment of the viscoelastic problem seems to be rather complex and the initial effective viscosity of the composite was given approximately by

$$\frac{\eta_{ve}}{\eta_o} = \frac{16}{\pi^4 k_p (f\phi)^{1/3}} \quad (2.13)$$

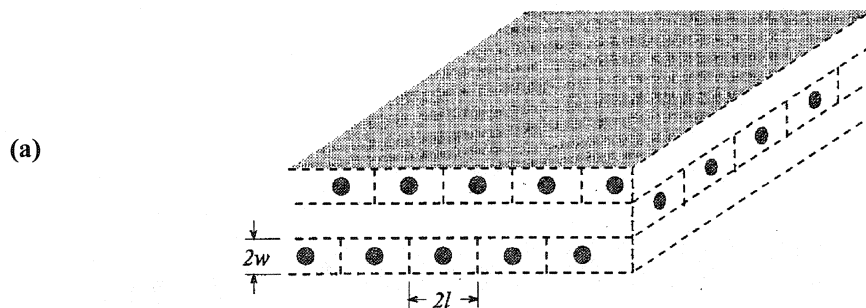
Figure 2.27 shows the viscosities due to different mechanisms as a function of volume fraction for in-plane loading. The viscosity due to viscoplastic flow  $\eta_{vp}$  increases strongly with increasing  $\phi$  due to the sensitive in-contact thickness dependence of the lubrication mechanism. On the contrary, the



viscoelastic creep viscosity decreases with increasing  $\phi$ . This is related to the decreasing relaxation time from the shortened diffusion path length  $d$ , with increasing packing density.



**Fig. 2.24** Schematic illustration of a dilute distribution of particles which rotate under a far stress field. (Wilkinson 1998)



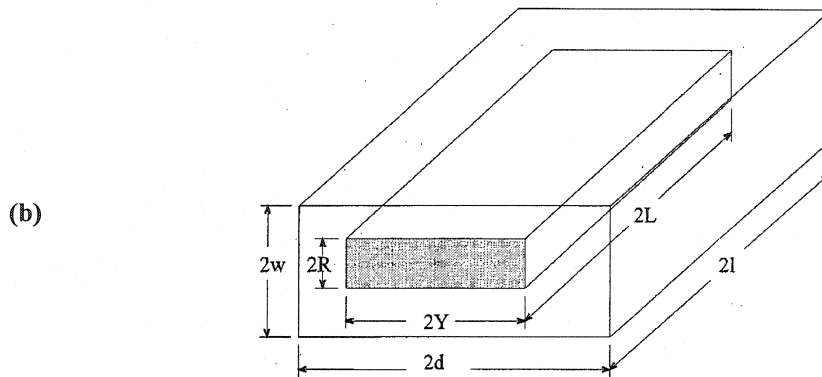


**Fig. 2.25 (a)** Geometry of an idealized whisker network and **(b)** geometrical parameters associated with a single cell surrounding each particle. (Wilkinson 1998)

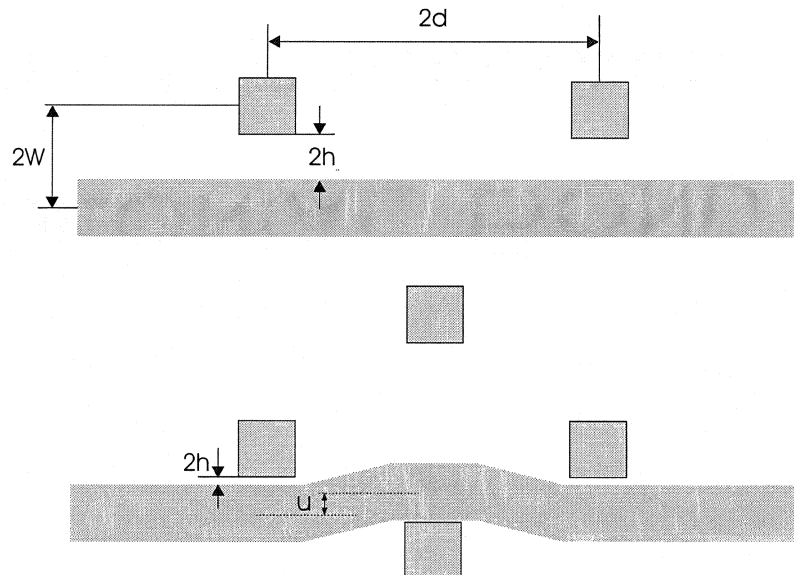


**Fig. 2.26** The simplified whisker bending configuration before and after creep. (Wilkinson 1998)

Figure 2.28 presents the effective viscosity as a function of volume fraction. For a fixed volume fraction the total viscosity increases with decreasing  $f$ . This reflects the effect of closer particle contact on the viscoplastic flow rate. It is noticeable that the solid curve representing the viscosity due to viscoelastic creep at minimum  $f = \phi^{1/2}$ , brackets the other curves.

Figure 2.29 summarizes the creep behavior of the composite materials studied in the form of creep mechanism map. The three main microstructural variables that were found to control creep in composites are volume fraction, aspect ratio and packing efficiency. In general, for a fixed packing efficiency, the total viscosity,  $\eta$ , of the composite increases with increasing volume fraction of reinforcement. It follows that the dominant mechanism changes from a viscoplastic to viscoelastic deformation mode. The boundary is seen to be sensitive to aspect ratio especially at high  $f$ . At a given volume fraction the dominant mechanism changes from viscoplastic to viscoelastic creep as  $f$  decreases. Also the extent of the viscoelastic creep field decreases as the aspect ratio of the fibers rises. This is due to a reduction in the required diffusion distance.

These models give a good picture of the overall creep behaviour of whisker or platelet-reinforced composites in general. The authors pointed out, however, that the continuous evolution of fiber network during creep must be considered because a gradual increase in stiffness of the particle network during deformation will definitely affect the creep response of the materials.

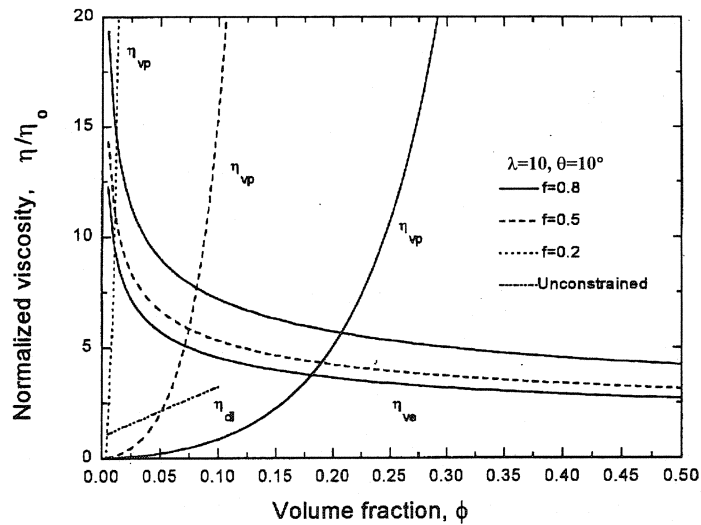
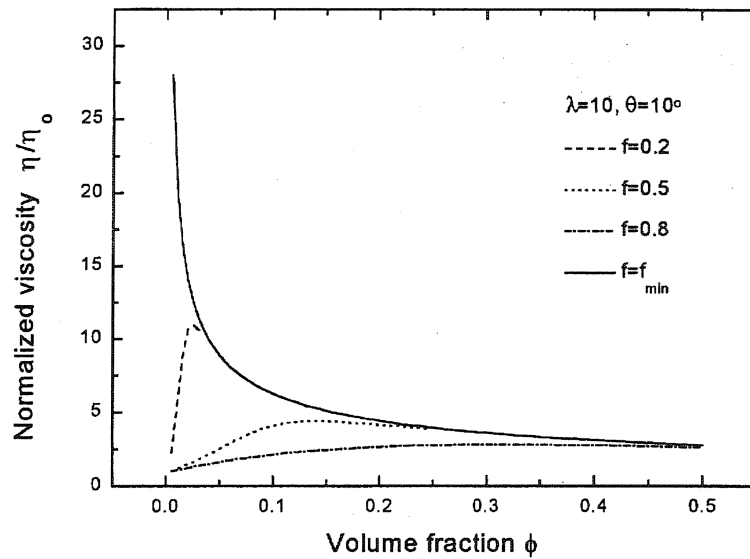
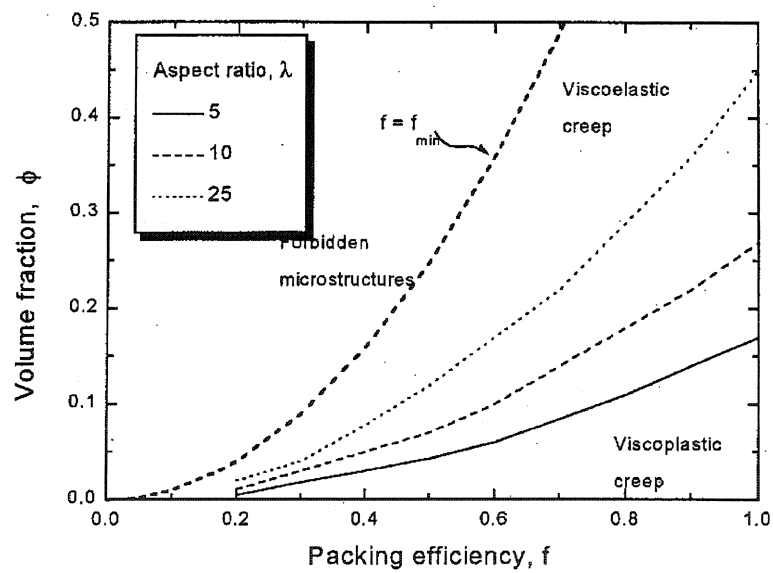


Fig. 2.27 Normalized viscosity  $\eta/\eta_0$  as a function of volume fraction  $\phi$  and packing anisotropy factor  $f$  for three mechanisms. (Wilkinson 1998)



**Fig. 2.28** Normalized total viscosity  $\eta/\eta_0$  as a function of volume fraction  $\phi$  and packing anisotropy factor. (Wilkinson 1998)



**Fig. 2.29** The boundary separating regions dominated by viscoelastic creep and viscoplastic creep of a constrained, oriented whisker network ( $\theta = 10^\circ$ ) loaded in the whisker plane. (Wilkinson 1998)

## 2.7 Residual stresses in Al<sub>2</sub>O<sub>3</sub>-SiC composites

The change in mechanical properties of composite materials is strongly affected by the residual stresses developed due to the thermoelastic mismatch between matrix and reinforcement phase. The premise is that the actual net stress felt by the material is determined by both the applied stress and the residual stresses. In the extreme, residual stresses can result in spontaneous microcracking on cooling. This section reviews the measurements of residual strains/stresses in Al<sub>2</sub>O<sub>3</sub>-SiC composites by diffraction methods.

### 2.7.1 SiC whisker reinforced alumina composites

Majumdar et al. (1988, 1989) studied the residual thermal stresses and strains in Al<sub>2</sub>O<sub>3</sub>-SiC<sub>w</sub> composites using neutron diffraction techniques offered by the intense pulsed neutron source (IPNS). The “white” spectrum enabled measurement of many peaks of both the matrix and reinforcement phases at the same time and in various spatial directions simultaneously. Strains were measured with respect to the local crystallographic coordinate system and not to a physical or specimen coordinate system. With the assumption of a cubic crystal structure for SiC whiskers, [111] was chosen as the axial direction and  $[2\bar{2}0]$  and  $[11\bar{2}]$  as the orthogonal axes in the (111) plane of the SiC whisker. Since the measured strains were the average of the whole volume of the specimen, the assignment of the axial and radial strains involved an averaging procedure. Figure 2.30 shows the measured lattice strains of SiC whiskers with the predicted results. As expected, the residual strains decrease with increasing temperature and the experimental results were found in reasonable agreement with those computed by both a composite cylinder model and an Eshelby model. Figure 2.31 shows the variation of the average hydrostatic strains in the whiskers and the matrix with temperature for a composite with 18% of whiskers. Assuming that the matrix is isotropic, the nearly equal strains displayed by the various  $\langle hkl \rangle$  reflections of the matrix phase indicate that it is, on average, in a state of pure hydrostatic tension. On the contrary, the whiskers are not in a state of pure hydrostatic compression and the hydrostatic strains of the whiskers were obtained by averaging the measured axial (111) and transverse (220) strains. Figure 2.33 shows the calculated

hydrostatic residual strains as a function of SiC content. As shown, an increment in whisker volume fraction increased the magnitude of tensile strains in the matrix and decreased the compressive strains in the whiskers. This led to a prediction that the matrix would eventually crack in the absence of externally applied stress when the SiC content reaches about 42% if the fracture strain of the alumina matrix is 0.1%.

It is noted, however, as mentioned by the authors, the high density of planar defects within SiC whiskers and the presence of whisker texture due to uniaxial hot pressing prevented proper averaging of the measured strains, resulting in some uncertainty in their analysis. Nevertheless, their work was an excellent demonstration of the non-destructive, bulk measurement of residual strain in the ceramic composites by TOF neutron diffraction techniques.

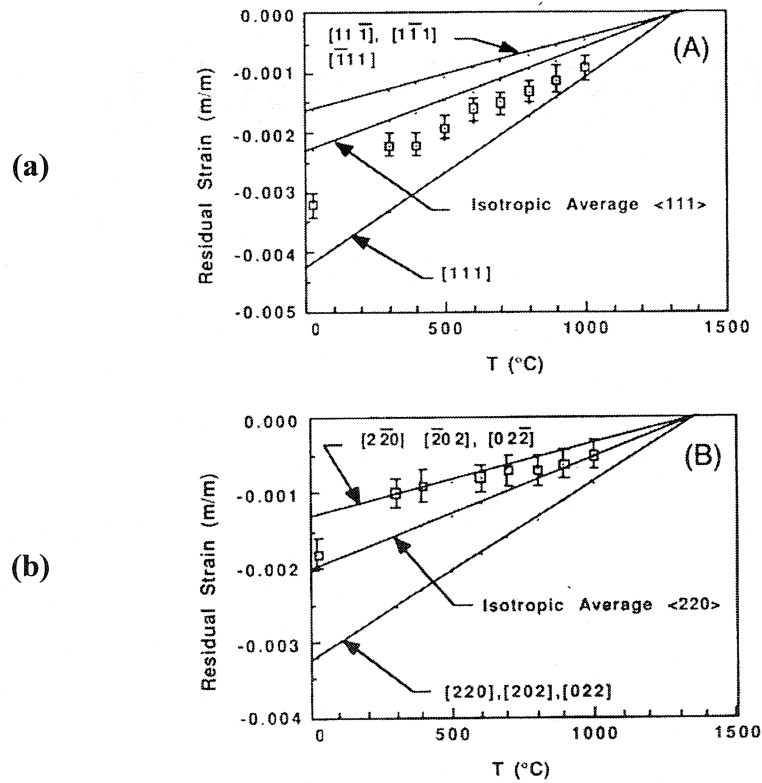


**Fig. 2.30** Comparison of computed strains (solid lines) and measured strains (symbols) in SiC whisker phase for (a) {111} and (b) {220} planes. (Majumdar et al. 1988)

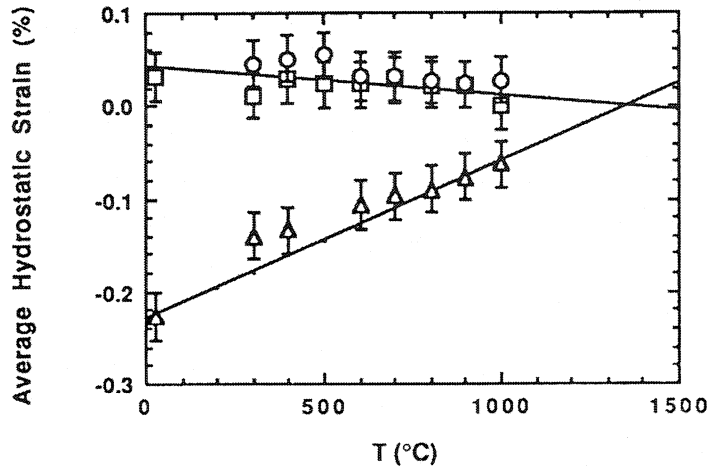


**Fig. 2.31** Comparison of computed (solid lines) and experimentally determined average hydrostatic strains (symbols) at various temperatures in the SiC whiskers and  $\text{Al}_2\text{O}_3$  matrix of a composite with 18 vol.% of whiskers ( $\square$  alumina (024),  $\circ$  alumina (006) and  $\Delta$  SiC. (Majumdar and Kupperman 1989)

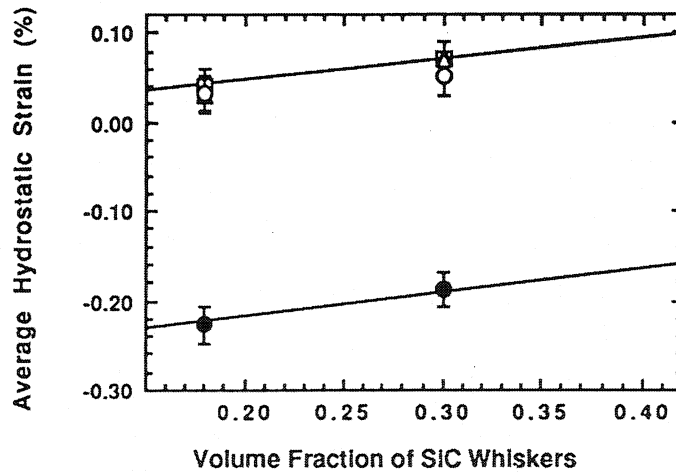


**Fig. 2.32** Comparison of computed (solid lines) and experimentally determined average hydrostatic strains (symbols) at room temperature and at two volume fractions of whiskers ( $\bullet$  SiC,  $\circ$  alumina (024),  $\square$  alumina (006) and  $\Delta$  alumina (104). (Majumdar and Kupperman 1989)

Predecki and his co-workers (1990, 1991) measured the residual strains in a hot pressed 29%  $\beta$ -SiC reinforced alumina composite using X-ray diffraction techniques. They chose the (146) peak for the matrix, and the (511) peak coinciding with (333) for SiC whiskers. All of the peaks are at high scattering angles, which was critical to reduce the error associated with determination of peak shift. To understand the effect of texture, they probed strains in the three mutually perpendicular planes using lattice strains versus  $\sin^2 \varphi$  method (Noyan and Cohen 1987). The sample geometry is shown in Fig. 2.32 and the calculated microstrains and microstresses are given in Table 2.3 and 2.4 respectively. The results show that  $\epsilon_{33}$  is algebraically always the smallest strain while  $\epsilon_{11}$  and  $\epsilon_{22}$  are nearly equal within experimental error, indicating the presence of whisker texture due to uniaxial hot pressing. Assuming an isotropic distribution of residual stresses in the matrix, they were able to calculate the residual stresses within SiC whiskers using a force equilibrium relation between the matrix and reinforcement phase.

It is seen from the calculated stresses that consideration of whisker texture, as expected, resulted in more anisotropic stresses and the stresses along  $X_1$  and  $X_2$  are approximately equal and are larger in magnitude than along the HPA. This is consistent with the transversely isotropic texture of whiskers as a result of uniaxial loading during hot pressing.

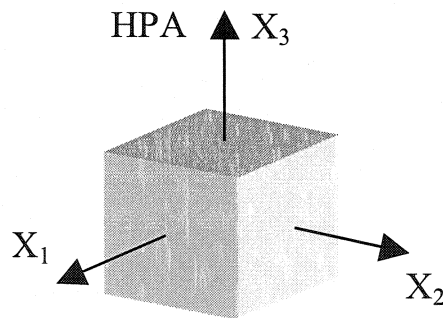


Fig. 2.33 The sample geometry for X-ray measurement. (Predecki et al. 1991)



**Table 2.3** The measured average residual strains obtained from the composite ( $\times 10^{-6}$ ). Standard deviations are  $50 \times 10^{-6}$  for matrix and  $50 \times 10^{-6}$  for whiskers. (Predecki et al. 1991)

| Face                | Matrix (146)    |                 |                 | Whisker (511) + (333) |                 |                 |
|---------------------|-----------------|-----------------|-----------------|-----------------------|-----------------|-----------------|
|                     | $\epsilon_{11}$ | $\epsilon_{22}$ | $\epsilon_{33}$ | $\epsilon_{11}$       | $\epsilon_{22}$ | $\epsilon_{33}$ |
| Face X <sub>1</sub> | 742             | 648             | 393             | -1484                 | -1480           | -1493           |
| Face X <sub>2</sub> | 687             | 732             | 337             | -1475                 | -1476           | -1545           |
| Face X <sub>3</sub> | 644             | 644             | 421             | -1486                 | -1489           | -1645           |

**Table 2.4** Residual microstresses in the composite (MPa). Standard deviations are 12 MPa for matrix and 30 MPa for whiskers. (Predecki et al. 1991)

| Method                      | Matrix        |               |               | Whiskers      |               |               |
|-----------------------------|---------------|---------------|---------------|---------------|---------------|---------------|
|                             | $\sigma_{11}$ | $\sigma_{22}$ | $\sigma_{33}$ | $\sigma_{11}$ | $\sigma_{22}$ | $\sigma_{33}$ |
| Quasi-isotropic matrix only | 497           | 492           | 380           | -1205         | -1192         | -921          |
| Both phases quasi-isotropic | 395           | 397           | 400           | -957          | -961          | -956          |

### 2.7.2 SiC particulate-reinforced alumina composites

Todd et al. (1997) studied the residual stresses in Al<sub>2</sub>O<sub>3</sub>-SiC<sub>p</sub> nano-composites using Time of Flight (TOF) neutron diffraction techniques. The size of SiC particles was 200 nm and four composites with SiC volume fraction of 0.04, 0.12, 0.24 and 0.35 were prepared. The measured lattice strains in the SiC phase were not dependent on (hkl), suggesting an isostrain state in SiC particles, whereas lattice strains in an alumina matrix phase showed (hkl) dependence, suggesting anisotropic strain state in the alumina matrix. Figure 2.33 shows the calculated average hydrostatic stresses from the measured strains as a function of SiC content.

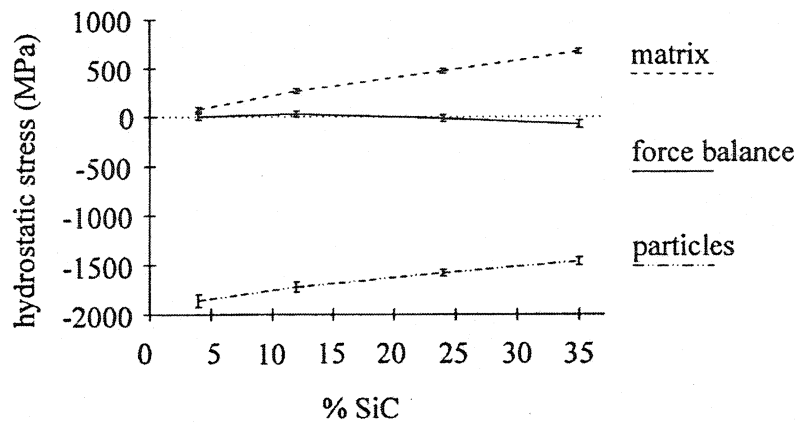


**Fig. 2.33** Average hydrostatic stresses measured in matrix, SiC particles and composite as a function of SiC content. (Todd et al. 1997)

Levin et al. (1994) studied the residual stress fields in 5-25wt% submicron-size SiC particle reinforced alumina composites by X-ray diffraction methods. The average microstresses in each phase and the stress fluctuations in the matrix were evaluated by a combination of reflection shift and line broadening analysis. Their peak shift measurements show that the average strains are hydrostatic and tensile in the matrix, compressive in the particles, as expected from the thermoelastic mismatch between alumina and SiC. With increasing SiC content, the average microstress in the alumina increased while that in the particles decreased, which is in accord with the internal force equilibrium condition. Their results of the line-broadening analysis for an alumina peak (416) indicated that both the size of coherently diffracted domains and the width of the microstrain distribution decrease with the volume fraction of SiC. Since the decrease in domain size was too fast to be accounted for by the increase in the SiC content, the authors concluded that the dislocation density must increase with particle volume fraction. On the other hand, the monotonic decrease in the width of overall microstrain distribution in the alumina was observed with increasing SiC content, which is not in agreement with the prediction from a statistical strain field model (Kreher and Molinari 1990, Kreher and Janssen 1992). This result necessarily invoked reduced contributions from both the particles and dislocations to the peak broadening as the volume fraction of

particles increases. To explain this, they suggested enhanced dislocation ordering with increasing dislocation density, and increasing hydrostatic strain components with a corresponding decrease in the shear stresses. These effects were related to the interactions between the stress fields due to adjacent dispersoids and relaxation processes, both of which lead to a redistribution of residual microstresses. Their TEM observations indicated a decrease in dislocation density with increasing SiC content, while the number of ordered dislocation networks increased.

**Table 2.5** Average principal microstresses in alumina-SiC nanocomposites with different SiC content (wt%). Values in parentheses are standard deviations. (Levin et al. 1994)

| 10% SiC                        | 15% SiC     | 20% SiC    | 25% SiC    |
|--------------------------------|-------------|------------|------------|
| Microstresses in SiC (MPa)     |             |            |            |
| -1712 (103)                    | -1764 (109) | -1487 (82) | -1278 (54) |
| -1848 (103)                    | -1516 (109) | -1412 (82) | -1343 (54) |
| -1782 (93)                     | -1761 (109) | -1524 (73) | -1407 (49) |
| Microstresses in alumina (MPa) |             |            |            |
| 218 (49)                       | 387 (73)    | 454 (57)   | 522 (58)   |
| 236 (49)                       | 333 (73)    | 432 (57)   | 549 (58)   |
| 253 (38)                       | 310 (57)    | 413 (44)   | 480 (45)   |

### 2.7.3 Summary

For SiC whisker reinforced alumina composites, the residual stresses, when expressed at the local crystal coordinate system as is with neutron diffraction techniques, were consistently higher than those measured in the sample coordinate system with X-ray diffraction methods. However, the difference was not large, which is probably due to the different procedures used for deriving stresses from strains and the presence of whisker texture. For SiC particulate reinforced alumina composites, the measurements from X-ray and neutron diffraction methods are in a good agreement. This may be related to the absence of reinforcement texture. All the models used for the calculation of residual stresses are based on the assumption that a purely elastic state of stress exists in the material, with no allowance for relaxation processes (Levin et al. 1993).

## **3. EXPERIMENTAL METHODS**

### **3.1 Introduction**

This chapter describes the procedures and instruments used to prepare samples for microscopy and the experimental setups employed for mechanical and structural characterisation of the samples. Neutron diffraction methods for texture and internal strain measurement are described in considerable detail because of their significance in the present investigation. X-ray diffraction is often compared with neutron diffraction to highlight the main advantages of the latter so far as this research project is concerned. The neutron diffraction experiments were conducted at Chalk River Laboratories of National Research Council (NRC), Chalk River, Ontario, Canada.

### **3.2 Microscopy**

#### **3.2.1 Optical microscopy**

Samples were sectioned perpendicular and parallel to the hot pressing direction. They were then mounted and processed by a automatic polishing machine (Struers PEDEMAX-2). First they were ground using metal bonded diamond discs (3M, 45  $\mu\text{m}$ ), followed by polishing down to 1  $\mu\text{m}$  diamond paste. After being cleaned in acetone or ethanol, samples were examined using optical microscopy (Model Axioplan 2, Carl Zeiss, Zena, Germany). The main purpose was to observe the whisker distribution within the matrix.

#### **3.2.2 Scanning electron microscopy**

Polished samples were thermally etched under vacuum at 1350°C for 1-2 h, which was aimed at revealing the general microstructure, especially the whisker distribution and matrix grain boundaries. Due to surface charging, samples S202 and S102 and pure alumina were gold coated before characterisation. The matrix grain size was estimated by the SEM (Model 515, Philips, Netherlands) micrographs using the Linear Intercept Method (LIM). Assuming the grain shape as tetrakaidecahedral (truncated octahedral), the

average grain size was obtained by multiplying a geometrical factor (1.56) to the measured average linear intercept length (Mendelson 1969).

### **3.2.3 Transmission electron microscopy**

Microscopy specimens were prepared by sectioning the samples normal to and parallel to the hot pressing direction. They were then manually ground to about 100  $\mu\text{m}$  using metal bonded diamond discs (3M) before mechanically polishing to a thickness of about 20  $\mu\text{m}$  using a dimple grinder (Gatan, Model 656). Thin disc specimens were then ion milled at 5kV, at double setting mode with a glancing angle of 5° until perforation using a Precision Ion Polishing System (PIPS) (Gatan model 691). Both conventional transmission electron microscopy (CTEM) (Philips CM12) and high-resolution electron microscopy (HRTEM) (FEG JEOL 2010F) were used to characterise the microstructure with emphasis on grain boundaries and interfaces.

## **3.3 Diffraction experiments**

### **3.3.1 Powder diffraction**

The residual stresses at various conditions were measured to better understand the creep behaviour of  $\text{Al}_2\text{O}_3\text{-SiC}_w$  composites. This requires that the crystal structures of both matrix and reinforcement phases be analysed through powder diffraction methods. Both X-ray and neutron powder diffraction patterns were obtained from the powder samples to characterise the identity, fraction of phases and their thermal stability at elevated temperature. For X-ray powder diffraction, powders are loaded into a thin layer, which requires the SiC whisker powders be ground well so that the texture effect is minimized. X-ray powder diffraction was performed using the Bruker D8 ADVANCE Powder X-ray Diffractometer at McMaster University. A Guinier camera which uses silicon powder as the standard was also used to measure the lattice parameters of reference samples precisely. Neutron powder diffraction was also carried out using the C2 high

resolution powder diffractometer and E3 materials science diffractometer attached to the National Research Universal (NRU) reactor at Chalk River Laboratories (CRL), Chalk River Ontario, Canada.

### 3.3.2 Neutron scattering

Neutrons are primarily scattered by atom nuclei and within a factor of 2 or 3 most atoms scatter neutrons equally well. Since the size of nuclei is about ten thousand times smaller than the wavelength of neutrons for diffraction, the scattering factors are essentially independent of angle. This is why it is termed nuclear or isotropic scattering. This is in contrast with X-rays that are primarily scattered by the electron cloud, which explains why the scattered intensity falls off significantly with increasing angle. The main advantage of neutron diffraction over X-ray diffraction is the high penetration depth, which enables the sampling of entire sample volumes in many cases as opposed to surface regions and avoids problems associated with defocusing at high tilt angle in X-ray diffraction (Kocks et al. 1998). However, it should be kept in mind that the low flux from the conventional neutron source results in longer counting times and lower spatial resolution than X-rays.

#### Production of thermal neutrons for materials science

In a nuclear reactor the neutrons developed in the fission process are allowed to scatter from the light atoms in a moderator of heavy water or graphite. Neutrons then lose energy, coming to thermal equilibrium with the moderator. The velocity distribution of these so called thermal neutrons is approximately that of a monatomic gas, at the reactor temperature  $T_m$ . The largest number of neutrons with velocity  $v_m$  is given in terms of  $T_m$  as

$$\frac{1}{2} m v_m^2 = \frac{3}{2} k T_m \quad (3.1)$$

Since  $T_m \approx 300$  K, the moderated neutrons are in the millielectron volt (meV) range. The wavelength of these neutrons is

$$\lambda_m = \left( \frac{h^2}{3mkT_m} \right)^{1/2} \quad (3.2)$$

As the mass of a neutron is about  $10^{-27}$  kg,  $\lambda_m \approx 1$  Å, which is suitable for diffraction from condensed matter. The neutron flux from such a reactor source takes on a Maxwellian distribution (Bacon 1975) and the actual number of neutrons  $N(\lambda)$  between  $\lambda$  and  $\lambda+d\lambda$ , per unit area per second is given as

$$N(\lambda) = \frac{2N^*}{\lambda} \left( \frac{E}{kT} \right)^2 \exp\left( -\frac{E}{kT} \right) \quad (3.3)$$

where  $N^*$  is the total number of neutrons of all wavelengths passing through unit area per second, i.e. the flux (typically  $10^{14}$  to  $10^{16}$  neutrons/cm<sup>2</sup>/s at a reactor core).  $E$  is the energy of any one neutron of a given wavelength  $\lambda$ . Figure 3.1 illustrates the neutron flux from the 150 MW NRU reactor where the optimal wavelength is close to 1.54 Å. Figure 3.2 presents the flux as a function of energy. Unlike conventional laboratory X-ray sources that have very sharp characteristic peaks in intensity, thermal neutrons exhibit a broad energy distribution. Therefore, for thermal neutrons monochromator crystals are used to choose a variety of wavelengths for diffraction. However, this also results in much less flux, especially for the wavelength far from the optimum. This can lead to much longer counting times being required than for x-ray diffraction.

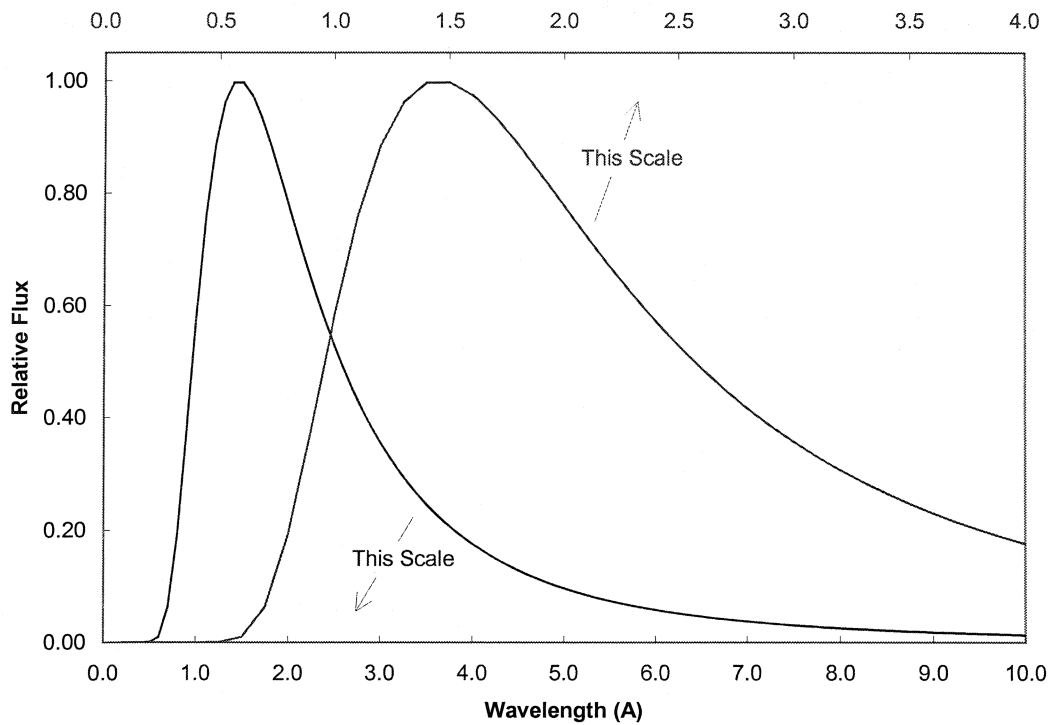


**Fig. 3.1** Relative thermal neutron flux as a function of wavelength in NRU reactor. (Courtesy K. T. Conlon)

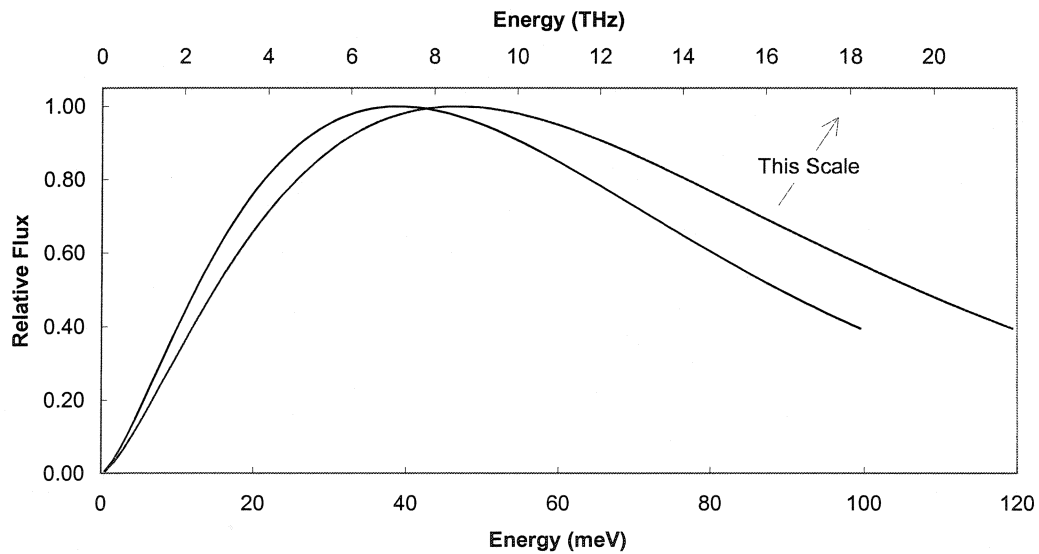


**Fig. 3.2** Relative thermal neutron flux as a function of energy. (Courtesy K. T. Conlon)



### 3.3.3 Texture and strain measurements

#### Instrumentation

Texture and strain measurements were carried out in the E3 diffractometer attached to the NRU reactor at CRL. Intensities were measured using a one-dimensional detector comprised of 32 wires corresponding to a maximum angular range of  $2.0^\circ$ . Typically, the middle 16 wires were turned on for texture measurements, and only the middle 8 wires were used for strain measurements. The angular divergence of the incident and diffracted beams was limited by use of Cd coated soller slits and the beam size by Cd beam stops. The spectrometer was controlled by means of a PDP-11 microcomputer connected to a VAX minicomputer. Controlling software was used to position the detector, experimental apparatus and scattering vector, as well as to execute the automated scans programmed in prior. Due to the varying flux over the course of a single experiment, the counting period was set to correspond to some fixed number of neutrons instead of a predetermined amount of time. (The flux of neutrons was constantly monitored by a counter placed in the beam path.)

#### Texture measurement

Texture measurement by neutron diffraction has been treated in detail by Brockmeir (1994). In the present investigation, a Ge single crystal was used as the monochromator and the (113) or (331) peak was chosen to select neutron beams with wavelength of about  $2.37 \text{ \AA}$  or  $1.83 \text{ \AA}$ . The specimen orientations were set by a 4-axis Eulerian cradle. Figure 3.3 shows a typical experimental set up for texture measurement and the specimen coordinates are defined in Fig 3.8. The nominal angular divergence of both incident and scattered beams is  $0.5^\circ$ . Typical set-up for texture measurements was to use 20.32 cm long soller slits separated by 2 mm on the scattered side, giving an angular resolution of  $1.1^\circ$ . Neutrons were sampled over a nominal solid angle in 2-theta of  $2.8^\circ$ , where the detector was centered on the Bragg peak of interest. Intensities for pole figure were measured on a grid consisting of 1020 points over a full hemisphere. One background pole figure was necessary for intensity normalization purpose, which was collected far from any possible Bragg angle. The measured intensity versus  $\eta/\chi$  angles (for definition of these angles see Fig. 3.8) was normalized

using programs developed at CRL (Root and Holden 1990), which include NEUTSORT, POLCON, SYMMET and POLAVG.

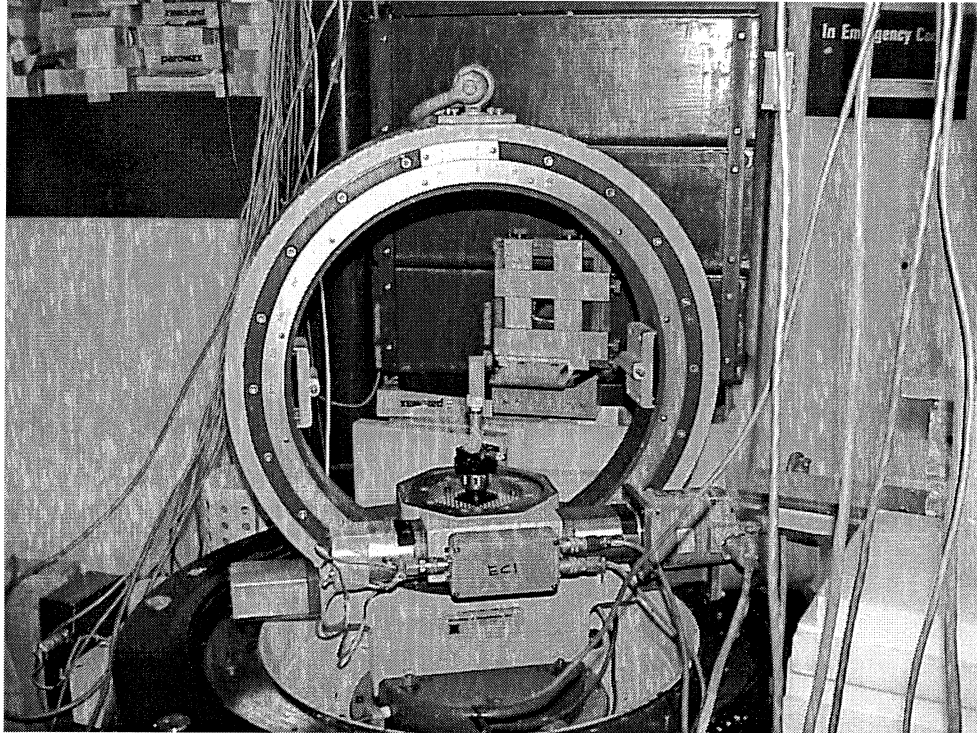


**Fig. 3.3** A photograph of the experimental setup of the E3 spectrometer for texture measurement.

### **Quantification of whisker distribution**

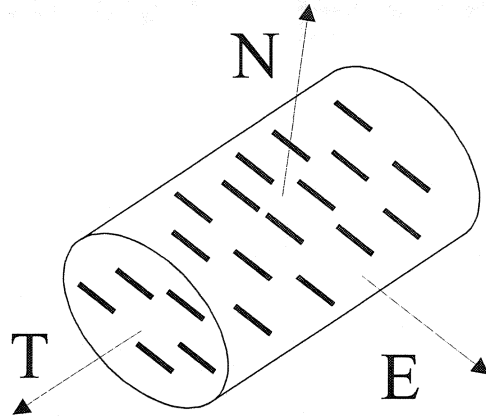
An angular distribution of whiskers with respect to hot pressing axis (HPA) can be obtained quantitatively from the neutron diffraction data. Several factors that influence the final calculation results are noted first. Essentially, the cubic crystal structure of SiC whisker and high density of planar defects (stacking fault and twinning) along the whisker axis complicate the analysis. Given the cubic crystal symmetry, it is impossible to find a reflection of SiC single crystal whose intensity at a given sample orientation can be uniquely related to the volume fraction of the whiskers possessing the same fiber orientation. In a previous neutron diffraction study (Root and Rack 1994) on SiC whisker reinforced aluminum alloy, a unique assignment was made between the whisker axis and the [111] crystallographic direction. This led to a direct interpretation of plots of diffraction peak intensity versus sample orientation as quantitative maps of the

whisker orientation. Strictly speaking, this argument is not rigorous since those off-axis {111} reflections always mingle with the on-axis (111) reflection. This is schematically shown in Fig. 3.5.

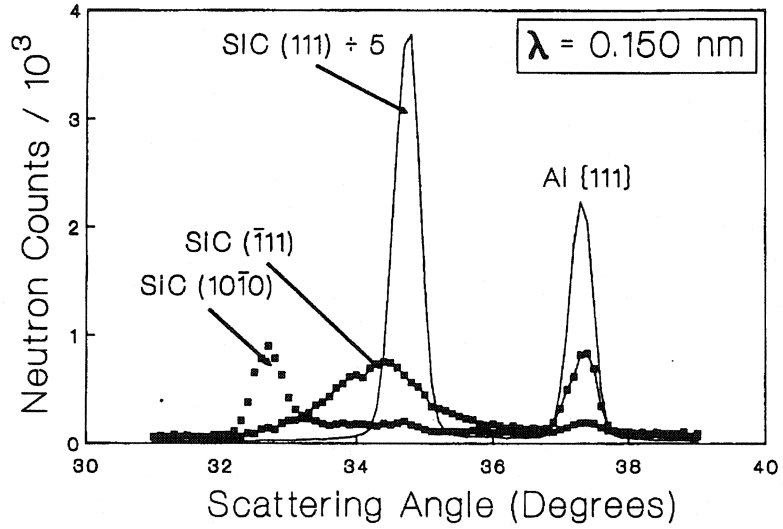
It is interesting that the highly aligned whiskers in metal matrix composite formed through high ratio extrusion enabled distinguishing the variants of {111} that are not parallel to the whisker axis by systematically orienting the sample. Figure 3.4(a) is a schematic representation of the composite sample used by the authors. As shown in Fig. 3.4(b) the  $(\bar{1}11)$  diffraction peak shifted to the lower scattering angle and is associated with remarkable broadening. Presumably, this is due to the high density of planar defects along the whisker axis that destroys the long-range order of  $(\bar{1}11)$  planes. This result suggests that if a measured peak is the sum of all {111} variants with considerable contribution from off-axis {111} reflections, it will develop significant asymmetry. Figure 3.6 shows two {111} SiC peaks from current studies that were measured with the angle between the scattering vector and HPA being 15 and 90°. Both have been fitted well with a Gaussian function, which excludes the presence of asymmetry associated with the peak. From this result it may be concluded that the contribution from off axis {111} reflections is insignificant and, thus, can be ignored. Angular distribution of whiskers with respect to the axis of interest was quantified by the following approach. First, the (111) SiC pole figure is constructed from the raw neutron diffraction data by NEUTSORT.EXE and POLCON.EXE, it is then rotated using SYMMET.EXE in such a way that the center of the pole figure is coincident with the axis of interest. Now, POLAVG.EXE is run, which generates a plot of the normalized average intensity around HPA as a function of the conical angle with respect to HPA. Suppose  $\langle I \rangle$  is the normalized average intensity at a given angular range,  $\phi+d\phi$ , then the actual volume fraction of whiskers within the angular range would be

$$\frac{\langle I \rangle \sin \phi}{\sum \langle I \rangle \sin \phi} \quad (3.4)$$

The related geometry is schematically shown in Fig. 3.7.



(a)



(b)

**Fig. 3.4** (a) A schematic of sample geometry and (b) diffraction peaks from 5% SiC whisker reinforced aluminum. The (111), ( $\bar{1}$ 11) and (10 $\bar{1}$ 0) peaks were measured 0, 70 and 90°, respectively from the extrusion direction. (Root and Rack 1995)

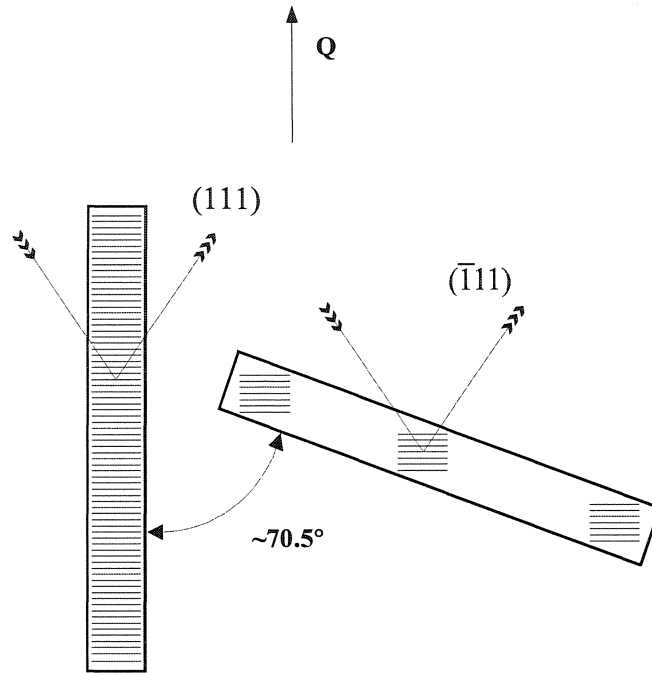


**Fig. 3.5** A schematic diagram showing the occurrence of scattering on (a) on-axis (111) planes whose scattering vector  $Q$  is parallel to whisker axis and (b) off-axis  $(\bar{1}11)$  planes of SiC whisker where the whisker axis is  $\sim 70.53^\circ$  from the scattering vector.

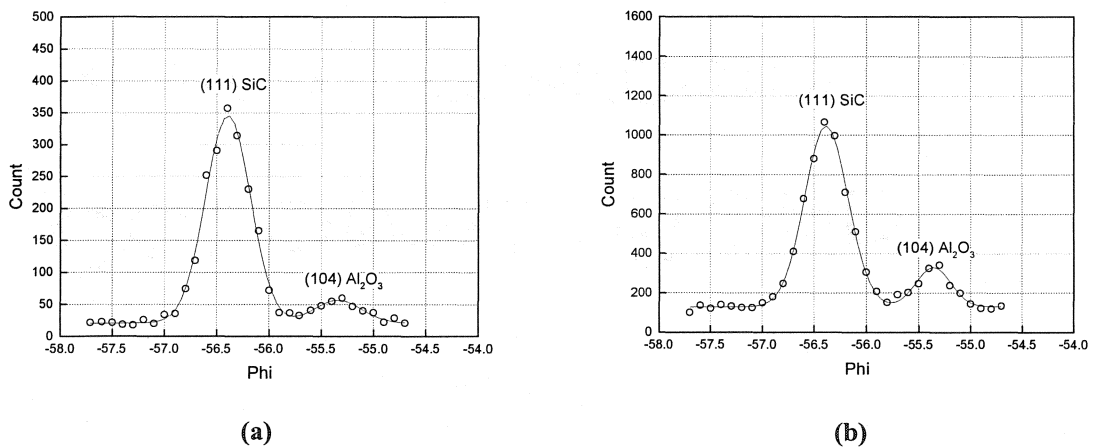


**Fig. 3.6**  $\{111\}$  SiC peaks measured from a S302 sample with the scattering vector (a) perpendicular and (b) parallel to HPA. The small peak is (104) alumina.

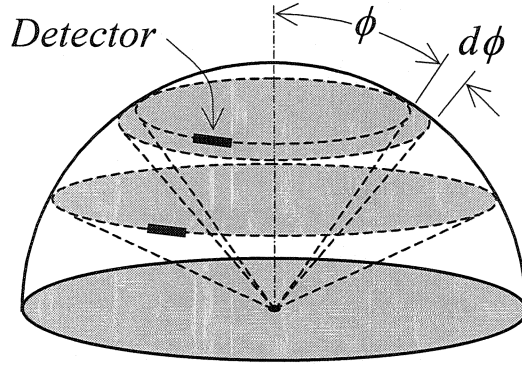


Fig. 3.7 The geometry for measuring angular whisker volume fraction.

### Fitting of neutron diffraction peaks

A neutron diffraction peak was defined by a set of (x, y) co-ordinates, where x is the position of the detector in degrees and y is the intensity of neutrons recorded in detector position x. The data were fitted to a 4-parameter function:

$$Y = b + A \exp \left[ -\frac{1}{2} \left( \frac{2\theta - 2\theta_{\sigma}}{\sigma} \right)^2 \right] \quad (3.5)$$

which defines a Gaussian function (characterized by amplitude A, mean position  $2\theta_{\sigma}$  and standard deviation  $\sigma$ ) superimposed upon a flat background (defined as b) using a Newton-Raphson least squares fitting algorithm. Subsequent calculations incorporating the Gaussian parameters were performed to determine the full width at half maximum (FWHM):

$$FWHM = 2\sqrt{\ln 2} \sigma \quad (3.6)$$

as well as the Integrated Intensity (I) of the peak:

$$I = A \sigma \cdot (2\pi)^{1/2} \quad (3.7)$$

The root mean square error  $\chi$  is given by:

$$\chi = \left( \frac{1}{N-5} \right) \cdot \sum_{i=1}^N \frac{(Y_i^c - Y_i^{obs})^2}{Y_i^{obs}} \quad (3.8)$$

and is used in subsequent calculations to calculate uncertainties for parameters defining the Gaussian function given above.

## Lattice strain measurement

The measurement of lattice strains using neutron diffraction has been reviewed extensively (e.g. Allen et al. 1985, Holden 1999). The principal idea is to consider the lattice as the inner strain gauge and the strain is calculated by measuring the change in scattering angle for a conventional reactor neutron source (constant wavelength) or the difference in the time of flight (TOF) for a spallation neutron source (continuous wavelength). Combining the definition of engineering strain and differentiation of Bragg's law results in the following equation that relates the lattice strain  $\varepsilon$  to the shift in Bragg angle  $\theta$ .

$$\varepsilon = \frac{\Delta d}{d_o} = -\cot \theta \Delta \theta \quad (3.9)$$

where  $d_o$  is a reference lattice spacing measured in a stress-free sample and  $\Delta \theta$  the shift in Bragg angle.

The true lattice strain is given as

$$\varepsilon = \ln \left( \frac{d}{d_o} \right) = \ln \left( \frac{\sin \theta_o}{\sin \theta} \right) \quad (3.10)$$

where  $\theta_o$  is a reference Bragg angle and  $\theta$  is that measured from the strained lattice. For small strain this further reduces to

$$\varepsilon \approx \frac{\sin \theta_o}{\sin \theta} - 1 \quad (3.11)$$

The error in the lattice strain can be assessed using the following total differential

$$d\varepsilon = \frac{\partial \varepsilon}{\partial \theta_o} d\theta_o + \frac{\partial \varepsilon}{\partial \theta} d\theta \quad (3.12)$$

from which the error is given as follows

$$|\Delta \varepsilon| = \sqrt{(\cot \theta_o \Delta \theta_o)^2 + (\cot \theta \Delta \theta)^2} \quad (3.13)$$

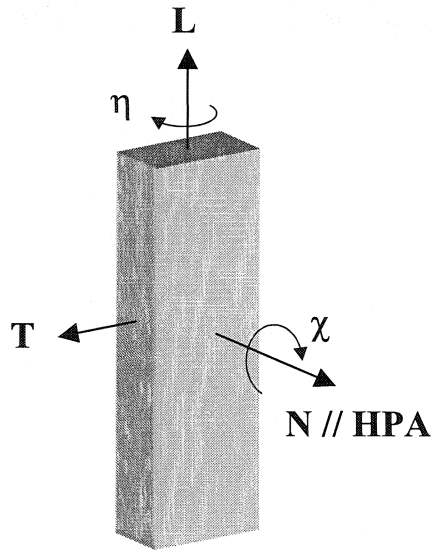


**Fig. 3.8** A schematic of the sample coordinate system for neutron diffraction measurement. Direction N is parallel to HPA.

In the present investigation, the detector was configured to sample neutrons over a solid angle of  $0.6^\circ$  and the position sensitive detector "rocked" over  $2\theta$  to sample the Bragg peaks of interest (the method is normally termed as a "rocking curve").

### **3.3.4 Residual strain/stress measurements at room temperature**

Residual stresses are self-equilibrating internal stresses existing in a free body even without external forces or constraints acting on its boundary. These stresses arise from the elastic response of the material to an inhomogeneous distribution of non-elastic strains (eigenstrains), such as plastic deformation, precipitation, phase transformation, misfit, thermal expansion strain, etc (Noyan and Cohen, 1987). Macrostress forms when one part of a body is moved relative to another while microstress arises when one microscopic region, a grain or a second phase particle, deforms differently than its surroundings, due to difference in its elastic or plastic response, compared to the rest of material. The measurement of residual strains in the  $\text{Al}_2\text{O}_3\text{-SiC}_w$  composites is complicated by the following reasons:



1. The crystal structure of SiC is not well defined. Powder diffraction patterns and HRTEM indicate that a single whisker mainly consists of 3C (FCC)  $\beta$ -SiC with a minor portion of regions with hexagonal crystal structure. It has been well studied that a very high density of planar defects along the fibre axis, say [111], developed during crystal growth, which, while maintaining the long range order of (111) plane, destroyed that of three other off-axis {111} planes. This is evidenced by a mushy background with the (111) peak in the powder diffraction pattern.
2. Whiskers are not randomly distributed within the matrix, which is to be characterised using neutron diffraction method.

In order to overcome the aforementioned difficulties, the residual strains were measured from those whiskers lying in the plane that is normal to the hot pressing direction. In doing so, the following assumptions were made:

1. There is no preferred rotational orientation around the whisker axis.
2. Each whisker is transversely isotropic with respect to the whisker axis.
3. There is a one-to-one correspondence between the observed (111) peak and the whisker orientation since the three sets of off axis {111} planes have lost their long-range order. In other words, each whisker is treated as if it has hexagonal crystal structure.
4. The observed (220) peak corresponds only to those whiskers whose axes are perpendicular to the scattering vector of (220) reflection. This approximation can be justified by the dependence of the observed (220) intensity on sample orientation. For instance, the maximum intensity was 15 times greater when the scattering vector is aligned parallel to the Poisson direction of the sample as opposed to the tensile direction. (see Fig. 3.9)

Because of the whisker texture, the averaging of internal strains for the whiskers as a whole is difficult. Therefore, averaging was performed only for those whiskers lying perpendicular to HPA.

The isotropic strain (or hydrostatic strain) is calculated as

$$\varepsilon_H = \frac{1}{3}(\varepsilon_c + 2\varepsilon_a) \quad (3.14)$$

For a transversely isotropic (in  $x_2$ - $x_3$  plane) body, the axial and hoop stresses can be calculated using the following relation:

$$\begin{pmatrix} \sigma_c \\ \sigma_a \\ \sigma_a \end{pmatrix} = \begin{pmatrix} C_{11} & C_{12} & C_{12} \\ C_{12} & C_{22} & C_{23} \\ C_{12} & C_{23} & C_{22} \end{pmatrix} \begin{pmatrix} \varepsilon_c \\ \varepsilon_a \\ \varepsilon_a \end{pmatrix} \quad (3.15)$$

It is to be noted that shear strain cannot be measured directly by diffraction methods and for a given crystal coordinate system, only normal stresses can be calculated from the measured normal strains. However, for a given sample coordinate system, a full set of strain tensors can be obtained from the measured strain versus  $\sin^2 \psi$  data (Noyan and Cohen 1987).

The elastic constants (in MPa) at room temperature have been reported (Tolpygo, 1961) as follows:

$$C_{11} = 5.215 \times 10^5 ;$$

$$C_{12} = 0.557 \times 10^5 ;$$

$$C_{22} = 4.971 \times 10^5 ;$$

$$C_{23} = 0.98 \times 10^5$$

The hydrostatic stress is then calculated as

$$\sigma_H = \frac{1}{3}(\sigma_c + 2\sigma_a) \quad (3.16)$$

The corresponding average hydrostatic stress in the matrix can be determined from the overall equilibrium equation:

$$\sigma_H^f V_f + \sigma_H^m V_m = 0 \quad (3.17)$$

where  $\sigma_H^f$  and  $\sigma_H^m$  and  $V_f$  and  $V_m$  are the average hydrostatic stresses and volume fraction of the whiskers and matrix.

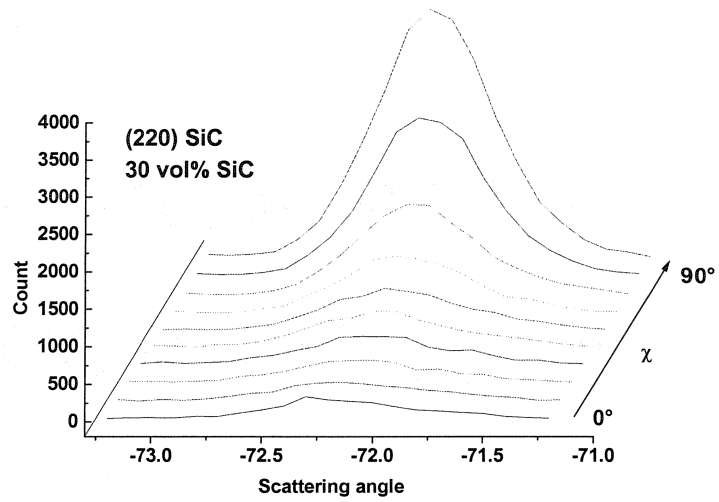


**Fig. 3.9** The measured (220) peaks of SiC whiskers at different  $\chi$  angle.

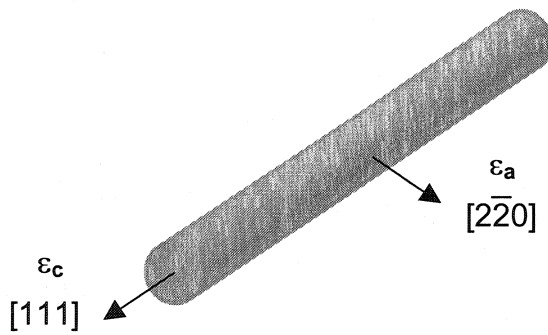


**Fig. 3.10** An illustration of average axial and hoop strains in the local crystal coordinate system of a whisker. The strains shown are measured from a billet of S302 sample, i.e. before creep.

### 3.3.5 In-situ high temperature neutron diffraction test

The C2 position-sensitive high resolution powder diffractometer was used for these experiments. This enabled excellent atmospheric control during testing and measurement of a wide range of scattering angle simultaneously. Vanadium cans were used to encapsulate the samples mounted inside a radiant heater-based furnace with a temperature range of 300 K to 2200 K. Figure 3.11 shows the inside view of the furnace with the vanadium can. During tests, care was taken to minimize the interaction volume of other components along the beam path, which is critical to obtain well-separated peaks from the composite specimens. Since there is no integrated creep machine available currently for in-situ scattering experiments,

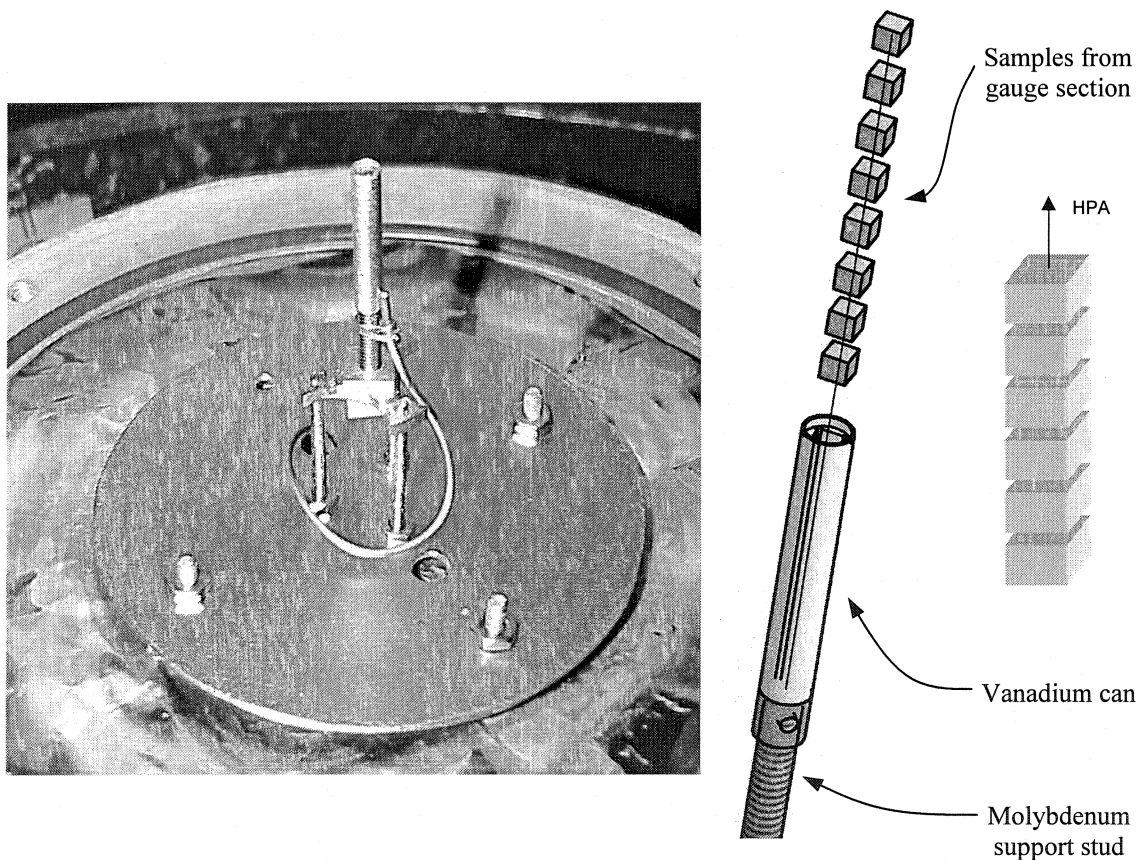


**Fig. 3.11** An inner view of the furnace for high temperature neutron diffraction tests. The vanadium can was used to encapsulate the samples.

an alternative approach was adopted for the stress relaxation study. First, the samples were deformed at elevated temperatures (1300 and 1400°C) up to 0.5 % strain before being rapidly cooled under load so as to ‘freeze’ any back stresses developed during forward creep in the structure. The samples were then unloaded and brought to the diffractometer for in-situ high temperature diffraction measurements. The scattering vector was approximately perpendicular to HPA and tensile axis. The test involved a rapid heating of the samples to 1400°C under vacuum followed by a soaking period up to one day during which the “powder patterns” were recorded continuously at time intervals typically in the range of 10 - 30 minutes.

### 3.4 Creep tests

#### 3.4.1 Tensile creep

The method of tensile test is similar to that developed by Carroll *et al.* (1989) in NIST. The testing system was based on an old creep frame (Denison and Son LTD, Model T48) with a new furnace and creep extensometry. Figure 3.12 shows an overview of the set up for the tensile creep test. Creep strain is measured by laser extensometry that consists of a single axis laser-scanning micrometer (LaserMike Model 501-195) and a processor (LaserMike Model 2020 SPC/SQC). Two flags made of highly refractory SiC or  $\text{Al}_2\text{O}_3\text{-SiC}_w$  composite are hung on the gauge section of the specimen, defining the gauge length. When the vertical scan of the laser beam passes through the test chamber of the furnace the interruption of the laser beam by the two flags is sensed by the detector, thus measuring the gauge length of the specimen (see Fig. 3.13). Two types of samples were used as shown in Fig. 3.14. Since the one with small curvature connecting the specimen head to the gauge section (at bottom in Fig. 3.14) was prone to premature failure at the transitional section, a larger radius was later introduced as a solution (top in Fig. 3.13). The dead-weight load is applied to the specimen through the lever in accordance with the calibrated loading factor. To minimize the elastic bending of tensile specimens at low temperatures, SiC pins used for connecting the specimens to the pull rods were lubricated by paraffin, which enables better specimen alignment (Krause Jr. *et al.* 2001). Care was taken to minimize fluctuation of air density along the beam path, which is critical to obtain a stable read-out from the laser data processor. The increase in noise level was quite severe at high

temperatures and considerable efforts were made to ensure the validity of the collected data, which included:

1. Minimize the size of channels at the wall of furnace that allow for the passage of laser beam. This is aimed at not only reducing the air density fluctuation along the laser path but also minimizing the damage to the laser micrometer from overheating.
2. Make sure secured sealing of the openings at top and bottom of the furnace around pull rods during test.
3. Reduce the distance between furnace and the windows of the laser machines.

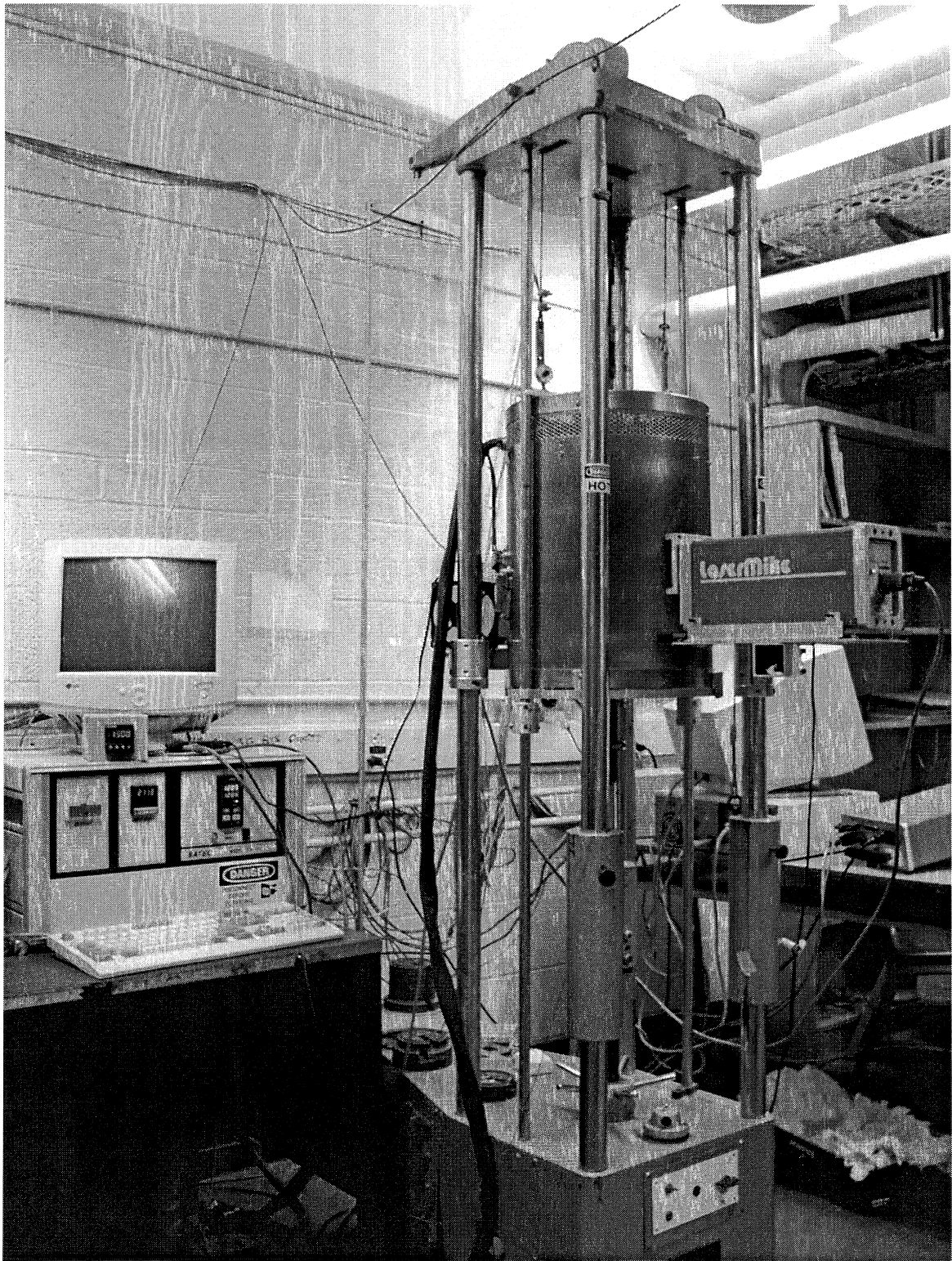
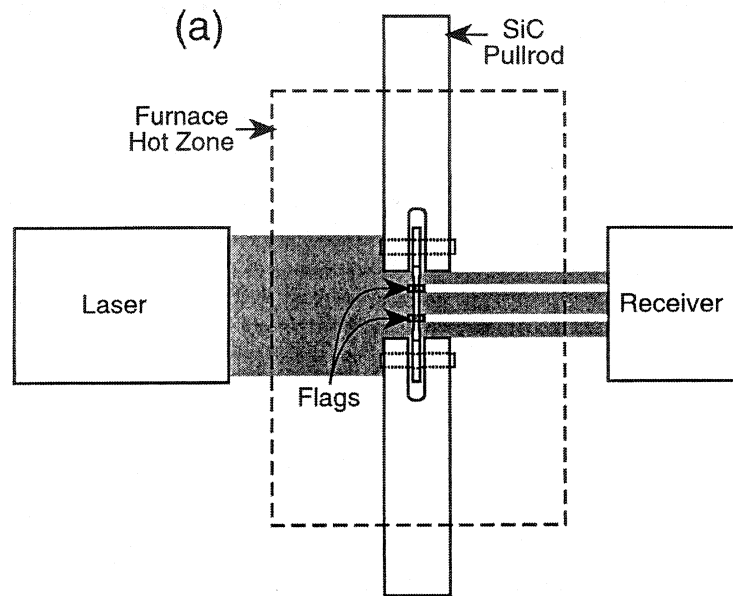
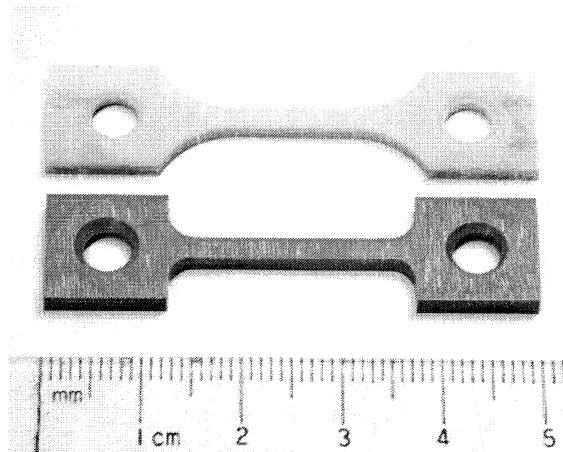


Fig. 3.12 A photograph showing the set up for the tensile creep test.



**Fig. 3.13** A schematic of creep strain measurement by laser extensometry (Carroll et al. 1989).



**Fig. 3.14** A photograph of tensile creep specimen of pure alumina (top) and composite (bottom). Different sample geometry is noted.



Prior to creep testing, in order to equilibrate the loading system, the sample was held for about half an hour at the target temperature with minimum load under which little or no deformation occurred. For stress relaxation test the load was manually reduced to the minimum under which the loading system still remained rigid.

The errors associated with creep strain measurement based on laser extensometry has been discussed in great detail by the workers in National Institute of Standards and Technology (NIST) (Carrol et al. 1989, Luecke et al. 1996 and Krause Jr. et al. 2001).

### **3.4.2 Compression creep**

Some compression creep tests were carried out, which were aimed to achieve high creep strain and investigate the effect of loading orientation on creep response. A detailed description of the experimental set up can be found elsewhere (HamSu 1997).

### **3.4.3 Creep data analysis**

Due to the limited number of tensile specimens combined with the experimental difficulties, more than one stress was applied to a single specimen during creep testing. For composites, the strain rates were sometimes found to decrease continuously with increasing time. Therefore, the calculated creep rates were somewhat overestimated. The creep rate was calculated by fitting the strain versus time curve as following:

The first pseudo steady-state strain rate immediately following the primary creep stage was obtained through fitting the whole creep curve including the primary regime. Once the stress was changed during creep, sufficient time was given to establish a pseudo steady - state creep stage. The corresponding creep rate was then found by fitting a linear function to it. Figure 3.16 shows a typical tensile creep curve obtained in our creep lab.

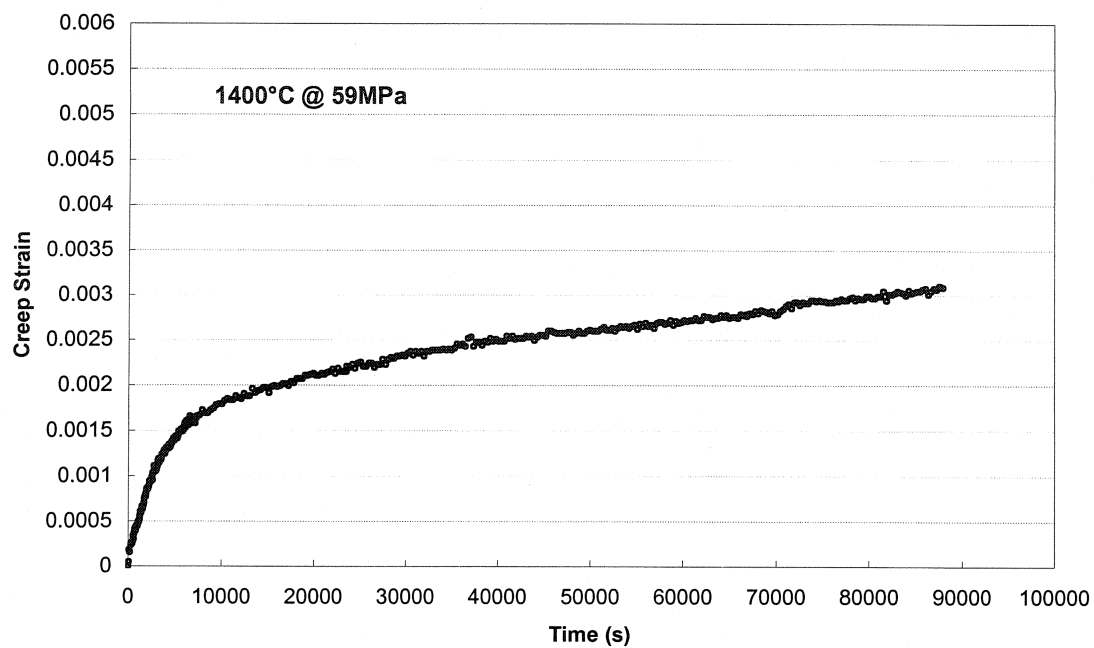


**Fig. 3. 15** A creep curve for 30% SiC whisker reinforced alumina at 1400°C under 59MPa.

## 4. MATERIALS PROCESSING

### 4.1 Introduction

This chapter describes the characterisation of the ceramic powders used, the colloidal processing procedures and the sintering of the ceramic samples. The important fundamentals underlying some of the processing methods are given in Chapter 2. Fine  $\alpha$ -alumina powders, pure SiC whiskers (Silar SC-9) and custom-mixed  $\text{Al}_2\text{O}_3$ -SiC<sub>w</sub> powders were obtained from Advanced Composites Materials Corporation (ACMC) (Greer, SC, USA). Three composites with 10, 20 and 30% of SiC whiskers were fabricated to study the influence of reinforcement loading on the creep behaviour. With the desire to have 'clean' grain boundaries, no sintering additives were used.

### 4.2 Crystallography of SiC whisker

Silicon carbide is known as a wide bandgap semiconductor, which is commonly manufactured by a carbothermic reduction process in which silica and carbonaceous materials are reacted at high temperature. The structural types are generally classified into cubic and hexagonal or rhombohedral phases and there are some 200 polytypes proven in existence (Robert 1993). All polytypes have a hexagonal frame with a carbon atom situated above the center of a triangle of Si atoms and underneath a Si atom belonging to the next layer. The distance,  $a$ , between neighboring silicon or carbon atoms is approximately 3.08 Å for all polytypes (Knippenberg 1963). The carbon atom is at the center of mass of the tetragonal structure outlined by the four neighboring Si atoms so that the distance between the C atom to each of the Si atoms is the same. This is shown in Fig. 4.1 The height of a unit cell,  $c$ , varies between the different polytypes. The ratio  $c/a$ , thus, differs from polytype to polytype, but is always close to the ideal for a closed packed structure. This ratio is for instance approximately 1.641, 3.271 and 4.908 for the 2H, 4H and 6H SiC polytypes respectively. The difference between the polytypes is the stacking order between succeeding double layers of carbon and silicon atoms. Figure 4.2 illustrates the most commonly observed SiC polytypes.

The crystal structure of SiC whisker was characterised using X-ray and neutron diffraction before and after different thermal treatments. This was aimed at understanding the structural, morphological stability of the phase at elevated temperature. For example, phase transitions will affect the internal strain fields within the composites and thus the mechanical behaviour. Figure 4.3 compares the neutron powder diffraction patterns from pure SiC whiskers before and after annealing. Apparently, annealing did not cause phase transition whatsoever. The SiC whiskers are indexed as the cubic SiC phase ( $\beta$ -3C) with a minor fraction of hexagonal SiC polytypes (4H, 6H etc.). It is noted that all the major peaks are associated with mushy background, which could be due to the presence of defects within the crystals and/or small crystallite size. Electron microscopy results provided direct evidence of the highly populated planar defects (stacking fault and twin) along the whisker axis, as shown in Fig. 4.2. Therefore, it was concluded that the peak broadening in the powder diffraction pattern is attributed to the presence of high-density planar defects within SiC crystals.

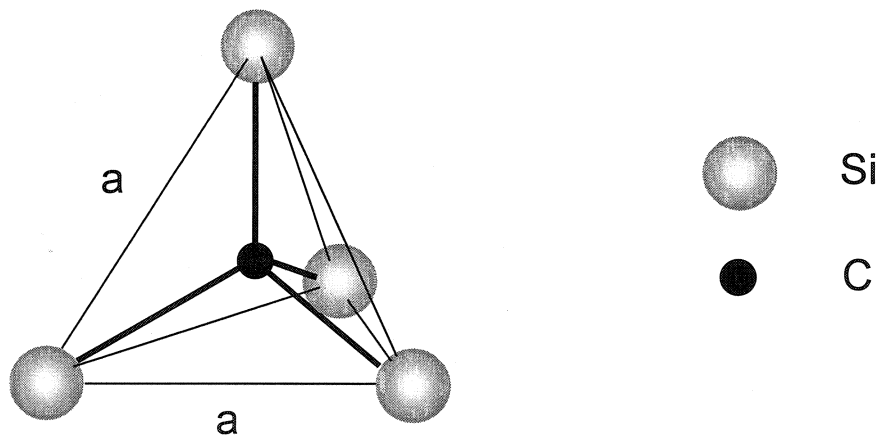


**Fig. 4.1** The tetragonal bonding of a carbon atom with the four nearest silicon neighbours.

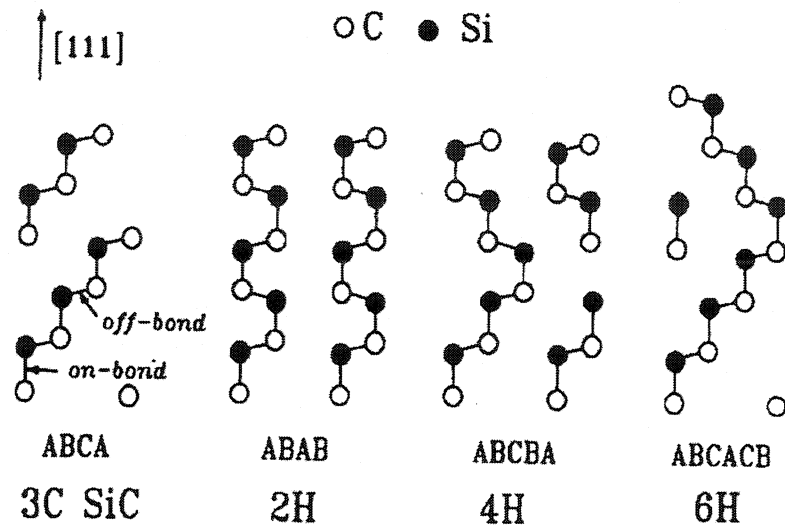


**Fig. 4.2** Illustration of atomic structures of some of the most common SiC polytypes described in the cubic  $(11\bar{2})$  plane and hexagonal  $(10\bar{1}0)$  plane. A, B and C denote the type of atomic layer, The bonds aligned along the cubic  $[111]$  axis are denoted as on-bonds otherwise off-bonds. (Park et al. 1994)

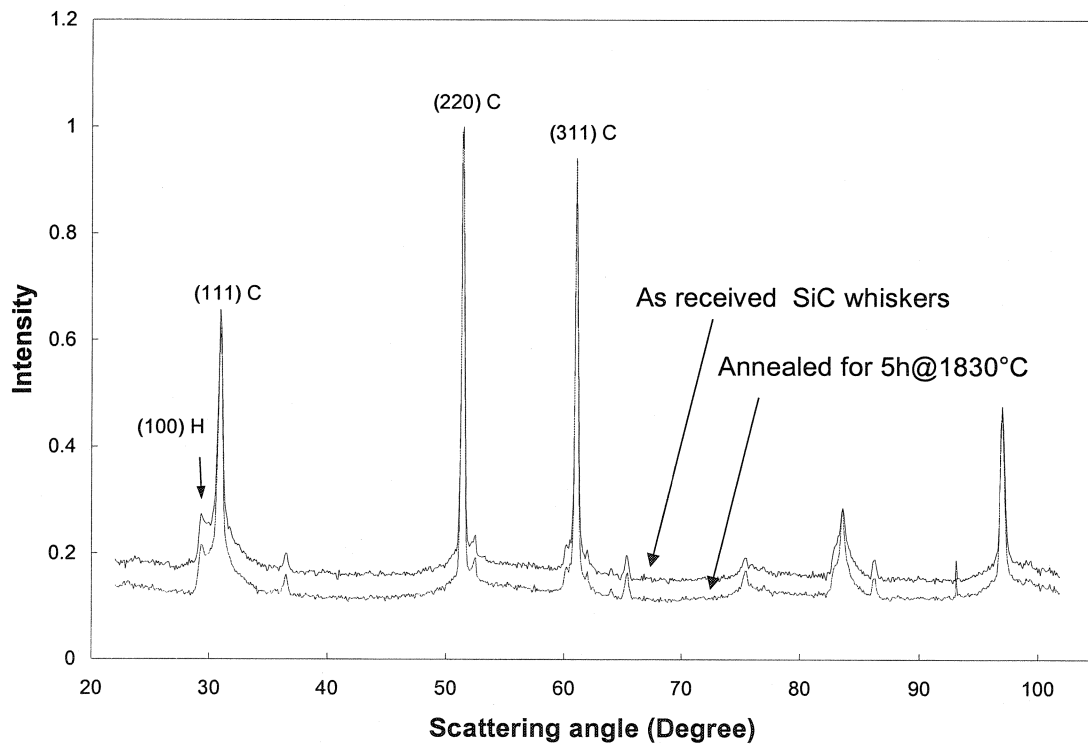


**Fig. 4.3** Neutron powder diffraction patterns from pure SiC whiskers before and after annealing.

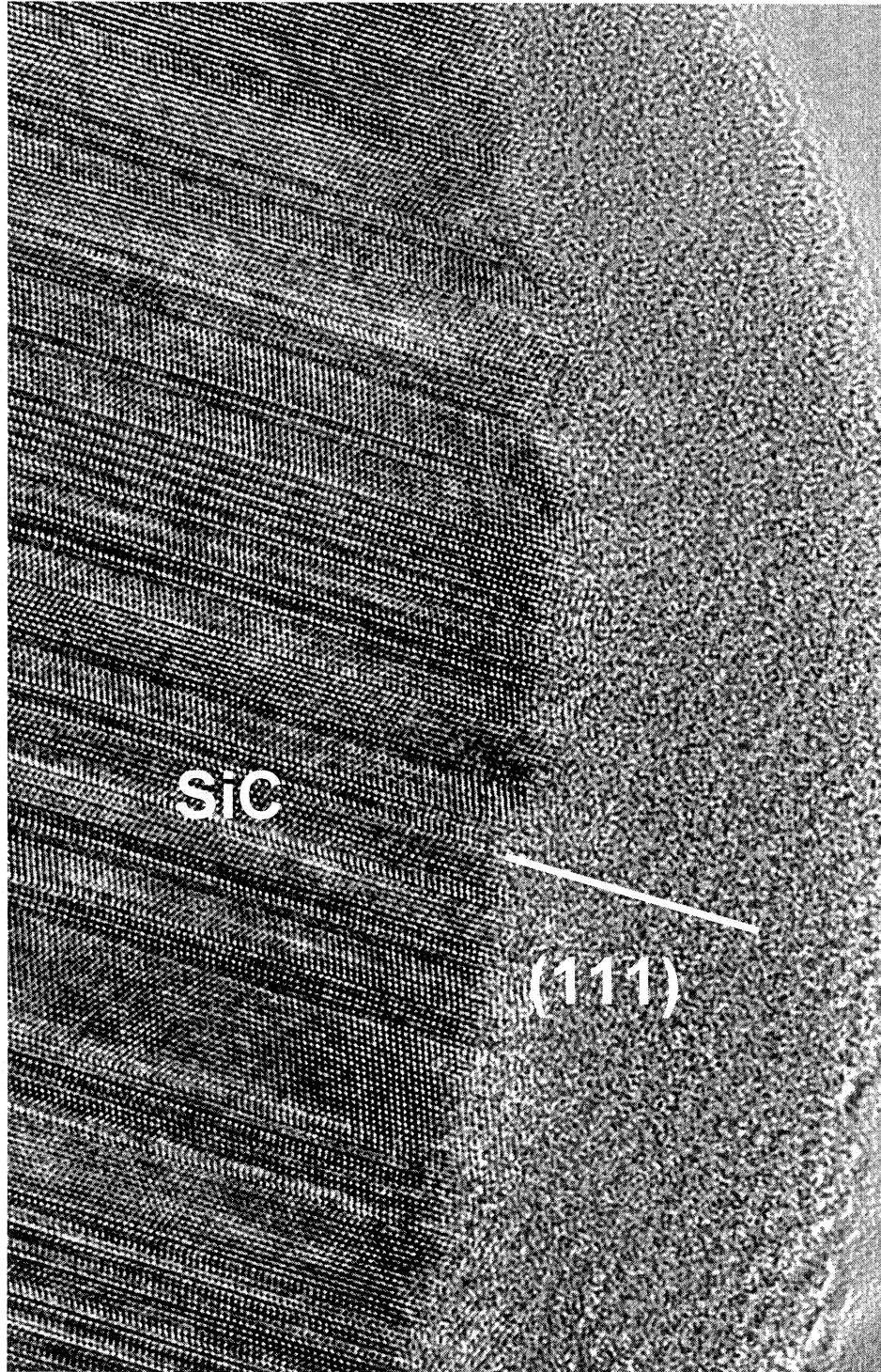


Fig. 4.4 A high resolution electron micrograph showing the planar defects within SiC phase.

### 4.3 Powder characterization

The Al<sub>2</sub>O<sub>3</sub> powder was used to fabricate the monolithic samples and the composites were made from the premixed Al<sub>2</sub>O<sub>3</sub>-SiC<sub>w</sub> powders. The specific surface area of the alumina powder was measured by the BET (Braunauer-Emmet-Teller) nitrogen gas absorption method (Autosorb-1, Quantachrome Co. Syosset, New York, USA). The particle size distribution in the alumina powder was measured by an optical transmission method (OTM). As shown in Figure 4.5, the alumina exhibits a very narrow size distribution. OTM analysis is not applicable to SiC whiskers since it assumes spherical particles, hence, the average diameter and aspect ratio were estimated from SEM images.

The chemical and morphological properties of powders would be expected to affect the processing and mechanical properties of the resulting composites. This is particularly important for colloidal processing where surface chemistry plays a critical role. Therefore, the surface chemistry of powders needs to be understood. There have been reports on the bulk and surface compositions and microstructure of SiC whiskers from different sources (Bradley *et al.* 1989, Karasek *et al.* 1989). Their results indicated that SC-9 whiskers from APMC consistently contained a surface oxide similar to that found in a Si-O-C glass rather than SiO<sub>2</sub>. Considering morphology, SC-9 whiskers showed the highest consistency in terms of straightness and low particulate content compared to those whiskers from other sources. The nominal concentrations of impurities are listed in Table 4.1.

**Table 4.1** Summary of characterisation of raw powders.

| Powder                                | Theoretical density(g/cm <sup>3</sup> ) | Average particle size (μm)    | Surface area (m <sup>2</sup> /g) |
|---------------------------------------|---|-------------------------------|----------------------------------|
| Al <sub>2</sub> O <sub>3</sub> (APMC) | 3.98                                    | 0.38(median)                  | 7.6334                           |
| SiC <sub>w</sub> (APMC)               | 3.21                                    | DIA 0.5-1; Aspect ratio 10-30 | Not measured                     |

**Table 4.2** Nominal content of impurities.

| Element | ppm  |
|---------|------|
| Ca      | 3700 |
| Mn      | 2400 |
| Al      | 1300 |
| Mg      | 800  |
| Fe      | 500  |

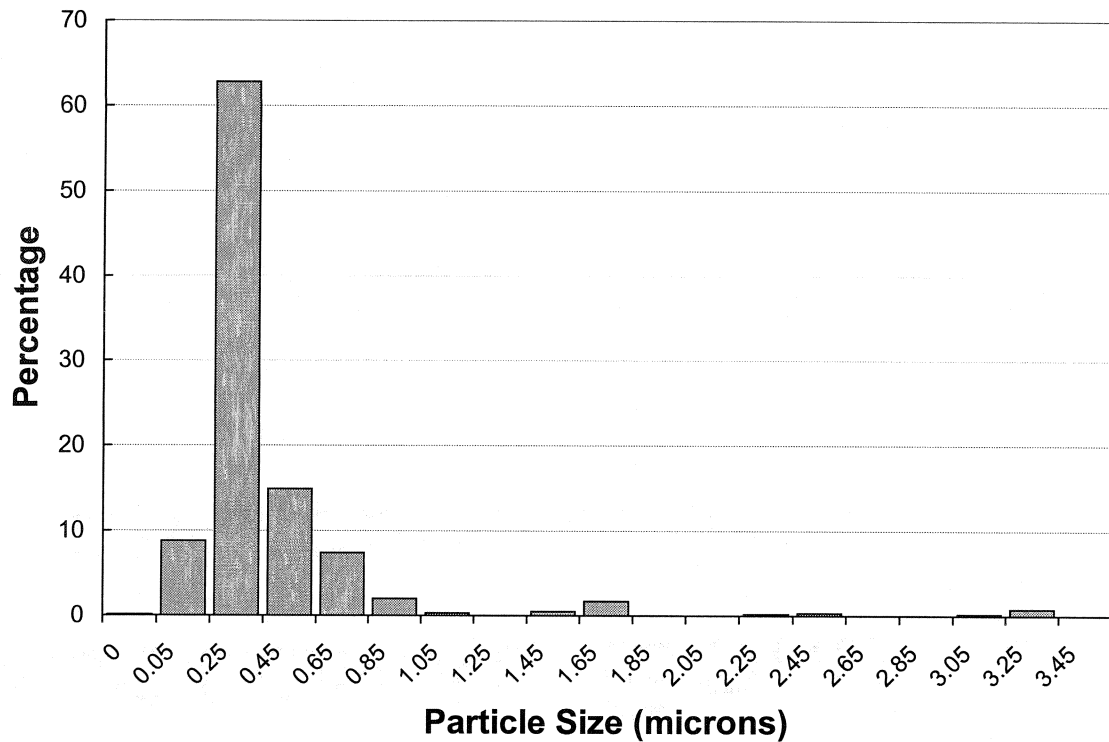


Fig. 4.5 Particle size distribution of raw alumina powder.

## 4.4 Ceramic powder processing

### 4.4.1 Introduction

To understand the effect of whisker network structure upon the creep response, composites with large differences in whisker alignment were desired. This was essentially approached through adjusting pH and solid loading of slurry. However, after hot pressing the overall whisker alignment was found to be similar irrespective of the pH value used to prepare the suspension. This led to preparing all the slurries with pH=2. However, it is only natural to start this section by explaining the effect of pH on the properties of  $\text{Al}_2\text{O}_3$ - $\text{SiC}_w$  suspension.



#### 4.4.2 Preparation of suspension

Figure 4.4 shows the measured zeta potential as a function of pH for alumina and SiC whisker powders. As shown, the alumina suspension showed IEP of  $\sim 8$ , which conforms to those reported in the literature (e.g. HamSu 1997, Jang et al. 1992). However, the SiC suspension behaved like  $\text{SiO}_2$  with IEP close to one. It appears that heteroflocculation of  $\text{Al}_2\text{O}_3$  and  $\text{SiC}_w$  can occur over a wide range of pH value between 2-7. Since the alumina particles are much smaller than SiC whiskers, it is likely that the heteroflocculation will draw the fine alumina particles onto the surface of the whiskers. If each single whisker is well coated with fine alumina particles on its surface, it might behave like a positively charged large alumina particle. Indeed the electrophoresis analysis on  $\text{Al}_2\text{O}_3$ - $\text{SiC}_w$  suspension under  $\text{pH}=2$  showed that SiC particles move in the same direction as  $\text{Al}_2\text{O}_3$  particles, affirming the heterointeraction between the two particles. This scenario was also described by Jang et al. (1992) (see Fig. 2.1). Therefore, if the pH at which the alumina particles are well dispersed also enables a strong heteroflocculation, the suspension should exhibit good stability as well. In terms of microstructural homogeneity, heteroflocculation is desired since the strong flocculation of one of or both particles would cause local segregation of phases. For example, if the alumina particles are preferentially flocculated, there will be whisker-free channels in the microstructure, which reportedly promote crack propagation (Swan et al. 1992), decreasing the toughening effect achieved through whisker reinforcement. To see the effect of pH on stability of a composite suspension, several slurries were prepared with the pH in the range of 2-10 and solid loading around 20%. Figure 4.7 shows the measured relative heights of solid after about 6 months. In general, significant sedimentation was observed at low pH while no or little sedimentation was found at high pH level. It is seen that the height of solid was lowest at  $\text{pH}=2$  while there was almost no sedimentation when the pH was between 6-8. In addition, the kinetics of sedimentation was found to be different at low pH. It was interesting to find that the initial settling rate was faster for  $\text{pH}=4$  than  $\text{pH}=2$ ; however, the latter caught up with the former gradually, reaching the lowest relative solid height. This suggests a higher stability at  $\text{pH}=2$  than  $\text{pH}=4$ , and the packing efficiency of the mixed particles is the highest at  $\text{pH}=2$  whereby it is inferred that flocculation between SiC whiskers is perhaps most limited. This result is consistent with earlier reports (Porter et al.

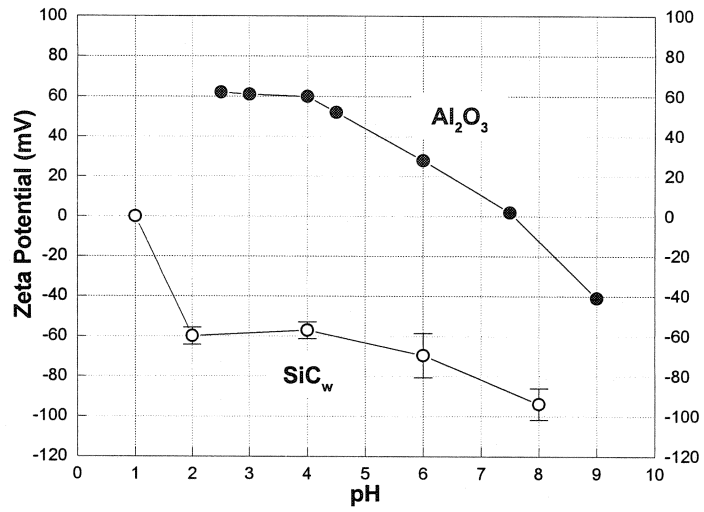


Fig. 4.6 Zeta potential as a function of pH for SiC and alumina suspensions.

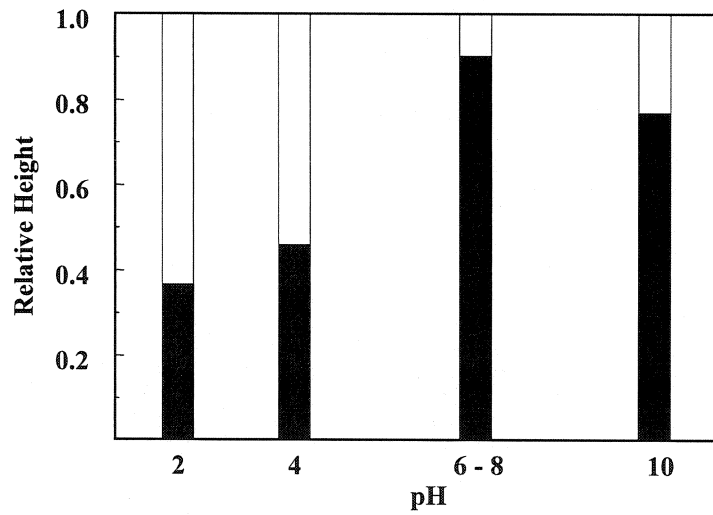


Fig. 4.7 Sedimentation of composite slurry at different pH values after about 6 months.

1987 and Porter 1989). It should be mentioned that the green density of  $\text{Al}_2\text{O}_3\text{-SiC}_w$  composite sample is largely dependent on the packing efficiency of whiskers.

During sedimentation, well-dispersed whiskers would tend to align with their axes perpendicular to the direction of gravity, while flocculated whiskers would maintain their orientation within the floc. As a result, different whisker distributions may be expected within a green body and the subsequent hot pressing might inherit this difference in spite of the overall increment in whisker alignment. In light of this hypothesis, slurries were prepared using pH=2 and pH=6, in an attempt to produce composites with well-aligned whiskers and randomly oriented whiskers respectively. Table 4.3 shows the recipes for preparation of slurries and consolidation methods. It was found that the viscosity increased with increasing pH for a given solid loading. Therefore, the solid loading was necessarily lowered with increasing pH, which enabled an appropriate viscosity for slip casting. The optimum solid loading should be a compromise between castability of the slurry and low shrinkage during the drying cycle. Figure 4.8 presents a flow chart for ceramic composite processing.

**Table 4.3** Experimental schemes for green body formation.

| Composite | SiC (vol.%) | pH | Solid Loading (vol.%) | Consolidation method       |
|-----------|-------------|----|-----------------------|----------------------------|
| S302      | 30          | 2  | 15-30                 | Slip casting               |
| S202      | 20          | 2  | 35-40                 | Slip casting               |
| S102      | 10          | 2  | 45-50                 | Slip casting               |
| S306      | 30          | 6  | 15                    | Slip casting               |
| G306      | 30          | 6  | 15                    | Slip casting + granulation |
| Alumina   | 0           | 2  | 50                    | Slip casting               |

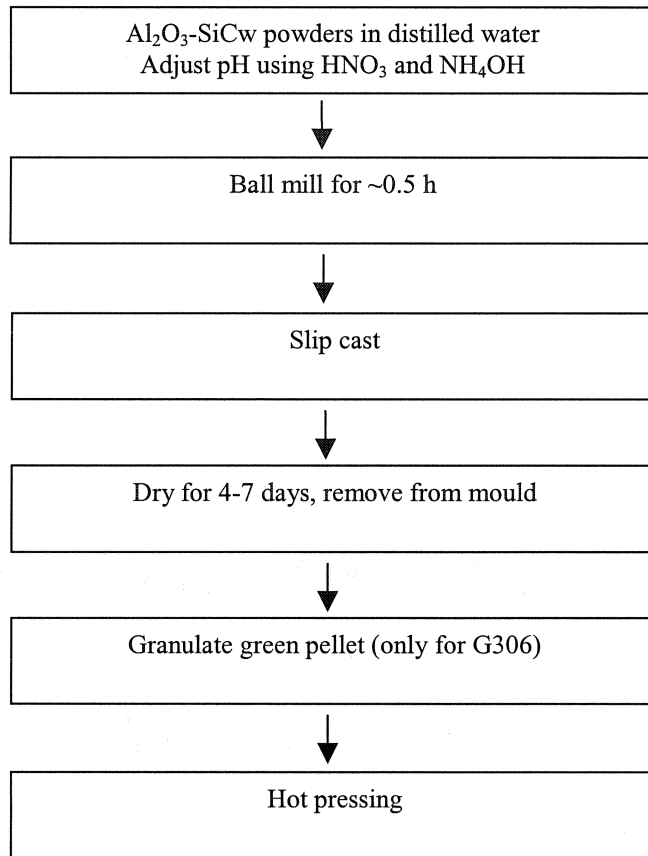


**Fig. 4.8** Slip casting processing flow chart.

#### 4.4.3. Sintering

Since the presence of whiskers raises the sintering pressure, relatively high sintering temperatures and loads were needed to achieve full densification. Figure 4.9 shows the recipes used for hot pressing, which were designed to produce a dense product with a similar grain size. Before being loaded into the graphite die for hot pressing, the dried green sample was mechanically ground so as to smooth the sample surfaces and fit into the die. Thin graphite foil was used to wrap the samples completely, which facilitated sample removal after hot pressing. Figure 4.10 shows a schematic diagram of the graphite die. Sometimes one or two spacers were used to hot press two or more samples at the same time.

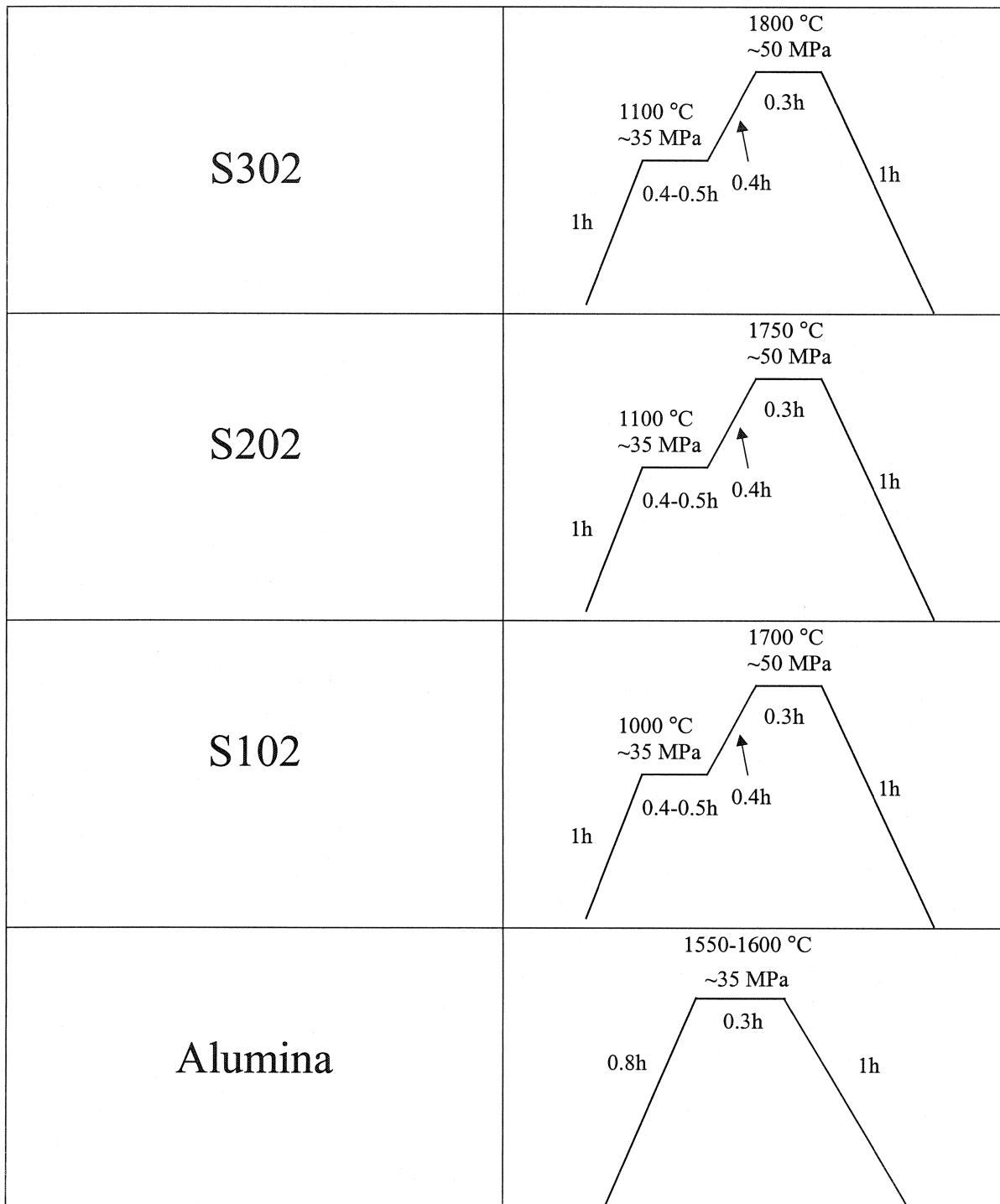
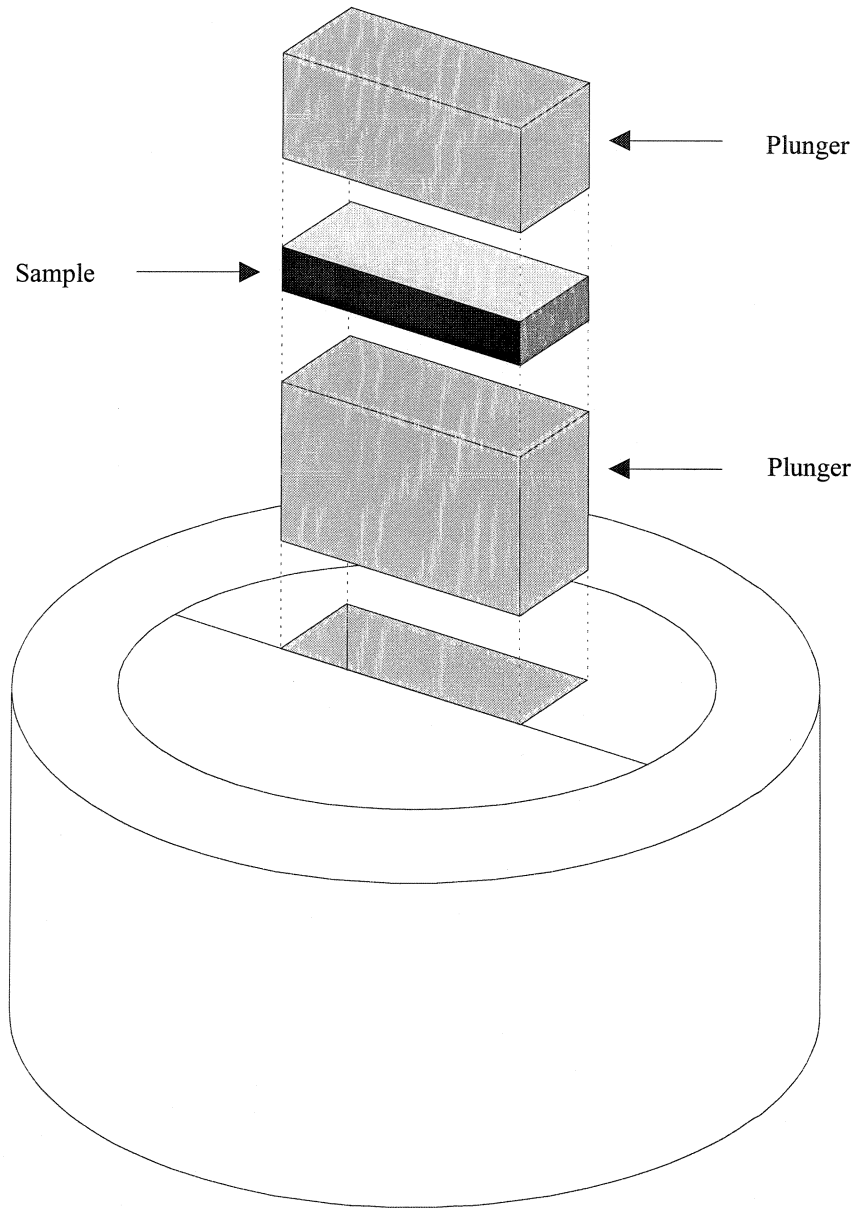


Fig. 4.9 Recipes for hot pressing.



**Fig. 4.10** Schematic illustration of graphite die for hot pressing.

## 5. RESULTS

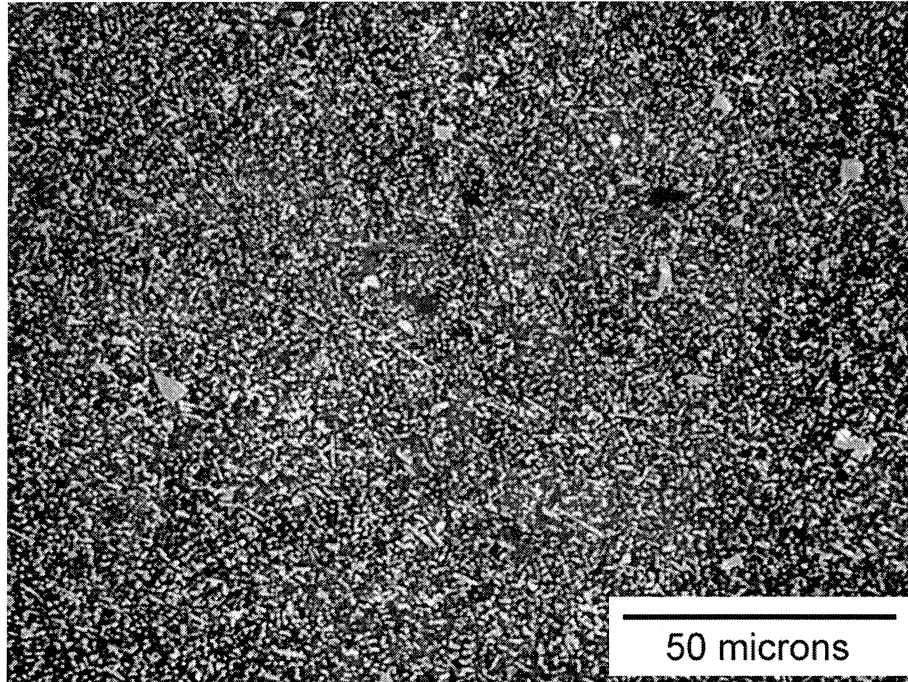
### 5.1 Introduction

This chapter consists of three parts. The first part describes the results from microstructural characterisation by optical microscopy, scanning electron microscopy (SEM). The second part includes the results from creep tests, which encompass creep curves, derivation of stress exponents and activation energies. The third part describes the results obtained from various neutron diffraction measurements.

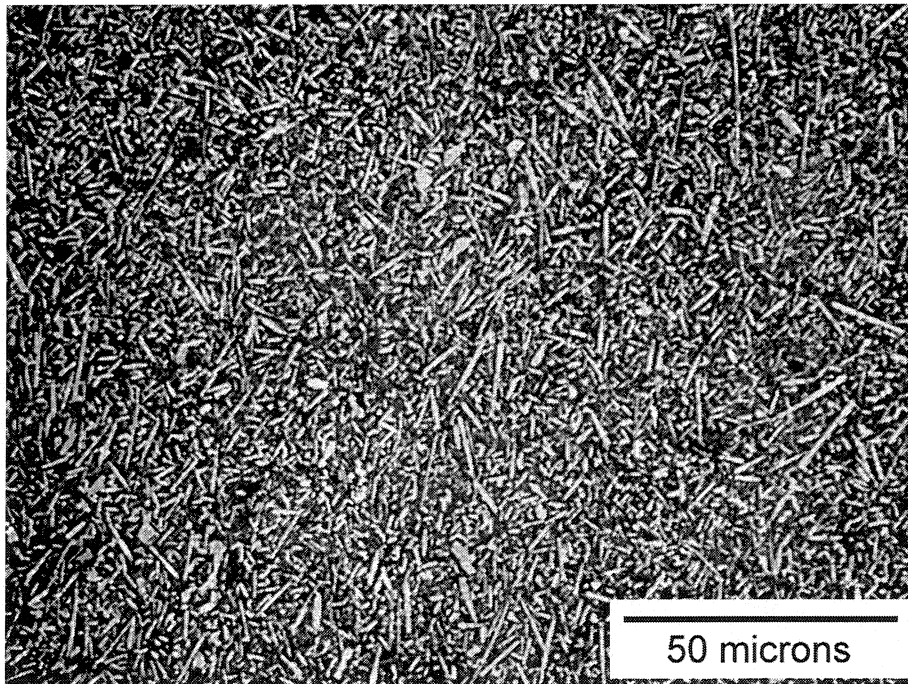
### 5.2 Microstructure

#### 5.2.1 Optical microscopy

Figure 5.1(a) shows an optical micrograph of 30% whisker reinforced alumina composite. As desired, whiskers are evenly distributed in the matrix with no indication of any local whisker agglomeration. In this orientation, most whiskers are seen 'end-on', which is a result of whisker alignment during uniaxial hot pressing. Some non-whisker type particles are also present in the microstructure. Figure 5.1(b) is taken from the same sample but with the surface perpendicular to the hot pressing axis (HPA) where many whiskers are seen 'edge-on'. It is evident that whiskers are randomly distributed in this orientation, indicating a transverse isotropy of whisker distribution with respect to HPA. Figure 5.2 includes two optical micrographs taken from a composite sample containing 20% SiC whiskers. They resemble those in Fig. 5.1 except for a lower density of whiskers. When the whisker loading is 10% as shown in Fig. 5.3, although the overall distribution of whiskers is still uniform, there are some distinct local features in the microstructure. For instance, in the Fig. 5.3(b) there is an indication of local whisker self-alignment. In addition, a frequent deviation from preferred whisker orientation is observed in the micrograph. This is related to the less restricted whisker movements during 'wet' processing period because of weak interaction among whiskers.



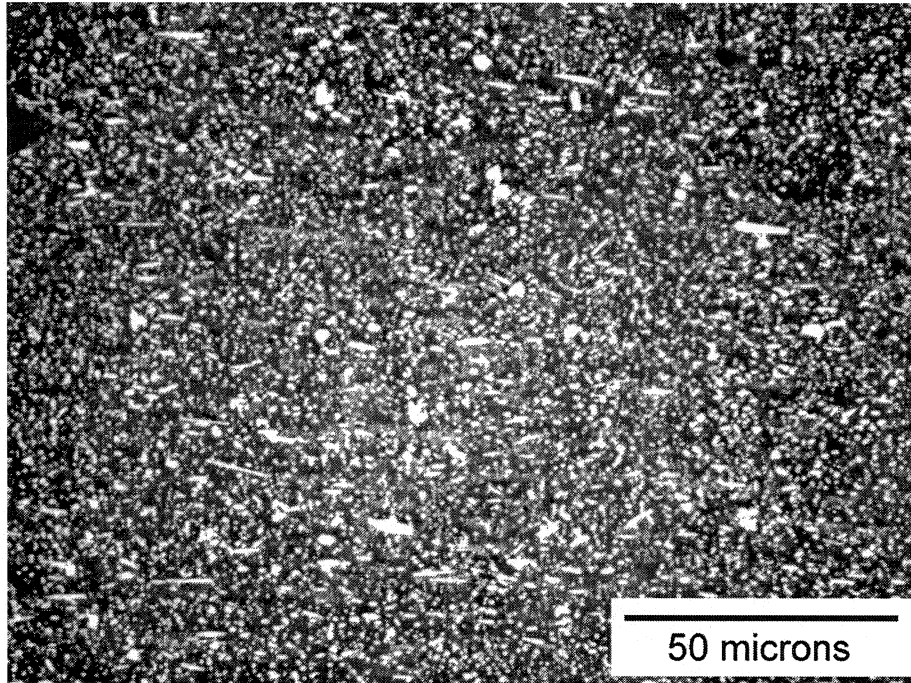
(a)



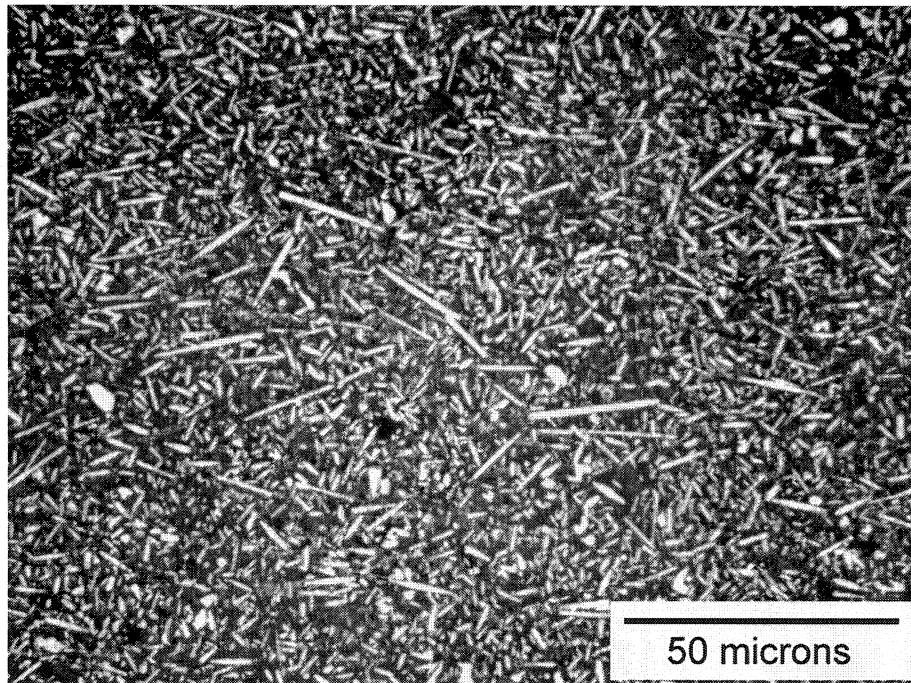
(b)

**Fig. 5.1** An optical micrograph of 30% SiC whisker reinforced alumina with the surface (a) parallel and (b) perpendicular to HPA.



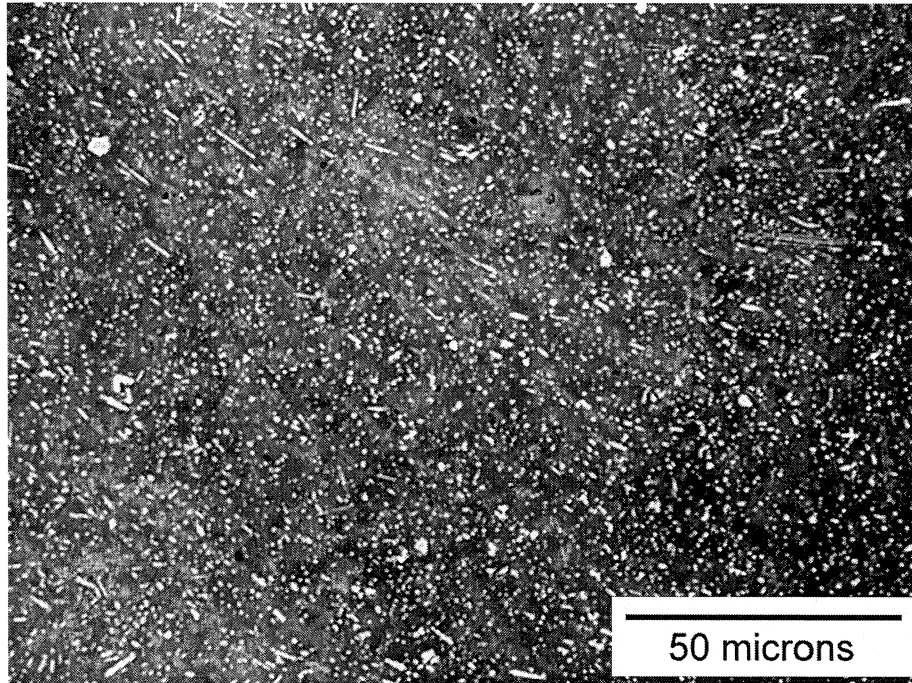


(a)

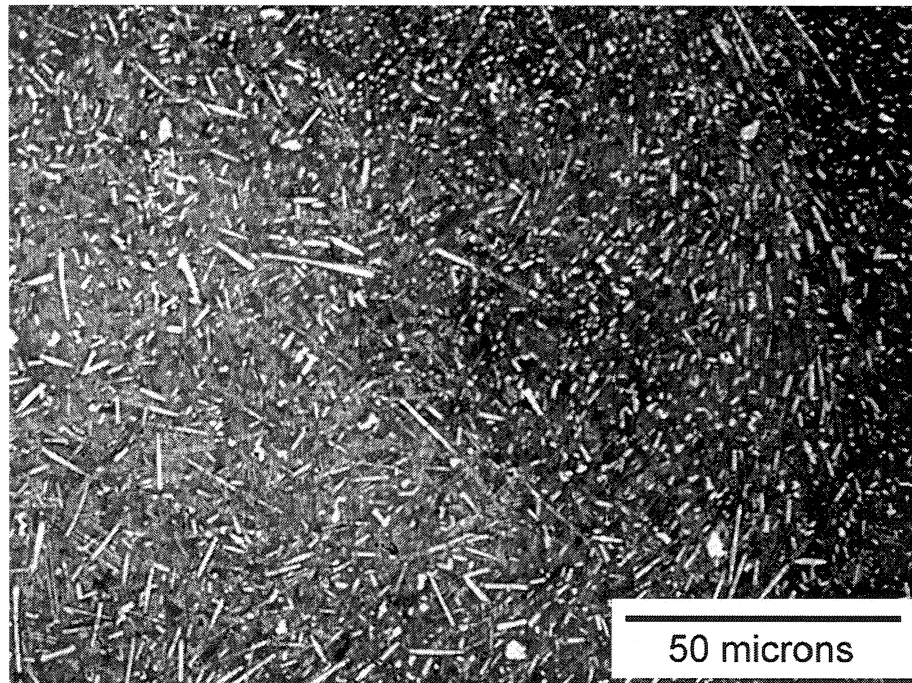


(b)

Fig. 5.2 An optical micrograph of 20% SiC whisker reinforced alumina with the surface (a) parallel and (b) perpendicular to HPA.



(a)



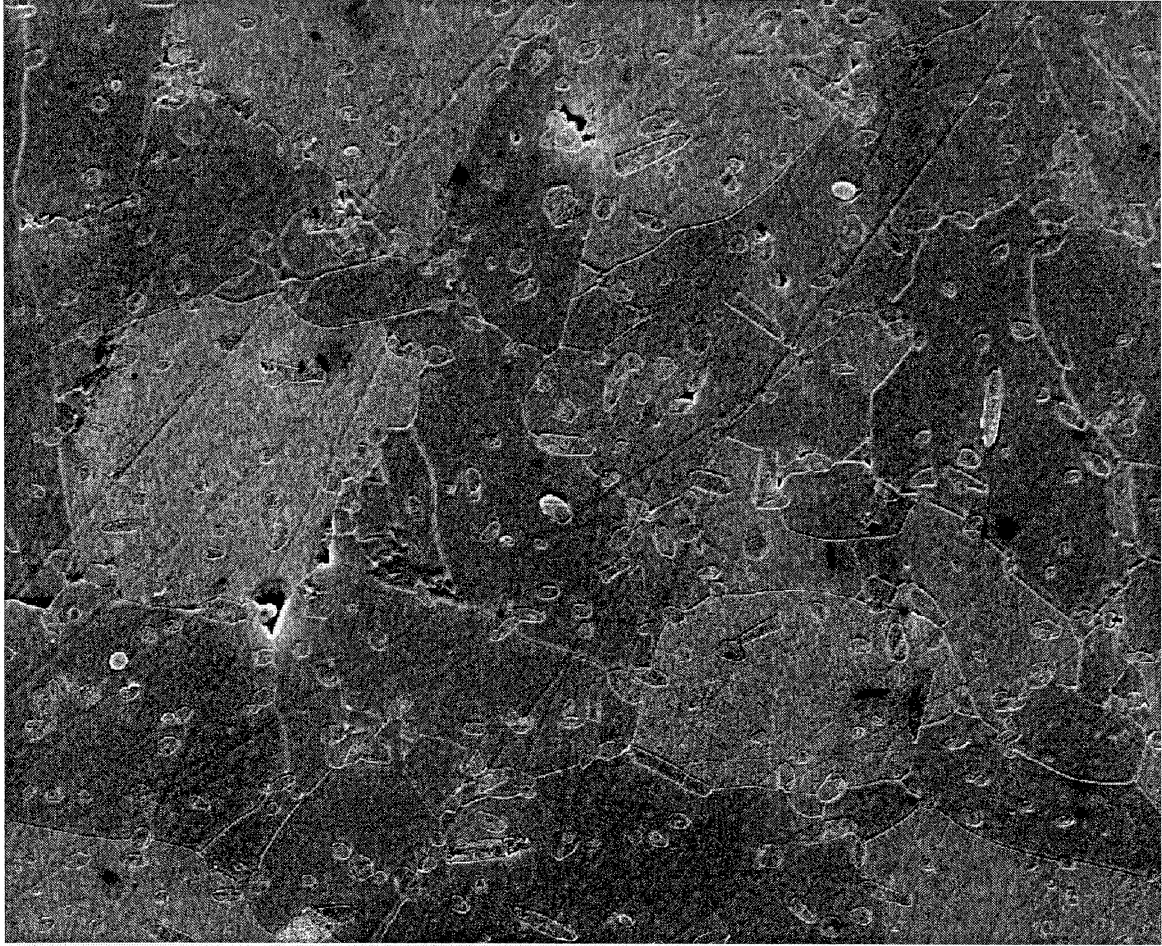
(b)

Fig. 5.3 An optical micrograph of 10% SiC whisker reinforced alumina with the surface (a) parallel and (b) perpendicular to HPA.

## 5.2.2 Scanning electron microscopy

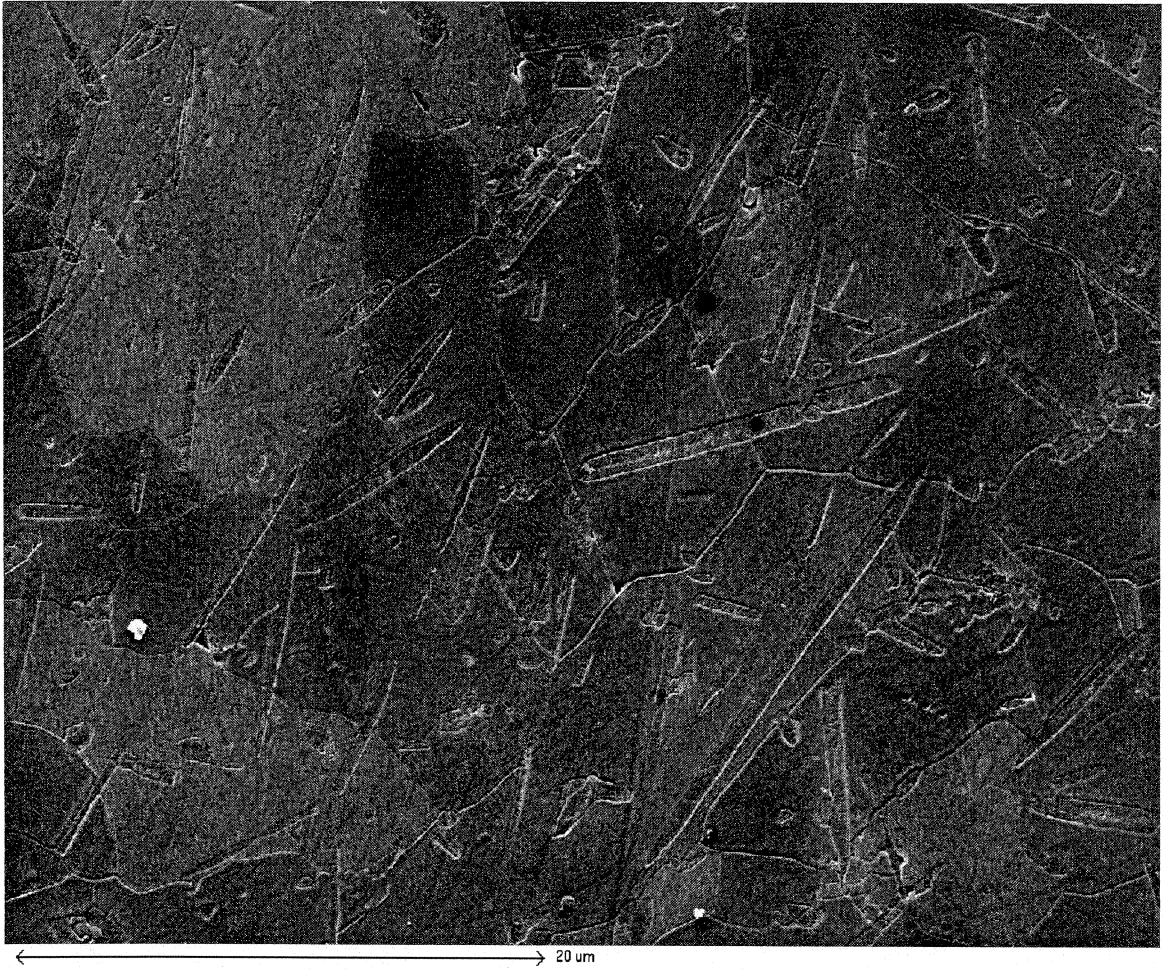
Figure 5.4(a) shows an SEM micrograph of the composite containing 10% SiC whiskers. The surface is parallel to the hot pressing direction and most whiskers are seen 'end-on'. It is seen that size of matrix grains is not uniform, however, most of them have much larger size than whiskers that are more or less uniformly distributed in the matrix with no segregation at grain boundaries. Figure 5.4(b) was taken from the same sample with the surface perpendicular to hot pressing axis, hence, most whiskers are seen more 'edge-on'. In this orientation, whiskers are frequently seen to lie across the matrix grain boundaries. The slightly different contrast in the matrix grains is due to the difference in grain orientation. Figure 5.5 shows a SEM micrograph of as processed S202 sample with the surface perpendicular to HPA. Here, most whiskers are seen 'edge-on' with no preferred orientation in the plane of observation and they often sit over several grains. Again there is no indication of whisker agglomeration. The matrix grain size is considerably smaller than that of S102.

Figure 5.6 shows a SEM micrograph taken from an as hot-pressed S302 sample. The sample surface was deeply etched by thermal treatment so that most alumina matrix grains have been removed from the sample surface, leaving only whiskers at the surface. Given such a high number density, these whiskers seem to have already formed an interconnecting network. It is also noted that the diameter of whiskers is quite uniform. Figure 5.7 presents a micrograph taken with the sample surface parallel to HPA. Here the overall uniform distribution of whiskers is noted, but locally they are often seen in close contact with each other. It appears that those whisker concentrated areas are associated with more extensive pores, indicating their susceptibility to thermal etching. It is also noteworthy that most whiskers are located at grain boundaries and junctions, especially at triple grain junctions. In addition, fine and uniform matrix grain size is evident from the micrograph.



(a)

**Fig. 5.4** SEM micrographs of S102 before creep with the surface (a) parallel and (b) perpendicular to HPA. Sample surface was gold coated.



**Fig. 5.4 (Continued)**

**(b)**

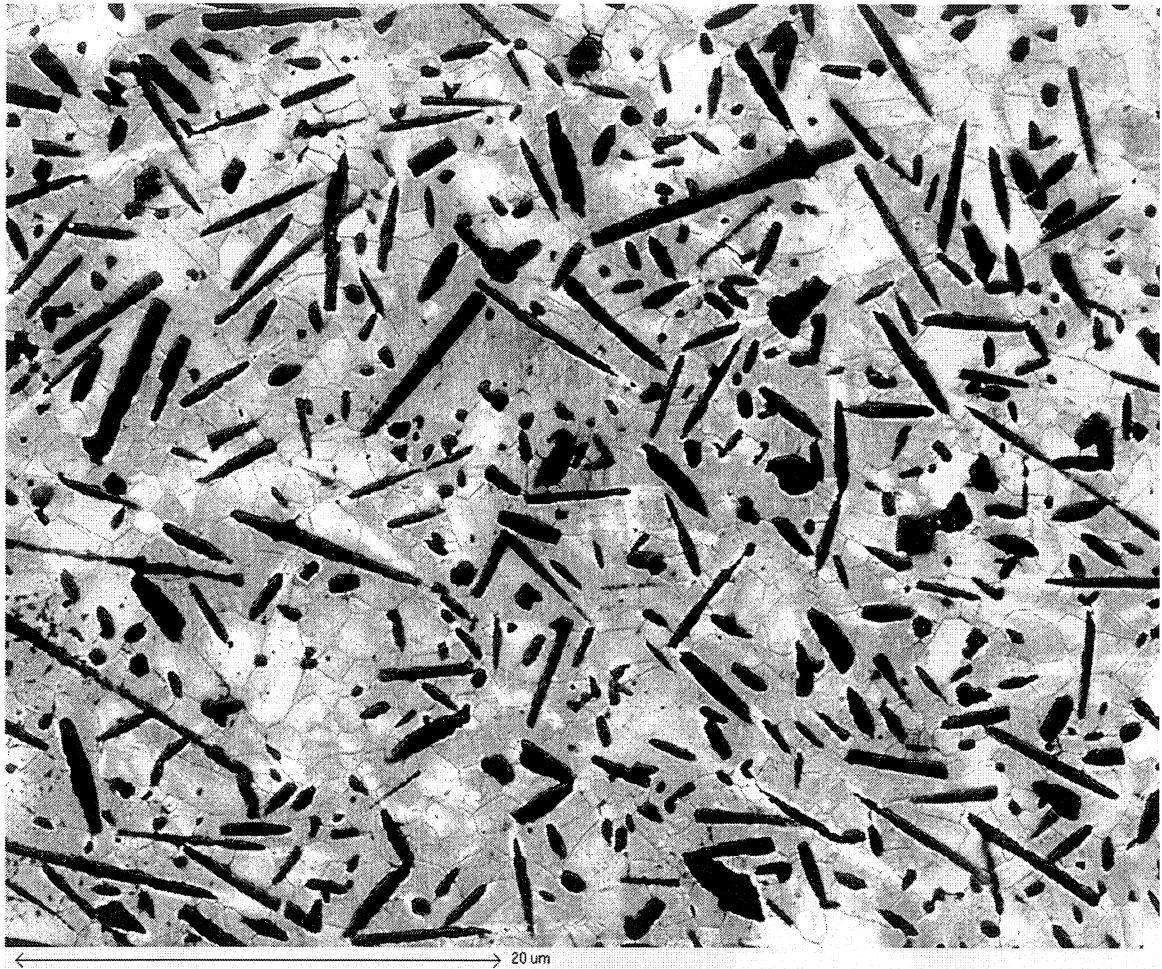


**Fig. 5.5** An SEM micrograph taken from a S202 composite with the sample surface perpendicular to HPA. Unlike S102, the sample surface was not coated with gold, since the surface charges are grounded through the interconnected whisker network.

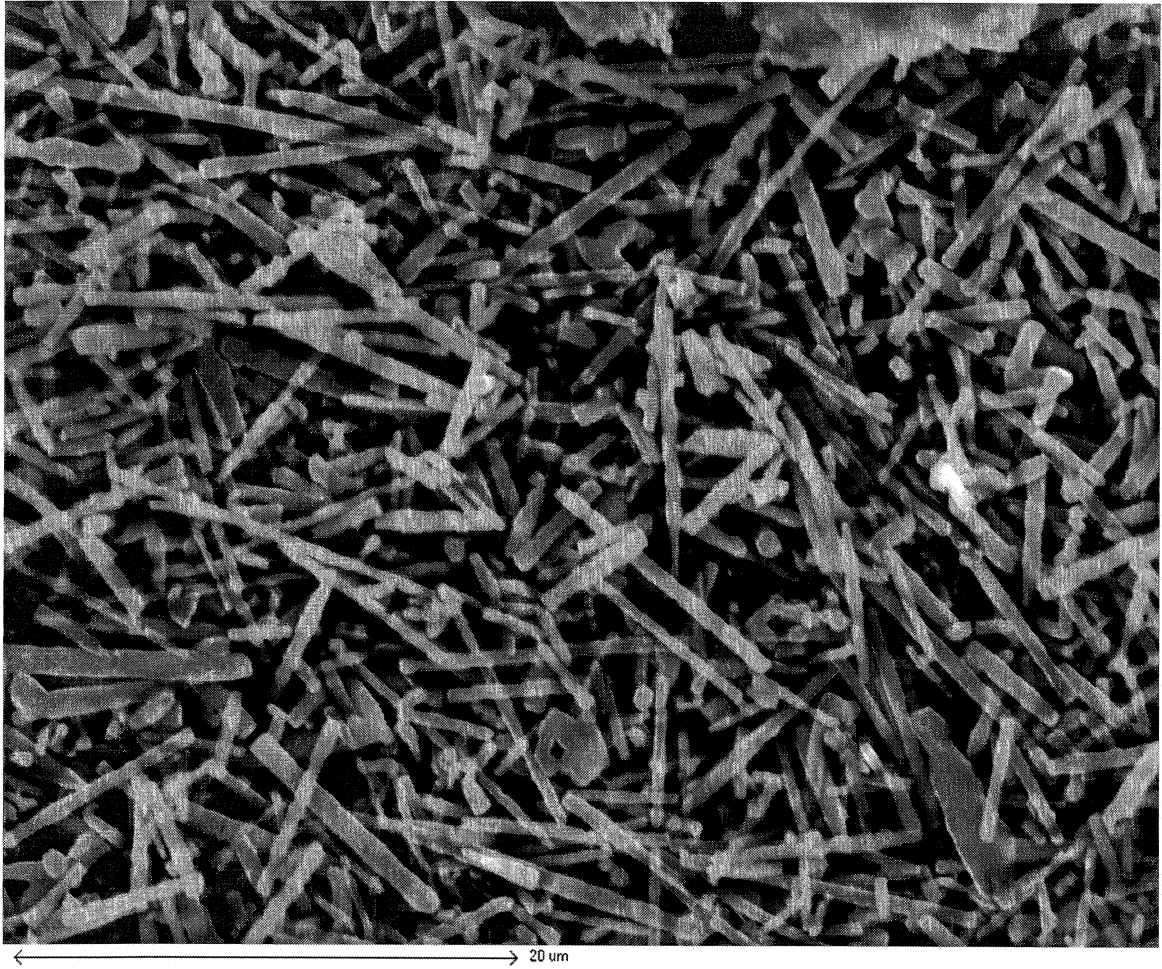


**Fig. 5.6** A SEM micrograph of S302 with sample surface perpendicular to HPA. The surface was thermally etched at 1400°C for 2 hours.

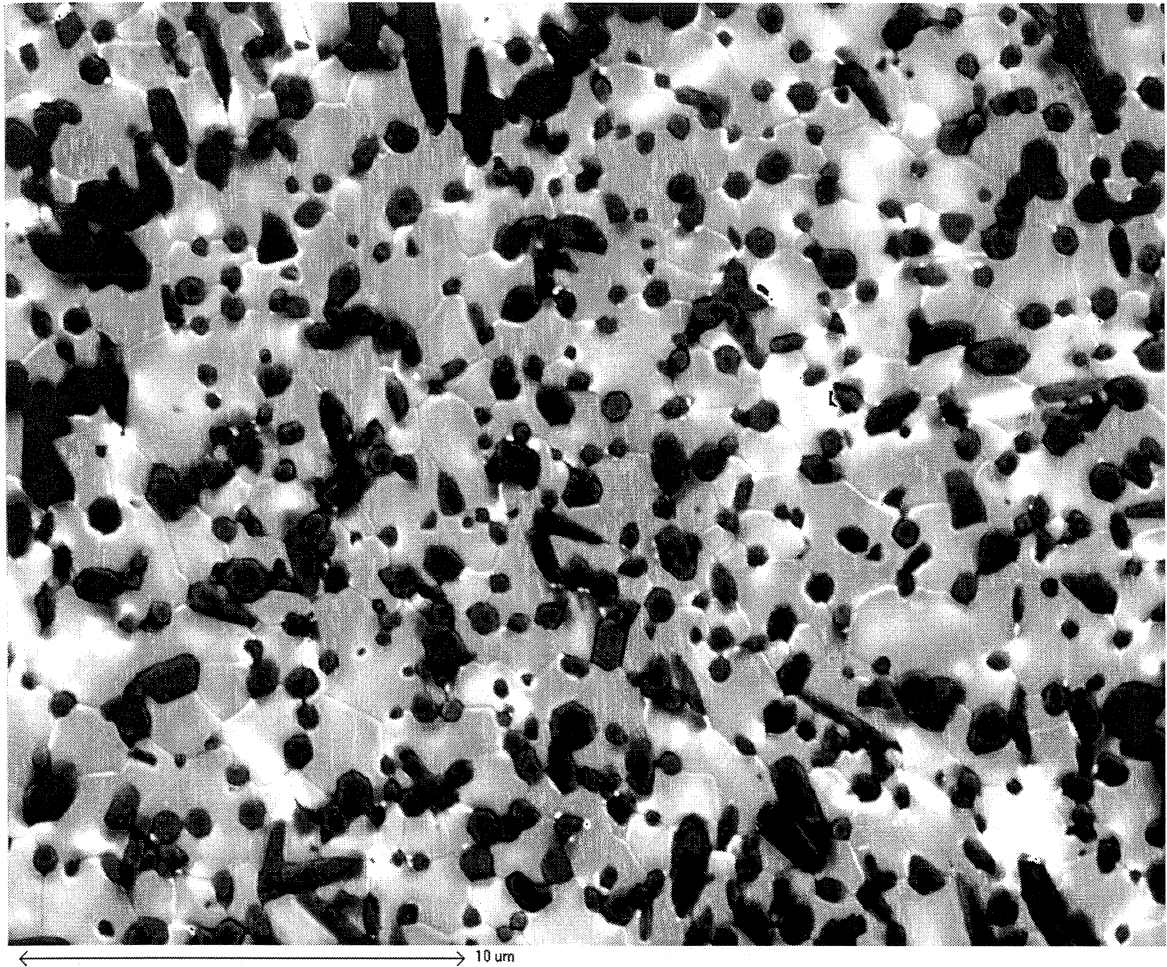


**Fig. 5.7** An SEM micrograph of S302 with the surface parallel to HPA. Thermal etching caused the surface porosities, esp. within whisker clusters.

Matrix grain size is measured from the SEM micrographs. Table 5.1 summarises the average grain size of all the materials fabricated.

**Table 5.1** Average grain size (in micrometer) for the composites and pure alumina.

|            | S102    | S202 | S302 | Alumina |
|------------|---------|------|------|---------|
| Grain size | 7.8±1.2 | 1-2  | 1-2  | 3.4±0.5 |



## 5.3 Creep

### 5.3.1 Introduction

Most samples were tested in tension. However, a limited number of compressive creep tests were also performed on S302 composites, which was aimed at achieving relatively larger strains than in tension. The results are organised in the following manner. First, some of the creep curves are shown, which permits a direct comparison either between different composites with different whisker content or for the same sample at different testing conditions. Then plots of strain rate vs. stress are presented in both unnormalized and grain size (or temperature) normalized formats. The latter allows for the derivation of stress exponents, and activation energies, and aids understanding the overall creep response over the stress range involved in terms of strain rate.

### 5.3.2 Shape of creep curves

Figure 5.8 presents a typical creep curve for a pure monolithic alumina at 1200°C. The sample was deformed under 74 MPa before the load was dropped to 19 MPa. From the creep curve, the primary creep stage is barely recognizable, however, close inspection reveals the presence of a large curvature up to 0.01 of the creep strain. Upon the load drop, there is no significant anelastic strain recovery. Rather, following a small elastic recovery we see continued creep at a much lower strain rate.

Figure 5.9 presents a creep curve for the S102 composite at 1400°C. Here, a significant primary creep is seen, which is followed by a well defined steady-state creep regime. Upon load drop there seems to be a period of limited anelastic strain recovery.

Figure 5.10 shows three creep curves for S202 composites at 1400°C under different stresses. As expected, creep rate increases with increasing applied stress. In general, the scatter in the data decreases with increasing deformation rate. It is clear that these creep curves exhibit more extensive primary creep than pure alumina.

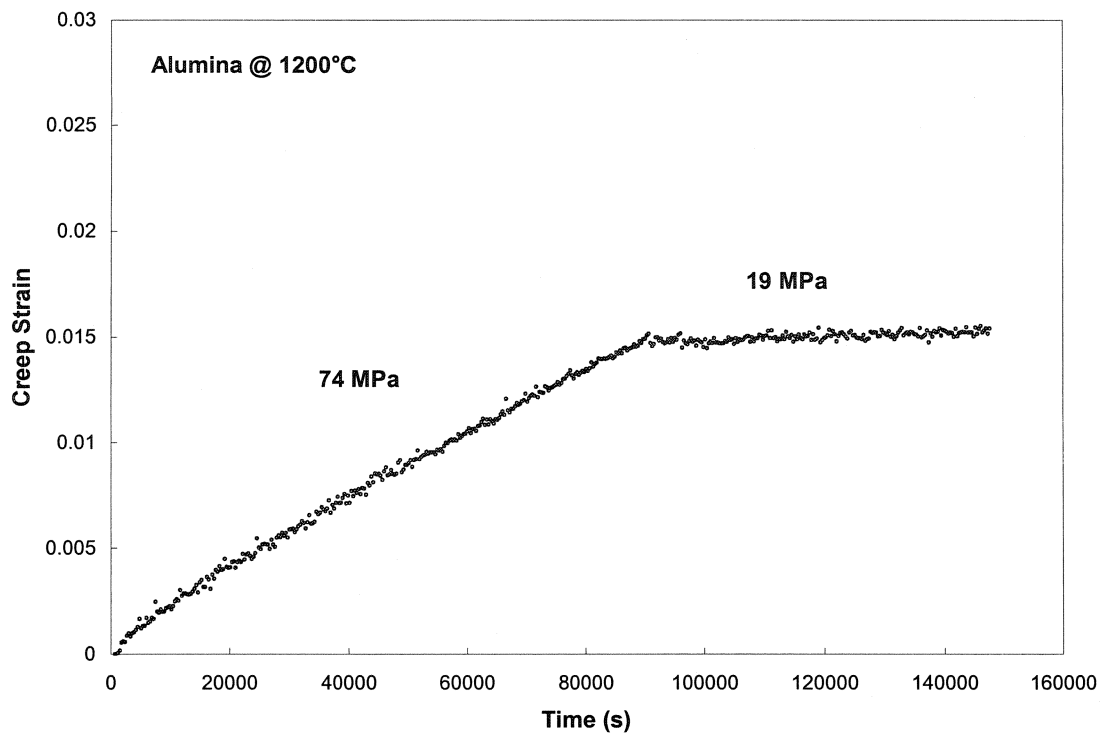


Fig. 5.8 A creep curve for a pure polycrystalline alumina at 1200°C.

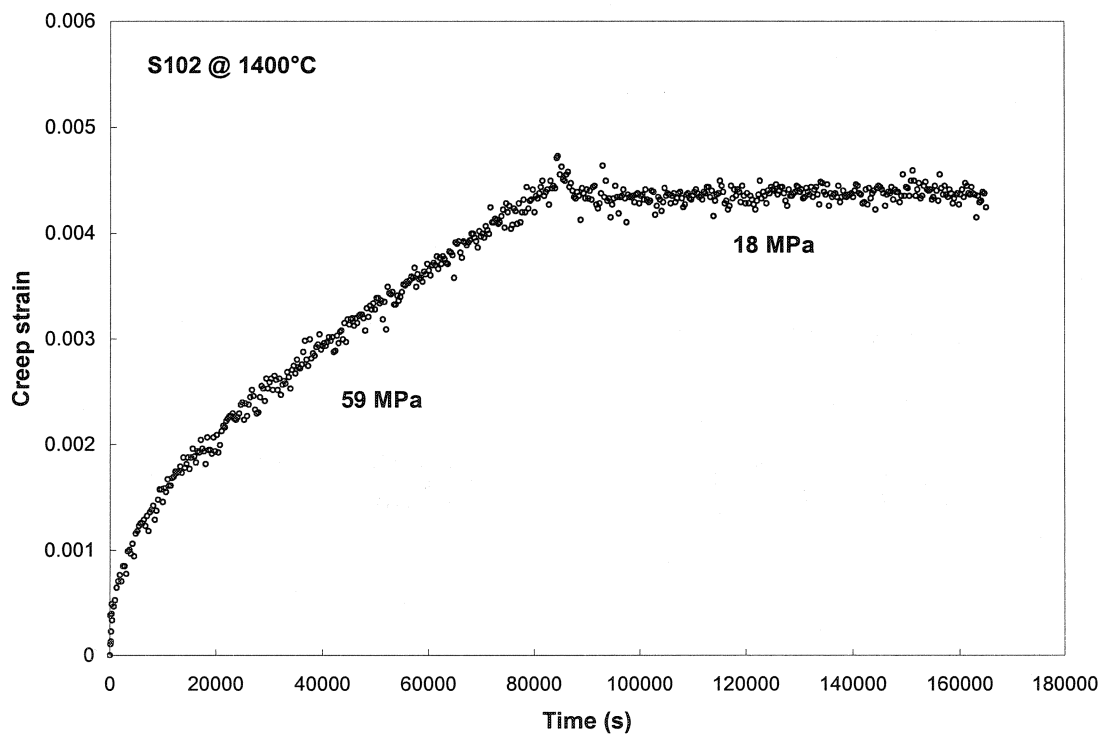
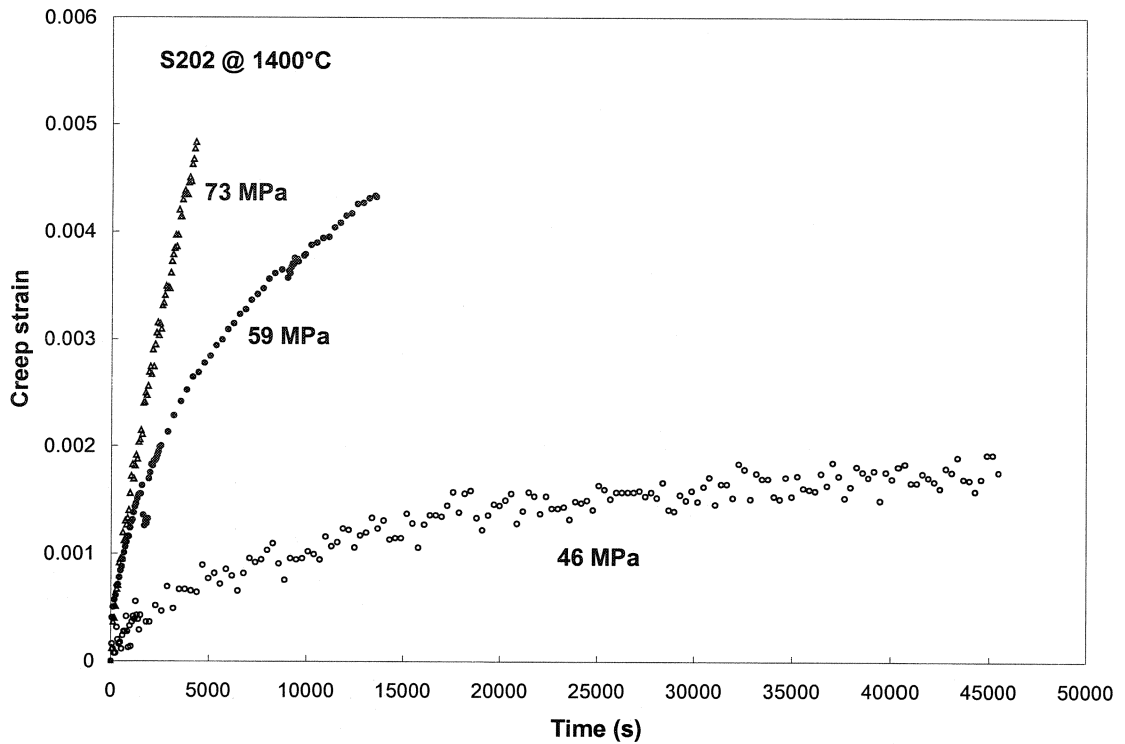


Fig. 5.9 A creep curve for a S102 composite at 1400°C.



**Fig. 5.10** Creep curves for 20% SiC whisker reinforced alumina composites at 1400°C.

Figure 5.11 shows creep curves from three composites with different SiC content. All of them exhibited more extensive primary creep than pure alumina. S102 however, shows less primary creep regime than S202 and S302 samples. Noting a similar matrix grain size for S302 and S202 samples, these creep curves seem to demonstrate a further increase in creep resistance when the whisker loading increases from 20 to 30%.

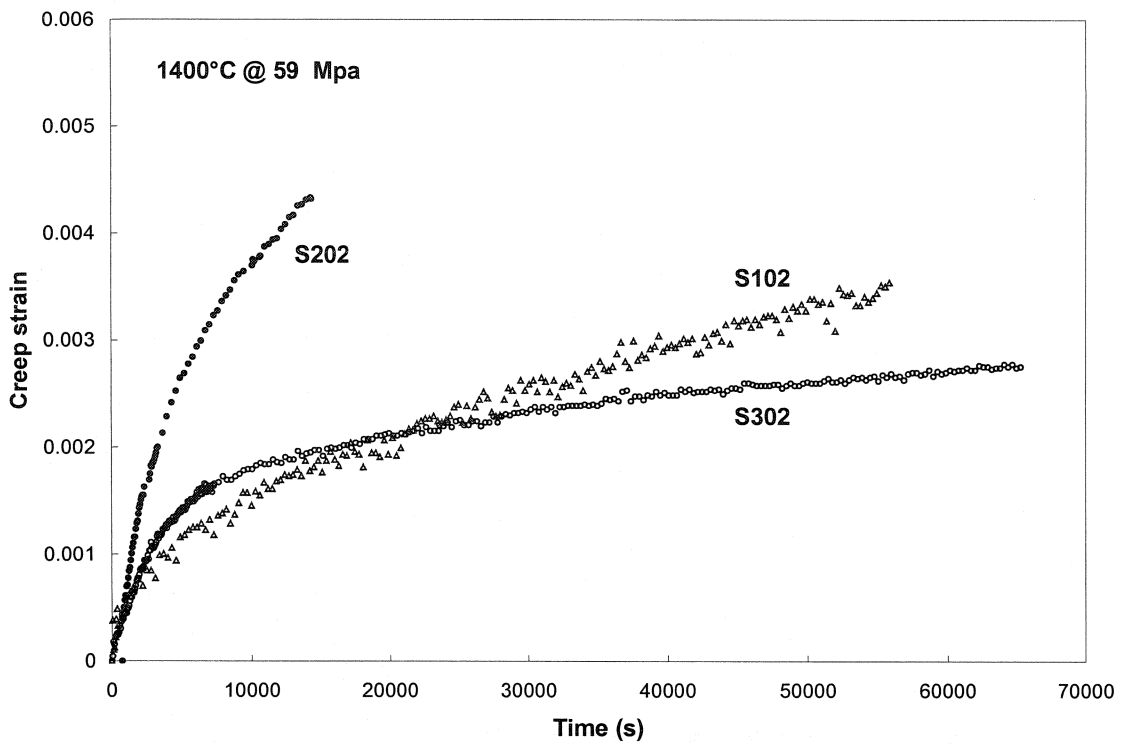


Fig. 5.11 Creep curves for the composites with different SiC content at 1400°C.

### 5.3.3 Steady-state strain rate plots

Figure 5.12 shows the steady-state strain rate plotted as a function of stress plot for S302 at 1200-1400°C. Data for pure alumina at 1200°C is also shown for comparison. As expected, the composite exhibited much lowered strain rate than the pure alumina especially towards low stress level. The measured stress exponents are about 4-5 for all the temperatures involved and they are included in the plot. There is no shift in stress exponent observed within the stress range studied. The high stress exponents may suggest that a different creep mechanism operates in the composites as compared with the pure alumina, while the similarity in the value of stress exponent with temperature and stress seems to indicate that a similar deformation mechanism is operative over the scope of testing conditions.

Figure 5.13 presents the creep data obtained from S202 composites at 1200-1400°C. Unlike S302, the stress exponent is strongly dependent on temperature, increasing from about 2.4 at 1300°C to about 7.2

at 1400°C and 6.3 at 1200°C. However, no shift in stress exponent was recorded for a given temperature within the stress range covered.

Figure 5.14 shows a strain rate vs. stress plot for S102 composites at 1200-1400°C, which exhibits very similar features as in S202 in terms of the temperature dependence of stress exponent. It is seen that the stress exponent increases from about 2.7 at 1300°C to about 7 at 1400°C and to as high as about 11 at 1200°C.

Figure 5.15-17 shows the grain size normalized steady-state strain rate vs. stress plots for three different composites at 1400°C, 1300°C and 1200°C respectively. It is assumed that grain boundary diffusion is dominant, i.e.  $\dot{\epsilon} \propto d^{-3} \sigma^n$ . In general, the creep rate decreases with increasing SiC content and this effect is more pronounced at high temperatures.

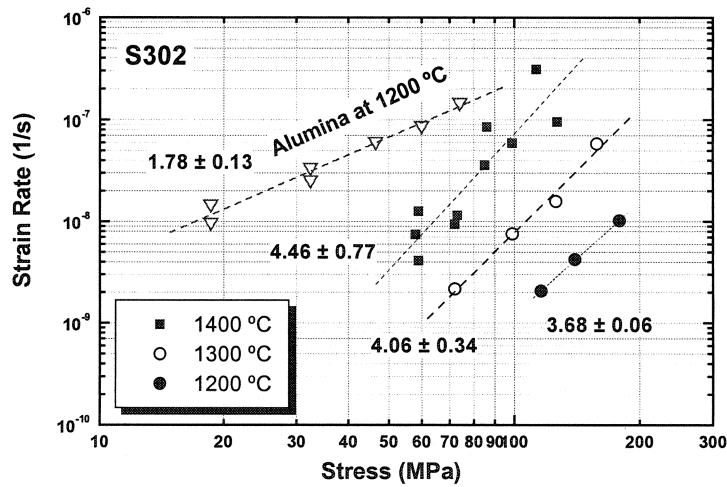


Fig. 5.12 Steady state strain rate as a function of applied stress for S302.

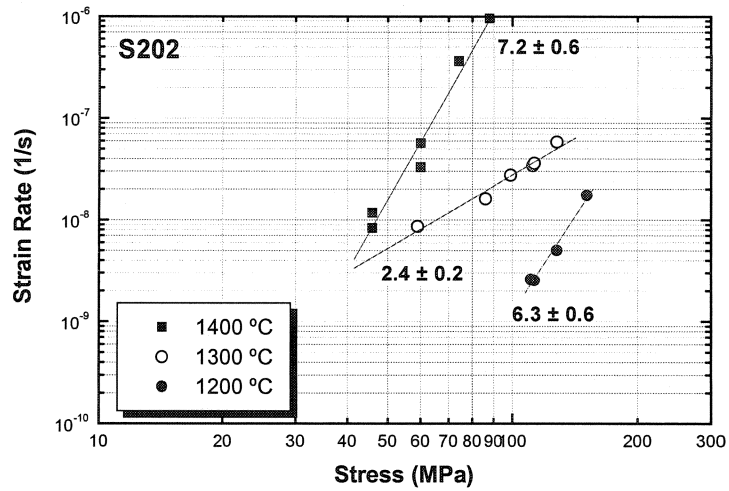


Fig. 5.13 Steady state strain rate as a function of applied stress for S202.

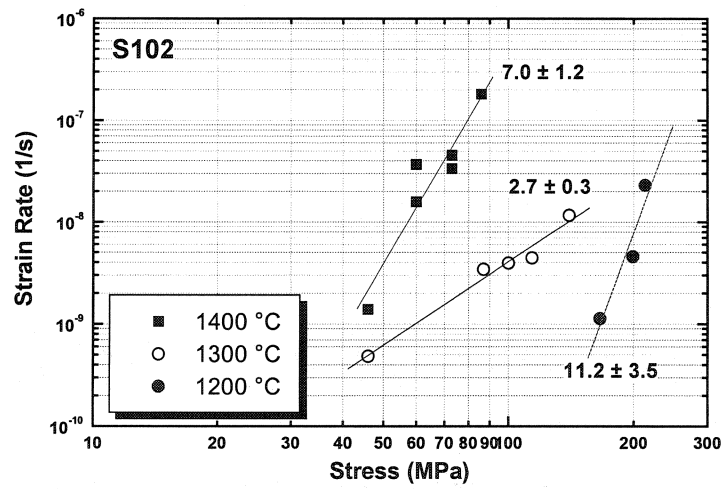


Fig. 5.14 Steady state strain rate as a function of applied stress for S102.

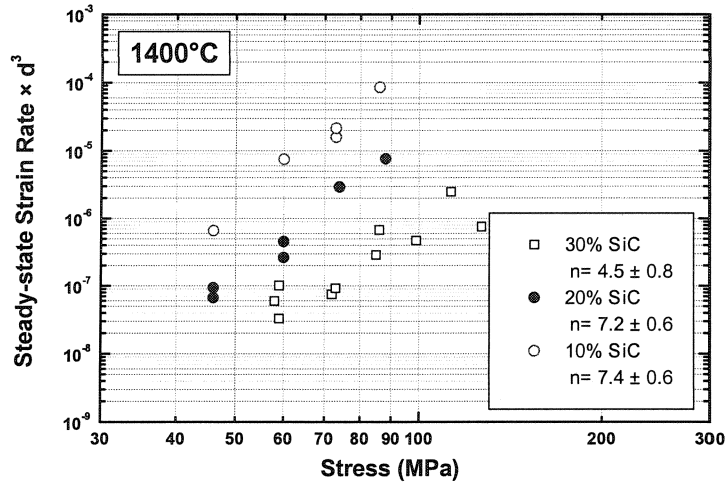


Fig. 5.15 Normalized steady state strain rate vs. stress plots at 1400°C for different SiC content.

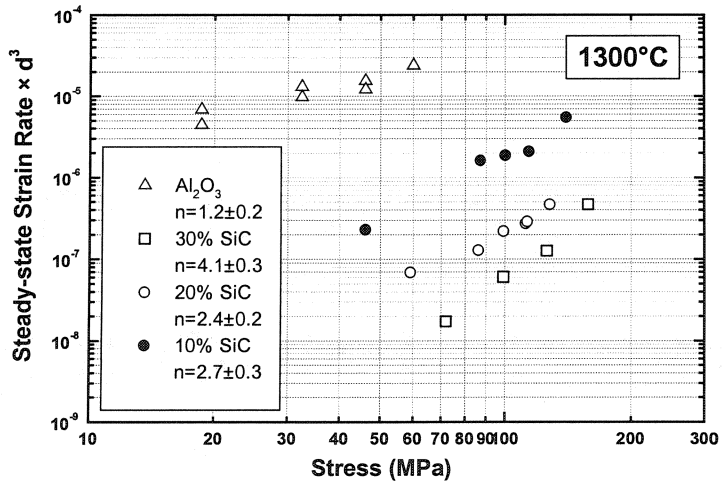


Fig. 5.16 Normalized steady state strain rate vs. stress plots at 1300°C for different SiC content.

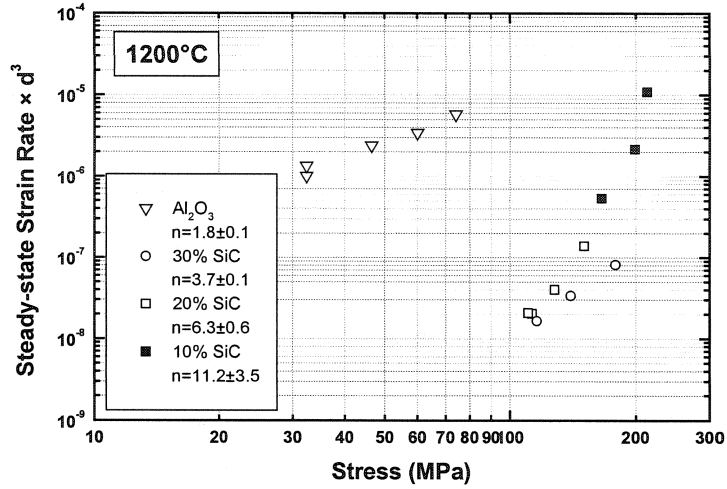


Fig. 5.17 Normalized steady state strain rate vs. stress plots at 1200°C for different SiC content.

### 5.3.4 Determination of activation energy

In the constitutive relationship of the form (see also eqn. 2.2)

$$\dot{\epsilon} = \frac{ADGb}{kT} \left(\frac{b}{d}\right)^p \left(\frac{\sigma}{G}\right)^n \quad (5.1)$$

the diffusion coefficient is given by

$$D = D_o \exp\left(-\frac{Q}{RT}\right) \quad (5.2)$$

where  $D_o$  is a frequency factor and  $Q$  is the enthalpy of the diffusion process which characterizes the creep deformation. True activation energy for the diffusion process is defined as

$$Q = -R \left[ \frac{\partial \ln D}{\partial (1/T)} \right]_{d,\sigma} \quad (5.3)$$

For a given composition if the stress exponent is known (independent of temperature), the true activation energy for creep can be determined from the variation of strain rate at constant stress as follows,

$$Q = -R \left[ \frac{\partial \ln \dot{\epsilon} G^{n-1} T}{\partial (1/T)} \right]_{d,\sigma,n} \quad (5.4)$$



True activation energy is often dependent on the applied stress and temperature.

In the literature pertinent to the present work, the apparent activation energy was often derived, which is defined as,

$$Q_a = -R \left[ \frac{\partial \ln \dot{\epsilon}}{\partial (1/T)} \right]_{d, \sigma} \quad (5.5)$$

Apparent activation energy is indicative of a single mechanism, thus insensitive to the applied stress and temperature.

Figure 5.18 shows an Arrhenius plot of steady-state strain rate vs.  $10^4/T$  for S302, which was used to calculate the apparent activation energy. Three stresses were used for independent derivations, which resulted in similar results. The average value was found to be  $178 \pm 35$  kJ/mole. The true activation energy was also obtained for S302 sample, since its stress exponent did not show a strong dependence on temperature. An average stress exponent of 4.1 was used for strain rate normalization (this presumes a single mechanism) and the value of  $G$  was estimated for each testing temperature from the following relationship:

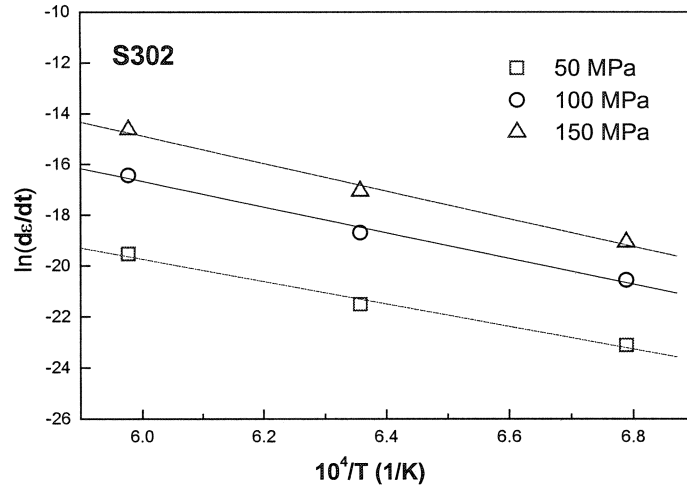
$$G = G_o - \frac{\partial G}{\partial T} T \quad (5.6)$$

where  $G$  is the extrapolated shear modulus of alumina at absolute zero, i.e. 171 GPa, and

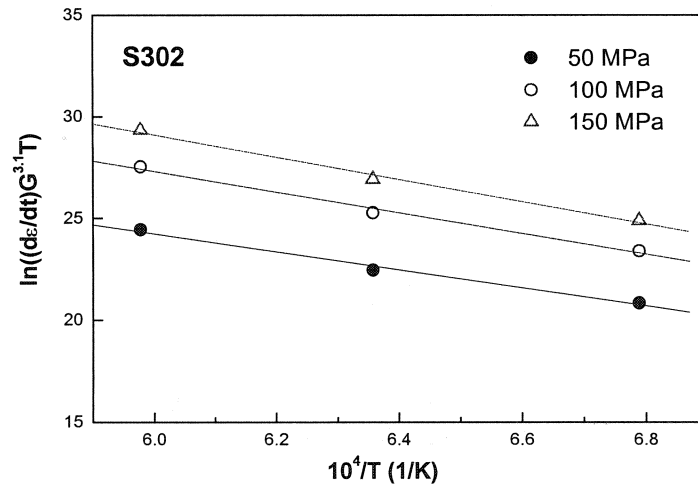
$$\partial G / \partial T = 23.4 \text{ MPaK}^{-1} \text{ (Chung and Simmons 1980).}$$

Figure 5.19 shows an Arrhenius plot of  $\ln(\dot{\epsilon}G^{n-1}T)$  vs.  $10^4/T$  for S302, from which the true activation energy was obtained.

Determination of activation energies for S202 and S102, however, was not feasible because of the strong dependency of stress exponent upon temperature.



**Fig. 5.18** Arrenius plots used to obtain the apparent creep activation energy for S302. Q is 421±38 kJ/mol at 100 MPa.



**Fig. 5.19** Arrenius plots used to obtain the true creep activation energy for S302.

**Table 5.2** The activation energies obtained for the composites. The numbers in parentheses are the associated uncertainties.

|                         | S102      | S202      | S302     |          |          |
|-------------------------|-----------|-----------|----------|----------|----------|
| σ (MPa)                 | 100       | 100       | 50       | 100      | 150      |
| Q <sub>a</sub> (kJ/mol) | 1221 (89) | 774 (109) | 366 (37) | 421 (38) | 453 (40) |
| Q (kJ/mol)              | N/A       | N/A       | 367 (36) | 423 (38) | 455 (40) |

### 5.3.2 Stress relaxation creep tests

The effect of strain recovery was studied in the tensile mode. Fig. 5.20 shows a relaxation creep curve for a S302 sample at 1400°C. As shown, upon load removal, there is rapid initial strain recovery followed by a slow recovery period. The recovered strain is  $\sim 10^{-3}$  during  $10^5$  s, which is about 35% of the total forward creep strain. It is noted that the shape of the backward creep curve seems to imply a continuous recovery process.

Figure 5.21 shows a relaxation curve for a S202 sample at 1400°C. The recovered strain is similar to that found in the S302 sample. However, this sample showed more rapid strain recovery during the initial stage and the recovery process seems to have completed within  $\sim 7 \times 10^4$  s after the load is dropped.

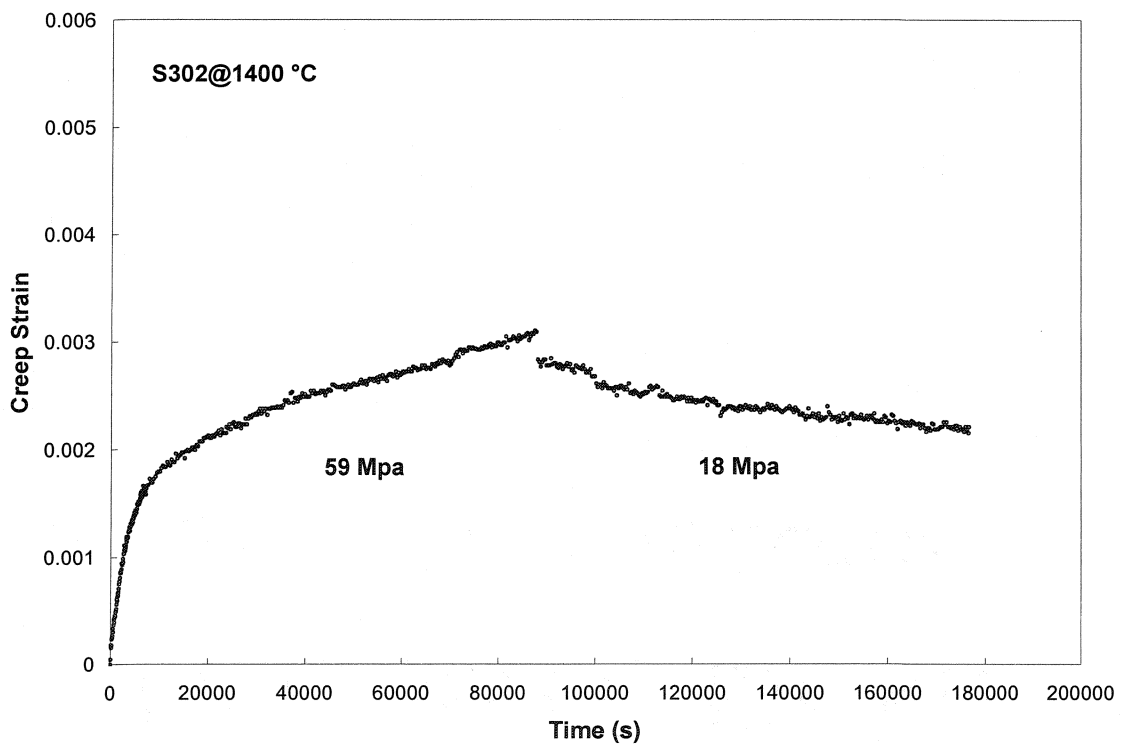
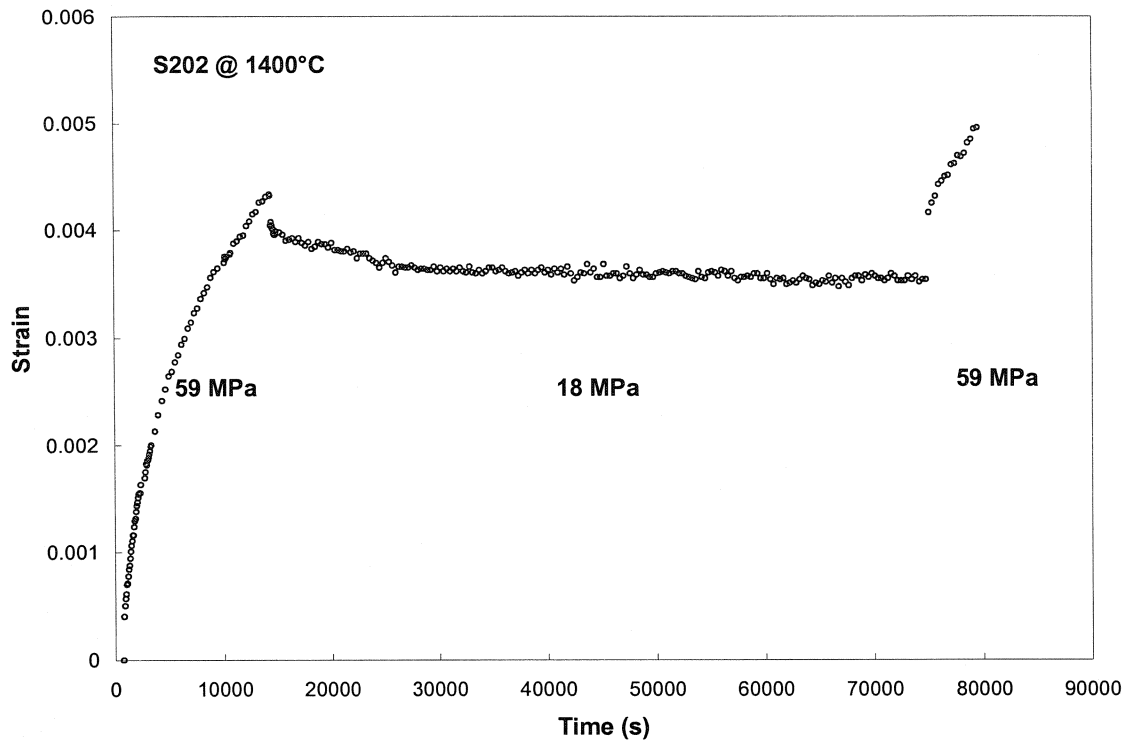


Fig. 5.20 The stress relaxation curve for S302.



**Fig. 5.21** The stress relaxation curve for S202.

## 5.4 Whisker Texture

Figure 5.22 is a schematic of the sample geometry and the coordinate system defined for texture measurement. Figures 5.23-26 show the (111) SiC pole figures measured from the composites by neutron diffraction techniques where the left figure corresponds to the green sample and the right figure the hot pressed sample. As expected, whisker alignment is already developed within green samples and further alignment is achieved after hot pressing.

The common feature in all pole figures is the concentration of multiple of random density (MRD) contours around the periphery of the pole figure, suggesting whisker alignment that decreases the angle between the whisker axes and the plane normal to HPA. Furthermore, the higher density of contours around the **L** direction indicates a preferred whisker orientation along the long dimension of the sample and this effect is more pronounced in the hot pressed samples with high whisker content.

Since there is no preferred orientation around the long axis of the whisker, the orientation of a single whisker within a sample can be described by two independent parameters,  $\chi$  and  $\eta$ , where the former is the angle between N and long axis of whisker and the latter the angle around N. If the normalized intensities are averaged for  $\eta$  for a given  $\chi$ , the cumulative (or integrated) volume fraction of whiskers can be mapped as a function of  $\chi$ , that is the angle between the long axis of whisker and HPA (N). Figure 5.27 presents the calculated volume fraction of whiskers whose axes lie within a given angular range with respect to the HP direction in S302 sample. Figure 5.28-31 shows the cumulative whisker volume fractions of the same set of samples. Results from S202 and S102 samples exhibit very similar patterns as S302. Figure 5.32 presents the calculated whisker distribution density curves for three different samples before and after HP. In spite of different whisker loading, the calculated distribution density curves lie close to each other for green samples and hot pressed samples respectively. Now, the average angle between L (tensile axis) and whisker axes can be found as

$$\bar{\varphi} = \frac{\int_0^{\pi/2} \varphi \psi(\varphi) d\varphi}{\int_0^{\pi/2} \psi(\varphi) d\varphi} \approx \frac{\sum_{i=1}^n \varphi_i \psi(\varphi_i) \Delta\varphi}{\sum_{i=1}^n \psi(\varphi_i) \Delta\varphi} \quad (5.7)$$

where  $\psi(\varphi)$  is the whisker distribution density function with respect to the tensile axis. The calculation shows that  $\bar{\varphi}$  is  $\sim 20^\circ$  for all composites irrespective of SiC content.

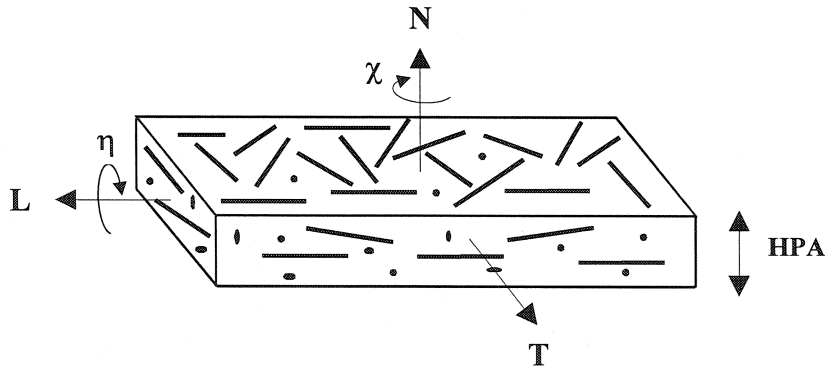
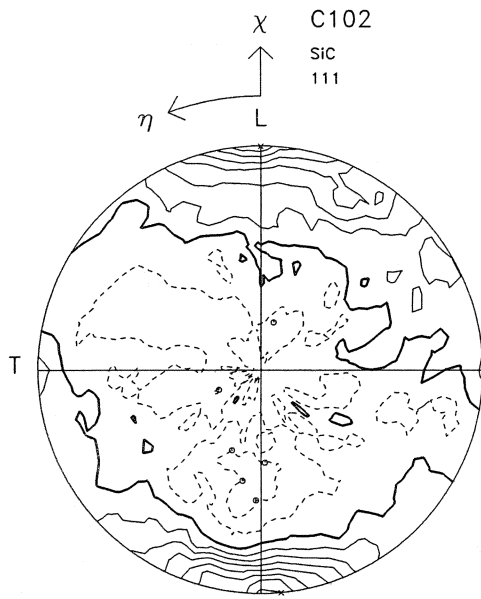
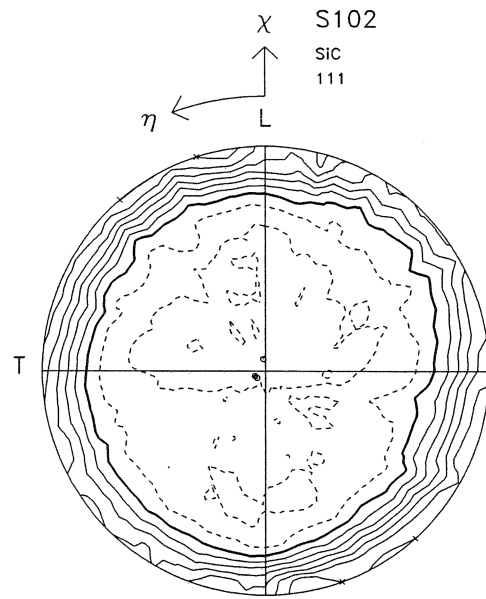


**Fig. 5.22** A schematic of the sample coordinate system for neutron diffraction measurement.



CENTRE IS N  
CONTOUR SEPARATION: 0.20 x RANDOM

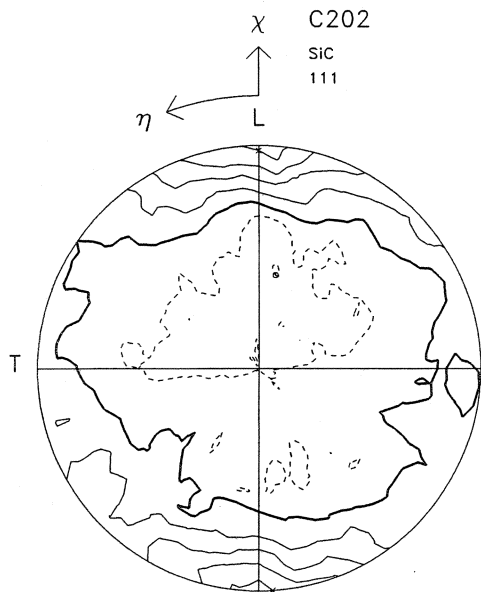
(a)



CENTRE IS N  
CONTOUR SEPARATION: 0.20 x RANDOM

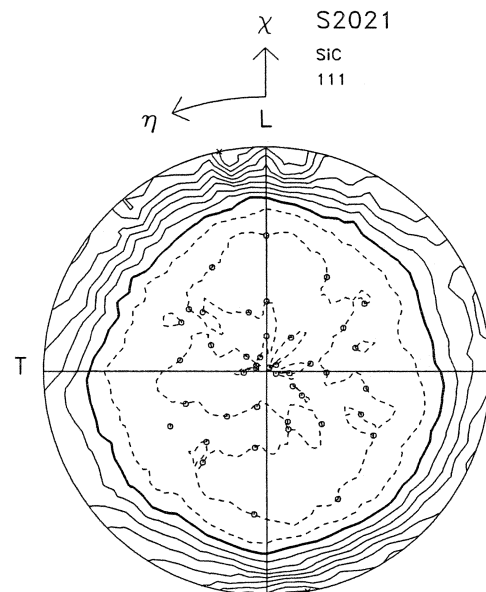
(b)

Fig. 5.23 Pole figures of  $(111)_{SiC}$  from (a) C102 and (b) S102.



CENTRE IS N  
CONTOUR SEPARATION: 0.20 x RANDOM

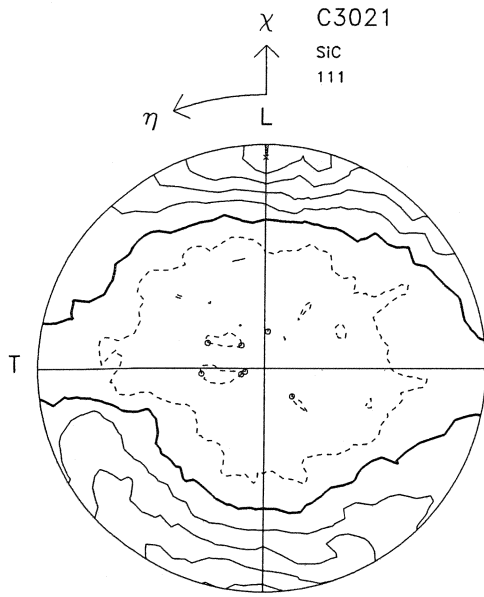
(a)



CENTRE IS N  
CONTOUR SEPARATION: 0.20 x RANDOM

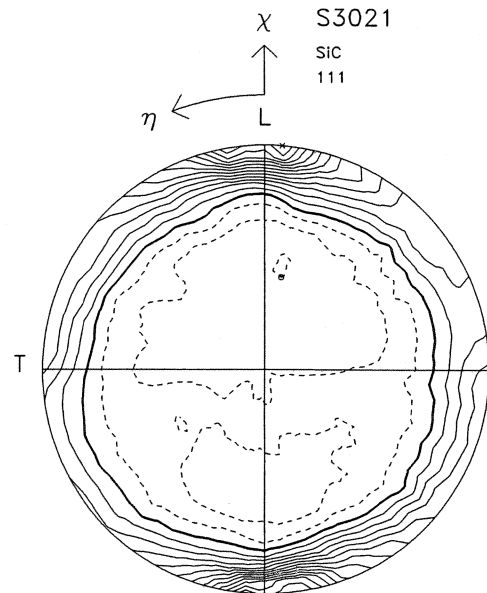
(b)

Fig. 5.24 Pole Figures of  $(111)_{SiC}$  from (a) C202 and (b) S202.



CENTRE IS N  
CONTOUR SEPARATION: 0.20 x RANDOM

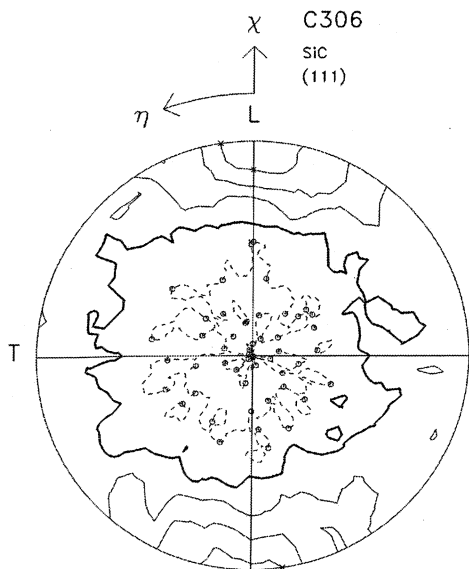
(a)



CENTRE IS N  
CONTOUR SEPARATION: 0.20 x RANDOM

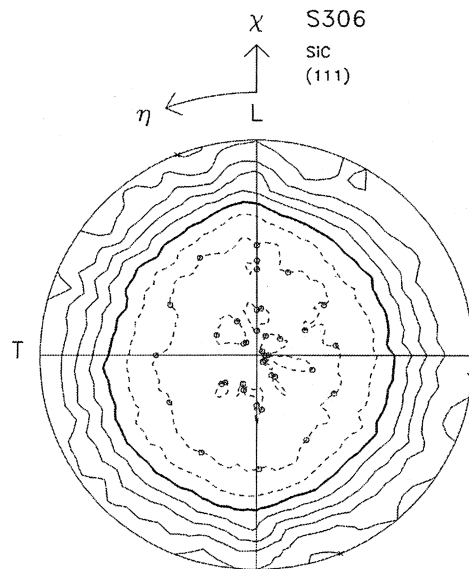
(b)

**Fig. 5.25 Pole Figures of  $(111)_{SiC}$  from (a) C302 and (b) S302.**



CENTRE IS N  
CONTOUR SEPARATION: 0.20 x RANDOM

(a)



CENTRE IS N  
CONTOUR SEPARATION: 0.20 x RANDOM

(b)

**Fig. 5.26 Pole Figures of  $(111)_{SiC}$  from (a) C306 and (b) S306.**

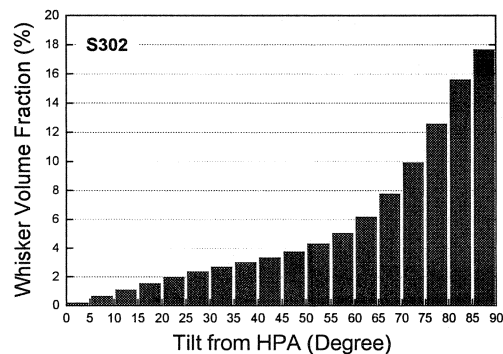
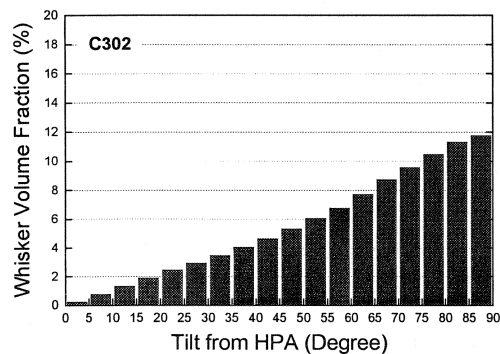
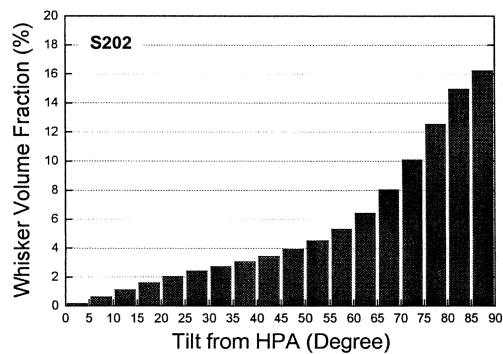
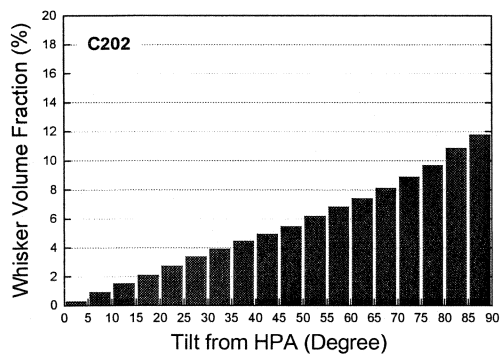
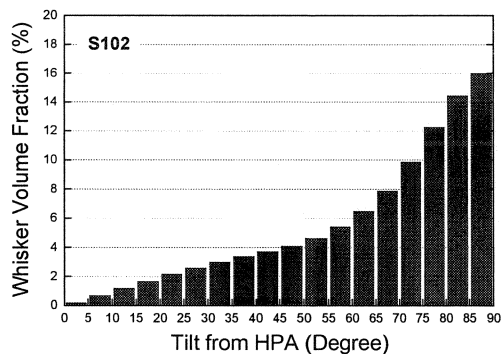
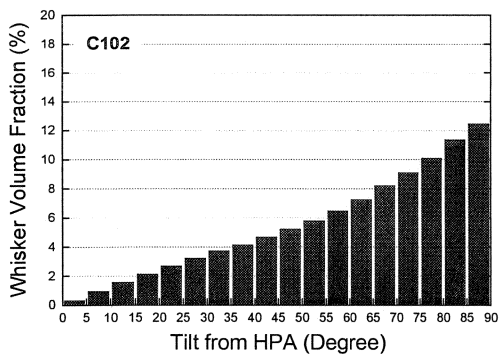


**Fig. 5.27** Angular distribution of whiskers with respect to HPA. The left are for green bodies while those on the right are for fired samples.



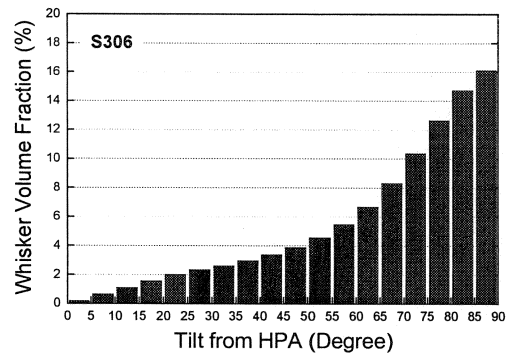
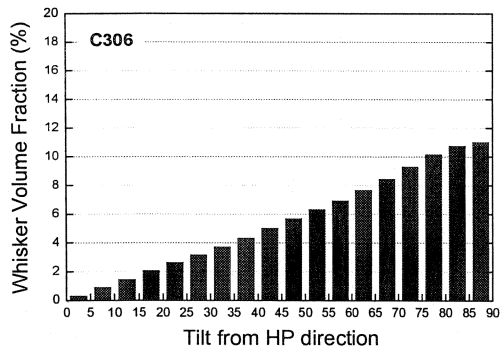


Fig. 5.27 (Continued)

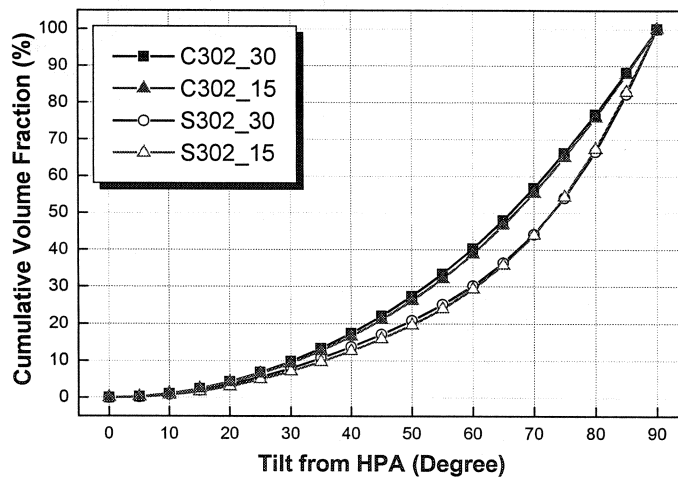


Fig. 5.28 Cumulative angular distribution of whiskers with respect to HPA for C302 and S302. The last two digits in the sample designation represent the solid loading for slip casting.

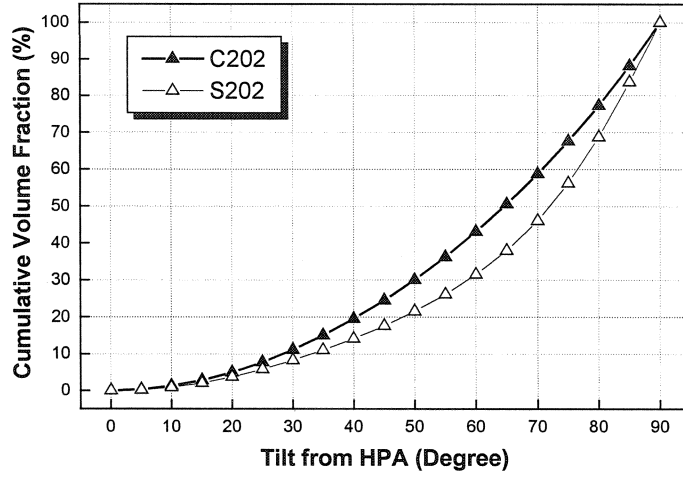


Fig. 5.29 Cumulative angular distribution of whiskers with respect to HPA for C202 and S202.

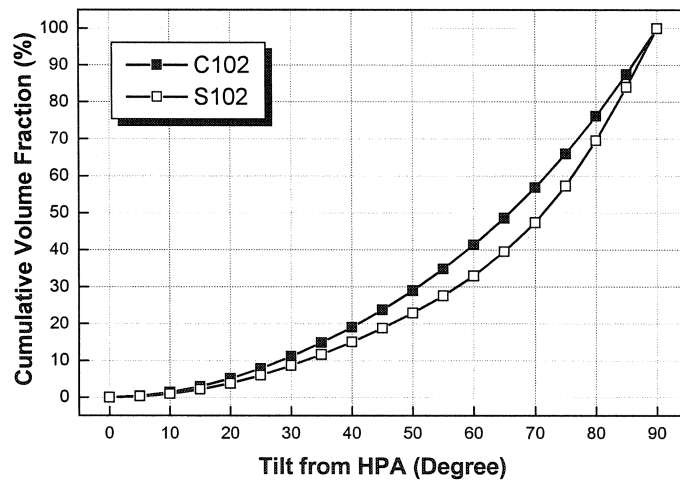


Fig. 5.30 Cumulative angular distribution of whiskers with respect to HPA for C102 and S102.

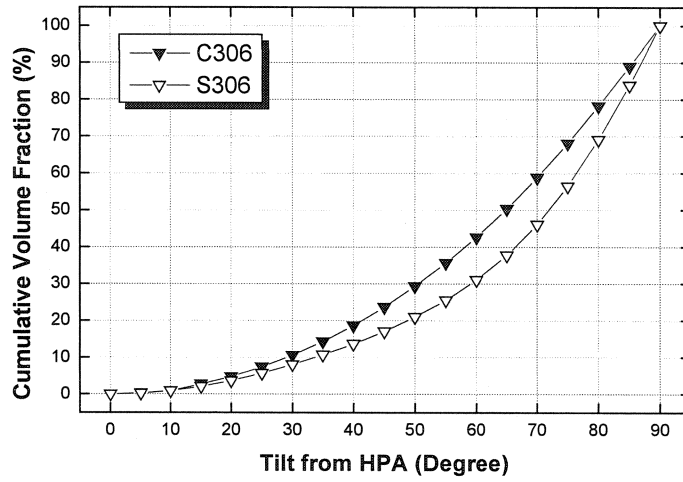


Fig. 5.31 Cumulative angular distribution of whiskers with respect to HPA for C306 and S306.

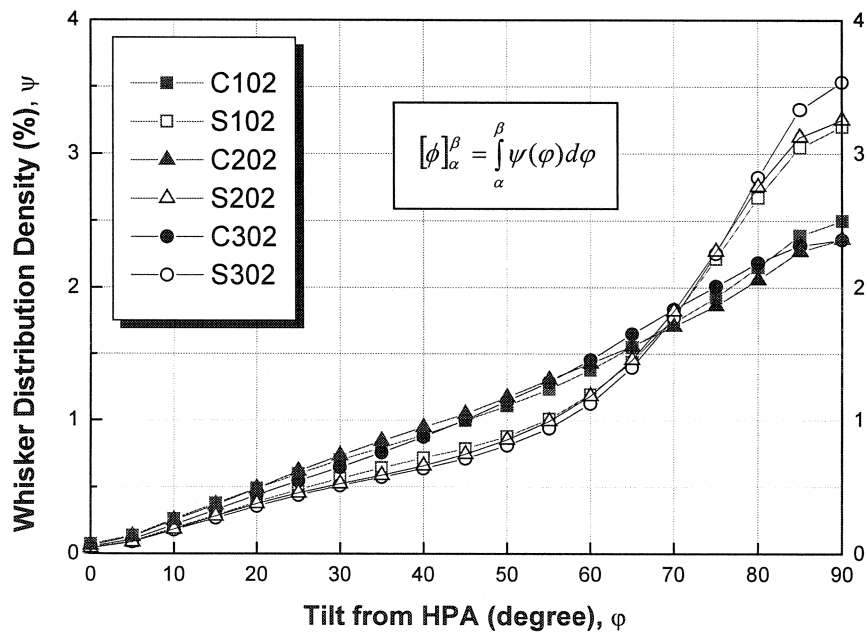


Fig. 5.32 Distribution density of whiskers with respect to HPA.

## 5.5 Residual strains/stresses at room temperature

Table 5.3 summarises the measured lattice strains at room temperature from the (111) and (220) SiC peaks and the corresponding hydrostatic strains and stresses calculated from them. Figure 5.33 plots the residual strains associated with the SiC phase as a function of SiC content from undeformed samples while Fig. 5.34 shows the residual hydrostatic stress within SiC phase as a function of SiC content.

It is seen that the lattice strain of SiC is much greater in the (111) direction than in (220), which is more pronounced with S102. Before creep, the magnitude of the (111) SiC strain increases with decreasing whisker volume fraction but not in a linear manner. The increment is small (<10%) when the whisker content decreases from 30 to 20% but large (>40%) when SiC content decreases from 20 to 10%. On the contrary, the (220) SiC strain decreases with decreasing SiC content but the dependence is much weaker than the (111) SiC strain. The calculated hydrostatic strain for SiC appears to be the same for S302 and S202 whilst that for S102 is ~20% higher. As expected, the same trend is seen for the calculated hydrostatic stresses. It is noted that tensile creep reduced the residual strain significantly especially the axial (111) SiC lattice strain. For instance, creep at 1400°C under 74 MPa for about one day reduced the axial strain by more than 30%. This corresponds to ~20% decrease in hydrostatic strain/stress.

The effect of annealing was also studied, which indicates that annealing itself only slightly reduces the residual strain especially the axial strain. For instance, annealing S302 for 2 days at 1400°C reduced ~6% of the axial strain and ~14% of hoop strain.

**Table 5.3** Lattice strains ( $\times 10^{-3}$ ) measured at room temperature for SiC whiskers. The computed stresses are given in MPa. Numbers in parenthesis are uncertainties. BC: before creep; AN: Annealed; AC: after creep.

| Sample     | Average lattice strains |                      | Hydrostatic strain  | Hydrostatic stress                             |
|------------|-------------------------|----------------------|---|--|
|            | (111) <sub>SiC</sub>    | (220) <sub>SiC</sub> | $\varepsilon_H = \frac{1}{3}(\varepsilon_c + 2\varepsilon_a)$ | $\sigma_H = \frac{1}{3}(\sigma_c + 2\sigma_a)$ |
| 212(302)BC | -3.65 (0.08)            | -1.16 (0.02)         | -1.99 (0.04)  | -1273 (26)                                     |
| 212(302)AN | -3.42 (0.08)            | -1.00 (0.05)         | -1.81 (0.06)  | -1155 (39)                                     |
| 5(302)AC   | -2.51 (0.09)            | -1.12 (0.03)         | -1.58 (0.05)  | -1015 (32)                                     |
| 201(202)BC | -3.95 (0.12)            | -1.00 (0.05)         | -1.98 (0.07)  | -1267 (47)                                     |
| 82(102)BC  | -5.65 (0.15)            | -0.81 (0.14)         | -2.42 (0.14)  | -1543 (92)                                     |

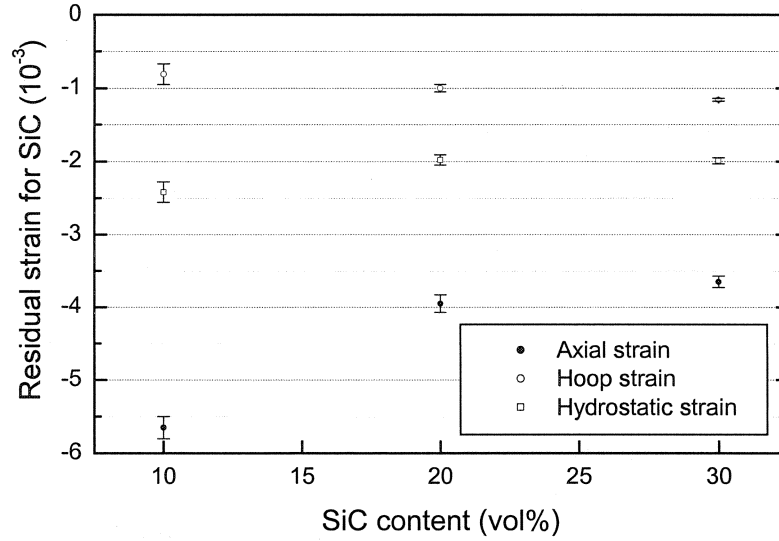


Fig. 5.33 The residual strains measured from SiC phase as a function of SiC content.

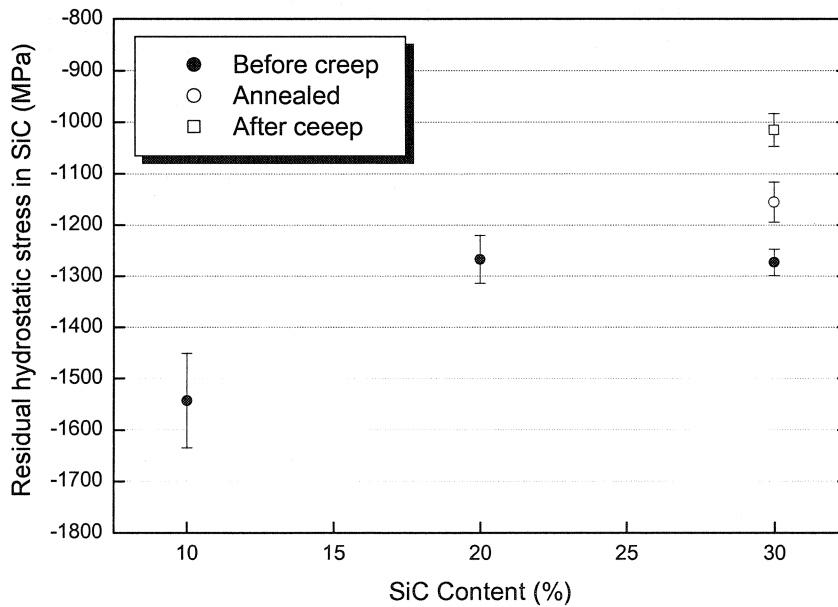


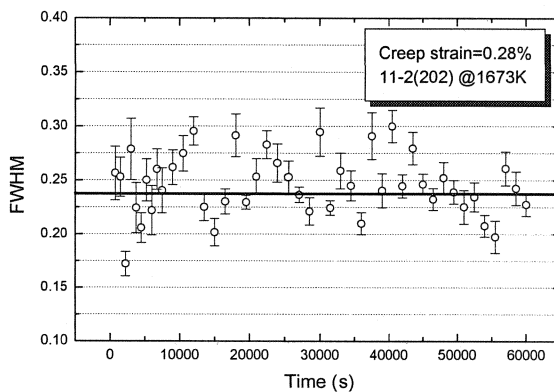
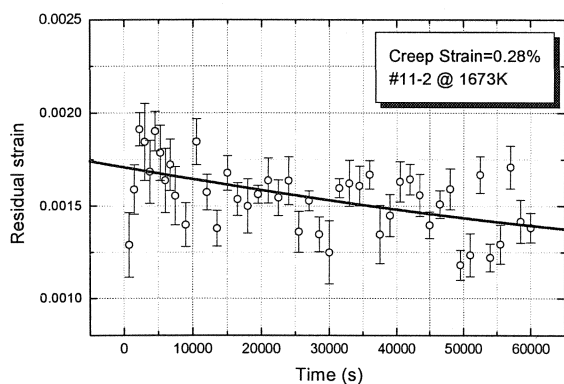
Fig. 5.34 The calculated residual stresses for SiC phase as a function of SiC content from neutron diffraction measurements.

## 5.6 In-situ high temperature neutron diffraction experiments

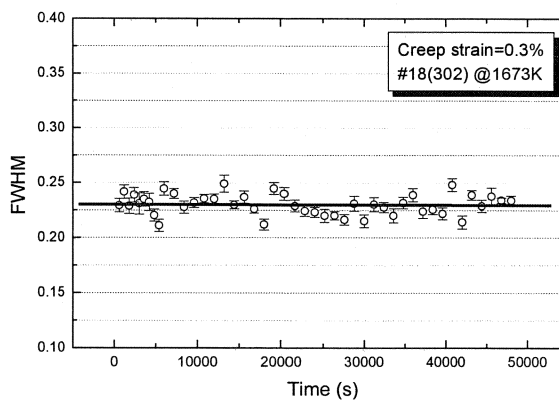
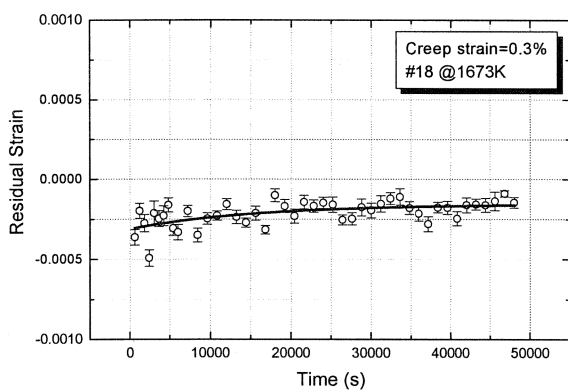
Hypothesizing that whisker bending is primarily responsible for the observed peak broadening and thus, the origin of the anelastic recovery, the variation of (111)<sub>SIC</sub> peak width with time was to be detected using an in-situ annealing test. It should be mentioned that because the beam size was much larger than the sample for the tests done in the C2 diffractometer, accurate measurement of lattice spacing was impractical (Root 2002). Therefore, the variation in lattice spacing (or strain) is to be followed rather than the absolute values. Figure 5.35 shows the calculated lattice strain and full width at half maximum (FWHM) as a function of annealing time for a S202 sample that had been deformed in tension at 1400°C to ~0.28% under 46 MPa. As shown, the FWHM did not seem to change with increasing annealing time. If there is indeed some change, it must be well within the range of experimental error. On the other hand, the residual strain is tensile and appears to decrease with increasing annealing time. However, the associated errors are too large to allow for further quantification.

Figure 5.36 shows the results on a S302 sample that had undergone 0.3% creep strain prior to the in-situ annealing experiment. The associated errors are much lower due to the higher whisker volume fraction in the sample. It is interesting to note that the residual strain is compressive in this case, which may suggest that the higher the whisker volume fraction, the higher the creep strain and annealing temperature required to put whiskers in tension. The residual strain appears to decrease slightly with increasing time but the FWHM remains the same throughout the duration of annealing.

Figure 5.37 shows the results from a S302 sample that had not been deformed before the in-situ annealing experiment. As expected, the residual strain is compressive and there is clearly a rapid initial drop in residual strain followed by a very slow decrease with increasing time. The corresponding FWHM seems to show a slight decrease with increasing time, but it is not conclusive again due to the large experimental errors involved.



**Fig. 5.35** The residual strain and FWHM of (111) SiC in sample #11-2(20% SiC) as a function of annealing time at 1400 °C.



**Fig. 5.36** The residual strain and FWHM of (111) SiC in sample #18(30% SiC) as a function of annealing time at 1400 °C.

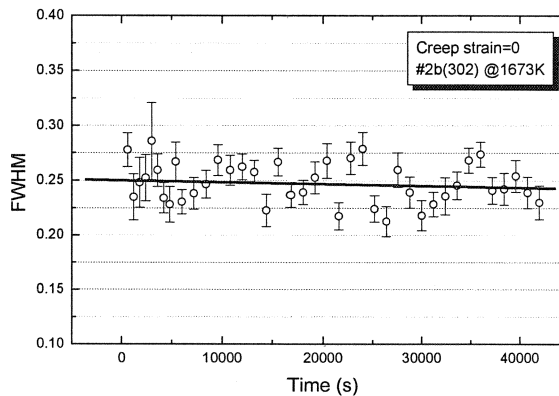
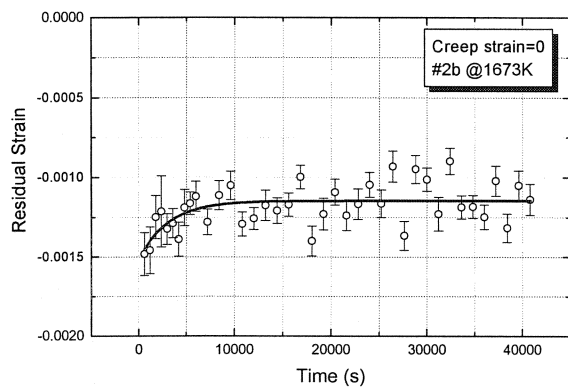


**Fig. 5.37** The residual strain and FWHM of (111) SiC in sample #2b(30% SiC) as a function of annealing time at 1400°C.

## 6. DISCUSSION

### 6.1 Introduction

This chapter is comprised of four main parts with each further divided into several sections with particular issues. The first part analyzes the effect of processing on the composite microstructure with emphasis on whisker distribution. The second part analyzes the creep data of pure alumina and composites with focus on the latter. The third part is devoted to understanding the time-dependent strain recovery behaviour exhibited by the composites. This part analyses results from those experiments designed to verify the preexisting model and introduces a new mechanism. In doing so some models are developed to simulate the experimental results. This chapter uses all pertinent information both from this work and literature, which often involves some data that are not included either in chapter 2 or chapter 5.

### 6.2 Influence of processing on microstructure

#### 6.2.1 Effect of pH

In the initial course of this work, the effect of slurry pH on the whisker distribution was of particular interest with the desire of varying the extent of whisker alignment to a sufficient degree thereby enabling study of the effect of whisker texture on creep behaviour. As shown in Fig. 5.25-26, the (111) pole figure measured from C306 showed little difference as compared to that from C302, indicating comparable average whisker alignment within the two samples. However, the (111) pole figures obtained from the subsequently hot pressed samples showed a remarkable difference in that S302 exhibited a preferred orientation along the long dimension of the sample while S306 did not. This implies different spatial distribution of whiskers within the green bodies, which is evidenced by the striking difference in the microstructure shown in Fig. 6.1 and 6.2. Suggested by the zeta potential measurement, it is likely that when the pH is 6, flocculation between like particles occurred, which led to the formation of whisker clusters throughout the microstructure. Since the whiskers are well interconnected within the clusters, during hot pressing, their motion will be highly restricted within the plane that is perpendicular to HPA.



However, when the pH is 2, whiskers are well dispersed, resulting in uniformly distributed whiskers with loose interparticle contacts in the green body. Consequently, during subsequent hot pressing whiskers will have more freedom to align themselves, thus, the preferred orientation along the long dimension of the sample is further enhanced. In spite of these differences, the quantified whisker volume fraction with respect to HPA showed a remarkable similarity as shown in Fig. 5.26.

These results seem to suggest that pH does not lend itself to a good control over the overall whisker texture level; nonetheless, it is a critical factor that contributes to the interparticle potentials in the suspension that determine the nature of the particle network (Lange et al. 1990). For instance, it has been shown that green bodies of pure alumina powder prepared by pressure filtration from well-dispersed slurries often released the stored strain energy through body flow (dissipation through plastic deformation) upon load removal while those prepared from the flocculated slurries exhibited elastic response. This was ascribed to the difference in particle network configuration (Lange and Miller 1987). It can be envisaged in binary colloidal systems where the inclusions form a network that if the elastic property of this network is sensitive to the pH, different mechanical response of consolidated bodies is expected. Therefore, the importance of pH cannot be emphasized more. As observed in this work, different pH led to a much different spatial distribution of whiskers in the matrix. It might be interesting to study the result of this difference from the mechanical response.

Although tape casting could be employed to achieve further alignment of whiskers, it requires use of additives and binders that will likely remain in the microstructure after firing. The resultant 'unclean' grain boundaries and interfaces will make the comparison with slip cast samples difficult (Hamsu 1997). Therefore, no tape casting was attempted.

### **6.2.2 Effect of SiC content**

Lange and Porter (1991) observed during pressureless sintering of alumina powders with moderate volume fraction of SiC whiskers that the relatively rigid whisker network constrains composite shrinkage but does

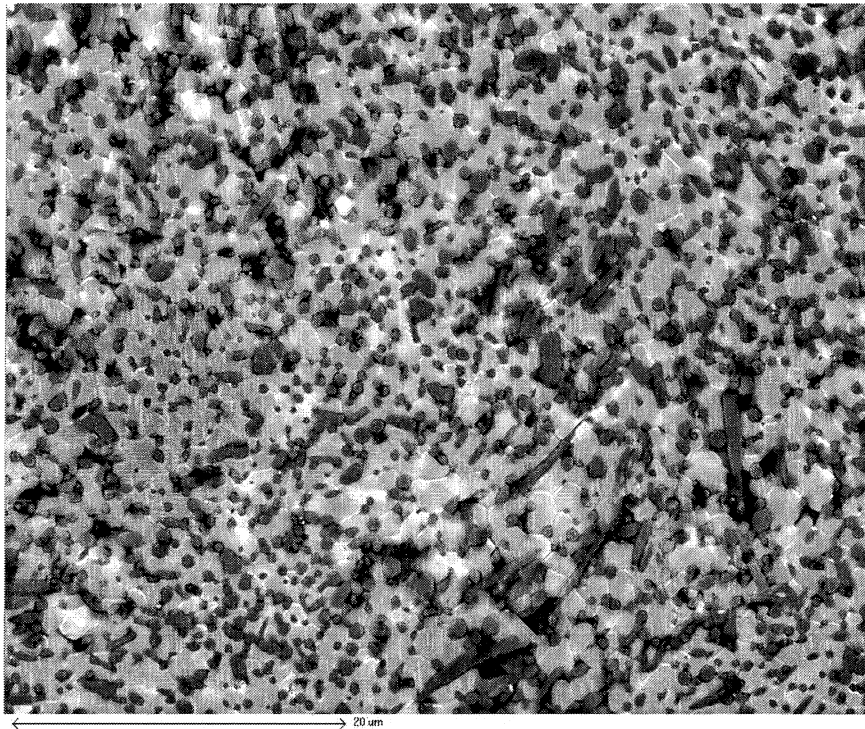


**Fig. 6.1** A SEM micrograph of S302 with the sample surface parallel to the HPA.

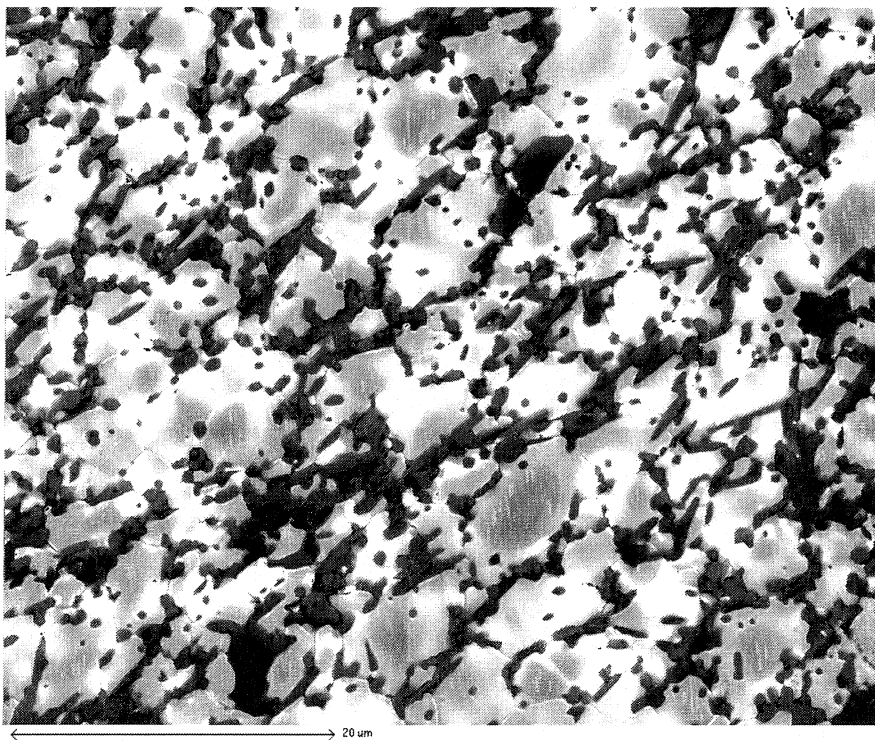


**Fig. 6.2** A SEM micrograph of S306 with the sample surface parallel to the HPA.

not prevent the powder within the network from shrinking onto the network. The much limited grain growth observed in S202 as compared with S102 implies a threshold whisker volume fraction existing between 10 and 20%. Above this critical volume fraction, whiskers form an interconnected network structure that has been known to hinder the densification process dramatically and limit the matrix grain growth during sintering (e.g. Yang and Stevens 1990). The average grain size of the composites studied here is comparable with that reported by Lin and Becher (1990, 1991) who used powders from the same source and adopted similar sintering temperature and pressure conditions.

It is widely recognized that the densification behaviour of a crystalline powder can be dramatically influence by an inert second phase. The densification rate normally decreases with increasing volume fraction of inclusions. De Jonghe et al. (1986) demonstrated that a very small volume fraction (3%) of inclusions would significantly limit the densification of a composite powder compact. Lange et al. (1991) suggested that it is the interaction between inclusions rather than the tensile stress generated in the shrinking matrix by the compressed inclusions that constrains composite densification. The inclusions in the network can be either touching or non-touching. For a non-touching network, a simple argument (Lange et al. 1991) suggested that the matrix powder between closely spaced inclusions will be denser and reach full density before the powder between widely spaced inclusions, resulting in a non-uniform density distribution during shrinkage. This was in accord with microstructural observations (Sudre et al. 1989). When the inclusions touch one another, the network itself cannot be densified, i.e. the composite cannot change its volume as the matrix powder attempts to densify. Therefore, to obtain a fully densified composite, deformation processing is necessary.

### **6.3 Creep of pure alumina**

The creep behaviour of pure alumina observed in the present investigation is consistent with that reported in the literature for fine-grained aluminas. Figure 6.3 compares some of the data available. It is noted that all the stress exponents fall between 1 and 2, which is not dependent on the stress state. This suggests similar creep mechanisms for the wide range of testing conditions involved. Although  $n=1$  is invariably due

to diffusional creep, the significance of  $n=2$  is not firmly established. However, the latter is often ascribed to the interfacial reaction controlled diffusional creep where the grain boundaries are not perfect source and sink for vacancies (Cannon and Langdon 1988).

A short-lived primary creep regime up to the creep strain of  $\sim 1\%$  has been found in pure alumina at  $1200^\circ\text{C}$  in tension, which conforms to the result of Robertson et al. (1991). They suggested that this effect is most probably due to the long-range redistribution of stress due to the grain size distribution. It is believed that the dominant mode of deformation at low strain is GBS accommodated by diffusion and both processes are grain size dependent. Therefore, there must be a transitional period where the load is redistributed from fine-grained regions that deform easier than coarser-grained regions.

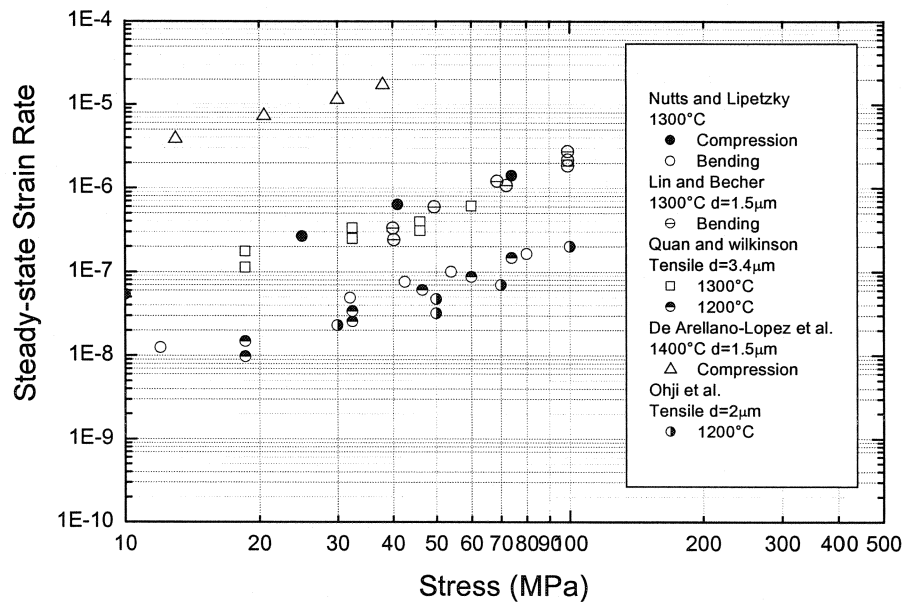


Fig. 6.3 Strain rate vs. stress plot for aluminas.

## 6.4 Creep of composites

### 6.4.1 Effect of SiC content on creep

In the present investigation, the improvement in tensile creep resistance through SiC reinforcements was substantial. The creep rates of composites were consistently 2-3 orders below that of pure alumina especially at low and moderate stress levels, as is shown in Fig. 5.16-17.

It is noted that whisker additions invariably caused significant primary creep, which becomes more extensive with increase in whisker loading as shown in Fig. 5.11. As suggested by Porter (1989) and Wilkinson (1998), this effect is likely due to the long-range stress relaxation processes in the presence of whiskers, which become more prominent when the whiskers form a network. It is believed that whiskers not only mechanically impede GBS but also increase the diffusion path and perhaps further limit the sources and sinks of vacancies. Furthermore, the presence of the whisker network will require more matrix grain shape change and the applied stress is transferred to the whiskers more effectively through the percolative path. Consequently, the resistance to GBS is increased and driving force for diffusional creep reduced, resulting in more extensive primary creep.

In general, the grain size normalized creep rate decreases with increasing whisker volume fraction as shown in Figs 5.15-17. Particularly, a remarkable reduction in strain rate is noted at high temperatures when the whisker loading increases from 20 to 30%, which is in contradiction with many studies where the creep rates were found to be weakly dependent on whisker loading so long as 15% whiskers are present (Lin and Becher, 1991 Xia and Langdon 1995, De Arellano-Lopez, 1993). It is commonly believed that the creep rate is essentially controlled by the whisker network, and that thus, above the critical volume fraction the benefit of having more whiskers will be limited (Wilkinson 1998). The possible influence of stress state on the effectiveness of whisker volume fraction is ruled out since there is one example (Nutt and Lipetzky, 1993) where the effect of an increase in whisker volume fraction remained significant up to 30% in bending configuration. It is likely that the critical volume fraction above which the benefit of increasing whisker volume disappears is dependent on microstructural details especially whisker distribution in the matrix.

Raj and Ashby (1971) derived the creep rate for materials containing inert particles at grain

boundaries where the GBS is controlled by diffusion through either lattice or grain boundaries. Their model predicts the following relation:

$$\dot{\epsilon} \propto \frac{\lambda^2}{r^3} \quad (6.1)$$

Where  $r$  is particle radius and  $\lambda$  is the inter-particle spacing. If the particle volume fraction,  $\phi$  follows

$$\phi \propto \left(\frac{r}{\lambda}\right)^3 \quad (6.2)$$

it can be shown that

$$\dot{\epsilon} \propto \frac{1}{d^3 r \phi^{2/3}} \quad (6.3)$$

where  $d$  is the matrix grain size and the grain boundary diffusion is assumed to be dominant. Figure 6.4 shows plots of strain rate vs. stress where the strain rate is normalized for both the grain size and whisker volume fraction. The normalization seems to bring the strain rates close to a single line at 1200°C but not at 1300°C and 1400°C. This suggests that the strain rate is more sensitive to the change in whisker volume fraction at high temperatures than what Eq. 6.3 predicts.

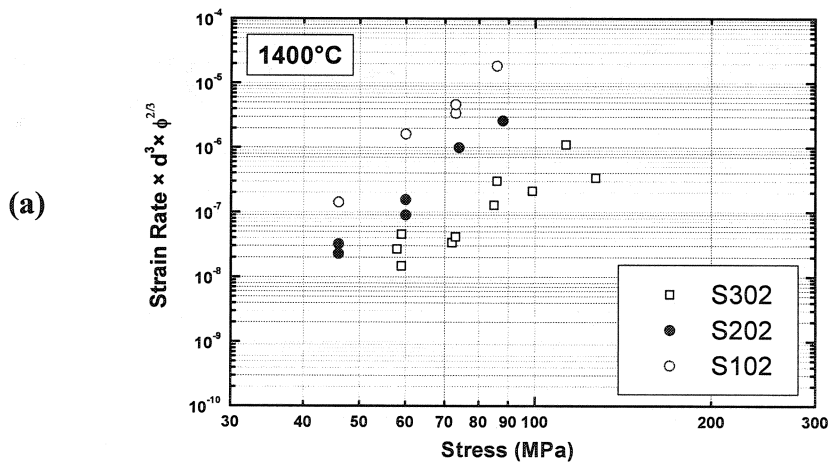
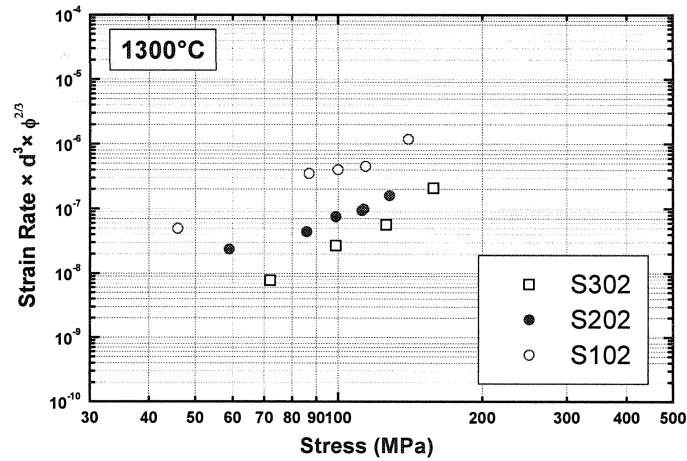


Fig. 6.4 Normalized strain rate vs. stress for composites with different whisker volume fraction at (a) 1400°C (b) 1300°C and (c) 1200°C.

(b)



(c)

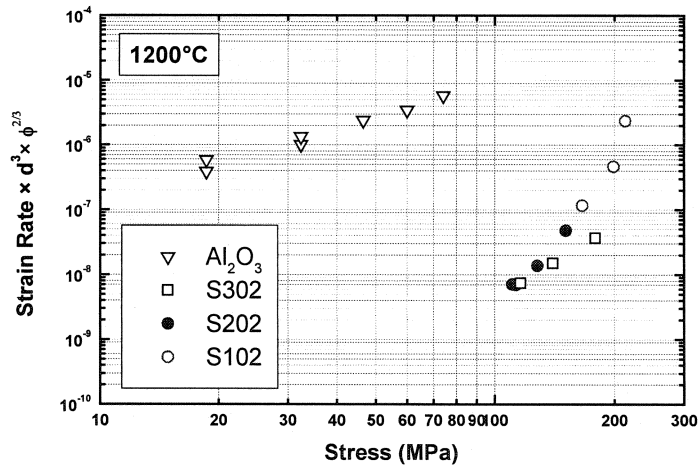


Fig.6.4 continued

## 6.4.2 Creep deformation mechanisms

### Stress exponent

Relatively high stress exponents were found regardless of SiC content in this study, which is more pronounced at 1400°C (see Fig. 5.15). This is in significant contrast with almost all the previous studies where compressive creep tests were employed, demonstrating that the stress exponent of the composites is dependent on the mode of creep testing and is higher in tension.

In general, the stress exponents obtained from tensile creep tests appear to be a much stronger function of temperature than of composition. However, it is noted further that this effect seems to be less significant for high whisker loading, i.e.  $\phi = 30\%$ , than for  $\phi \leq 20\%$ . From Fig. 5.15 and 5.16, it is seen that the stress exponent is much lower at  $1300^\circ\text{C}$  (2-3) than at  $1400^\circ\text{C}$  (7-8) and  $1200^\circ\text{C}$  (6-11). The increase in stress exponent from  $1300^\circ\text{C}$  to  $1400^\circ\text{C}$  is in a good agreement with the results of Lin and Becher (1990) who found an increase in stress exponent from  $\sim 2.3$  to 7-8 with  $\sigma \geq 125\text{MPa}$  for 20% whisker-reinforced alumina composites in bending configuration, see also Fig 2.14(a). It is important to note, however, that at  $1400^\circ\text{C}$  they observed a marked change in stress exponent above a critical stress while no such transition was observed during tensile creep in this study. In ceramic materials the large increase in stress exponent is often due to the onset of extensive cavitation (e.g. Lin and Becher 1990, Carroll and Tressler 1989) and this has been firmly established through TEM observations in SiC whisker reinforced alumina composites (e.g. Lin and Becher 1990, Nutt and Lipetzky 1993, De Arellano-Lopez 1993). Figure 6.5 shows a TEM micrograph taken from a crept S302 sample. Therefore, it is concluded that no shift in stress exponent during tensile creep strongly indicates that cavitation creep is much more active in tension even at low stresses.

Unlike in tension, the stress exponents derived from compressive creep tests showed very weak temperature dependence regardless of SiC content (e.g. De Arellano-Lopez et al. 1990, Nutt and Lipetzky 1990). This suggests that the effect of temperature, as far as the stress exponent is concerned, is more significant when the composite is deformed in tension presumably due to the enhanced contribution from cavity formation and oxidation to the strain generation processes. Apparently, the two mechanisms are highly temperature dependent. However, it is important to realize that the stress exponents of composites are not a monotonic function of temperature, which implies that the creep rate is related to the temperature, applied stress and microstructure in a much more complex manner in tension than in compression and bending.

The low values of stress exponent (2-3) at  $1300^\circ\text{C}$  for  $\phi \leq 20\%$  draw particular attention, which seems to suggest that the strengthening effect of whisker reinforcement is maximized at  $1300^\circ\text{C}$ . Here, the



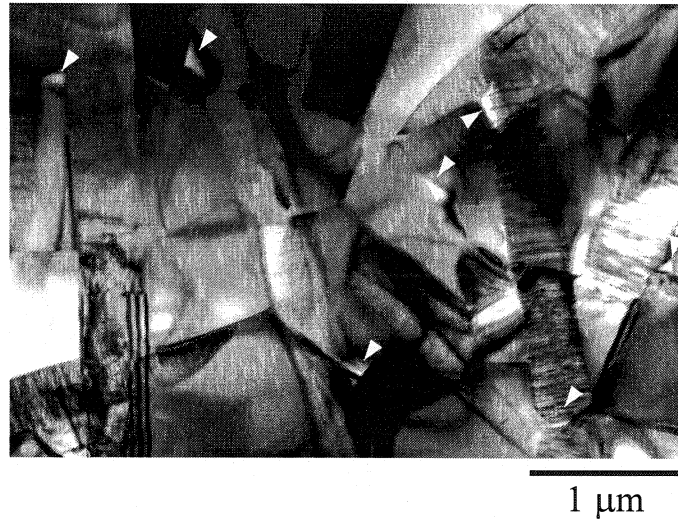


**Fig. 6.5** A TEM micrograph taken from a S302 sample that has been deformed to ~0.4% at 1400°C. Arrows indicate cavities.

low strain rate sensitivity on stress is probably due to a compromise between the main creep mechanisms, namely, cavitation creep, GBS and diffusional creep. Probably, well above or below 1300°C cavitation creep is predominant over the other creep mechanisms. It has been known that cavitation creep is stress-activated process and is associated with high stress exponent (Carroll and Tressler 1989).

For a given temperature, similar stress exponents were found for the composites with different SiC content, which seems to suggest that similar creep mechanisms are operative. Also, as mentioned above, there was no shift in stress exponent within the range of stress covered, implying no major change in creep mechanisms for a given temperature. This is in contrast with the bilinearity observed in the strain rate vs. stress plots obtained from compressive and bending creep tests. In these tests it was found that below a critical stress the damage accumulation is less extensive and can be accommodated (e.g. Lipetzky et al. 1988, Porter 1989, Lin and Becher 1990 and Nutt and Lipetzky 1991, 1993).

It should be mentioned that due to the limited number and erratic nature of experimental data points at 1200°C, it is difficult to be used for a reasonable comparison. Nonetheless, at 1200°C all the composites studied showed much superior creep resistance than pure alumina.

## Activation energy

In the pertinent literature, the activation energy often refers to the apparent one. However, true activation energies were obtained in some studies (e.g. Xia and Langdon 1995). Therefore, it is necessary to understand the difference between these two energies. By differentiating Eq. 2.2, it can be shown for a constant stress exponent that the true activation energy,  $Q$  and the apparent activation energy,  $Q_a$  are related by the following expression (Mohamed and Langdon 1976)

$$Q = Q_a + RT \left\{ 1 + \frac{(n-1)T}{G} \left[ \frac{\partial G}{\partial T} \right]_{d,\sigma} \right\} = Q_a + f(T, n) \quad (6.4)$$

For Newtonian flow, i.e.  $n=1$ , this relation reduces simply to

$$Q = Q_a + RT \quad (6.5)$$

When the thermal energy term,  $RT$  is much less than the activation energy, one can write

$$Q \approx Q_a$$

However, since  $(\partial G / \partial T)_{d,\sigma}$  is negative, the situation is uncertain for  $n > 1$ . Table 6.1 shows the computed  $f(T, n)$  for a range of  $n$  and  $T$ , which indicates that  $f(T, n)$  is more sensitive to the former than the latter. However, the overall difference between  $Q$  and  $Q_a$  is very small, and thus, can be ignored.

**Table 6.1** Computed difference between  $Q$  and  $Q_a$ , i.e.  $f(T, n)$  in Eq. 6.4. The unit is kJ/mol.

| T (K) | n=1   | n=2  | n=3  | n=4  | n=5   | n=6   | n=7    |
|-------|-------|------|------|------|-------|-------|--------|
| 1473  | 12.25 | 9.16 | 6.06 | 2.97 | -0.12 | -3.21 | -6.30  |
| 1573  | 13.08 | 9.49 | 5.90 | 2.32 | -1.27 | -4.86 | -8.45  |
| 1673  | 13.91 | 9.78 | 5.65 | 1.52 | -2.61 | -6.74 | -10.87 |

In order to identify the controlling diffusion mechanism during creep of ceramics, it is common practice to compare the activation energy obtained from the creep tests with the activation energies found for the diffusion of cations and anions through the lattice or grain boundary. Table 6.2 provides the activation energies for diffusion in polycrystalline alumina. As shown, diffusion of oxygen ions is much easier along grain boundaries while that of Al ions is slightly enhanced. This led to the notion that in fine-

grained alumina the diffusional creep is controlled by the grain boundary diffusion of aluminum ions (e.g. Coble and Guerard 1963).

For S302 the apparent activation energy was not strongly dependent on the applied stress (see Table 5.2), and it falls closely in the range of those reported for diffusion of cation and anion in alumina. This probably indicates that grain boundary diffusion is dominant in this sample and the diffusional kinetics are weakly dependent on the applied stress.

Figure 6.6 shows the Arrhenius plots for S202 and S102 samples. Obviously, the apparent activation energy is strongly dependent on both stress and temperature. However, the activation energy is least sensitive to the temperature roughly around  $\sigma=100$  MPa, and perhaps is least sensitive to the stress around 1300°C. An activation energy of  $774\pm 109$  kJ/mol is found for S202 at  $\sigma=100$  MPa, which is similar to that for lattice diffusion of oxygen ion. This may indicate that lattice diffusion of oxygen ions is rate controlling. However, a much higher activation energy ( $1221\pm 89$  kJ/mol) is found for S102 at the same stress level, which cannot be correlated to the diffusional kinetics of either species of the matrix. Therefore, some other mechanisms are responsible for the high activation energy, which most probably involve damage accumulation processes.

The curvature in the Arrhenius plot indicates more than one creep rate-controlling process existing, with different activation energies, with the curvature in the temperature range where the activity of the mechanisms is comparable (Poirier 1985). Here, the transitions in creep mechanism seem to occur around 1300°C for composites with 20 and 30% of SiC whiskers.

**Table 6.2** Activation energies (in kJ/mol) for diffusion in  $\text{Al}_2\text{O}_3$ . (Frost and Ashby 1982)

| Ion               | Lattice Diffusion |                 | Boundary Diffusion |                 |
|-------------------|-------------------|-----------------|--------------------|-----------------|
|                   | $\text{Al}^{3+}$  | $\text{O}^{2-}$ | $\text{Al}^{3+}$   | $\text{O}^{2-}$ |
| Activation energy | 477               | 636             | 419                | 380             |

As shown in Fig. 6.6, it appears that at high temperature the activation energy increased with increasing stress. This may be due to the enhanced cavity formation as suggested by the work of Carroll and Tressler (1989) who found about a two-fold increase in the activation energy when the applied stress is

above the threshold stress for creep damage. At low temperature, however, the activation energy decreased with increasing stress and this effect is more prominent in S102 than in S202. This can be explained at least phenomenologically by considering a sharp increase in stress exponent from  $\sim 3$  at  $1300^{\circ}\text{C}$  to  $6-11$  at  $1200^{\circ}\text{C}$ . However, the physical reason behind is not clear.

It is also noted that in the high stress region the activation energy shifts from a low to high value with increase in temperature, which implies that the creep rate controlling processes are non-sequential (or parallel-concurrent) and the strain rates are additive. However, at a low stress level, the strain generation processes appear to be sequential (mutually accommodating processes) and the slowest process dominates the creep rate, not necessarily the creep strain (Poirier 1985). Figure 6.6(c) provides a curved surface  $\ln \dot{\epsilon} = f(1/T, \ln \sigma)$  that is schematically constructed from the experimental data. These results may indicate the importance of GBS and grain boundary diffusion with increasing whisker volume fraction as far as the effect of matrix grain size is concerned. However, as shown in Fig. 6.7(b), the activation energies determined from bending or compressive creep tests do not show any dependency on whisker volume fraction. This suggests that when the composite is tested in compression or bending the cavitation creep is not as much dominant component of the total strain as in tension, and thus is not sensitive to the volume of SiC whiskers.

In summary, the activation energies obtained from the creep tests provide useful information. However, it is important to note that many ceramic materials show enhanced rates whichever ion has the lower mobility and the effective diffusivity found from the creep tests was not always close to the that for slowly moving specie along the fastest path (Burton 1977). Therefore, the positive inference of creep rate controlling mechanisms requires examination of some other parameters as well and more importantly, the microstructure.

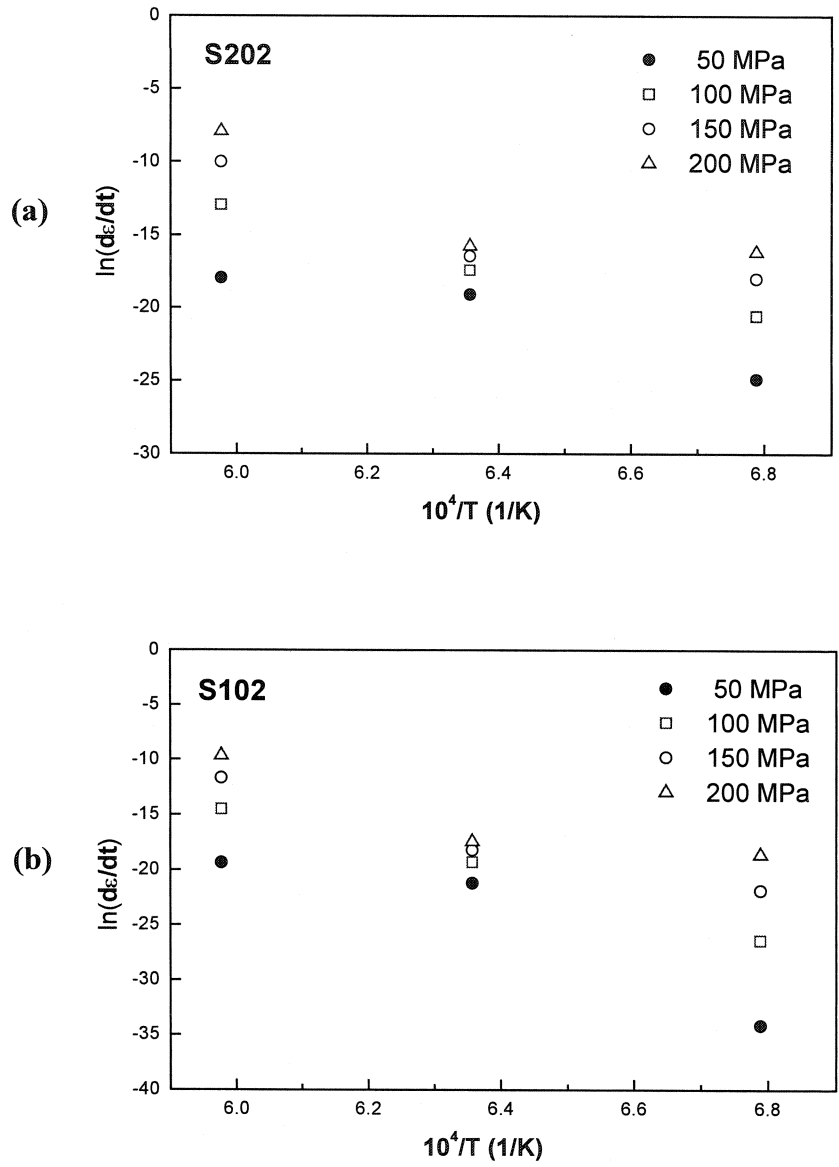


**Fig. 6.6** Plot of logarithmic strain rates vs.  $10^4/T$  for (a) S202 and (b) S102. (c) Schematic representation of the mechanical state by a surface  $\ln \dot{\epsilon} = f(1/T, \ln \sigma)$ .

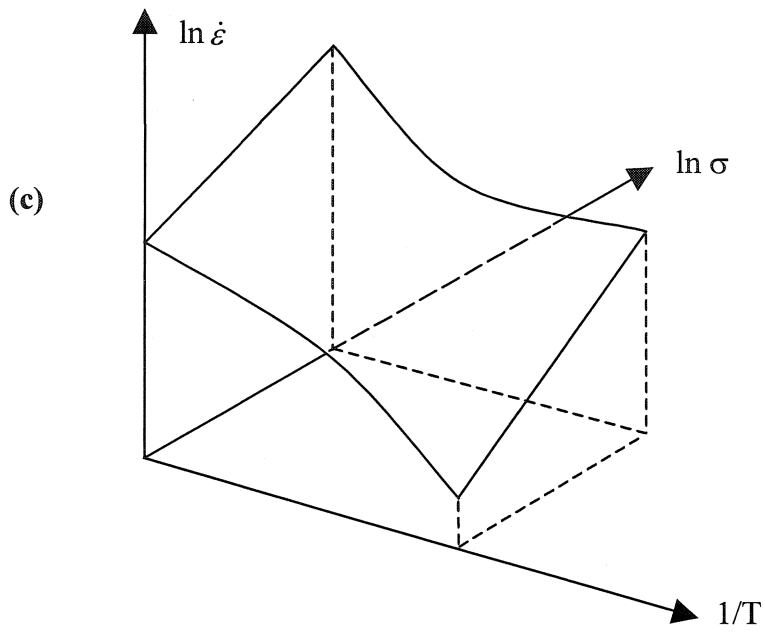
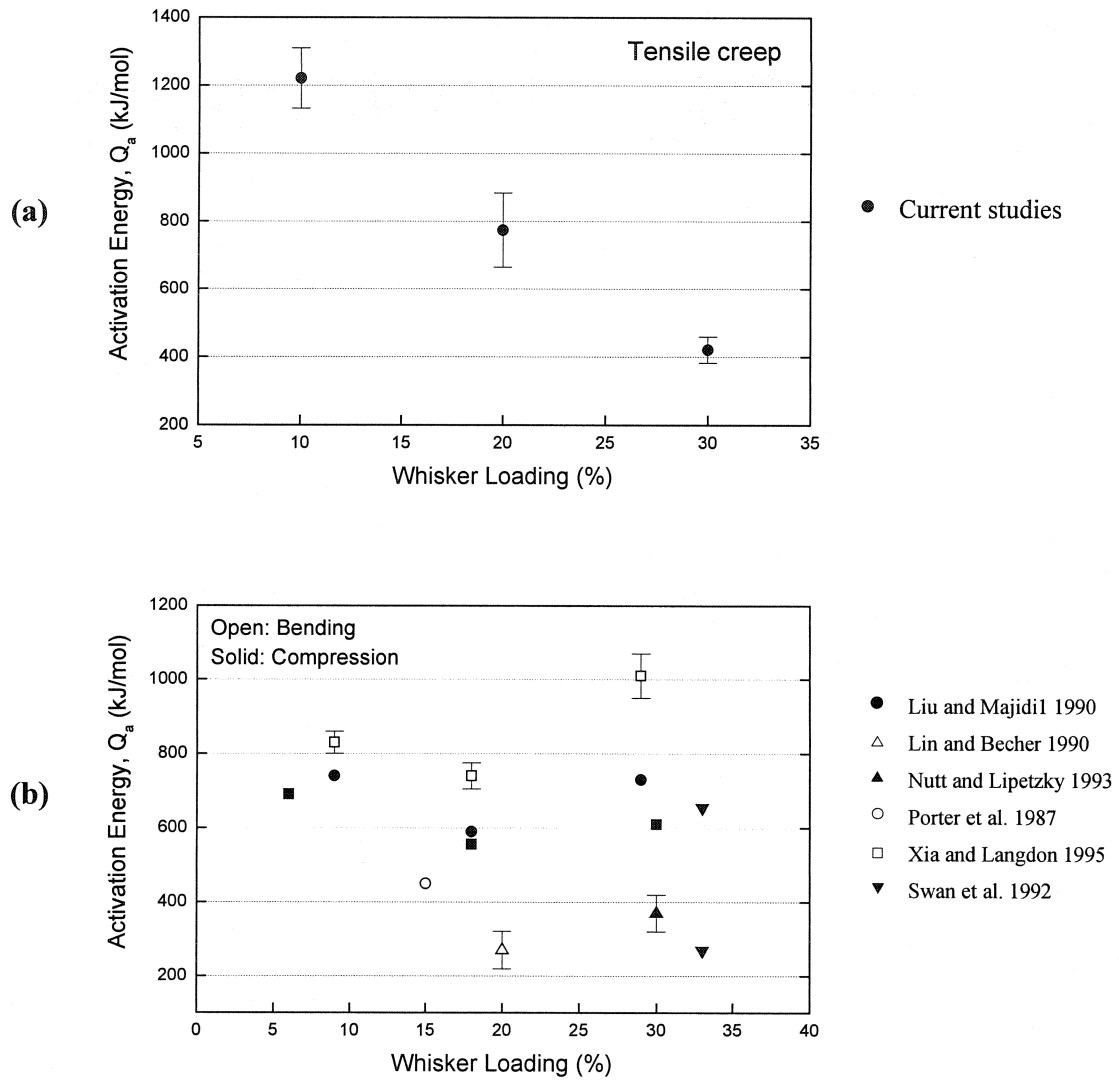


Fig. 6.6 (Continued)



**Fig. 6.7** Plot of apparent activation energy vs. whisker loading from (a) tensile (current studies) and (b) Bending and compressive creep tests in the literature.

### 6.4.3 Residual stresses

It has long been known that residual stresses play an important role in understanding the structure/property relationship in many materials especially multi-phase systems. In the present investigation, the development and evolution of residual stresses were followed. In doing so the effect of creep on redistribution of residual stresses was the main interest, which was expected to shed some light on the load transfer processes during creep.

The measured residual stresses and strains at room temperature (see Table 5.3) from this work are in a good agreement with the previous reports (e.g. Predecki et al. 1991, see also Table 2.3-2.4 for comparison) on similar composites. As shown in Table 5.3, the (111) SiC lattice strain is reduced substantially parallel to the tensile direction after creep. This can be understood by considering the effect of annealing and applied stress.

When a composite material is held at elevated temperatures without applied stress, internal stresses will be relaxed through matrix creep. The extent of relaxation will depend on the annealing temperature and holding time. If an external load is applied during annealing, it will build up elastic stresses within the matrix and reinforcement phases upon loading. From force equilibrium one can write

$$\sigma = \phi \bar{\sigma}_i + (1 - \phi) \bar{\sigma}_m \quad (6.6)$$

where  $\sigma$  is the applied stress,  $\phi$  is the volume fraction of inclusions,  $\bar{\sigma}_i$  is the average stress within inclusions and  $\bar{\sigma}_m$  the average stress in the matrix. However, creep of either phase will reduce the magnitude of these stresses and a new force equilibrium is established. Assuming that the stress in the matrix diminishes, the stress within the reinforcement phase will approach

$$\sigma = \phi \bar{\sigma}_i \quad (6.7)$$

When the material is unloaded, the stress within the inclusions will decrease until another force equilibrium is reached between matrix and inclusions. If the material is cooled before the matrix is fully relaxed some effect of the applied stress can be retained at room temperature. If the material is cooled under load, the effect of the applied stress can be maximized.



It is anticipated that the effect of residual stress upon creep is only appreciable well below the stress-free temperature and becomes more significant with decreasing temperature. Figure 6.8 shows the measured lattice spacing of (111) SiC planes as a function of temperature. Apparently, the residual lattice strain is compressive and dependent on temperature, which increases more or less linearly with decreasing temperature. Table 6.2 summarizes the average residual stresses/strains estimated from the measured lattice spacing of the (111) SiC planes. It is noted that before creep deformation the residual strain remained appreciable even at 1400°C, however, after creep it is greatly reduced. Although annealing alone can relax the residual lattice strains, it is likely that the applied tensile stress is the key to having significant relaxation of (111) SiC strain. This may suggest that a significant load transfer occurred during creep deformation. Figure 6.9 schematically illustrates evolution of the residual stress within the matrix and fibers at various condition of temperature and applied stress.

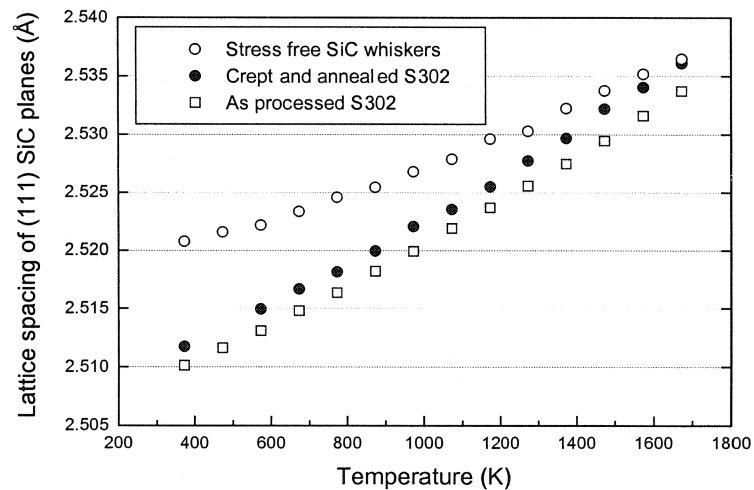


**Fig. 6.8** Plot of lattice spacing of (111) SiC planes vs. temperature. The applied tensile stress reduced the lattice strain of (111) SiC.

**Table 6.3** Average microstrains and microstresses estimated from the measured (111) SiC lattice spacing vs. temperature. The composite contains 30% whiskers. Numbers in parentheses are uncertainties.

| MICROSTRAINS        |                        |                        |                        |                        |                        |
|---------------------|------------------------|------------------------|------------------------|------------------------|------------------------|
|                     | 1000°C                 | 1100°C                 | 1200°C                 | 1300°C                 | 1400°C                 |
| Deformed            | $-1.01 \times 10^{-3}$ | $-10^{-3}$             | $-6.14 \times 10^{-4}$ | $-4.48 \times 10^{-4}$ | $-1.45 \times 10^{-4}$ |
| Undeformed          | $-1.88 \times 10^{-3}$ | $-1.87 \times 10^{-3}$ | $-1.7 \times 10^{-3}$  | $-1.41 \times 10^{-3}$ | $-1.09 \times 10^{-3}$ |
| MICROSTRESSES (MPa) |                        |                        |                        |                        |                        |
| Deformed            | -555 (31)              | -553 (27)              | -336 (19)              | -244 (19)              | -79 (18)               |
| Undeformed          | -1031 (15)             | -1029 (19)             | -927 (16)              | -768 (18)              | -589 (12)              |

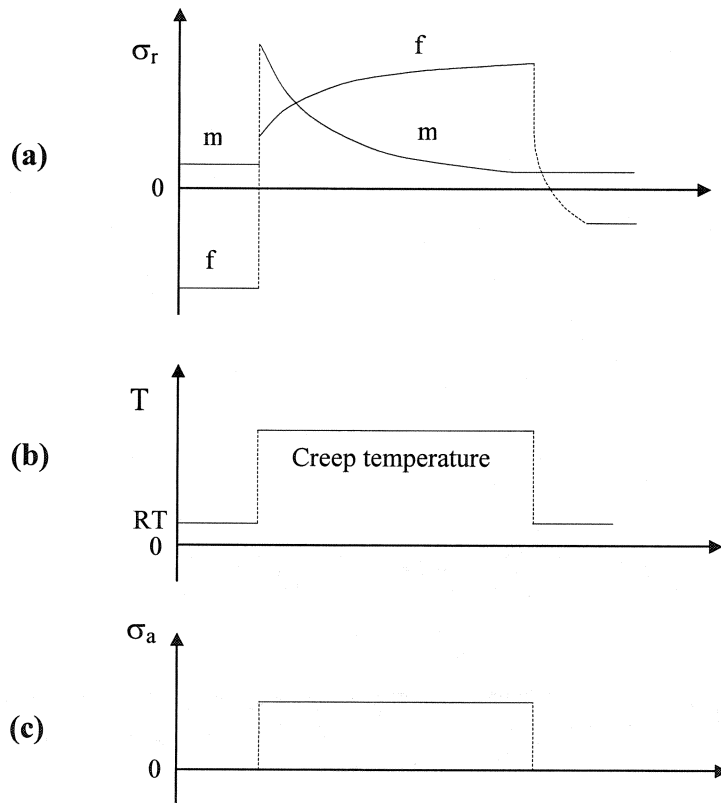


**Fig. 6.9** Schematic illustration of evolution of (a) residual stress within matrix (m) and fibers (f) with varying (b) temperature and (c) applied stress.

In Fig. 5.35, it is interesting to note that (111) SiC lattice strains measured from the deformed S202 samples were tensile while those from the deformed S302 samples were compressive. It has been shown (Majumdar and Kupperman, 1989 and Todd et al. 1997) that the residual stresses within

reinforcements at room temperature decrease with increasing volume fraction. If this is true up to the stress-free temperature, i.e. around 1400°C, the residual stresses in S202 should be more compressive than S302 without pre-deformation. Therefore, it is again the applied stress that is responsible for putting the whiskers in tension along the loading direction.

When the load is removed during creep, a relaxation process commences, the driving force being the elastic energy stored in the whisker network. Presumably the network recovers more strain than the surrounding matrix, thus, a new residual stress field is generated, which is superimposed on the residual stress field originated from the thermal elastic mismatch that is present without pre-deformation. At present, the differential strain recovery between the matrix and reinforcements would result in tensile strain within SiC whiskers, which counterbalances the compressive residual strain formed without deformation otherwise. If the former is larger than the latter, a net tensile state is obtained.

#### **6.4.4 Effect of grain size and whisker aspect ratio**

The low creep rate of S102 is most likely due to its large grain size. The present study seems to suggest the importance of grain size on creep rate in the absence of whisker network at relatively low temperatures. Figure 6.10 shows the plot of strain rate vs. stress for different temperatures, where the strain rates are not normalized for matrix grain size. As shown, S102 exhibited much lower strain rates than S302 at 1200°C and slightly lower at 1300°C. However, an inverse grain size effect is seen at 1400°C. These results are in a reasonably good agreement with Lin and Becher (1995 and 1996) who reported that the creep resistance of 10% SiC whisker-reinforced alumina composites improved with matrix grain size at 1200°C but not at 1300°C. They ascribed this to a reduced GBS contribution to the creep strain.

The effect of whisker aspect ratio upon creep response needs to be understood with constant whisker content. If the whisker content is well below the percolation for network formation, the reduction in aspect ratio will increase the number density of the whiskers, lending more whiskers available for impeding the grain boundary sliding. Indeed, Lin and Becher (1995) showed that a reduction in whisker

aspect ratio by increasing the ball-milling time led to about one order decrease in creep rate in 10% SiC whisker reinforced alumina composite at 1200 and 1300°C.

When the volume of fibers are just enough for network formation, the reduction in fiber aspect ratio could eliminate the network structure because the percolative threshold is raised. This might bring about a qualitative change in creep mechanism.

If the fiber content is well above the percolation level and the reduction of fiber aspect ratio is not large enough to prevent the formation of a whisker network, the change in creep response, if any, will be dictated by the change in the properties of the fiber network. It is anticipated that a network formed by shorter fibers, having more fibers on the percolative path and higher stiffness, is capable of bearing more load. Consequently, the matrix is subject to lower load, resulting in a decrease in creep rate.

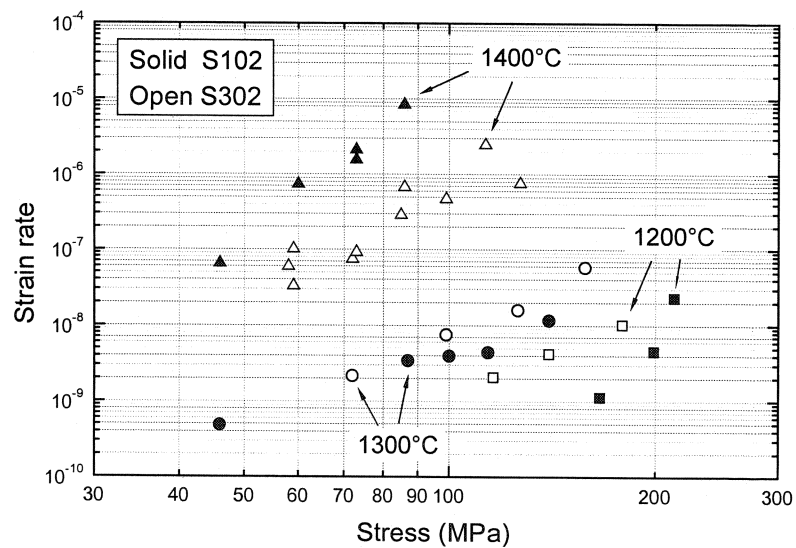


Fig. 6.10 Plot of strain rate vs. stress for S302 ( $d \sim 2\mu\text{m}$ ) and S102 ( $d \sim 8\mu\text{m}$ ).

## 6.5 Anelastic recovery

### 6.5.1 Basic considerations and observations

As stated previously, incorporation of more than about 15% SiC whiskers into alumina matrices gave rise to significant anelastic strain recovery upon load removal, whilst no such behaviour was found in pure polycrystalline alumina or with dilute amount of whiskers (e.g. Porter 1989, Gu et al. 1994). It has also been reported that the magnitude of the recovered strain is not strongly dependent on the accumulated strain at which the sample is unloaded (Gu et al. 1994, 1995). The presence of a three-dimensional whisker network is commonly believed to be responsible for this behaviour and the percolation threshold for a strong network was assessed to be around 12% with the whisker aspect ratio of 20 (Wilkinson 1998). The hypothesis is that, upon loading, the whiskers in the percolative paths undergo bending deformation, storing elastic strain energy. This energy is to be released when the load is removed, leading to a high degree of strain recovery (Porter 1989, Gu et al. 1994 and 1995, Wilkinson 1998). According to this model, high whisker aspect ratio should be associated with more strain recovery. However, the study by Gu et al. (1994) showed exactly the opposite, i.e. the composite reinforced by shorter whiskers recovered more strain as shown in Fig. 2.20. Moreover, it was found in the same study that an alumina matrix reinforced by spherical SiC particles also exhibited comparable strain recovery. This raises the question as to whether a fibrous inclusion geometry is key to having such anelastic strain recovery.

Figure 6.11 shows a stress relaxation curve for a S202 sample during tensile creep. Unlike in Fig. 5.21, here, the strain recovery process is much slower but the recovered strain is significant. It is noted that although the applied stress before unloading was different for the two relaxation curves, the recovered strain was similar, i.e.  $\sim 0.001$ . These results may indicate that the recovered strain is not strongly dependent on the applied stress so long as it is above a critical level and the kinetics of recovery is dependent on microstructural details, perhaps primarily on the elastic property of the whisker network.

In order to elucidate the origin of anelastic recovery in the whisker reinforced alumina composites, it would be ideal to measure the signature of the recovery in-situ. However, there was no such experimental set up at the Chalk River Laboratories where the neutron diffraction experiments were carried out. An

alternative in-situ high temperature neutron diffraction measurement adopted in the present study (described in detail in Chapter 4) was possible because of the slow relaxation processes that take place typically over at least  $7 \times 10^4$  seconds.

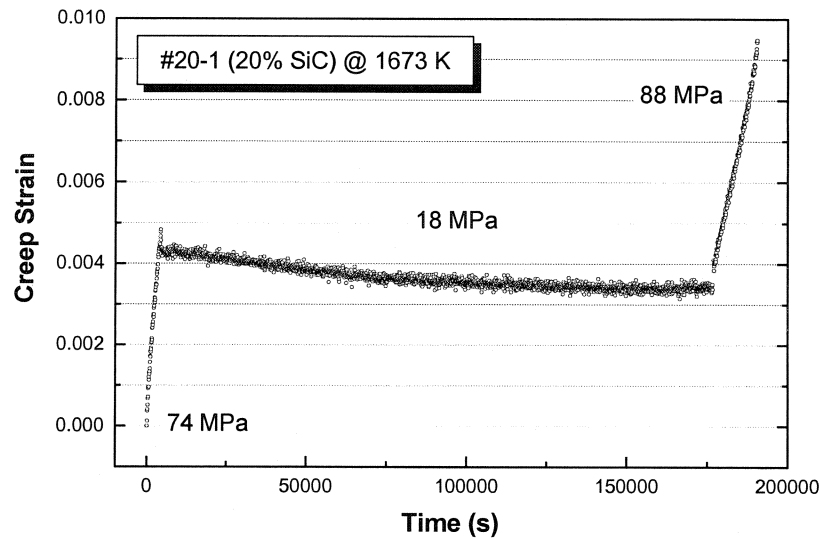
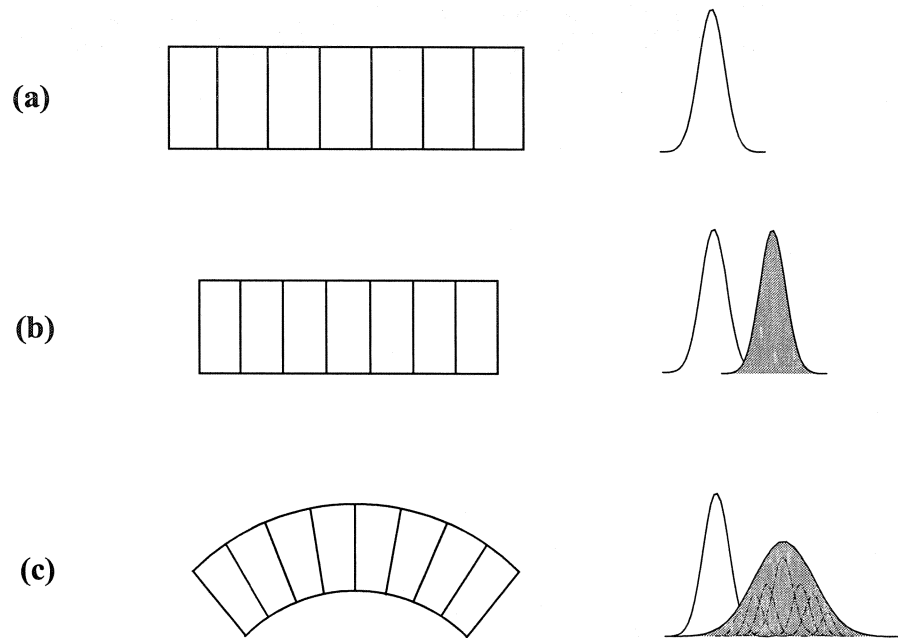


Fig. 6.11 The creep stress relaxation curve for a S202 sample.

### 6.5.2 Peak broadening

Figure 6.12 schematically illustrates the effect of lattice deformation on the position and shape of a reflection profile. In general, a uniform strain field only causes a shift in peak position with no change in peak shape. For instance, as shown in Fig. 6.12(b), the uniaxial compression simply shifts the peak to a higher scattering angle. However, any non-uniform strain distribution should lead to a change in peak shape. Figure 6.12(c) shows an example of pure bending that causes peak broadening. It is then important to realize that the change in position of diffracted peaks can be used to calculate an average normal strain, whereas the change in peak shape can be used to obtain information related to the strain distributions. The latter is in practice a formidable task due to many uncertainties and complexity associated with the deconvolution processes. However, it is worth much effort since it is actually the extremes of the strain

distribution, rather than its average, which have the greatest relevance to the mechanical properties (Todd and Derby 1993).



**Fig. 6.12** Schematic illustrations of change in peak position and shape due to lattice deformation. **(a)** without deformation **(b)** uniaxial compression and **(c)** pure bending. The shaded peaks are after deformation.

Suppose that whisker bending is the origin of anelastic strain recovery and that the change in the (111) SiC peak width is determined primarily among all possible reasons by the extent of whisker bending. It follows that during forward creep whiskers would undergo bending deformation, and thus, result in (111) SiC peak broadening. When the load is removed, however, the reverse process takes place where the extent of whisker bending would decrease with a concomitant decrease in peak width. This hypothesis is schematically illustrated in Fig 6.13. It is important to recognize the reversibility of this process, which requires the amount of whisker bending gained during forward creep be the same as that reduced during recovery. To verify the whisker bending model in fact it is useful, before performing the in-situ annealing experiment, to compare the (111) SiC peaks at room temperature from specimens that have various thermal

and deformation histories. Figure 6.14(a) compares the (111) SiC peaks measured from a single tensile specimen before and after creep with the scattering vector coincident with the tensile direction. Those whiskers in the Bragg condition are shaded in the schematic illustrations. The shift in scattering angle owing to the slight difference in wavelength has been compensated. First of all, it is seen that there is no significant change in peak shape after creep. The shift in peak position to a lower scattering angle is

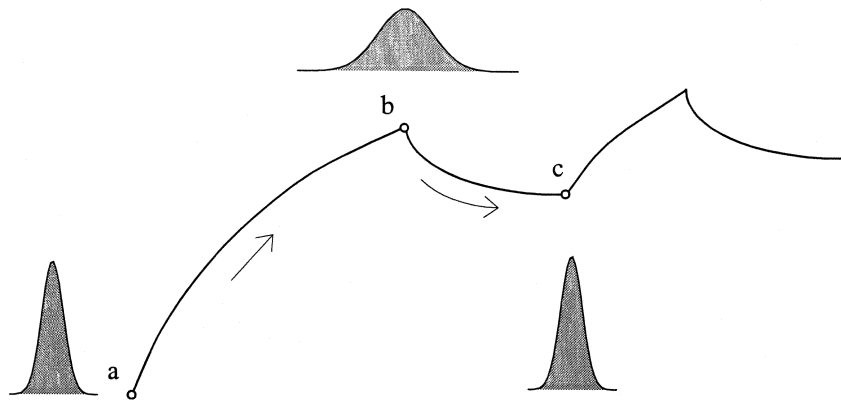
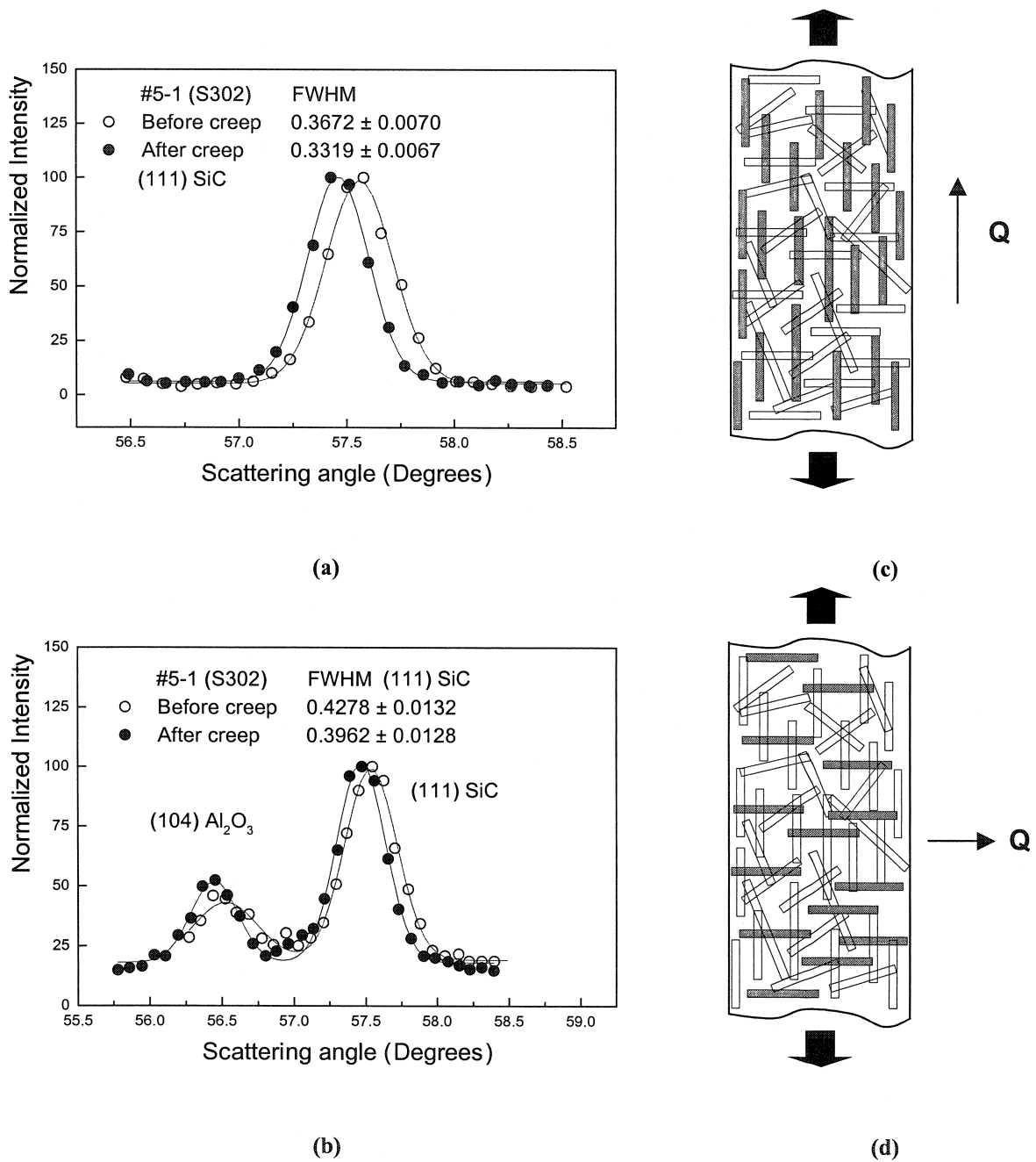


**Fig. 6.13** Schematic of peak width changes according to the whisker bending model.

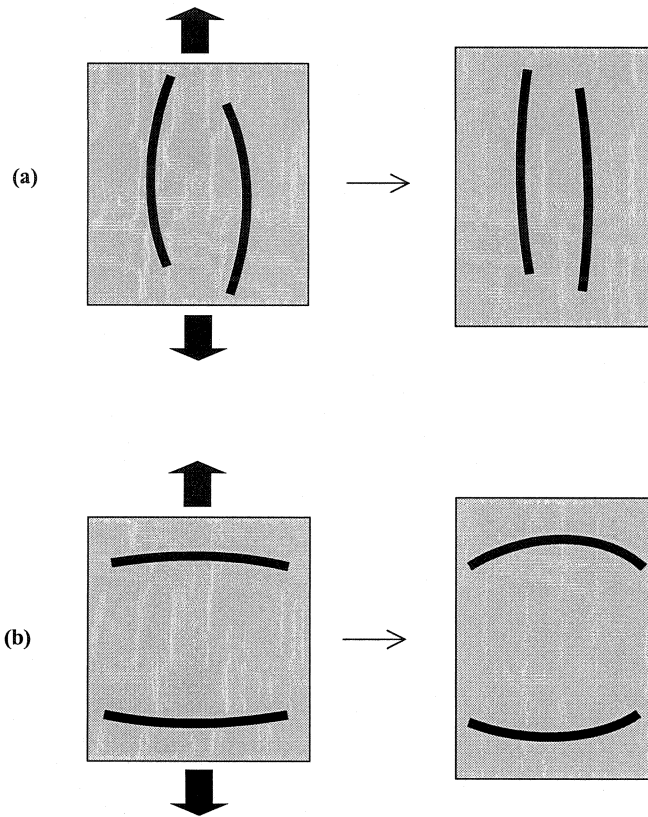
consistent with the reduced compressive residual strain as a result of the applied tensile stress. The measured peak width after creep is actually slightly less than that measured before creep. This result may be understood with the aid of the schematic illustration in Fig. 6.15(a) where the tensile stress causes a decrease in the extent of bending for the whiskers aligned parallel (or nearly parallel) to the tensile axis. This simple argument follows that those whiskers orientated perpendicular (or nearly perpendicular) to the tensile direction should undergo more bending deformation under the tensile stress, which is shown schematically in Fig. 6.15(b). Figure 6.14(b) shows the (111) SiC peaks measured with the scattering vector perpendicular to the tensile direction. The peaks seem to be slightly wider in this case as compared to those in Fig. 6.14(a). However, there is again no increase in peak width after creep deformation, and instead, a decrease in peak width is recorded. In addition, the difference in peak width is actually comparable to that seen in Fig. 6.14(a).

Figure 6.16 shows another example where (111) SiC peaks were measured consecutively from two different specimens which are nominally the same except that one of them has been deformed. The





**Fig. 6.14** Comparison of (111) SiC peaks measured from a single specimen before and after creep with the scattering vector nearly (a) parallel to the tensile direction and (b) perpendicular to tensile axis. Schematic illustrations for (c) Q//L and (d) Q⊥L.



**Fig. 6.15** Schematic illustration of whisker bending upon the applied tensile stress for the whiskers oriented nearly (a) parallel and (b) perpendicular to the tensile axis.

shift in peak position is consistent with the previous example. However, within the range of experimental error, there seems to be no difference in the measured peak width between the two specimens. It should be mentioned that all the deformed samples for neutron diffraction measurements were cooled with the load on so as to “freeze” any recoverable elastic strains. Since there is no change (or even decrease) in the (111) SiC peak width after creep deformation, it appears that the applied stress did not cause significant peak broadening during forward creep.

Since it appears that the whisker network can be compressed more ‘effectively’ to a much higher strain than in tension, it may be necessary to ask whether more whisker bending can be achieved under high compressive strain. In light of this, (111) SiC peaks were measured from a composite specimen that has been deformed to 0.7% in compression a composite specimen that was deformed in tension to 0.4%. In

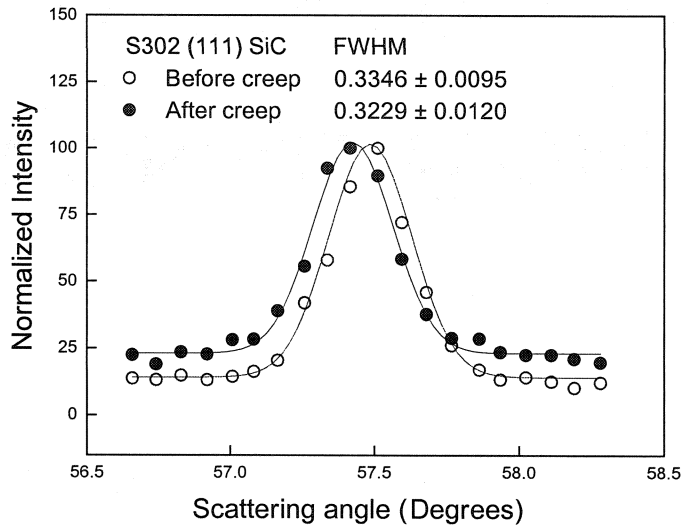


**Fig. 6.16** Comparison of (111) SiC peaks measured before and after creep. The instrumental broadening remained constant.

theory it is possible to subtract the physical broadening from the measured peak, however, it is possible only when there is no textural difference between the standard sample (here the pure SiC whiskers) and the sample of interest. Unfortunately, this was not the case in the present investigation due to the whisker texturing within the composites as a result of uniaxial hot pressing. However, it is still possible to study the measured peaks in a qualitative manner. The (111) SiC peaks measured from the composites seem to be wider than those from stress-free powders, suggesting a somewhat peak broadening effect within densified composites. Assuming Gaussian profiles for both the instrumental and physical broadening the following relation holds (Klug and Alexander 1974):

$$FWHM^2 = FWHM_I^2 + FWHM_p^2 \quad (6.8)$$

from which the physical broadening can be estimated. Here,  $FWHM_I$  represents the instrumental broadening and  $FWHM_p$ , the physical broadening. By comparing the results that are included in Table 6.4, it becomes clear that the difference is small. Therefore, it may be concluded that a higher compressive creep strain does not result in more significant broadening of (111) SiC peak, thus, more whisker bending. This seems to be in accord with the observation during four point bending creep that the amount of

recovered strain is not strongly dependent on the accumulated total strain at which the recovery process is initiated (Gu et al. 1995).

Although the analysis of peak width measured at room temperature at various conditions indicates a weak relation between (111) SiC peak width and creep deformation, it still does not exclude the scenario in which the (111) SiC peak width decreases (no matter how small it is) during the relaxation period. This effect can be studied by comparing the peak width before and after relaxation or by measuring the peak width in-situ during relaxation. Nonetheless, it suffices to say here that the change in whisker bending, if indeed takes place, does not manifest itself through the change in the (111) SiC peak width within the resolution of neutron diffraction technique employed in this study.

The results of peak width measurement from the in-situ neutron diffraction experiments (See Fig. 5.35 and 5.36) however, showed essentially no measurable change in peak width within the experimental resolution during relaxation. Therefore, it may be said that the extent of whisker bending does not alter significantly during relaxation. This raises two possibilities. One possibility is, as hypothesized, whiskers indeed straighten up during relaxation, however, as mentioned earlier the change is too small to be detected due to the limited instrumental resolution. This requires recourse to non-conventional diffraction methods, like X-ray synchrotron diffraction or high energy pulsed neutron diffraction. However, it should be kept in mind that even with a higher instrumental resolution, as long as there are other factors contributing to the change in peak width other than whisker bending, separation of the contribution from whisker bending alone would be very difficult. The other possibility is that the effect of whisker bending is trivial in relation to the observed strain recovery, which requires one to seek for some other mechanisms for relaxation.

**Table 6.4** The estimated Gaussian physical broadening.

| Testing mode | Creep strain (%) | $FWHM_p$            |
|--------------|------------------|---------------------|
| Compressive  | 0.7              | $0.1259 \pm 0.0545$ |
| Tensile      | 0.4              | $0.1054 \pm 0.0578$ |

## 6.5.2 Modeling of whisker bending

### Assumptions

The effect of fiber bending on peak broadening is estimated with the following assumptions:

1. There is only hydrostatic (or dilatational) distortion of unit cells after bending and Bragg's law is still applicable for the bent crystal.
2. The amount of bending is small and the outer fiber macrostrains are equal to the extreme lattice strains.

### Geometrical consideration

Figure 6.17 shows the simplified whisker bending geometry. If the average radius of curvature for the whisker is  $\rho$  and whisker diameter  $D$ , the maximum interplanar spacing of the basal plane in tension would be

$$d_t = d_o \left( 1 + \frac{D}{2\rho} \right) \quad (6.9)$$

while the minimum, found in compressive side, is

$$d_c = d_o \left( 1 - \frac{D}{2\rho} \right) \quad (6.10)$$

where  $d_o$  is the lattice spacing at the neutral plane.

For constant wavelength diffraction, the application of Bragg's law leads to

$$\left( 1 + \frac{D}{2\rho} \right) \sin \theta_t = \left( 1 - \frac{D}{2\rho} \right) \sin \theta_c \quad (6.11)$$

where  $\theta_t = \theta_o + \frac{\Delta\theta}{2}$  and  $\theta_c = \theta_o - \frac{\Delta\theta}{2}$ , which correspond to the Bragg angles for  $d_t$  and  $d_c$

respectively.

Therefore,

$$\frac{\rho}{D} = -\frac{1}{2} \tan \theta_o \cot \frac{\Delta\theta}{2} \quad (6.12)$$

and when  $\Delta\theta$  is small, it can be reduced to

$$\frac{\rho}{D} = -\frac{\tan \theta_o}{\Delta\theta}$$

Therefore, with small change in lattice spacing, the corresponding change in Bragg angle is inversely related to the radius of the bending curvature. Fig. 6.18 (a) shows the calculated results using the Eq. 6.12.

Assuming a simple three point bending geometry and a constant radius of curvature for the whisker, the radius of curvature can be estimated using the following two equations

$$\sin \alpha \approx \frac{L}{2\rho} \quad (6.13)$$

$$\Delta h = \rho(1 - \cos \alpha) \quad (6.14)$$

Therefore,

$$\rho = \frac{L}{4} \left( \frac{L}{2\Delta h} + \frac{2\Delta h}{L} \right) \quad (6.15)$$

If  $\Delta h \ll L$ , then

$$\rho \approx \frac{L^2}{8\Delta h} \quad (6.16)$$

Figure 6.18(b) shows the calculated results using Eq. 6.12.

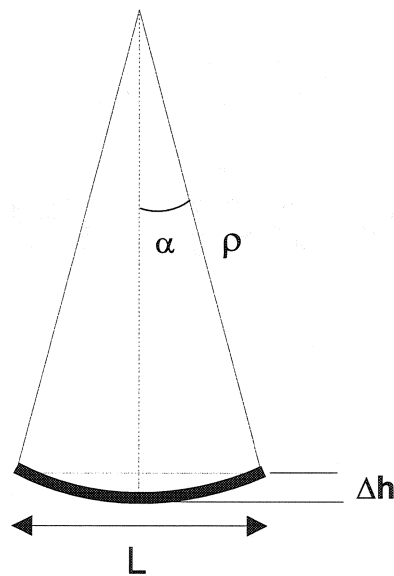
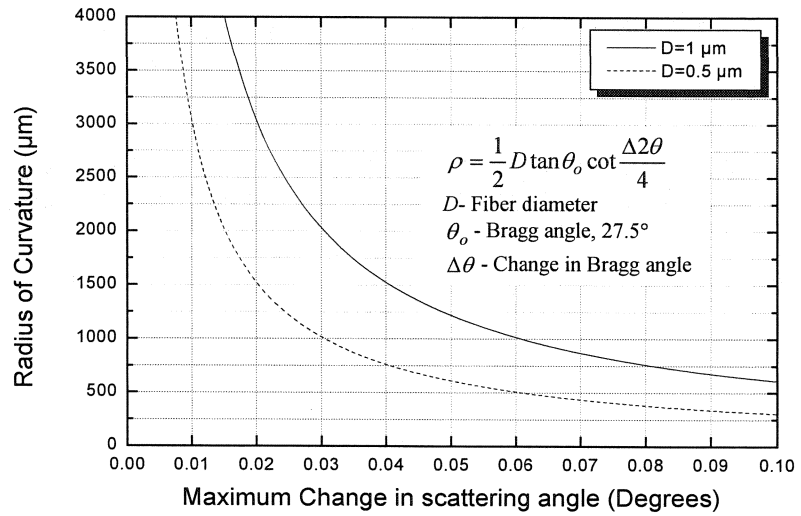
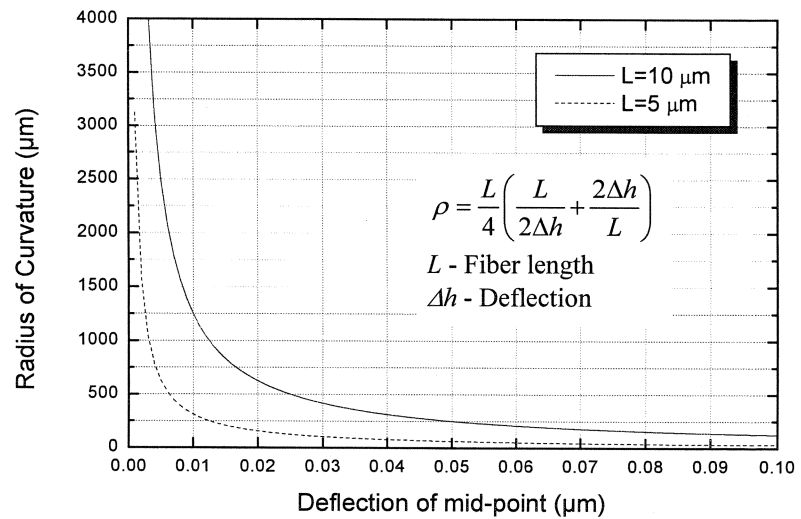


Fig. 6.17 A schematic of whisker bending geometry.



(a)



(b)

**Fig. 6.18 (a)** The calculated radius of whisker curvature versus maximum change in scattering angle **(b)** The calculated radius of whisker curvature versus mid-point deflection.

## Estimation of peak broadening

Broadening of the line profile of diffraction peaks from polycrystalline crystallites can be caused by the small size of coherently diffracting domains (size effect) and non-uniform distribution of microstrains within the crystallites. In addition, other sources of broadening include slit widths, sample size, penetration in the sample and imperfect focusing etc. and they are categorized as instrumental broadening. To correct for this broadening in the pattern of the sample, it is necessary to obtain a standard peak from a suitable powder sample.

The variance in scattering angle for a pure diffraction peak (i.e. without instrumental broadening) is given as (Wilson 1962 and Klug and Alexander 1974)

$$W_{2\theta} = \langle (2\theta - \langle 2\theta \rangle)^2 \rangle = 4 \tan^2 \theta \langle \varepsilon_{hkl}^2 \rangle \quad (6.17)$$

where

$$\varepsilon_{hkl} = \frac{\Delta d_{hkl}}{d_{hkl}} \quad (6.18)$$

Without size broadening the following relation holds for a Gaussian peak

$$FWHM = 2\sqrt{2 \ln 2} \sigma = 2\sqrt{2 \ln 2} \sqrt{W_{2\theta}} \quad (6.19)$$

where  $\sigma$  is the standard deviation.

The total broadening is given in Eq. 6.8, i.e.

$$FWHM^2 = FWHM_I^2 + FWHM_p^2$$

where the physical broadening

$$FWHM_p = 4\sqrt{2 \ln 2} \tan \theta \sqrt{\langle \varepsilon_{hkl}^2 \rangle} \quad (6.20)$$

and  $FWHM_I$  is the instrumental broadening which varies with Bragg angle according to the Cagliotti equation (Cagliotti et al. 1958)

$$FWHM_I = u \tan^2 \theta + v \tan \theta + w \quad (6.21)$$

where  $u$ ,  $v$ ,  $w$  are constants related to the geometry of collimation.

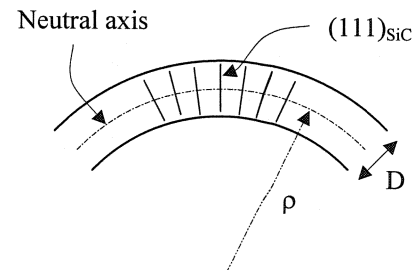


Fig. 6.19 Simplified geometry of whisker bending.



The inhomogeneous strain field is normally assumed to take on a Gaussian distribution,

$$P_{hkl}(\varepsilon) = \frac{1}{\sqrt{2\pi}e_{hkl}} \exp\left(-\frac{(\varepsilon_{hkl} - \langle \varepsilon_{hkl} \rangle)^2}{2e_{hkl}^2}\right) \quad (6.22)$$

where  $e_{hkl}$  is the root mean square (RMS) strain, i.e.

$$e_{hkl} = \sqrt{\langle \varepsilon_{hkl}^2 \rangle} \quad (6.23)$$

which describes the distribution of the strain field around the average lattice strain,  $\langle \varepsilon_{hkl} \rangle$ . Now, the fraction of crystallites whose lattice strain along [hkl] falls between  $\varepsilon_1$  and  $\varepsilon_2$  can be evaluated by the integral (Wang et al. 1994):

$$P_{hkl}(\varepsilon_1, \varepsilon_2) = \int_{\varepsilon_1}^{\varepsilon_2} p(\varepsilon) d\varepsilon = \frac{1}{2} \left[ \operatorname{erf}\left(\frac{\varepsilon_2 - \langle \varepsilon_{hkl} \rangle}{\sqrt{2}e_{hkl}}\right) - \operatorname{erf}\left(\frac{\varepsilon_1 - \langle \varepsilon_{hkl} \rangle}{\sqrt{2}e_{hkl}}\right) \right] \quad (6.24)$$

In case of whisker bending, it is convenient to follow the plane that is perpendicular to the whisker axis, i.e. (111) plane (see Fig. 6.19). The outer fiber strain calculated by continuum mechanics is  $\frac{D}{2\rho}$

where  $D$  is the fiber diameter and  $\rho$  the radius of the curvature. With a small degree of bending, this strain is assumed to equate the maximum bending strain of (111) plane at the fiber surface in tension,

$$\varepsilon^* = \frac{D}{2\rho} = \frac{d'_{111} - d''_{111}}{d''_{111}} \quad (6.25)$$

where  $d''_{111}$  is the d-spacing at neutral plane and  $d'_{111}$  the maximum. Note that the 'volume fraction' of crystallites whose d-spacing is in extreme diminishes, it is approximated that

$$\frac{D}{2\rho} = 3e_{111} \quad (6.26)$$

where  $e_{111}$  is the RMS strain, i.e. the standard deviation of the normal distribution.

This approximation restricts the 'volume fraction' of crystallites having their bending strains between  $-\frac{D}{2\rho}$  and  $\frac{D}{2\rho}$  be 99.7% of the total crystal volume. Now, the physical broadening due to whisker bending is expressed as

$$FWHM_p = \frac{2}{3} \sqrt{2 \ln 2} \tan \theta_0 \left( \frac{D}{\rho} \right) \quad (6.27)$$

This model predicts that the magnitude of physical broadening is proportional to the fiber diameter and inversely related to the radius of bending curvature.

Figure 6.20 presents the calculated physical peak broadening as a function of whisker bending using Eq. 6.27 and Eq.6.16. Apart from Gaussian distribution (Model 3), two other models (Model 1 and 2) were used to describe the bending strain distribution. Model 1 assumes a uniform distribution of bending strains between maximum and minimum, which led to the largest change in peak width among all the models. For instance, when the mid-point of the fiber travels by the length of fiber diameter, this model predicts  $\sim 0.015^\circ$  change in FWHM whereas model 2 predicts  $\sim 0.009^\circ$ . The prediction by model 2 is between that by model 1 and 3.

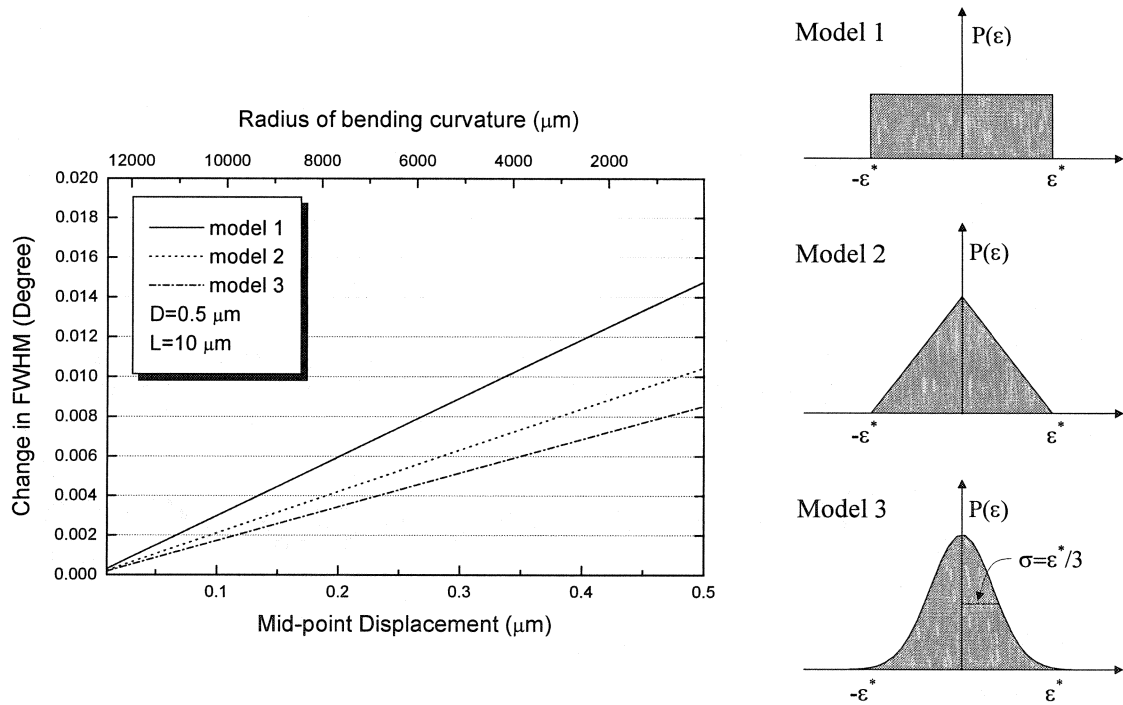


**Fig. 6.20** The calculated FWHM as a function of whisker bending. If the probability of finding lattice strain between  $\epsilon$  and  $\epsilon+d\epsilon$  is  $P(\epsilon)d\epsilon$ , model 1 assumes a linear function of  $P(\epsilon)$ , model 2, a uniform  $P(\epsilon)$  and model 3, a Gaussian profile of  $P(\epsilon)$ .

## Estimation of whisker bending from the recovered strain

The recovered strain that has been measured can be used to evaluate the extent of average whisker bending.

Assuming that all the elastic strain energy is stored in the form of pure whisker bending, it follows that

(Landau and Lifshitz 1986):

$$\frac{1}{2} E_c \varepsilon_r^2 = \phi \left( \frac{E_s I_s}{2\pi R^2 \rho^2} \right) \quad (6.28)$$

where

$E_c$  - Young's modulus of composite;

$E_s$  - Young's modulus of whisker;

$\varepsilon_r$  - The recovered strain;

$\phi$  - Whisker loading;

$R$  - the radius of whisker;

$\rho$  - the radius of curvature;

$I_s$  - Second moment of whisker, i.e.  $\frac{1}{2} \pi R^4$  ;

Since  $E_s \geq E_c$ ,

$$\rho = \sqrt{\frac{\phi E_s}{2 E_c} \frac{R}{\varepsilon_r}} \geq \sqrt{\frac{\phi}{2} \frac{R}{\varepsilon_r}} \quad (6.29)$$

Putting in the typical values:  $\phi=0.15$ ;  $\varepsilon_r=0.001$  and  $R=0.25 \mu\text{m}$ , gives

$$\rho \geq 68.5 \mu\text{m}$$

This corresponds to an upper limit of the change in FWHM as  $0.004^\circ$ , which is difficult to be detected.

It should be mentioned that the above calculation overestimated the elastic energy within the composites as a whole, which gave the upper bound of the change in peak width. Because it is based on the assumption that the recovered strain is linearly related to the applied stress, thus, ignores the time dependency of the recovery process. In fact, this is only true for the very beginning of the recovery period after load removal. However, as shown in Fig. 5.8, the alumina matrix essentially recovers no elastic strain.

This suggests that the driving force for anelastic strain recovery is primarily the elastic energy stored in the inclusion network, which is dissipated through the plastic deformation of the surrounding matrix during otherwise instantaneous recovery process. This is evidenced by the observation that at low temperatures the recovery process becomes more limited because of the increased matrix viscosity.

### 6.5.3 Speculation on the origin of strain recovery

Since the whisker-bending model cannot account for many of the results presented earlier regarding the strain recovery behaviour in the composites, we have to seek for other possibilities. Among many two phase ceramic composite systems where anelastic strain recovery was found, SiC particulate-reinforced alumina composite seems to deserve particular attention, since this system exhibited a very similar strain recovery behaviour to SiC whisker-reinforced alumina composite. First of all, this system showed strain recovery phenomenon only when the inclusion volume fraction reaches about 15%, which suggests it is also associated with a network effect. Secondly, the magnitude of recovered strain in this system is comparable with that recorded in SiC whisker-reinforced alumina composites. However, since no bending effect is associated with spherical particles, there must be a different mechanism that is responsible for the observed strain recovery behaviour therein. One possibility is localized elastic point contacts between particles where large strain can be achieved under low stress owing to Hertzian contact (Timoshenko and Goodier 1970). Figure 6.21(a) illustrates the Hertzian contact phenomena between spherical particles.

According to Hertz (1881), for two spherical bodies in contact as shown in the figure, the following relation holds

$$h = \text{constant} \times F^{2/3} \quad (6.30)$$

where  $h$  is the change in the distance between the centers of two spheres and  $F$  the applied load. In fact, it has been shown that this relation remains true for any finite bodies in contact (Landau and Lifshitz, 1986). One such example is shown in Fig. 6.21(b) where cylindrical rods are in contact. For identical finite bodies

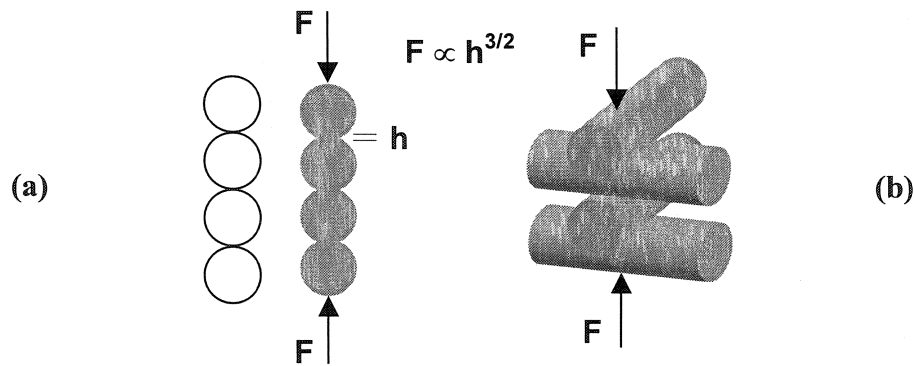


**Fig. 6.21** Schematic illustration of Hertzian contact phenomena between (a) spheres and (b) rods in contact.

(e.g. spheres) in contact along the loading direction, it can be easily shown that for a constant applied load the total elastic contact energy increases linearly with increasing contact number. This may be used to qualitatively explain the fact that there is little or no strain recovery in a dilute system, e.g. 5% SiC whisker reinforced alumina composite (Gu et al. 1995). For spherical particles randomly distributed in a matrix, it can be easily envisaged that the interparticle contacts will be limited to short range when the inclusion volume fraction is well below point-to-point percolation ( $\sim 16\%$ ). Therefore, the localized elastic deformation due to Hertzian contact will be short-lived and relaxed quickly through plastic flow of the surrounding matrix and perhaps particle rearrangement as well. However, particles become more interactive by forming more contacts as their volume fraction increases and the accommodation processes become increasingly difficult once a percolative particle network is formed. In other words, the applied load is transferred to the particle network more effectively. The stored elastic energy within the constrained particle network can be released with the aid of matrix flow only when the load is removed. The same argument should be applicable for the whisker network as well. However, the presence of whisker texture due to uniaxial hot pressing will likely cause anisotropic elastic response of the whisker network. Therefore, for instance, when the composite is loaded along HPA, more contact strain is expected as compared to being loaded perpendicular to HPA.

Prediction of the magnitude of recoverable strain is an elusive task, the main reason being the difficulty of estimating the local contact force. However, two simple models have been developed for different reinforcement geometries, namely, sphere and whisker (or cylindrical rod).

For the whisker network loaded in-plane (perpendicular to HPA), local contact forces can be roughly estimated by considering the force equilibrium during external tensile loading due to rotation of the whiskers. Figure 6.22(a) shows a highly simplified unit cell for calculating the contact forces. If we assume the surrounding matrix induces rotation of the misaligned whisker, then at the contact points normal forces are generated. The magnitude of these contact forces can be estimated by comparing the moment formed by the shear stress acting along the matrix whisker interface (see Fig. 6.23):

$$M_{\tau} = 4 \int_0^{\pi/2} LR^2 \tau \cos \omega d\omega = 4LR^2 \tau = 2LR^2 \sigma \sin 2\theta \quad (6.31)$$

where  $R$  and  $L$  is radius and average segment length of whiskers,  $\omega$  is the angle around the whisker axis and  $\theta$  the misorientation angle. With the counter balancing moment due to contact forces  $F_p$

$$M_n = F_p L \quad (6.32)$$

from which the local contact force is determined to be

$$F_p = 2R^2 \sigma \sin 2\theta \quad (6.33)$$

The displacement due to contact deformation is given as (Landau and Lifshitz 1986)

$$h = F_p^{2/3} \left[ \frac{9}{2} \left( \frac{1-\nu^2}{E} \right)^2 \frac{1}{R} \right]^{1/3} \quad (6.34)$$

Then the strain at the loading direction is given by

$$\varepsilon = \frac{2h}{L} \tan \theta = \frac{2R}{L} \left[ \frac{3\sqrt{2}\sigma(1-\nu^2)}{E} \right]^{2/3} (\sin 2\theta)^{2/3} \tan \theta \quad (6.35)$$

Assuming  $\sigma = 50$  MPa,  $\langle \theta \rangle = 20^\circ$ ,  $\nu = 0.2$ ,  $R/L = 0.1$  and  $E = 427$  GPa, the unit cell model predicts a strain of  $\sim 3.3 \times 10^{-4}$  at the loading direction. This is in the same order of those experimentally observed, i.e.

$\sim 8 \times 10^4$ . It is also noted that this model predicts increasing strain with decrease in whisker aspect ratio, which is in accord with the experimental results of Gu et al. (1994).

For a percolating path of whiskers along the loading direction, the total strain due to contact deformation can be approximated as follows

$$\varepsilon^{Total} = \frac{\sum_{i=1}^n h_i \sin \theta_i}{\sum_{i=1}^n L_i \cos \theta_i} \quad (6.36)$$

Using Eq. 6.33 and 6.34, it becomes

$$\varepsilon^{Total} = \frac{\sum_{i=1}^n 2(2R^2 \sigma \sin 2\theta_i)^{2/3} \left[ \frac{9}{2} \left( \frac{1-\nu^2}{E} \right)^2 \frac{1}{R} \right]^{1/3} \sin \theta_i}{\sum_{i=1}^n L \cos \theta_i} \quad (6.37)$$

Therefore,

$$\varepsilon^{Total} = \frac{2R}{L} \left[ \frac{3\sqrt{2}\sigma(1-\nu^2)}{E} \right]^{2/3} \frac{\langle (\sin 2\theta_i)^{2/3} \cdot \sin \theta_i \rangle}{\langle \cos \theta_i \rangle} \quad (6.38)$$

Here

$$\langle \sin \theta_i (\sin 2\theta_i)^{2/3} \rangle = \sum_{i=1}^m P(\theta_i) \sin \theta_i (\sin 2\theta_i)^{2/3} \Delta\theta_i; \quad (6.39)$$

$$\langle \cos \theta_i \rangle = \sum_{i=1}^m P(\theta_i) \cos \theta_i \Delta\theta_i \quad (6.40)$$

$$\text{where } \sum_{i=1}^m P(\theta_i) \Delta\theta_i = 1 \quad (6.41)$$

Here,  $P(\theta_i)$  is the whisker orientation distribution function that can be learnt from the fiber texture analysis and  $m$  is the number of angles covered during texture measurement. Assuming a random whisker distribution, i.e.  $P(\theta_i) = 2/\pi$ , The total strain is given as

$$\varepsilon^{Total} = \frac{6}{7} \frac{\Gamma(5/6)\Gamma(2/3)}{\sqrt{\pi}} \frac{R}{L} \left[ \frac{3\sqrt{2}\sigma(1-\nu^2)}{E} \right]^{2/3} \quad (6.42)$$

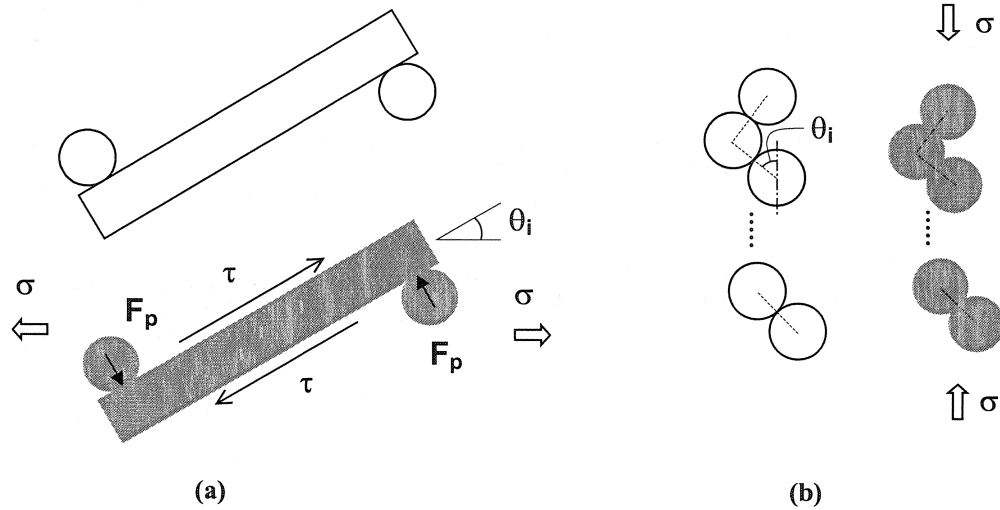


**Fig. 6.22** Illustration of load transfer due to the far field stress acting on constrained (a) fibers and (b) spherical particles through contact deformation.

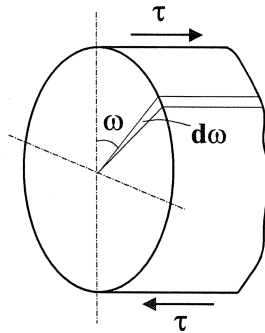


**Fig. 6.23** Geometry for calculating the moment due to the shear stress on the whisker surface.

Figure 6.24(a) shows the total strain as a function of the applied stress assuming  $R/L = 0.1$ . It is seen that the results are in the same of order of magnitude with those observed during creep in bending (e.g. Gu et al. 1994) and in tension (see Fig. 6.11). It is noted the unit cell model with an average misaligned angle predicts lower strains as compared to the approach where the distribution of whisker orientation is considered.

A similar approach can be used for spherical particle network that is under compression. Figure 6.22(b) illustrates the geometry of particles in contact. Under the applied stress  $\sigma$ , local contact stresses  $\sigma^*$  will develop around the particles, which can be found as follows:



$$\sigma^* = \sigma\zeta \quad (6.43)$$

where  $\zeta$  is a factor relating the average contact normal stress borne by the inclusions to the applied stress.

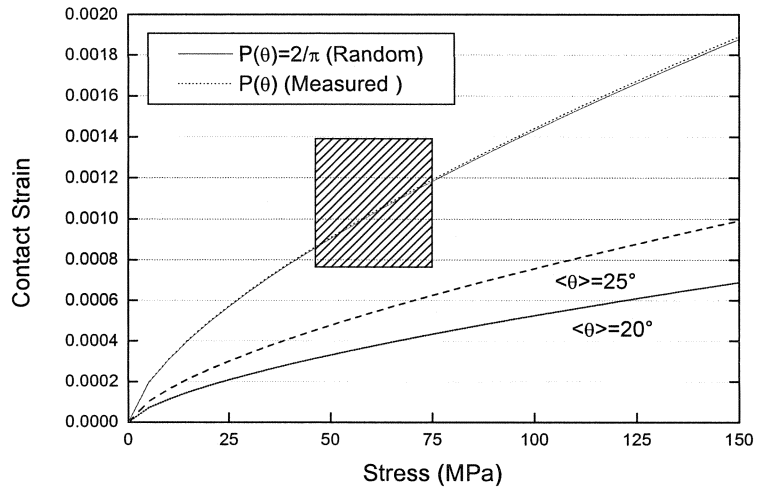
Now, the total strain can be written as

$$\varepsilon^{Total} = \frac{1}{2} \left[ \frac{3\sigma\zeta\pi(1-\nu^2)}{\sqrt{2}E} \right]^{2/3} \frac{\langle (\cos\theta_i)^{5/3} \rangle}{\langle \cos\theta_i \rangle} \quad (6.44)$$

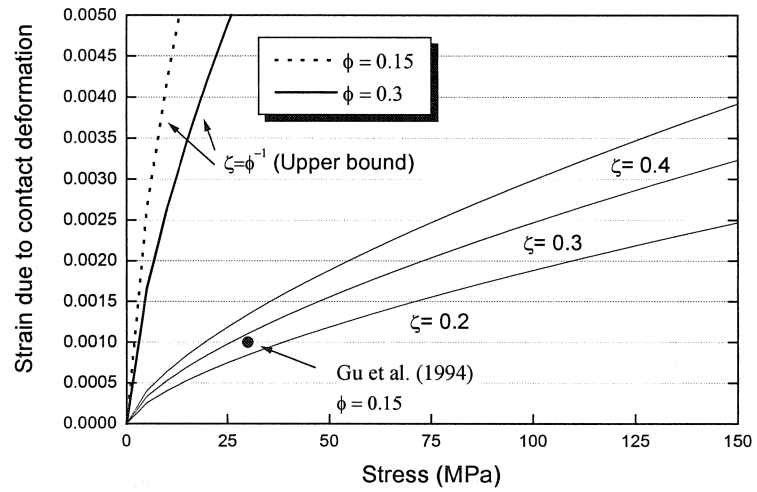
For randomly distributed particles, it becomes

$$\varepsilon^{Total} = \frac{\sqrt{3}\pi^{3/2}}{15\Gamma(2/3)\Gamma(5/6)} \left[ \frac{3\sigma\zeta\pi(1-\nu^2)}{\sqrt{2}E} \right]^{2/3} \quad (6.45)$$

Figure 6.24(b) shows the calculated strains as a function of applied stress and the factor,  $\zeta$ . The upper bound of  $\zeta$  is given assuming the entire applied load is borne by the inclusions. Two volume fractions are used for calculation, i.e.  $\phi=0.15$  and  $0.3$ . The simulation indicates that the experimental result (Gu et al. 1994) is consistent with  $\zeta \approx 0.3$ . This suggests that the local normal stresses responsible for inclusion contact deformation are very small presumably because the shear portion of the local contact stresses will facilitate rearrangement of the particles in such a way that the normal contact strains is minimized.



(a)



(b)

**Fig. 6.24** Computed strains due to local contact deformation as a function of applied stress. **(a)** for whisker network. The shaded area covers the recovered strains that have been measured experimentally. **(b)** for percolative spherical particles.

## 7. SUMMARY AND CONCLUSIONS

This research project involved fabrication of the SiC whisker-reinforced alumina composites using ceramic powder colloidal processing methods and creep testing of these composites in tension. During the course of this work neutron diffraction techniques have been used extensively to characterize the whisker texture and internal stresses/strains at various conditions.

The distribution of whiskers within the alumina matrix was found to be dependent on the slurry pH. At low pH (2-4) positively charged fine alumina particles seemed to be attracted to the negatively charged surface of SiC whiskers. This prevented the formation of large whisker flocs in the suspension and led to, after sintering, a uniform distribution of whiskers within the fine-grained alumina matrix. At high pH ( $\geq 6$ ) strong flocculation between like particles seemed to occur, which resulted in whisker agglomerates and larger grain size in the final products. However, the neutron diffraction measurements indicated somewhat unexpectedly that the overall whisker alignment could not be altered dramatically by adjusting slurry pH.

In this study the improvement in the tensile creep resistance of alumina through SiC whisker additions (10-30 vol%) has been found to be substantial (typically  $10^2$ - $10^3$  times decrease in creep rates). The whisker loading appears to be an important factor in decreasing the strain rate up to 30 vol% in tension. This leads to the conclusion that the creep rate is not controlled solely by the whisker network and that those whiskers that are not included in the percolative path may remain as an effective source for a further increase in creep resistance. This may be explained by considering the number density of whiskers available for resisting grain boundary sliding, provided that the thermal oxidation of SiC whiskers is not severe enough to promote extensive cavitation.

The matrix grain size remains an important factor in determining the overall creep rate in tension, as evidenced by the low creep rates measured for the composite with 10% SiC whiskers that has a large matrix grain size.

The stress exponent was found to be much higher and more temperature dependent in tension than in compression. The former implies significant contributions from other creep mechanisms than diffusional creep whilst the latter suggests a complex relationship between all the attendant creep mechanisms. For all composites, the activation energies found at a moderate stress were within the range of those reported. It is noteworthy that the activation energy was dependent on SiC content, seeming to decrease with increasing SiC content. This is believed to indicate the increasingly important role of grain boundary diffusion and GBS as SiC content increases and, perhaps, SiC content-dependent cavitation creep rate.

Significant anelastic strain recovery was observed following tensile creep of the composites with 20 and 30% SiC whiskers and the magnitude of recovered strains was consistent with those measured in four point bending creep tests. This combined with a lack of significant strain recovery with 10% SiC whiskers, proves that the whisker network is the key to having a high degree of anelastic strain recovery. The kinetics of strain recovery appears to be dependent on the elastic properties of the whisker network, which are likely dependent on the sample orientation with respect to the loading direction.

Experimentally, the effect of whisker bending was not significant enough to be readily measured by conventional diffraction methods, which requires recourse to much superior instrument resolution. A more plausible explanation of the anelastic strain recovery is the local contact deformation between elastic inclusions. The simple models based on Hertzian contact mechanics seem to predict the magnitude of recoverable strain reasonably well, which provides a useful framework for further development with more sophisticated treatments.

## REFERENCES

- Abuhasan, A., Balasingh and Predecki, P., *J. Am. Ceram. Soc.*, 1990, **73**, 2474.
- Allen, A. J., Hutchings, M. T., Windsor, C. G. and Andreani, C., *Advances in Physics*, 1985, **34**, 4, 445-473.
- Arons, R. M. and Tien, J. K., *J. Mater. Sci.*, 1980, **15**, 2046-2058.
- Barthés-Biesel, D. and Acrivos, A., *Int. J. Multiphase Flow*, 1973, **1**, 1.
- Bachelor, G. K., *J. Fluid Mech.*, 1971, **46**, 813.
- Becher P. F. and Wei, G. C., *J. Am. Ceram. Soc.*, 1984, **67**, 12, C267.
- Bouvard, D. and Lange, F. F., *Acta metall. mater.* 1991, **39**, 3083.
- Bradley, S. A., Karasek, K. R.; Martin, M. R.; Yeh, H. C. and Schienle, J. L., *J. Am. Ceram. Soc.*, 1989, **72**, 4, 628-638.
- Brady, J. E. and Holum, J. R., *Fundamentals of Chemistry*, 2nd edition, John Wiley and Sons, 1984, 408.
- Brockmeier, H. G., *Mater. Sci. For.*, 1994, **157-162**, 59.
- Burton, B., *Diffusional Creep of Polycrystalline Materials*, Trans Tech Publications, 1977, 30-37.
- Caglioti, G., Paoletti, A. and Ricci, F. P., 1958, *Nucl. Instrum.*, **3**, 223-228.
- Cannon, R. M., Rhodes, W. H. and Heuer, A. H., *J. Am. Ceram. Soc.*, 1980, **63**, 1-2, 46-53.
- Cannon, W. R. and Langdon, T. G., *J. Mat. Sci.*, 1988, **23**, 1, 1-20.
- Cannon, W. R. and Haig, S., *Plastic Deformation of Ceramics*, Ed. R. C. Bradt et al. 1995, Plenum Press, New York, 381-392.
- Carroll, D. F., Tressler, R. E., *J. Am. Ceram. Soc.*, 1989, **72**, 1, 49.
- Carroll, D. F., Wiederhorn, S. M and Roberts, D. E., *J. Am. Ceram. Soc.*, 1989, **72**, 9, 1610.
- Chang, J. C., Lange, F. F., Pearson, D. S. and Pollinger, J. P., *J. Am. Ceram. Soc.*, 1994, **77**, 5, 1357-1360.
- Chokshi, A. H. and Porter, J. R., *J. Am. Ceram. Soc.*, 1985, **68**, c144.
- Chung, D. H. and Simmons, G., *J. Appl. Phys.*, 1968, **39**, 5316.
- Clark, J. P. and Flemings, M. C. *Sci. Am.*, 1986, **255**, 50-57.

- Coble, R. L., *J. Appl. Phys.*, 1963, **34**, 1679.
- Coble, R. L. and Guerard, Y. H., *J. Am. Ceram. Soc.*, 1963, **46**, 353.
- De Arellano-Lopez, A. R., Cumbreira, F. L., Dominguez-Rodriguez, A., Goretta, K. C. and Routbort, J. L., *J. Am. Ceram. Soc.*, 1990, **73**, 1297.
- De Arellano-Lopez, A. R., Dominguez-Rodriguez, A., Goretta, K. C. and Routbort, J. L., *J. Am. Ceram. Soc.*, 1993, **76**, 1425.
- De Arellano-Lopez, A. R., Dominguez-Rodriguez, A., Goretta, K. C. and Routbort, J. L., *J. Am. Ceram. Soc.*, 1995, *Plastic Deformation of Ceramics*, Ed. R. C. Bradt et al. 1995, Plenum Press, New York, 533-542.
- De Arellano-Lopez, A. R., Melendez-Martinez, J. J., Dominguez-Rodriguez, A., Routbort, J. L., *Scripta Mater.* 2000, **42**, 10, 987-991.
- De Arellano-Lopez, A. R., Dominguez-Rodriguez, A., Routbort, J. L., *Acta Mater.*, 1998, **46**, 18, 6361-6373.
- De Arellano-Lopez, A. R., Melendez-Martinez, J. J., Dominguez-Rodriguez, A., Routbort, J. L., Lin, H. T. and Becher, P. F., *J. Am. Ceram. Soc.*, 2001, **84**, 7, 1645-1647.
- De Jonghe, L. C., Rahaman, M. N. and Hsueh, C. H., *Acta Mater.*, 1986, **34**, 7, 1467-1471.
- Descamps, P., O'Sullivan, D., Poorteman, M., Descamps, J. C., Leriche, A. and Cambier, F. *J. Euro. Ceram. Soc.*, 1999, **14**, 2475-2485.
- Donaldson, K. Y., Venkateswaran, A., Hasselman, D. P. H. and Rhodes, J. F., *Ceram. Eng. Sci. Proc.*, 1989, **10**, 9-10, 1191-1211.
- Einstein, A., *Annalen der Physik*, (4), 1906, **19**, 289.
- Einstein, A., *Annalen der Physik*, (4), 1911, **34**, 591.
- Evans, A. G. and Langdon, T. G., *Prog. Mater. Sci.* 1976, **21**, 171.
- Grannan, D. M., Garland, J. C. and Tanner, D. B., *Phys. Rev. Lett.*, 1981, **46**, 375-378.
- Gu, W. Z., Porter, J. R. and Langdon, T. G., *Ceram. Trans.*, 1994, **46**, 307.
- Gu, W. Z., Porter, J. R. and Langdon, T. G., *J. Am. Ceram. Soc.*, 1994, **77**, 1679-1681.
- Gu, W. Z., Porter, J.R. and Langdon, T.G., *Key Eng. Mater.*, 1995, **104-107**, 2, 873-880

- Gu, W., Porter, J. R. and Langdon, T. G., *Ceram. Eng. Sci. Proc.*, 1995, **16**, 1, 242-252.
- Ham-Su, R., Ning, X. G. and Wilkinson, D. S., *Proc. of 10th Intl. Conf. On Comp. Mats.*, Woodhead Publishing LTD., Cambridge, U.K., 1995, **4**, 679.
- Ham-Su, R., Ph D thesis, McMaster University, Hamilton, Canada, 1997.
- Hansson, T., O'Meara Colette, Rundgren, K., Svensson, P., Warren, R. and Wasen, J., *Plastic Deformation of Ceramics*, Edited by. Bradt, R. C. et al., Plenum Press, New York, 1995, 519-532.
- Hart, E. W., *J. Eng. Mater. Tech.* 1976, **98**, 193-202.
- Herring, C., *J. Appl. Phys.*, 1950, **21**, 437.
- Herzt, H., *J. Math.(Crelle's J.)*, 1881, **92**.
- Holden, T. M., *J. Neutron Research*, 1999, **7**, 291.
- Hollenberg, G. W., Terwilliger, G. R. and Gordon, R. S., *J. Am. Ceram. Soc.*, 1971, **54**, 4, 196-199.
- Holmes, J. W., *J. Mater. Sci.*, 1991, **26**, 1808-1814.
- Holmes, J. W., Park, Y. H. and Jones, J. W., *J. Am. Ceram. Soc.*, 1993, **76**, 5, 1281-1293.
- Jakus, K. and Wiederhorn, S. M., *J. Am. Ceram. Soc.* 1988, **71**, 10, 832-836.
- Jang, H. M., Moon, J. H. and Jang, C. W., *J. Am. Ceram. Soc.*, 1992, **75**, 12, 3369-3376.
- Kallmes, O. J. and Cort, H., *Tappi*, 1960, **43**, 737.
- Karasek, K. R., Bradley, S. A., Donner, J. T., Martin, M. R., Heynes, K. L. and M. R., Yeh, H. C., *J. Mater. Sci.*, 1989, **24**, 1617.
- Karasek, K. R., Bradley, S. A., Donner, J. T., Yeh, H. C. and Schienle, J. L and Fang H. T., *J. Am. Ceram. Soc.*, 1989, **72**, 10, 1907-1913.
- Kelly, A. and Street, K. N., *Proc. Roy. Soc. London*, 1986, **328**, 705-710
- Kingery, W. D., Bowen, H. K. and Uhlmann, D. R., *Introduction to Ceramics*, John Wiley & Sons Inc., 1976.
- Klug, H. P. and Alexander, L. E., *X-ray diffraction procedures*, second edition, Wiley, New York, 1980, 618-708.
- Knippenberg, W. F., *Philips Research Reports*, 1963, **18**, 3, 161-274.
- Kocks, U. F., Tome, C. N. and Wenk, H. R., *Texture and Anisotropy*, Cambridge University Press, 1998.

- Krause Jr., R. F., Wiederhorn, S. M. and Kubler, J. J., *J. Am. Ceram. Soc.*, 2001, **84**, 145-152.
- Kreher, W. and Janssen, R., *J. Eur. Ceram. Soc.*, 1992, **10**, 167.
- Kreher, W. and Molinari, A., *J. Mech. Phys. Solids*, 1990, **38**, 115-118.
- Kupperman, D. S., Majumdar, S., MacEwen, S. R., Hitterman, R. L., Singh, J.P., Roberts, R.A. and Routbort, J.L., *Review of Progress in Quantitative Nondestructive Evaluation*, 1988, **7B**, 961-969.
- Landau, L. D. and Lishitz, E. M., *Theory of Elasticity*, 3rd edition, Pergamon Press, 1986.
- Lange F. F. and Porter, J. R., Unpublished work. 1991.
- Lange, F. F., Clark, D. R. and Davis, B. I., *J. Mater. Sci.*, 1980, **15**, 611-615.
- Lange, F. F., *J. Am. Ceram. Soc.*, 1989, **72**, 1, 3-15.
- Lange, F. F., Lam, D., Sudre, O., Flinn, B. D., Folsom, C., Velamakanni, B. V., Zok, F. and Evans, A. G., *Mat. Sci. and Eng.* **A144**, 1991, 143-152.
- Lange, F. F., Miller, K. T., *Am. Ceram. Soc. Bulletin*, 1987, **66**, 10, 1498-1504.
- Lange, F. F., Velamakanni, B. V., Chang, J. C., Pearson, D. S., *Proceedings of the Riso International Symposium on Metallurgy and Materials Science, Structural Ceramics Processing, Microstructure and Properties*, 1990, 57-78.
- Levin, I., Kaplan, W. D. and Brandon, D. G., *Acta mater.* **42**, 4, 1147-1154, 1994.
- Lin, H. T. and Becher, P. F., *J. Am. Ceram. Soc.*, 1990, **73**, 1378-1381.
- Lin, H. T. and Becher, P. F., *J. Am. Ceram. Soc.*, 1991, **74**, 1886-1893.
- Lin, H. T. and Becher, P. F., *Plastic Deformation of Ceramics*, Ed. R. C. Bradt et al. 1995, Plenum Press, New York, 543-553.
- Lin, H. T., Alexander, K. B. and Becher, P. F., *J. Am. Ceram. Soc.*, 1993, **79**, 1530-1536.
- Lipetzky, P., Nutt, S. R. and Becher, P. F., *Mat. Res. Soc. Symp. Proc.* **120**, 1988, 271-277.
- Lipetzky, P., Nutt, S. R. and Koester, D. A. and Davis, R. F., *J. Am. Ceram. Soc.*, 1991, **74**, 6, 1240-1247.
- Liu, D. S. and Majidi, P. A., *Ceram. Eng. Sci. Proc.*, 1990, **11**, 7-8, 745-753.
- Luecke, W. E. and French, D., *J. Am. Ceram. Soc.*, 1996, **79**, 1617-1626.
- Luthra, K. L. and Park, H. D., *J. Am. Ceram. Soc.*, 1990, **73**, 1014-1023.
- Majumdar, S. and Kupperman, D., *J. Am. Ceram. Soc.*, 1989, **72**, 312-313.



- Majumdar, S., Kupperman, D. and Singh J., *J. Am. Ceram. Soc.*, 1988, **71**, 858-863.
- Mendelson, M. I., *J. Am. Ceram. Soc.*, 1969, **52**, 8, 443-446.
- Morrell R. and Ashbee, K. H. G., *J. Mater. Sci.* 1973, **8**, 1271.
- Moulson, A. J., *J. Mater. Sci.*, 1979, **14**, 1017.
- Mukherjee, A. K., Bird, J. E. and Dorn, J. E., *Trans ASM*, 1969, **62**, 155-177.
- Nabarro, F. R. N., *Report of a Conference on Strength of Solids*, The Physical Society, London, 1948, **75**.
- Nan, C. W., *Prog. Mater. Sci.*, 1993, **37**, 1.
- Niihara, *J. Ceram. Soc. Japan, International Edition*, 1991, **99**, 10, 945-952
- Niihara, K. and Nakahira, A., *Advanced structural inorganic composites*, Ed. Vincenzini, P., Elsevier Science, Trieste, Italy, 1990, 637-664.
- Noyan, I. C. and Cohen, J. B., *Residual Stress, Measurement by Diffraction and Interpretation*, 1987, Springer Verlag.
- Nutt, S. R., Lipetzky, P. and Becher, P. F., *Mater. Sci. Eng.*, 1990, **A126**, 165-172.
- Nutt, S. R. and Lipetzky, P., *Mater. Sci. Eng.*, 1993, **A166**, 199.
- Nutt, S. R., *J. Am. Ceram. Soc.*, 1985, **67**, 6, 428-431.
- Nutt, S. R., *J. Am. Ceram. Soc.*, 1988, **71**, 3, 149.
- O'Meara, C.O., Suihkonen, T., Hansson, T. and Warren, R., *Mater. Sci. Eng.*, 1996, **A209**, 1-2, 251-259.
- Ohji, T., Nakahira, A., Hirano, T., Niihara, K., *J. Am. Ceram. Soc.*, **77**, 12, 1994, 3259-3262.
- Ohji, T., *Trans. ASME*, 2001, **123**, 64-69.
- Orowan, E., *Proc. Phys. Soc.*, 1940, **52**, 8-22.
- Park, C. H., Cheong, B. H., Lee, K. H. and Chang, K. J., *Phys. Rev. B*, 1994, **49**, 4485-4493.
- Park, Y. H. and Holmes, J. W., *J. Mater. Sci.*, 1992, **27**, 6341-6351.
- Poirier J. P., *Creep of crystals*, Cambridge University Press, 1985.
- Porter, J. R., Lange, F. F. and Chokshi, A. H., *Bull. Am. Ceram. Soc.*, 1987, **66**, 343.
- Porter, J. R., *Mat. Sci. Eng.* 1989, **A107**, 1-2, 127-132
- Porter, J. R., Xia, K. N. and Langdon, T. G., *Metals & Ceramic Matrix Composites: Processing, Modeling & Mechanical Behaviour*. Ed. R. B. Bhagat et al. 1990, 381-389.

- Predecki, P., Abuhasan, A. and Barrett, Adv. X-ray Anal. 1988, **31**, 231.
- Predecki, P., Abuhasan, A. and Barrett, Adv. X-ray Anal. 1991, **34**, 643.
- Rahaman, M. N., *Ceramic Processing and Sintering*, Marcel Dekker, Inc. 1995.
- Raj, R. and Ashby, M. F., *Met. Trans.* 1971, **2**, 1113-1127.
- Robert, F. D., *Inst. Phys. Conf. Ser.* 1994, **137**, 1.
- Robertson, A. G., Wilkinson, D. S. and Caceres, H. C., *J. Am. Ceram. Soc.*, 1991, **74**, 5, 915.
- Romero, J. C., Arsenault, R. J. and Krause, R. F. Jr., *Mater. Sci. Eng.*, 1995, **A201**, 1-2, 13-23.
- Root, J. H., Private communication, 2003.
- Root, J. H. and Rack, H. J. *Materials Science Forum*, 1994, **157-162**, 1475-1480.
- Sudre, O., Lam, D. C. C. and Lange, F. F., *Mat. Res. Soc. Proc.*, 1989, **155**, 309-318.
- Swan, A. H., Swain, M. V. and Dunlop, G. L., *J. Euro. Ceram. Soc.*, 1992, **10**, 317-326.
- Tiegs, T. N.; Becher, P. F., *Am. Ceram. Soc. Bull.*, 1987, **66**, 2, 339-342.
- Timoshenko, S. and Goodier, J. N., *Theory of elasticity*, McGraw-Hill, New York, 1951, 409-414.
- Todd, R. I., Bourke, M. A. M. Borsa, C. E. and Brook R. J., *Acta mater.* 1997, **45**, 4, 1791-1800.
- Tolpygo, K. B., *Sov. Phys.–Solid State (English Translation)*, 1961, **2**, 2367-2376.
- Tuffe, S., Dubois, J., Jorand, Y. and Fantozzi, G., *Ceramics International*, 1994, **20**, 6, 425-432.
- Van Wyk, C. M., *J. Txt. Inst.*, 1946, **37**, T285.
- Wang, Y. R., Liu, D. S., Majidi, A. P. and Chou T. W., *Ceram. Eng. Sci. Proc.*, 1990, **10**, 9-10, 1154-1163.
- Wang, X. L., Hubbard, C. R., Alexander, K. B., Becher, P. F. Fernandez-Baca, J. A. and Spooner, S., *J. Am. Ceram. Soc.*, 1994, **77**, 6, 1569.
- Wei, G. C. and Becher P. F., *J. Am. Ceram. Soc. Bull.*, 1985, **64**, 2, 298.
- Wilkinson, D. S. and Ham-Su, R., *Proc. of Euromat 97*, The Netherlands, 1997, **2**, 145-148.
- Wilkinson, D. S. and Pompe, W., *Acta Mater.* 1998, **46**, 4, 1357-1369.
- Wilkinson, D. S., *J. Am. Ceram. Soc.*, 1998, **81**, 2, 275-299.
- Wilson, A. J. C., *Proc. Phys. Soc.*, 1963, **81**, 41-46.
- Wilson, A. J. C., *X-ray Optics*, 2nd ed., Methuen, London, 1962.
- Xia, K. N. and Langdon, T. G., *Mat. Res. Soc. Symp. Proc.* **120**, 1988, 265-270.

Xia, K. N. and Langdon, T. G., *Acta Metall. Mater.*, 1995, **43**, 4, 1421-1427.

Xia, K. N. and Langdon, T. G., *J. Mater. Res.*, 1995, **10**, 2925-2932.

Xu, X and Holmes J. W., *J. Am. Ceram. Soc.*, 1993, **76**, 10, 2695-2700.

Yang, M. and Stevens. R., *J. Mater. Sci.*, 1990, **25**, 4658.

Zallen, R., *The Physics of Amorphous Solids*, 1983, John Wiley & Sons Inc.